DTIC FILE COPY

MENTATION PAGE

Form Approved
OMB No. 0704-0188

1a.		1b. RESTRICTIVE MARKINGS

AD-A224 504   ed

2a.	3. DISTRIBUTION / AVAILABILITY OF REPORT
2b. DECLASSIFICATION / DOWNGRADING SCHEDULE	~~Unlimited~~ Approved for public release distribution is unlimited

4. PERFORMING ORGANIZATION REPORT NUMBER(S)	5. MONITORING ORGANIZATION REPORT NUMBER(S)
AFOSR 88-0029B	AFOSR-TR- 90 0837

6a. NAME OF PERFORMING ORGANIZATION	6b. OFFICE SYMBOL (If applicable)	7a. NAME OF MONITORING ORGANIZATION
Mass. Institute of Technology		AFOSR

6c. ADDRESS (City, State, and ZIP Code)	7b. ADDRESS (City, State, and ZIP Code)
77 Mass. Avenue Cambridge, MA 02139	Bolling Air Force Base Washington, DC 20332-6448

8a. NAME OF FUNDING / SPONSORING ORGANIZATION	8b. OFFICE SYMBOL (If applicable)	9. PROCUREMENT INSTRUMENT IDENTIFICATION NUMBER
AFOSR	NA	AFOSR-88-0089

8c. ADDRESS (City, State, and ZIP Code)	10. SOURCE OF FUNDING NUMBERS			
	PROGRAM ELEMENT NO.	PROJECT NO.	TASK NO.	WORK UNIT ACCESSION NO.
Bolling Air Force Base Washington, DC 20332-6448	61102F	2302	B1	

11. TITLE (Include Security Classification)
Research into Traveling Wave Control in Flexible Structures (U)

12. PERSONAL AUTHOR(S)
Andreas H. von Flotow

13a. TYPE OF REPORT	13b. TIME COVERED	14. DATE OF REPORT (Year, Month, Day)	15. PAGE COUNT
final	FROM 1/11/88 TO 28/2/90	June 15, 1990	

16. SUPPLEMENTARY NOTATION

17.	COSATI CODES		18. SUBJECT TERMS (Continue on reverse if necessary and identify by block number)
FIELD	GROUP	SUB-GROUP	Active control, flexible structures, sensor, wave propagation.

19. ABSTRACT (Continue on reverse if necessary and identify by block number)

This report summarizes 16 months of research into travelling wave control in flexible structures. The report consists of a brief executive summary highlighting the main results of the research publications collected in the appendix.

**DTIC
S ELECTE
JUL 27 1990
D**

20. DISTRIBUTION / AVAILABILITY OF ABSTRACT	21. ABSTRACT SECURITY CLASSIFICATION
☒ UNCLASSIFIED/UNLIMITED ☒ SAME AS RPT. ☒ DTIC USERS	Unclassified
22a. NAME OF RESPONSIBLE INDIVIDUAL ~~Andreas H. von Flotow~~ SPENCER T. WU	**22b. TELEPHONE (Include Area Code)** ~~(617) 253-4865~~ (202) 767-	**22c. OFFICE SYMBOL** NA

DD Form 1473, JUN 86   Previous editions are obsolete.

90 07 26 019 (U)

Final Report

on

Research into Traveling Wave Control in Flexible Structures

performed at

Department of Aeronautics and Astronautics
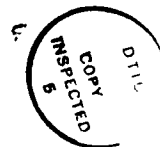Massachusetts Institute of Technology

for the

Air Force Office of Scientific Research

(Grant AFOSR-88-0029B)

Nov 1, 1988 – Feb 28, 1990

Summary

This report summarizes 16 months of research into active control of elastic wave propagation in flexible structures. The research was performed collaboratively between three graduate student research assistants; Simon Collins, Doug MacMartin, and Darryll Pines, and two faculty supervisors; Professors Steve Hall and Andy von Flotow.

The report format is that of a brief executive summary supported by an extensive appendix containint the research publications generated in the course of this research.

The research performed can be broken into two major fields;

1. Broadband damping by impedance matching the control system to the underlying wave (or dereverberated) impedance of a flexible structure. Prof. Hall and Doug MacMartin contributed most strongly to this research.

2. Sensor development for purposes of wave observation and control. Prof. von Flotow and Simon Collins and Darryll Pines contributed most strongly to this research.

The executive summary of the next few pages consists of two separate sections corresponding to these two thrusts of the research.

Sensors for Wave Observation and Control

The prior few years of research into active control of wave propagation have repeatedly yielded the suggestion that a factor that strongly limited achievable performance was the difficulty of sensing the quantities of interest; the amplitudes of the individual wave types simultaneously present in any vibrating structure. With this research project we made the development of such sensors a high priority for the first time.

The MS thesis of Simon Collins, due to be finished in July, 1990, was started under this funding. Simon focuses upon spatial convolution of strain signals with continuous, distributed piezo-film PVDF sensors. He is interested in performing, through spatial convolution, some of the acausal temporal filtering required of the wave control designs of the past few years. The theory for this is developed in his first paper on this topic, [8] and experimental results are presented for sensors which can be interpreted as wave number filters. The experiments are performed with bending waves on a one-dimensional beam.

Darryll Pines, for his PhD thesis research, is investigating arrays of point sensors, distributed PVDF sensors, and arrays of PVDF and point sensors. His goal is to deveolop wave type/wave number sensors, and to employ them in a wave control demonstration. He is building upon his own MS thesis research, [9], in which active control of wave propagation was strongly limited by the use of a strain rather than wave sensor. Darryll's first paper on his PhD research [10] is essentially a catalog of examples of arrays of discrete point sensors used to infer the wave-number/wave-type spectra of one-dimensional structural waveguides (beams and rods). Any type of point sensors can be used; accelerometers and strain gages are obvious choices. Pines develops criteria for spacing of these point sensors, and for the temporal filtering that is applied to each sensor signal before they are combined into signals representing individual wave types. Important drivers in this design are: 1. the assumed dispersion characteristics of the waveguide, 2. the assumed spectrum of the signal to be detected, and 3. the noise characteristics of the individual point sensors.

Dereverberated Mobility/$\mathcal{H}_\infty$ Power Flow Approach

The goal of this research is broadband active control of structures with significant uncertainty. If the uncertainty in modal frequencies is of the same order as the modal spacing, then methods such as finite elements are not appropriate for modelling the structure [1,2]. The resulting large order model is extremely sensitive to small parameter changes, in the prediction of natural frequencies, and especially in the prediction of mode shapes. As a result, much of the information contained in such a model is meaningless.

An alternative approach is to use wave-based models of the structure. In Miller *et al.* [3], the structure is represented as being composed of one-dimensional waveguides. These meet at junctions, and only the junction at which the control acts needs to be modelled. The control law can be derived based only on a model of the local dynamics, and this model is not dependent on uncertainty in the remainder of the structure. However, arbitrary structures may be difficult to model using this approach because of the difficulty in obtaining an accurate wave description.

For a general structure, a local model of the dynamics near the actuator and sensor pair is still desirable. MacMartin and Hall [4,5] have used a dereverberated mobility [6] model instead of a wave model. The response at a point can be considered to be the sum of two parts: a *direct field*, due to the local dynamics; and a *reverberant field*, which is caused by energy reflected back from other parts of the structure. The term "dereverberated" implies that the "reverberant" part of the response has been removed before computing the mobility. The dereverberated mobility may be approximated through the use of the cepstrum [6] of the impulse response, or by taking the average of the log magnitude of the transfer function.

The fundamental distinction between this and wave approaches is the ability to treat generic structures. While the concept of direct and reverberant fields is based on wave ideas, there is no requirement to actually identify a local wave model. All that is needed is the input/output behavior at the driving point, which may be found from experimental data, calculated from some nominal model, or found analytically, perhaps even from a wave model. This indicates another important advantage of this modelling approach – the ability to use experimental data to generate a measurement based model.

The control design approach for this model should guarantee stability and provide "good"

performance. For a lightly damped system, the power dissipated by the control system is a measure of the damping that is achieved, and guarantees stability if it is positive at all frequencies. Ideally, a compensator that dissipates the most power possible at every frequency is desired. This compensator is in general noncausal, and cannot be implemented. Miller *et al.* [3] maximize the frequency weighted power dissipation associated with the control, using Weiner-Hopf techniques to ensure causality. The drawback to this optimization is that it will allow power to be generated at some frequencies in order to achieve greater power dissipation at other frequencies. Since the driving point mobility of a structure is positive real, stability can be guaranteed by requiring that the compensator be positive real. Using this result, Miller *et al.* approximate their optimal compensator with a positive real form. The final result is suboptimal because the positive real constraint is applied in a somewhat *ad hoc* manner.

MacMartin and Hall [4] enforce the positive real constraint by minimizing the maximum value over frequency of the power flow into the structure. This can be reformulated as an $\mathcal{H}_\infty$ control problem, as opposed to the $\mathcal{H}_2$ approach of Miller *et al.* This minimization results in power being dissipated at all frequencies, so that closed loop stability is guaranteed. The importance of a certain frequency range can be increased through the use of a weighting function.

The dereverberated mobility/$\mathcal{H}_\infty$ power flow approach has been applied to several examples [4], and has also been demonstrated succesfully in an experiment [7]. This approach to modelling and control design allows significant damping to be added to many modes of a structure, without the large effort in system identification, off-line computation, and compensator complexity that would be required of many control design techniques.

References

[1] von Flotow, A. H., "The Acoustic Limit of Structural Dynamics," in *Large Space Structures: Dynamics and Control,* Atluri and Amos (ed.), Springer-Verlag, 1988, pp. 213-238.

[2] Hodges, C. H. and Woodhouse, J., "Theories of Noise and Vibration Transmission in

Complex Structures," *Reports on Progress in Physics,* Vol. 49, 1986, pp. 107-170.

[3] Miller, D. W., Hall, S. R. and von Flotow, A. H., "Optimal Control of Power Flow at Structural Junctions," *Proceedings of the 1989 American Control Conference,* Pittsburgh, PA, June 1989.

[4] MacMartin, D. G. and Hall, S. R., "An $\mathcal{H}_\infty$ Power Flow Approach to Control of Uncertain Structures," *Proceedings of the 1990 American Control Conference,* San Diego, CA, May 1990, pp. 3073-3080, to appear in *J. of Guidance Control and Dynamics.*

[5] MacMartin, D. G., *An $\mathcal{H}_\infty$ Power Flow Approach to Control of Uncertain Structures,* S.M. Thesis, Department of Aeronautics and Astronautics, M.I.T., Cambridge, MA, Feb. 1990.

[6] Lyon, R. H., *Machinery Noise and Diagnostics,* Butterworth Publishing, June 1987.

[7] MacMartin, D. G., and Hall, S. R., "Structural Control Experiments Using an $\mathcal{H}_\infty$ Power Flow Approach," to be presented at *1990 AIAA Guidance Navigation and Control Conference,* Portland, OR, Aug. 1990.

[8] Miller, D. W., Collins, S. A., and Peltzman, S. P., "Development of Spatially Convolving Sensors for Structural Control Applications," *Proceedings of the 31st AIAA SDM Conference,* April 1990, Long Beach, CA.

[9] Pines, D. J., and von Flotow, A. H., "Active Control of Bending Wave Propagation at Acoustic Frequencies," in press, *J. of Sound and Vibration,* 1990.

[10] Pines, D. J., and von Flotow, A. H., "Development of Wave-mode Observers for Active Wave Control of One-Dimensional Structures," *Proceedings of the International Congress on Recent Developments in Air and Structure Borne Sound and Vibration,* March 6-8, 1990, Auburn Univ.

Appendix

This appendix collects the research publications funded primarily by this contract.

Contents:

MacMartin, D. G., *An $\mathcal{H}_\infty$ Power Flow Approach to Control of Uncertain Structures,* S.M. Thesis, Department of Aeronautics and Astronautics, M.I.T., Cambridge, MA, Feb. 1990.

Miller, D. W., Hall, S. R. and von Flotow, A. H., "Optimal Control of Power Flow at Structural Junctions," *Proceedings of the 1989 American Control Conference,* Pittsburgh, PA, June 1989.

Miller, D. W., and Hall, S. R., "Experimental Results Using Travelling Wave Power Flow Techniques," *Proceedings of the ASME 1989 Winter Meeting,* Dec. 1989.

MacMartin, D. G. and Hall, S. R., "An $\mathcal{H}_\infty$ Power Flow Approach to Control of Uncertain Structures," *Proceedings of the 1990 American Control Conference,* San Diego, CA, May 1990, pp. 3073-3080, to appear in *J. of Guidance Control and Dynamics.*

MacMartin, D. G., and Hall, S. R., "Structural Control Experiments Using an $\mathcal{H}_\infty$ Power Flow Approach," to be presented at *1990 AIAA Guidance Navigation and Control Conference,* Portland, OR, Aug. 1990.

Miller, D. W., Collins, S. A., and Peltzman, S. P., "Development of Spatially Convolving Sensors for Structural Control Applications," *Proceedings of the 31st AIAA SDM Conference,* April 1990, Long Beach, CA.

Pines, D. J., and von Flotow, A. H., "Development of Wave-mode Observers for Active Wave Control of One-Dimensional Structures," *Proceedings of the International Congress on Recent Developments in Air and Structure Borne Sound and Vibration,* March 6-8, 1990, Auburn Univ.

An $\mathcal{H}_\infty$ Power Flow Approach to Control of Uncertain Structures

by

Douglas G. MacMartin

B.A.Sc. University of Toronto (1987)

SUBMITTED IN PARTIAL FULFILLMENT OF THE
REQUIREMENTS FOR THE DEGREE OF

Master of Science
in
Aeronautics and Astronautics
at the
Massachusetts Institute of Technology
February 1990

Signature of Author _____

Department of Aeronautics and Astronautics
October 27, 1989

Certified by _____

Professor Steven R. Hall
Thesis Supervisor, Department of Aeronautics and Astronautics

Accepted by _____

Professor Harold Y. Wachman
Chairman, Department Graduate Comittee

An $\mathcal{H}_\infty$ Power Flow Approach to Control of Uncertain Structures

by

Douglas G. MacMartin

Submitted to the Department of Aeronautics and Astronautics
on October 27, 1989 in partial fulfillment of the
requirements for the Degree of Master of Science in
Aeronautics and Astronautics

Abstract

A technique is described for generating guaranteed stable control laws for uncertain, modally dense structures with collocated sensors and actuators. By ignoring the reverberant response created by reflections from other parts of the structure, a dereverberated mobility model can be developed which accurately models the local dynamics of the structure. This is similar in many respects to a wave based model, but can treat more general structures, not only those that can be represented as a collection of waveguides. This model can be determined directly from transfer function data using an analysis technique based on the complex cepstrum. In order to minimize the effect of disturbances propagating through the structure, the power dissipated by the controller is maximized in an $\mathcal{H}_\infty$ sense. This guarantees that the controller is positive real, and thus that the system will remain stable for any structural uncertainty. The approach is demonstrated for several examples. Experimental results on a beam in bending are presented. The controller based on this approach is much more effective than simple collocated rate feedback. Significant damping was added to many modes of the structure, without requiring a detailed or high order model of the beam.

Thesis Supervisor: Dr. Steven R. Hall, Sc.D.,
     Boeing Assistant Professor of
     Aeronautics and Astronautics

Acknowledgements

Contents

List of Figures

Chapter 1

Introduction

1.1 Motivation and Background

Broadband active control of flexible structures is difficult for several reasons. Structures tend to be very lightly damped, modally rich, and difficult to model in detail, due to their large sensitivity to parameter variations. It is well known [4] that for many applications, there are likely to be many flexible modes within the desired bandwidth of a structural control system. This is due in part to the light damping that would be anticipated, for example in large space structures, which implies that many modes can contribute to the performance. Also, performance requirements may push the bandwidth higher directly, for example in noise control of machinery, where the bandwidth must clearly include acoustic frequencies, and therefore many flexible modes.

One of the problems associated with broadband control of structures is the uncertainty in the plant model. A state space model of a structure must be at best an approximation, since the true structure is infinite-dimensional. Finite element methods are typically used to model a structure, and are sometimes capable of modelling the lowest modes quite accurately. However, in the region of high modal density, any model is likely to be highly inaccurate. Models of structures with

8

closely spaced modes in particular tend to be extremely sensitive to small parameter changes, in their prediction of natural frequencies, and especially in their prediction of mode shapes. As a result, the actual structure to which the control will eventually be applied may differ significantly from the model for which it was designed. Thus some knowledge about the uncertainty must be taken into account when designing the controllers.

A variety of approaches have been used to deal with uncertainty in the plant model. One typical approach is to treat the uncertainty as a multiplicative error which is totally unstructured. Bounds are specified on the magnitude of the perturbation, while the phase is assumed unknown. In this case, stability can be guaranteed by requiring that the closed loop complementary sensitivity be bounded above by the inverse of the maximum singular value of the uncertainty bound [11]. Thus for the nominal plant $G(s)$, if the true plant is given by

$$G_{\text{true}}(s) = (I + L(s))G(s) \tag{1.1}$$

then the system is stable with feedback matrix $K(s)$ if

$$\bar{\sigma}\left(G(j\omega)K(j\omega)(I + G(j\omega)K(j\omega))^{-1}\right) < \frac{1}{L_m(\omega)} \quad \forall \ \omega \tag{1.2}$$

where $\bar{\sigma}(\cdot)$ is the maximum singular value, and L_m is a function which satisfies

$$L_m(j\omega) \geq |\bar{\sigma}(L(j\omega))| \quad \forall \ \omega \tag{1.3}$$

This approach is reasonable for truly unstructured uncertainty such as unmodelled high frequency dynamics, and also may not be overly conservative for some parametric, or structured uncertainty. However, for lightly damped, modally dense systems, this approach will be extremely conservative. If the poles and zeroes are close together, a small parameter error may result in the true pole lying at the frequency of the modelled zero. The model error required in this case is significantly larger than the plant itself [7]. This would imply that almost no control can be

9
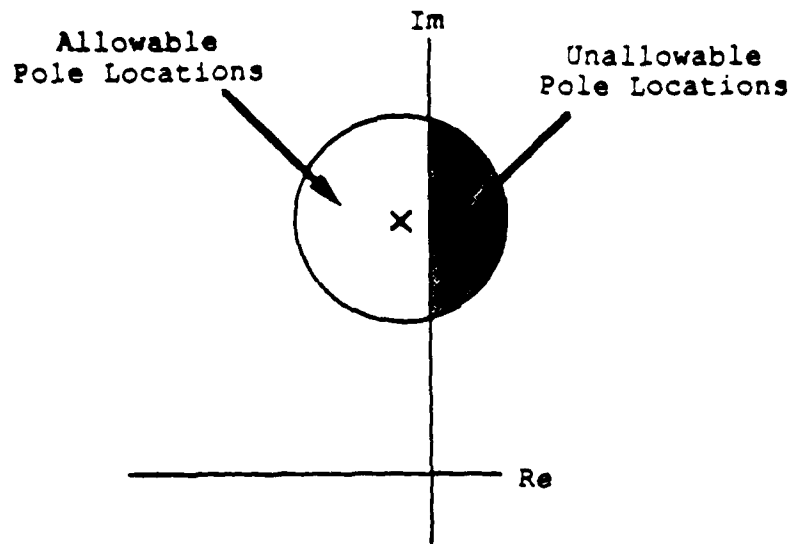
Figure 1.1: No knowledge of uncertainty direction may result in physically impossible pole locations

applied in this region, and thus that nothing can be done to damp this mode. The problem lies in the assumption of no knowledge about the direction of uncertainty. In fact, since the structure is known to be stable yet lightly damped, there can be far more uncertainty in the imaginary part of the pole location, or frequency, than in the real part [5], as shown in Figure 1.1. Though the relative error in the real part is large, the absolute error is small compared to the frequency, since right half plane poles are not possible.

This conservative stability robustness test can be relaxed by taking advantage of the positivity of structures. A transfer matrix G is positive real if

$$G(s) + G^T(-s) \geq 0 \quad \forall \ \text{Re}(s) > 0 \tag{1.4}$$

and strictly positive real if the first inequality is strict [1]. Any strictly positive real compensator will be stabilizing for any positive real plant. If the perturbation matrix L is defined as just the deviation of the plant from the positive real condition, then stability can be guaranteed if the compensator is both strictly positive real and

satisfies the earlier singular value test (Equations (1.2) and (1.3)) for this smaller perturbation [37].

Another approach for dealing with uncertainty in some parameters is the Maximum Entropy/Optimal Projection (MEOP) approach by Bernstein and Hyland [5]. The goal of MEOP is to force the LQG algorithm to provide a more robust controller, by including information about parametric uncertainty into the plant model. This is done by using a stochastic model of the plant uncertainty. This approach yields compensators with good performance over the entire range of parameters, at the expense of a cumbersome numerical algorithm. However, there is no guarantee of stability using this method. The μ-synthesis approach by Doyle [12] also allows for some structure in the uncertainty, and allows the performance to be optimized not just for the nominal model, but for any model within the specified uncertainty bounds. Control architectures such as HAC/LAC (High-Authority Control/Low-Authority Control) [2], hierarchic control [18,20], and many others such as [3], have been designed to deal with the spillover problems associated with uncertainty in modelling structures. Other approaches have also been developed to deal with control design for uncertain structures; a good review of many of these can be found in [25].

Many of these approaches to control design for uncertain structures begin with a large order, detailed nominal model of the structure, and deal with uncertainty by attempting to model it, as well as the nominal plant, in some fashion. However, if the nominal model contains significant error, then the detailed information it contains is meaningless, and has no effect other than to increase the computational burden associated with the control design. Indeed, for broadband control of a modally rich structure, the dimension of the plant required to model each mode may be prohibitive for many control design techniques. Instead, only the information that can be accurately modelled should be included in the description of the plant [5].

With this philosophy, there has been r ich research on the use of wave based

models for use in structural control. Early work in this field includes that of Vaughan [39], who identified a matched termination as being an appropriate control law for a beam, and gave suitable approximations for the implementation of the irrational transfer functions required. More recently, a number of researchers have done both theoretical [17,23,28,35,41] and experimental [29,32,33,40] work in wave-based control for structures. The assumption in all of this research is that the local dynamics can be accurately modelled, and that an effective control system can be derived based only on this information. The control derivations either attempt to eliminate reflection or transmission by controlling elements of the scattering matrix, or are optimal approaches, based on maximizing some quantity such as the power dissipation.

Mace [23] derives the control necessary to cancel the incoming disturbances by creating waves of opposite sign. This methodology can only be effectively applied to one-dimensional waveguides. For a Timoshenko beam, Hagedorn and Schmidt [17] maximize the power flow out of the beam to obtain 'energy valves' that allow energy to travel in one direction, but not the other. The modelling formalism of Miller *et al.* [28], or that of von Flotow [41] allows the analysis of somewhat more general structures, including any arbitrary network of waveguides. In this framework, control laws can be developed to set certain elements of the scattering matrix to zero, or to maximize the power flow out of the structure. The experimental results cited earlier have all applied wave control to beams. Von Flotow and Shäfer [40] designed control laws to modify elements of the scattering matrix, and compared their results with those for modal control. Optimal control techniques were tested by Miller and Hall [29].

These wave control methods have demonstrated that good performance can be achieved on a structure without requiring knowledge of uncertain information such as the modal frequencies. One drawback to many of the wave-based approaches is that they cannot always be applied to a general structure, at best being able to

treat networks of waveguides.

Of particular relevance to this thesis is the optimal control approach of Miller
et al. [28]. The structure is represented as being composed of one-dimensional
waveguides which meet at junctions, and only the junction at which the control
acts is modelled. Using Weiner-Hopf techniques to ensure causality, Miller et al.
maximize the frequency weighted power dissipation associated with the control.
The drawback to this approach is that it will allow power to be generated at some
frequencies in order to achieve greater power dissipation at other frequencies. If
there is a mode of the system at such a frequency, it may be destabilized by this
compensator. This problem is corrected by approximating the optimal compensator
with a positive real form, which is guaranteed to be stabilizing. The final result,
then, is suboptimal, because the positive real constraint is applied in a somewhat
ad hoc manner. Thus while this design procedure is attractive, an approach which
treats more general structures and provides a guarantee of stability is desired.

1.2 Approach

This thesis describes a new approach to the modelling and control of uncertain
structures that will guarantee both stability robustness and performance robustness.
Much of the material presented here has been summarized in a previous paper [24].

The goal is to obtain a compensator that will provide broadband damping to the
structure. This might be used in conjunction with a low order modal compensator
which could provide good performance on those modes that could be well modelled.
Thus this could be used as the low authority controller in a HAC/LAC architecture
[2], rather than the rate feedback typically used. Rate feedback is guaranteed to
be stable, but it is not necessarily optimal. In general it is possible to add more
damping to a structure than can be obtained through rate feedback [29].

The model used in this thesis is the dereverberated mobility at a collocated and

dual actuator/sensor pair [22]. Only that part of the response which is due to the local dynamics is retained in the model. This can be shown to correspond in the frequency domain to an averaging, or smoothing, of the transfer function. This model bears some relationship to the wave approach of [28], but it is more general, as it allows structures which are not networks of waveguides to be treated.

Since the driving point mobility of a structure is positive real, stability can be guaranteed by requiring that the compensator be positive real. This is assured by minimizing the maximum value over frequency of the power flow into the structure. This minimax problem can be reformulated as an $\mathcal{H}_\infty$ optimization problem, and then solved using existing software. This results in a compensator which dissipates power at all frequencies. Taking energy as the Lyapunov function shows that the closed loop system must be stable for all plants, provided that the sensors and actuators are not mismodelled. Extensions based on the results of Slater [37] to allow for actuator and sensor dynamics, time delays, or actuators and sensors that are not collocated, are possible but are not treated here.

1.3 Overview

The remainder of this thesis is divided into six chapters. Chapter 2 presents some of the necessary mathematical background. This includes some theory on $\mathcal{H}_\infty$ control, and results on spectral factorization from [15] that will be needed in Chapter 4. Some of the wave mode theory of [26] is also presented, this will be used in deriving transfer functions in later chapters. In Chapter 3, the approach to modelling is presented, and parallels will be drawn with existing wave approaches. Both a computational approach based on the calculation of the complex cepstrum, and a simpler approach based on smoothing the transfer function are presented. The formulation of the control problem appears in Chapter 4. The unconstrained problem is solved first, with no requirement that the solution be causal. The solution to the

14

causal problem is solved by representing it as an $\mathcal{H}_\infty$ control problem, and state-space methods are given to obtain this representation. Chapter 5 demonstrates the approach for several examples. Experimental results on a 24 foot brass beam are presented in Chapter 6. These are compared with previous experimental results using rate feedback and $\mathcal{H}_2$ optimal wave control on the same structure in [29]. Finally, Chapter 7 presents the main conclusions and contributions of the thesis, and discusses a number of possible extensions to this research.

Chapter 2

Mathematical Preliminaries

In Chapter 4, the $\mathcal{H}_\infty$ control design approach will be required, as will a number of results on state space spectral factorizations. Some elements of wave mode theory will also be useful in deriving open and closed loop transfer functions in the examples in Chapter 5. In the interest of simplifying the later discussions, the necessary mathematical background will be presented here.

2.1 $\mathcal{H}_\infty$ Control

A good reference for $\mathcal{H}_\infty$ theory is Francis' book [15], from which much of the following material is drawn. Before discussing the $\mathcal{H}_\infty$ control design method, a number of definitions are required. First, define the Hardy space $\mathcal{H}_\infty$:

Definition 1 *$\mathcal{H}_\infty$ is the space of all complex functions of a complex variable which are analytic and bounded in the open right half plane.*

Thus, $G(s) \in \mathcal{H}_\infty$ if $G(s)$ is both stable and proper. (Though it need not be strictly proper.)

Definition 2 *The norm* $\|\cdot\|_\infty$ *on* $\mathcal{H}_\infty$ *is given in the scalar case by*

$$\|G(s)\|_\infty = \sup_{\text{Re}(s)>0} |G(s)| \tag{2.1}$$

Thus, the infinity norm is the supremum of a function in the right half plane. In the matrix function case, the infinity norm is the supremum of the largest singular value of the matrix. From the maximum modulus theorem, it can be shown that any function analytic and bounded in some region achieves its maximum over that region on the boundary, thus

$$\|G(s)\|_\infty = \sup_{\omega \in \mathcal{R}} |G(j\omega)| \tag{2.2}$$

Furthermore, if we consider G to be an operator acting on some (in general, vector) variable x, then the norm of G can be written as an induced operator norm as

$$\|G(s)\|_\infty = \sup_{x \in \mathcal{H}_\infty} \frac{\|Gx\|_2}{\|x\|_2} \tag{2.3}$$

$$= \sup_{\substack{x \in \mathcal{H}_\infty \\ \|x\|_2=1}} \|Gx\|_2 \tag{2.4}$$

This defines the infinity norm in terms of a norm over $\mathcal{H}_2$, which we have yet to define.

Definition 3 $\mathcal{H}_2$ *is the space of all complex functions of a complex variable which are analytic in the open right half plane, and satisfy*

$$\sup_{\xi>0} \left[\frac{1}{2\pi} \int_{-\infty}^{\infty} Tr\left\{ |G(\xi + j\omega)|^2 \right\} d\omega \right] < \infty$$

The norm $\|\cdot\|_2$ *on* $\mathcal{H}_2$ *is the square root of the left hand side of the above expression, which can be shown to be equivalent to*

$$\|G(s)\|_2 = \left[\frac{1}{2\pi} \int_{-\infty}^{\infty} Tr\left\{ |G(j\omega)|^2 \right\} d\omega \right]^{1/2} \tag{2.5}$$
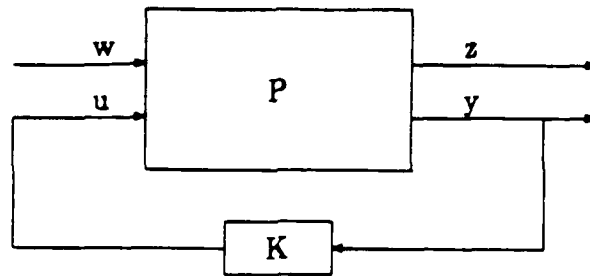
Figure 2.1: Four Block Problem

Further, define *inner* and *outer* functions, using the notation

$$G^{\sim}(s) = G^{T}(-s) \tag{2.6}$$

Definition 4 *A matrix G in $\mathcal{H}_{\infty}$ is inner if $G^{\sim}G = I$. G is outer if it has no zeroes in $\text{Re}(s) > 0$.*

Thus an inner function has unit magnitude, is stable, and purely nonminimum phase. An outer function is minimum phase. Note that multiplication by an inner function does not change either the $\mathcal{H}_{\infty}$ or the $\mathcal{H}_2$ norm of a matrix function.

Now consider the standard four-block control problem, as shown in Figure 2.1. The goal is to find a stabilizing compensator K from the sensed output y to the control input u which will minimize in an appropriate sense the closed loop transfer function from the disturbance w to the controlled variable z. This transfer function is given by the lower linear fractional transformation

$$H(P, K) = P_{wz} + P_{wy}K(I - P_{uy}K)^{-1}P_{uz} \tag{2.7}$$

Note that w contains all disturbance sources, including both process and measurement noise. Similarly, z contains all the quantities to be minimized, including both state and control penalties. In general, the plant P includes the system, actuator and sensor dynamics, and the dynamics of any weighting on w or z.

18

This representation of the problem is standard in the $\mathcal{H}_\infty$ control formulation. The standard Linear Quadratic Gaussian (or $\mathcal{H}_2$) problem can also be written as the same four block problem, the only distinction being the norm used in the optimization, and the implicit assumptions about the characteristics of the disturbance. In the context of LQG, the disturbance is gaussian white noise, and the $\mathcal{H}_2$-norm of the controlled variable is minimized. If the disturbance can accurately be characterized in this form, then LQG may be the appropriate technique to use. The $\mathcal{H}_\infty$ problem instead minimizes the $\mathcal{H}_\infty$-norm of the transfer function from w to z. From the definition of the operator induced norm Equation (2.4), the appropriate interpretation of the disturbance is the worst case disturbance, having unit power at a single frequency (which corresponds to the maximum amplification of the transfer function). Thus $\mathcal{H}_\infty$ is suited to problems in which the disturbances are likely to have significant narrowband energy at a poorly characterized frequency [6].

Define the notation

$$G(s) = \left[\begin{array}{c|c} A & B \\ \hline C & D \end{array}\right] = C(sI - A)^{-1}B + D \qquad (2.8)$$

Hence G can be represented by the finite dimensional system of ordinary differential equations

$$\dot{x} = Ax + Bu$$

$$y = Cx + Du \qquad (2.9)$$

Then the **four-block** transfer function matrix in Figure 2.1 may be represented as

$$P = \left[\begin{array}{c|cc} A & B_1 & B_2 \\ \hline C_1 & D_{11} & D_{12} \\ C_2 & D_{21} & D_{22} \end{array}\right] \qquad (2.10)$$

The $\mathcal{H}_\infty$ control problem formulated in this way can be solved using state space methods via an iterative solution to two Riccati equations. These are presented in

[13] with some slightly restrictive assumptions, and in [16] for the general case. The iteration searches for the minimum value of the $\mathcal{H}_\infty$ norm of $H(P, K)$, denoted γ. It is worth noting that at this optimal solution, $H(P, K) = \gamma$ everywhere; the closed loop transfer function is a constant function of frequency.

In addition to the purely LQG solution and the $\mathcal{H}_\infty$ solution to the four-block problem, a combined problem can be studied with a constraint on the $\mathcal{H}_\infty$ performance in an $\mathcal{H}_2$ optimization [6]. This allows a design trade-off between $\mathcal{H}_\infty$ objectives and $\mathcal{H}_2$ objectives, resulting in a compensator that combines the benefits of each. This problem simplifies immensely if the same quantity is penalized in both the $\mathcal{H}_\infty$ and $\mathcal{H}_2$ formulations. In this case, it is equivalent to a maximum entropy problem [31], the solution to which is readily obtainable from the same two Riccati equations as before [30]. In fact, this is equivalent to simply removing the iteration in the $\mathcal{H}_\infty$ solution procedure.

2.2   Spectral Factorization

As is the case for $\mathcal{H}_\infty$ theory, a good reference on spectral factorization is Francis [15], in which the details of the following results are given. The algorithms and theorems will be presented here without proof.

Before proceeding with the definition of a spectral factor and the algorithm for computing it, some additional results from Equation (2.8) are useful. From the definition (2.6) and the expansion in Equation (2.8),

$$G^{\sim}(s) = \left[\begin{array}{c|c} -A^T & -C^T \\ \hline B^T & D^T \end{array} \right] \tag{2.11}$$

The inverse of G can be expressed by writing G in differential equation form (Equation (2.9)), and manipulating to obtain the input as a function of the output,

$$G^{-1}(s) = \left[\begin{array}{c|c} A - BD^{-1}C & BD^{-1} \\ \hline -D^{-1}C & D^{-1} \end{array} \right] \tag{2.12}$$

Of course, this is valid provided $D \neq 0$, so that G^{-1} is proper. For notational purposes, define

$$A^\times = A - BD^{-1}C \qquad (2.13)$$

Finally, if T is a nonsingular transformation matrix, then

$$\left[\begin{array}{c|c} A & B \\ \hline C & D \end{array}\right] = \left[\begin{array}{c|c} T^{-1}AT & T^{-1}B \\ \hline CT & D \end{array}\right] \qquad (2.14)$$

Now, define the spectral factorization of $G(s)$.

Definition 5 *Consider $G(s)$ square with $G^\sim = G$, G and G^{-1} proper with no poles on the imaginary axis, and $G(\infty) > 0$. Then G_- is a spectral factor of $G(s)$ if*

$$G = G_-^\sim G_- \qquad (2.15)$$

and

$$G_-, G_-^{-1} \in \mathcal{H}_\infty \qquad (2.16)$$

G_- is a co-spectral factor of G if, instead of the first condition,

$$G = G_- G_-^\sim \qquad (2.17)$$

with the second condition still holding.

Note that if G_- is a spectral factor of G, then G_-^T is a co-spectral factor of G^T. Thus the same algorithm may be used to compute either the spectral factor, or the co-spectral factor.

From the definition, it is clear that the goal is to split G into two components, one of which is stable and minimum phase, the other of which is anti-stable and purely non-minimum phase. The approach is to find two subspaces, one corresponding to the unstable part of G, and the other corresponding to the stable part of G^{-1}, or the minimum phase part of G. Then if the two spaces are complementary, that is,

21

they are independent and together span the entire space, then G can be factored into the two desired components.

For G given as in Equation (2.8), the subspace corresponding to the stable part of G is denoted $\mathbf{X}_-(A)$, and that corresponding to the unstable part is $\mathbf{X}_+(A)$. The subspace corresponding to the minimum phase zeroes of G is the same as that corresponding to the left half plane poles of G^{-1}, or $\mathbf{X}_-(A^\times)$.

A transfer matrix $G(s)$ satisfying the conuitions in the definition of the spectral factor can be written as

$$G = D + G_1 + G_1^\sim \tag{2.18}$$

where G_1 is stable, minimum phase, and strictly proper. Find a minimal representation of G_1:

$$G_1 = \left[\begin{array}{c|c} A_1 & B_1 \\ \hline C_1 & 0 \end{array}\right] \tag{2.19}$$

Thus from Equations (2.11), (2.18) and (2.19),

$$G = \left[\begin{array}{cc|c} A_1 & 0 & B_1 \\ 0 & -A_1^T & -C_1^T \\ \hline C_1 & B_1^T & D \end{array}\right] \tag{2.20}$$

Since A_1 is stable and $-A_1^T$ is anti-stable,

$$\mathbf{X}_+(A) = \operatorname{Im}\left[\begin{array}{c} 0 \\ I \end{array}\right] \tag{2.21}$$

where $\operatorname{Im}(\cdot)$ denotes the image of $(\cdot)$.

At this point, some results about Hamiltonian matrices are required.

Definition 6

$$H = \left[\begin{array}{cc} A & -R \\ -Q & -A^T \end{array}\right] \tag{2.22}$$

is a Hamiltonian matrix if Q and R are symmetric, and R is either positive semidefinite or negative semi-definite.

The following results all require that H have no eigenvalues on the imaginary axis, and that (A, R) be stabilizable.

If R in Equation (2.22) is zero, then there exists a unique matrix X satisfying the Lyapunov equation

$$A^T X + XA + Q = 0 \tag{2.23}$$

and the modal subspaces of H are given by

$$\mathbf{X}_+(H) = \text{Im} \begin{bmatrix} 0 \\ I \end{bmatrix} \tag{2.24}$$

$$\mathbf{X}_-(H) = \text{Im} \begin{bmatrix} I \\ X \end{bmatrix} \tag{2.25}$$

Note that due to the assumption of (A, R) being stabilizable, this holds only for stable A.

Now consider the case with general R. There exists a unique symmetric matrix X denoted

$$X = Ric\{H\} \tag{2.26}$$

which stabilizes $A - RX$, and satisfies the Riccati equation

$$A^T X + XA + Q - XRX = 0 \tag{2.27}$$

Again,

$$\mathbf{X}_-(H) = \text{Im} \begin{bmatrix} I \\ X \end{bmatrix} \tag{2.28}$$

Furthermore, $\mathbf{X}_-(H)$ and $\text{Im} \begin{bmatrix} 0 \\ I \end{bmatrix}$ are complementary.

Now, return to the spectral factorization problem. The modal subspace $\mathbf{X}_+(A)$ is given by Equation (2.21). It remains to find a representation for $\mathbf{X}_-(A^\times)$, and

23

show that the two are complementary. However,

$$A^\times = \begin{bmatrix} A_1 & 0 \\ 0 & -A_1^T \end{bmatrix} - \begin{bmatrix} B_1 \\ -C_1^T \end{bmatrix} D^{-1} \begin{bmatrix} C_1 & B_1^T \end{bmatrix} \tag{2.29}$$

$$= \begin{bmatrix} A_1 - B_1 D^{-1} C_1 & -B_1 D^{-1} B_1^T \\ C_1^T D^{-1} C_1 & -(A_1 - B_1 D^{-1} C_1) \end{bmatrix} \tag{2.30}$$

is a Hamiltonian matrix. Thus $\mathbf{X}_-(A^\times)$ is given by Equation (2.28), with

$$X = Ric\left\{A^\times\right\} \tag{2.31}$$

and this modal subspace is complementary to $\mathbf{X}_+(A)$.

Defining the transformation matrix

$$T = \begin{bmatrix} I & 0 \\ X & I \end{bmatrix} \tag{2.32}$$

and applying (2.11), then

$$G = \left[\begin{array}{cc|c} A_1 & 0 & B_1 \\ -(C_1 + B_1^T X)^T D^{-1} (C_1 + B_1^T X) & -A_1^T & -(C_1^T + X B_1) \\ \hline C_1 + B_1^T X & B_1^T & D \end{array} \right] \tag{2.33}$$

From this, one can check that

$$G_-(s) = \left[\begin{array}{c|c} A_1 & B_1 \\ \hline D^{-1/2}(C_1 + B_1^T X) & D^{1/2} \end{array} \right] \tag{2.34}$$

satisfies both Equations (2.15) and (2.16).

For $D \neq 0$, the spectral factor of G can be found with this algorithm from the solution to a single Riccati equation. Results also exist for $D = 0$, for example in [42].

2.3 Wave Modelling

This section briefly summarizes a few of the results of Miller [26] that will be used in subsequent chapters.

The partial differential equation (PDE) of a structural member can be transformed into the frequency domain, and written in state space form as

$$\frac{dy}{dx} = A(\omega)y \tag{2.35}$$

where y is a vector of generalized displacements and internal forces at the cross-section x. The eigenvalues of A correspond to wave modes that travel independently. Thus there exists a transformation matrix Y relating the cross-sectional variables y to the wave mode amplitudes w. Since these wave modes travel independently, there exists a diagonal transmission matrix ξ relating the wave mode amplitudes at one position x_1 to those at another. Thus

$$w(x_2, \omega) = \xi(x_2, x_1, \omega)w(x_1, \omega) \tag{2.36}$$

At a junction, such as a boundary where actuator forces act, the wave modes can be split into incoming (w_i) and outgoing (w_o) elements. Partitioning y into displacements u and forces f, then the transformation Y at a junction can be written as

$$\begin{bmatrix} u \\ f \end{bmatrix} = \begin{bmatrix} Y_{ui} & Y_{uo} \\ Y_{fi} & Y_{fo} \end{bmatrix} \begin{bmatrix} w_i \\ w_o \end{bmatrix} \tag{2.37}$$

The boundary condition at the junction relates the displacements u and internal forces f to externally applied forces Q. This can be written as

$$\begin{bmatrix} B_u & B_f \end{bmatrix} \begin{bmatrix} u \\ f \end{bmatrix} = Q \tag{2.38}$$

Using these two equations, the outgoing wave mode amplitudes w_o can be expressed in terms of the incoming wave mode amplitudes w_i and the forces Q:

$$w_o = Sw_i + \Psi Q \tag{2.39}$$
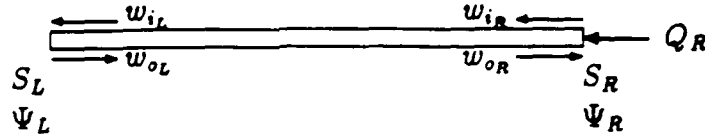
Figure 2.2: One Dimensional Waveguide

S is the open-loop scattering matrix, relating the outgoing waves to the incoming waves. Ψ describes how applied forces Q create outgoing waves. In terms of the previously defined matrices in Equations (2.37) and (2.38),

$$S \quad = \quad -[B_u Y_{uo} + B_f Y_{fo}]^{-1} [B_u Y_{ui} + B_f Y_{fi}] \tag{2.40}$$

$$\Psi \quad = \quad [B_u Y_{uo} + B_f Y_{fo}]^{-1} \tag{2.41}$$

Now consider a closed-loop structure, with feedback from the cross-sectional displacements u to the applied forces Q of the form

$$Q = Ku \tag{2.42}$$

Then the closed-loop scattering matrix can be shown to be

$$S_{CL} = [I - \Psi K Y_{uo}]^{-1} [S + \Psi K Y_{ui}] \tag{2.43}$$

The closed-loop transfer functions of a structural waveguide can also be calculated with this wave approach, using a phase closure algorithm. Consider a simple one-dimensional structure as shown in Figure 2.2. To find the transfer function between applied forces Q at one end (say, for example, the right end), and the generalized displacements y at this end, one would proceed as follows:

$$w_{oL} \quad = \quad S_L w_{iL} \tag{2.44}$$

$$w_{oR} \quad = \quad S_R w_{iR} + \Psi_R Q_R \tag{2.45}$$

$$w_{iL} \quad = \quad \xi w_{oL} \tag{2.46}$$

$$w_{iR} \quad = \quad \xi w_{oL} \tag{2.47}$$

26

where ξ is the transmission matrix from one end of this structure to the other. Combining these equations yields

$$w_{i_R} = \xi S_L \xi w_{o_R} \tag{2.48}$$

$$w_{o_R} = (I - S_R \xi S_L \xi)^{-1} \Psi_R Q_R \tag{2.49}$$

So finally, the relationship between the displacements u and the forces Q

$$u = (Y_{uo} + Y_{ui} \xi S_L \xi)(I - S_R \xi S_L \xi)^{-1} \Psi_R Q_R \tag{2.50}$$

A minor extension of this result that can be useful but that does not appear in [26] is to calculate the envelope of possible transfer functions in Equation (2.50) for unknown lengths. This corresponds to maximizing or minimizing Equation (2.50) with respect to the length parameter in ξ. For simple structures, such as a uniform beam, this is not difficult, but in general the result is too complicated to be of much value.

As an example of the the ory presented in this section, consider a uniform free-free Bernoulli-Euler beam, with bending stiffness EI, and mass per unit length ρA. The PDE for this structure is

$$EI \frac{\partial^4 v}{\partial x^4} + \rho A \frac{\partial^2 v}{\partial t^2} = 0 \tag{2.51}$$

Define the wave number k by

$$k = \sqrt{\frac{\rho A}{EI}} \sqrt{\omega} = c_0 \sqrt{\omega} \tag{2.52}$$

The transformation from cross-sectional to wave mode variables is given by

$$y = \begin{bmatrix} v \\ v' \\ \hline -EIv''' \\ EIv'' \end{bmatrix} = \begin{bmatrix} 1 & 1 & 1 & 1 \\ jk & k & -jk & -k \\ \hline jEIk^3 & -EIk^3 & -jEIk^3 & EIk^3 \\ -EIk^2 & EIk^2 & -EIk^2 & EIk^2 \end{bmatrix} w \tag{2.53}$$

27

where the partitions indicated correspond to those of Equation (2.37). v and v' are the deflection and slope of the beam at the boundary, respectively, and $-EIv'''$ and EIv'' are the internal shear force and moment, respectively. The wave modes consist of a leftward and rightward travelling wave, and left and right evanescent waves that do not oscillate spatially, but decay with distance. The transmission matrix ξ is

$$\xi = \begin{bmatrix} e^{-ik\ell} & 0 \\ 0 & e^{-k\ell} \end{bmatrix} \tag{2.54}$$

The boundary condition of a free end is specified by

$$\begin{bmatrix} 0 & 0 & -1 & 0 \\ 0 & 0 & 0 & -1 \end{bmatrix} \begin{bmatrix} u \\ f \end{bmatrix} = \begin{bmatrix} F \\ M \end{bmatrix} \tag{2.55}$$

where F and M are the externally applied moment and force. These are assumed to act in the same direction as the deflections v and v', so that a positive product of F and v, and of M and v', results in a positive power flow into the beam. Equations (2.40) and (2.41) give the open loop scattering and wave generation matrices as

$$S = \begin{bmatrix} -j & 1+j \\ 1-j & j \end{bmatrix} \tag{2.56}$$

$$\Psi = -\frac{1+j}{2EIk^3} \begin{bmatrix} 1 & k \\ 1 & -jk \end{bmatrix} \tag{2.57}$$

Open and closed loop transfer functions for the beam can then be calculated from Equations (2.43) and (2.50).

Chapter 3

Modelling

The intent of this chapter is to develop a useful model for control design for uncertain modally dense systems. It has been pointed out [19,41] that modes are not useful in this case. The modal frequencies and mode shapes are extremely sensitive to small parameter variations, and are particularly sensitive if the modes are closely spaced. Therefore, much of the information contained in a modal model is often incorrect. This then leads to a difficulty in modelling the uncertainty in a useful, and not overly conservative manner. The modal model also leads to large dimension systems, and an associated computational burden.

The detailed information in a modal model may also be unimportant. While knowledge of the exact mode shapes and frequencies may not be available, this does not imply that nothing is known about the structure, or that nothing can be done to control it. A reasonable control system can be designed without relying on this information. Recognizing this, and recognizing the difficulties associated with a modal approach, a modelling technique is desired which uses a simplified model of the structure, containing only the information that can be accurately determined.

3.1 Dereverberated Mobility Model

The following discussion is restricted to the case where a sensor and actuator are collocated. When this model is ultimately used for control design, this will of course result in suboptimal compensators, since each actuator will only have feedback from a collocated sensor. However, under the assumption of significant uncertainty, while some information about the behavior of the structure can still be determined at the driving point, there is very little information that can be relied upon about the behavior between an actuator and sensor which are separated by many wavelengths of the disturbance. This restriction is therefore reasonable for the control of higher frequency modes, or low authority control. If desired, the low frequency modes which can be well modelled could then be controlled with a high authority control in a HAC/LAC architecture. In this approach, then, a multi-input multi-output structure with actuator and sensor pairs at different locations would be modelled as several separate, single-input single-output systems. Each of these would have collocated actuators and sensors, and the modelling and control design for each of them would be performed independently.

Several approaches other than modal analysis have been used in the past to model structures with significant uncertainty. Statistical Energy Analysis, or SEA [21], is a field which has seen much research, for example in the analysis of machinery vibration. The response of individual modes to the driving noise is not calculated, and only the average response is used. The structure is split into subsystems, and the average energy in each of these subsystems is calculated from coupling factors between them, loss factors within each of them, and the power flow into each subsystem from the driving noise. The result is a description of the structure that includes information about the average energy distribution, and where power is being dissipated. As its name suggests, though, SEA is an analysis tool, and the resulting model is not directly applicable for control design.

Wi: Incoming Disturbances

Wo: Outgoing Disturbances

Actuator/Sensor Pair
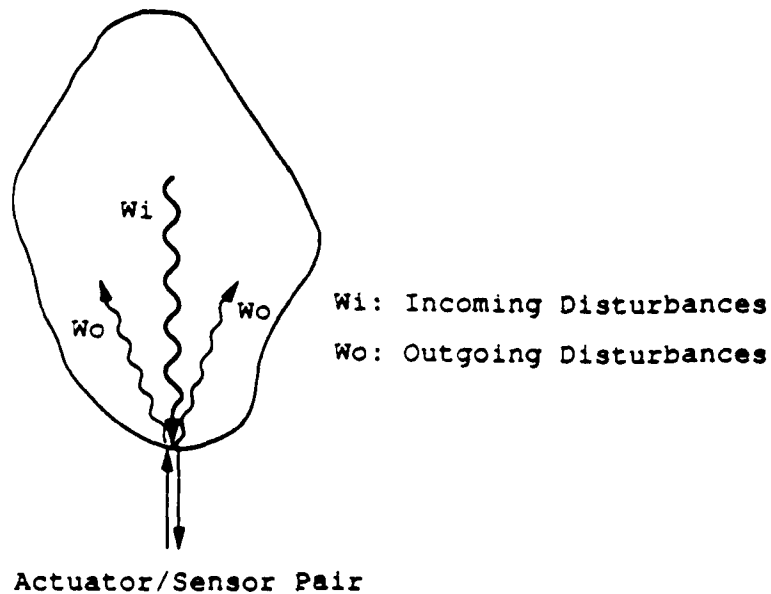
Figure 3.1: Wave behavior in an arbitrary structure

Wave-based models have been used not just for the analysis of structures, but as a basis for control design as well [17,23,28,29,32,33,35,39,40,41]. Here, a local model based on the partial differential equation (PDE) that applies to the structural member at the point in question is developed. The wave model contains the same information as the PDE, however, depending on the control design approach, there may be other implicit assumptions that introduce problems, such as ignoring the effect of boundary conditions at other points of the member on the local response. In most studies, the structural members have been simple one dimensional waveguides, and the structures analyzed have been restricted to those that could be well represented by networks of such waveguides. It may be difficult, however, to obtain a wave description for many complicated structures, because not all structures can be well represented in this manner.

For some arbitrary structure, as shown in Figure 3.1, insight into the nature of the problem can still be obtained from a wave approach. Various disturbances are created at certain points in the structure and propagate through it. At any point in

the structure, such as at an actuator, the disturbance will be scattered. In general, each of the resulting outgoing disturbances will eventually affect any global cost criterion. Thus without a detailed and accurate description of how each outgoing wave propagates, the goal of the control system should be to minimize the energy of each of these disturbances. Since the scattering behavior is a function of only the local dynamics, this goal can be achieved with only a local model of the structure.

An alternative approach to waves for obtaining such a model is to represent the structure by its dereverberated driving point mobility [22]. The mobility is the ratio of a generalized velocity and a generalized force, or the inverse of the mechanical impedance [14]. It is the transfer function between two variables whose product is the power flow into the structure, thus the sensors and actuators must be both collocated and dual. The response at a point can be considered to be the sum of two parts: a *direct field*, due to the local dynamics; and a *reverberant field*, which is caused by energy reflected back from other parts of the structure. The term "dereverberated" implies that the "reverberant" part of the response has been removed before computing the mobility. It should be possible to model the direct field more easily and accurately than the reverberant field, as it depends only on a few parameters, while the reverberent field depends on the entire structure. For the same reason, it is the reverberant field that contains greater detail, and requires more degrees of freedom to model. Thus by using the dereverberated mobility, a lower order model can be used that is based only on the details of the structure which can be accurately modelled.

3.2   Cepstral Analysis Approach

The dereverberated mobility may be calculated through the use of the cepstrum [22] of the impulse response. The cepstrum is the inverse Fourier transform of the log of the complex spectrum, and is a function of time. For the impulse response

$y(t)$, the complex spectrum is given by

$$Y(\omega) = \int_0^\infty y(t)e^{-j\omega t}dt \qquad (3.1)$$

Since a structural system is causal, $y(t)$ should be 0 for $t < 0$. Also,

$$\log Y = \log|Y| + j\phi_y \qquad (3.2)$$

where the log magnitude is an even function of frequency, and the phase ϕ_y is an odd function. The complex cepstrum is given by

$$C_y(t) = \mathcal{F}^{-1}(\log Y) \qquad (3.3)$$

$$= \mathcal{F}^{-1}(\log|Y|) + \mathcal{F}^{-1}(j\phi_y) \qquad (3.4)$$

and is purely real. The inverse Fourier transform is given by

$$\mathcal{F}^{-1}(Y(\omega)) = \frac{1}{2\pi}\int_{-\infty}^{\infty} Y(\omega)e^{j\omega t}d\omega \qquad (3.5)$$

The low time portion of the cepstrum corresponds to the direct response, and the high time portions correspond to the reverberant response, with spikes at times corresponding to the return times of the impulse from the rest of the structure. Windowing the cepstrum before the first of these yields the direct response, which can then be transformed back to the frequency domain to yield the dereverberated impulse response.

The truncation time to choose can be based on the level of confidence in the impulse response data. This illustrates one of the differences between the dereverberated mobility and a local wave model, that being direct control over how much of the structure is included in the model. By truncating the cepstrum at the appropriate point, some information about the rest of the structure is maintained while the details of it are ignored. Thus the control design is provided with more information, allowing it to generate a better controller.

The fundamental distinction between this and wave approaches is the ability to treat generic structures without having to represent them with a wave model. While the concept of direct and reverberant fields is based on wave ideas, there is no requirement to actually identify a local wave model. All that is needed is the input/output behavior at the driving point, which may be found from experimental data, calculated from some nominal model, or found analytically, perhaps even from a wave model. This approach is shown schematically in Figure 3.2 for the transfer function from force to collocated velocity at one end of a free-free beam.

This structure provides an interesting example, since the dereverberated mobility can also be found directly from the wave approach described in Section 2.3. The reverberant field is created by reflections from the far end of the beam, so if the scattering matrix for this end is set to zero, the dereverberated mobility can be calculated from Equation (2.50). The result is

$$\frac{\dot{y}}{F} = \frac{\sqrt{2}}{(\rho A)^{3/4}(EI)^{1/4}} \cdot \frac{1}{\sqrt{s}} \tag{3.6}$$

This can be scaled so that the transfer function is just

$$\frac{\dot{y}}{F} = \frac{1}{\sqrt{s}} \tag{3.7}$$

The cepstrum for both the true and dereverberated structures can also be calculated from theory:

$$C_{y_{true}} = \mathcal{F}^{-1}\left\{ \log \frac{\prod_{i=1}^{\infty}(s - z_i)}{\prod_{i=1}^{\infty}(s - p_i)} \right\} \tag{3.8}$$

$$= \begin{cases} \frac{2}{t}\left(\sum_{i=1}^{\infty} e^{-\zeta_{p_i}\omega_{p_i}t}\cos(\omega_{p_i}t) - \sum_{i=1}^{\infty} e^{-\zeta_{z_i}\omega_{z_i}t}\cos(\omega_{z_i}t)\right) & t > 0 \\ 0 & t \leq 0 \end{cases} \tag{3.9}$$

$$C_{y_{derev}} = \mathcal{F}^{-1}\left\{ \log \frac{1}{\sqrt{j\omega}} \right\} \tag{3.10}$$

$$= \begin{cases} \frac{1}{2t} & t > 0 \\ 0 & t \leq 0 \end{cases} \tag{3.11}$$
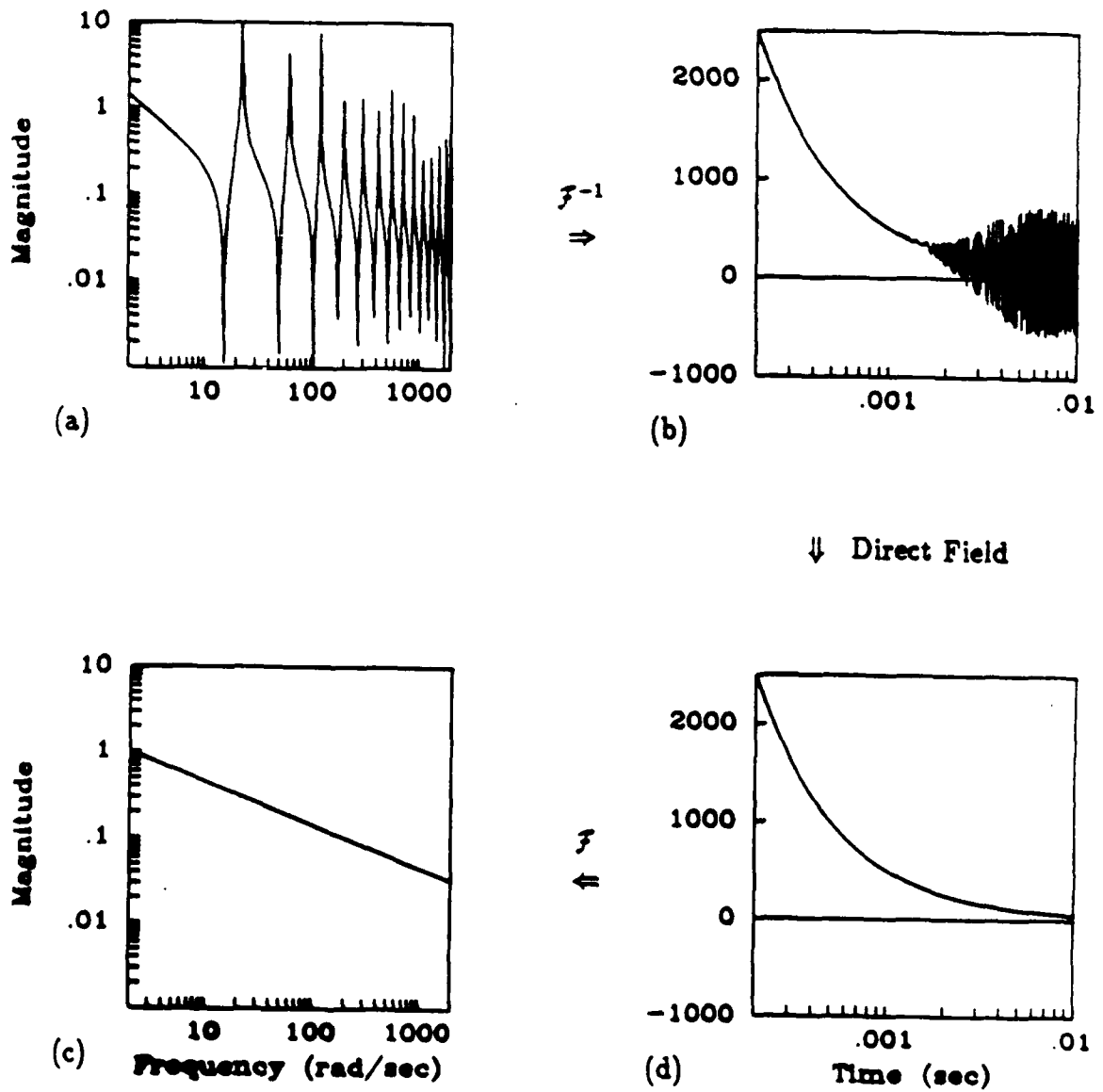
34

Figure 3.2: Calculation of dereverberated mobility from complex cepstrum. Transfer function (a) and cepstrum (b) of a free-free beam, dereverberated cepstrum (c) and dereverberated transfer function (d).

The sum in Equation (3.9) is over all poles $p_i = \varsigma_{p_i}\omega_{p_i} + j\omega_{p_i}$ and zeroes $z_i = \varsigma_{z_i}\omega_{z_i} + j\omega_{z_i}$.

These are the functions plotted in Figure 3.2. It should be emphasized that this theoretical approach would *never* be used in practice to compute the cepstrum. It does, however, provide a validation of the approach. The correct dereverberated mobility cannot be found exactly by simply truncating the cepstrum of the reverberant structure in Figure 3.2(b) to obtain the dereverberated cepstrum in Figure 3.2(c). If straight truncation were used, though, the resulting dereverberated mobility would be the convolution of Figure 3.2(d) with a *sinc* function, and this would not differ significantly from the desired function in the region of interest.

Further details on the calculation of the cepstrum, and its use in removing reverberation can be found in [9,38]. In general, however, it is not necessary to go through the procedure of computing the cepstrum, truncating it, and transforming back to the frequency domain.

3.3   Smoothing Approach

There is an alternative, less accurate, but much simpler way to calculate the dereverberated mobility. This is based on the observation that the effect of ignoring the reverberant field is to smooth out the transfer function. If no energy returns from beyond some closed surface surrounding the actuator, then this is equivalent to the structure beyond this surface either being infinite in extent, or having perfectly absorbing boundary conditions. This has also been shown [19,36] to be equivalent to the logarithmic mean of the original transfer function.

Hodges and Woodhouse [19] demonstrate this by showing that the assumptions that lead to using the smoothed transfer function in place of the original transfer function also lead to using a dereverberated model in place of the original reverberant system, and that these two new systems are equivalent. This is shown by consid-

36

ering the mean power input to a system by an excitation source with a broadband spectrum, and comparing the modal interpretation with the wave interpretation.

Skudrzyk [36] considers the transfer function of a reverberant system, and the affect of damping. As damping is added, the maxima of the transfer function decrease, and the minima increase. Eventually the transfer function is a smooth curve at the average of these maxima and minima. This response curve is therefore that that would be obtained if the system were sufficiently damped and sufficiently large, so that the reflected waves do not contribute significantly to the response. The dereverberated system is therefore obtained by increasing the damping and size of the system, and has a transfer function which is the logarithmic mean of the original transfer function. This response curve corresponds to the amplitude of the direct field that is generated by the input.

Thus another way to compute the dereverberated mobility is simply to take a logarithmic average of the magnitude of the transfer function. This is not surprising, considering that the cepstral analysis approach described earlier is essentially the same as low-pass filtering the logarithmic frequency response. The phase can be determined uniquely from Bode's Gain-Phase Theorem [8], using the fact that the dereverberated mobility is positive real. In practice, this method should be adequate. Fitting the result with a rational polynomial gives a model that captures the essential dynamics of the system over a wide frequency range that encompasses many modes, with only a small number of poles and zeroes.

Figure 3.3(a) and (b) shows the transfer function of a free-free Bernoulli-Euler beam. Rather than evaluating the system response only on the $j\omega$ axis, however, the transfer function is plotted for part of the right half complex plane; that is, as a function of both the real and imaginary parts of the Laplace transform variable s. The familiar sharp peaks and valleys associated with lightly damped structures only appear near the imaginary axis. Farther away from the axis, the effect of individual modes is smeared out, and the transfer function becomes smooth. Since the dere-
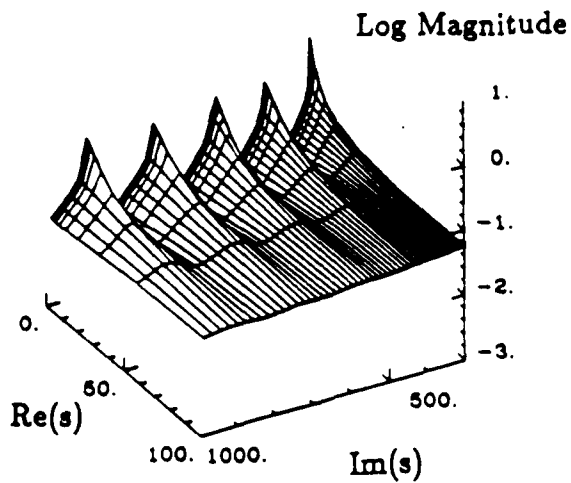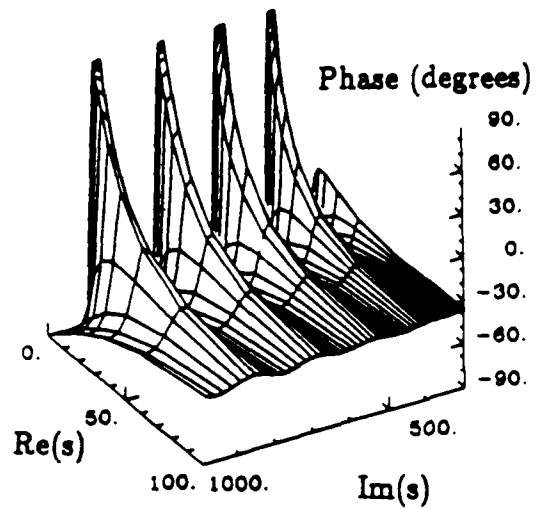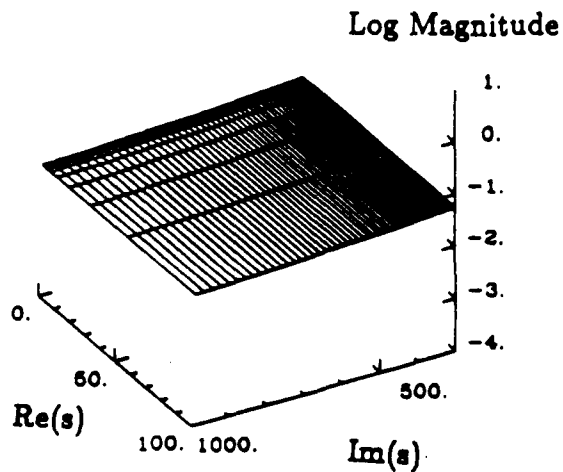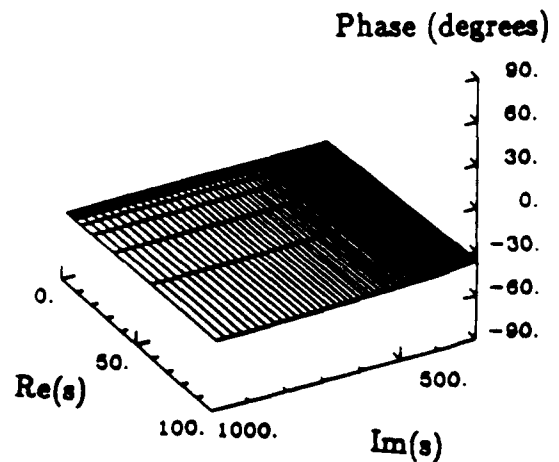
Figure 3.3: Transfer function of a beam evaluated as a function of both the real and imaginary parts of the complex Laplace variable: magnitude (a) and phase (b) of a finite beam, and magnitude (c) and phase (d) of the dereverberated beam.

38

verberated system can be obtained from the original system by adding damping, as noted earlier, it is the dereverberated mobility to which the transfer function approaches as the real part of the Laplace variable increases. Therefore, if the goal of the control system is to move the poles away from the axis, this smooth transfer function should be a good approximation to the structure. The significance of this figure for control design will be discussed further in Chapter 4. Figure 3.3(c) and (d) shows the dereverberated transfer function for the same system. The dereverberated mobility is a good approximation to the structure everywhere except near the $j\omega$ axis.

As an example of the dereverberated mobility approach on a modally dense structure, consider the transfer functions plotted in Figure 3.4. The graph shows an experimental transfer function measured from endpoint moment to endpoint slope rate on a pinned-free brass beam suspended in the laboratory at M.I.T. (This beam is discussed in more detail in Chapter 6.) Note the high modal density above a few tens of hertz; it seems reasonable that a control design that relied upon the exact location of each mode would be undesirable. The average amplitude, however does not depend at all on the length of the beam or the nature of the boundary condition at the far end. Also plotted in the figure is the theoretical response of a semi-infinite Bernoulli-Euler beam (the straight line, calculated again from the wave approach of Section 2.3), and the average response, which differs from the Bernoulli-Euler prediction only at low and high frequencies. It is this average response that would be the appropriate dereverberated admittance, though the straight line approximation would probably be adequate if the central frequency range is the range of interest.

The dereverberated mobility model is not intended to accurately represent the structure; it clearly fails in this regard. However, it is hoped that this will be a useful model for the design of control systems for the structure. While the resonant and anti-resonant details of the full reverberant mobility are not explicitly modelled,
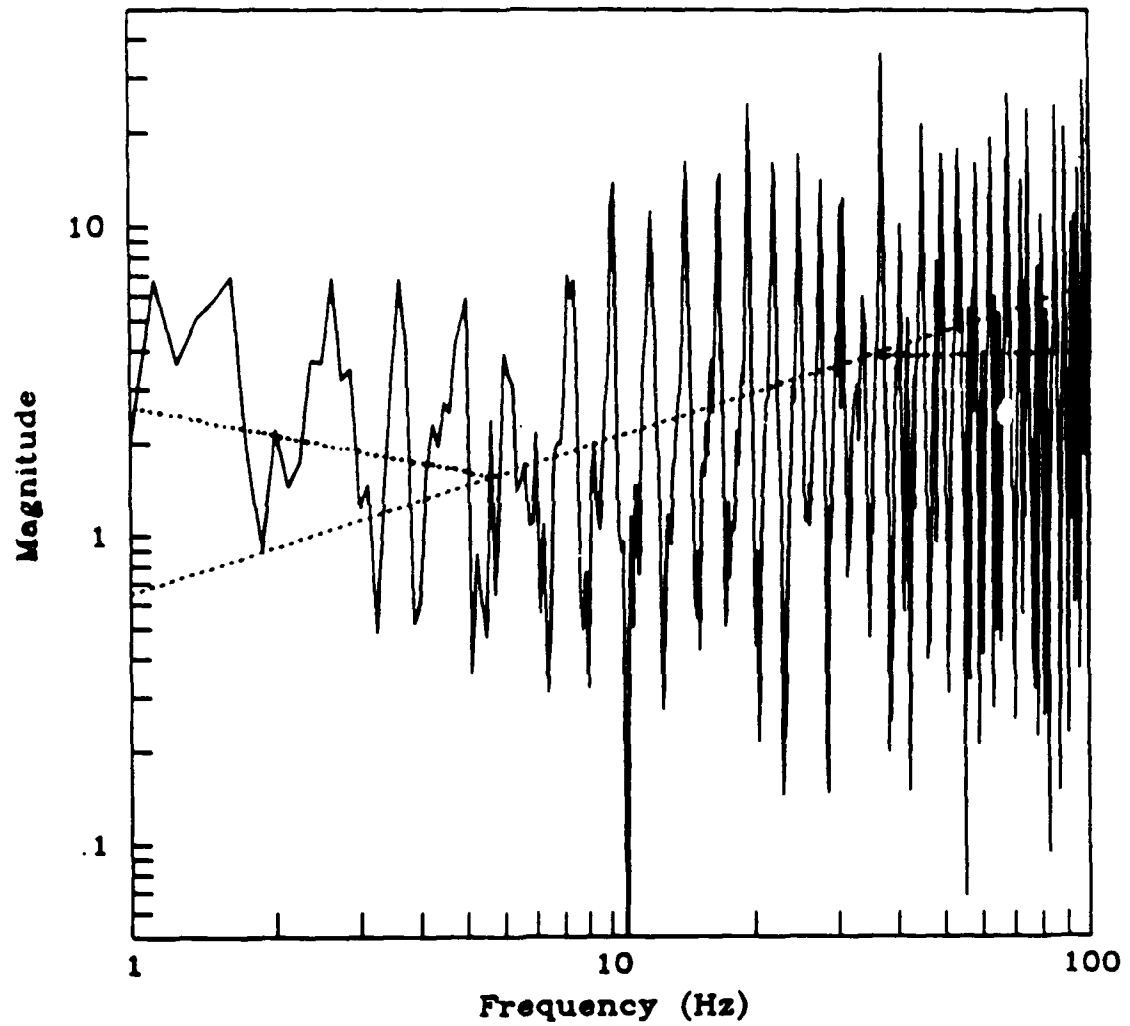
Figure 3.4: **Example of dereverberation: experimental transfer function (solid), theoretical semi-infinite transfer function (dashed) and dereverberated mobility (dotted).**

40

the reverberant field is composed of waves whose behavior is governed by the local dynamics of the controlled junction each time they pass through it. Thus if the local dynamics can be appropriately modified based on a local model, then the complete reverberant field can be controlled.

Chapter 4

Control Design

The previous chapter described the modelling approach used, while this chapter focuses on the design of the control system for this model. There are two main objectives to be satisfied by the control design. It must be guaranteed to be stabilizing for all possible plants, and it must provide good performance, again for all possible plants. In order to guarantee stability, positive real feedback from velocity to force will be required. One could, for example, select rate feedback, which is guaranteed to be stable, but this does not necessarily give the best performance that could be achieved. Velocity feedback is only one possible choice of positive real feedback; the object of this chapter is to derive the optimal positive real compensator.

The criterion to be used for optimality will be the minimum power flow into the structure. That is, power extracted from the structure will be maximized. Power flow is the appropriate quantity to minimize to provide active damping of the structure, and allows a guarantee of stability by ensuring that the power flowing into the structure due to the control is always negative.

Miller et al. [28] minimized the $\mathcal{H}_2$ norm of the power flow. This required some assumptions about the power spectral density of the disturbance entering the junction. In the actual structure, this is related to the control through the disturbance that previously departed the junction. In the wave model, however, it was assumed
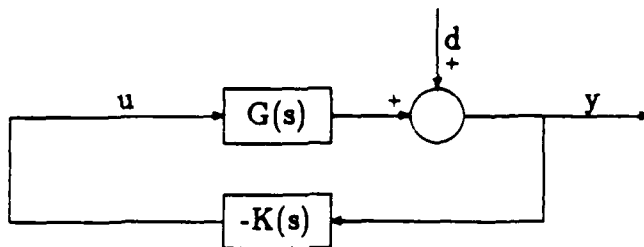
Figure 4.1: System Block Diagram I

constant and independent of the control. As a result, in general the compensators obtained allowed power to be added at some frequencies, since this behaviour could not destabilize the design model. This problem can be avoided by minimizing the power flow in an $\mathcal{H}_\infty$ setting. For an open-loop system, the power removed by the controller is zero. If the closed loop power flow is guaranteed to be no worse at all frequencies, then the closed loop system is guaranteed to be stable. In fact, it is sufficient to place a constraint on the maximum value of the power flow which guarantees it to be negative at all frequeucies. An $\mathcal{H}_2$ optimization [6] can then be used, which may improve the overall performance.

Define $G(s)$ to be the dereverberated driving point mobility, and assume some disturbance input d to be additive at the output. Then the output y is related to the input u and the disturbance via

$$y(s) = G(s)u(s) + d(s) \tag{4.1}$$

as shown in Figure 4.1. As yet, no assumptions have been made about the nature of the disturbance.

Recall that in Chapter 2 the noise assumptions made in $\mathcal{H}_\infty$ and $\mathcal{H}_2$ optimizations were discussed. Now consider this in the context of the model defined in Chapter 3. The disturbance d in Equation (4.1) can be thought of as originating from two sources: the original disturbance input to the real structure, and the reverberant field ignored in the modelling process. This second source will have significant

43

power at the modal frequencies, and if the closed loop damping is still relatively small, then in steady state this will be much larger than the physical disturbance. Thus the disturbance spectrum in Equation (4.1) consists of significant power in narrowband but unknown frequency ranges, which are exactly the assumptions indicated in Chapter 2 as being appropriate for $\mathcal{H}_\infty$ minimization.

4.1   Unconstrained Optimum

Before finding a compensator which minimizes the worst case power flow, consider finding the compensator which minimizes the power flow at each value of the Laplace transform variable s. The control law is of the form

$$u = -Ky \tag{4.2}$$

where the explicit dependence on the Laplace transform variable has been dropped. Solving for the control in terms of the disturbance from Equation (4.1) gives

$$u = -(I + KG)^{-1}Kd \tag{4.3}$$

$$= Hd \tag{4.4}$$

Then the output can also be represented in terms of the disturbance as

$$y = (I + GH)d \tag{4.5}$$

The instantaneous power flow into the structure is the product of the input $u(t)$ and the output $y(t)$, since $G(s)$ is an mobility. The average power flow can be expressed as a time integral of the instantaneous power flow [27],

$$P_{ave} = \lim_{T \to \infty} \frac{1}{2T} \int_{-T}^{T} y^T(t)u(t)\,dt \tag{4.6}$$

Making use of Parseval's theorem, this can be transformed into the frequency domain:

$$P_{ave} = \frac{1}{2} \int_{-\infty}^{\infty} \left(u^H(j\omega)y(j\omega) + y^H(j\omega)u(j\omega) \right) \frac{d\omega}{2\pi} \tag{4.7}$$

44

The integrand of the right hand side of Equation (4.7) represents the steady state, or average, power flow into the structure as a function of frequency [27]. For convenience, the average power flow at each frequency can be defined without the factor of $\frac{1}{2}$, as

$$P(\omega) = u^H(j\omega)y(j\omega) + y^H(j\omega)u(j\omega) \tag{4.8}$$

where $(\cdot)^H$ indicates Hermitian, or complex conjugate transpose. The Hermitian operator is not analytic in the complex plane. Instead, the appropriate operator is the analytic continuation of the conjugate from the $j\omega$ axis to the remainder of the plane. This operator is denoted $(\cdot)^\sim$ and is defined as in Chapter 2 as

$$F^\sim(s) = F^T(-s) \tag{4.9}$$

Substituting the earlier expressions for u and y into Equation (4.8) yields

$$P(\omega) = d^\sim \{H^\sim(I + GH) + (I + GH)^\sim H\} d \tag{4.10}$$

This equation gives the power flow into the structure as a function of the compensator. The optimal value of H is that which minimizes the expected value of this expression at each point in the complex plane. Since the power flow is a scalar, it is equal to its trace. So

$$\text{Cost}(s) = \text{E}\left[\text{Trace}\{dd^\sim [H^\sim(I + GH) + (I + GH)^\sim H]\}\right] \tag{4.11}$$

$$= \text{Trace}\{\Phi_{dd} [H^\sim(I + GH) + (I + GH)^\sim H]\} \tag{4.12}$$

where $\Phi_{dd} = \Phi_{dd}^T = \text{E}[dd^\sim]$ is the power spectral density of the disturbance d.

Making use of the symmetry in (4.12) gives that at the optimum,

$$H^\sim = H \tag{4.13}$$

Using this result, then differentiation gives

$$\frac{\partial(\text{Cost})}{\partial H} = 2\Phi_{dd} + \Phi_{dd}H(G + G^\sim) + (G + G^\sim)H\Phi_{dd} = 0 \tag{4.14}$$

From this equation, the optimal H is given by

$$H_{opt} = -(G + G^{\sim})^{-1} \tag{4.15}$$

provided this inverse exists. If it does not exist, this implies that if Φ_{dd} is full rank, Equation (4.15) is valid, and an infinite amount of power can be extracted from the structure. If Φ_{dd} is singular, then Equation (4.15) is not valid, however in this case, Equation (4.14) is not sufficient to uniquely determine H. Since in general the approach of this thesis deals with SISO systems, this case is not too significant a restriction on the applicability of this result. Non-scalar Φ_{dd} will only arise if a structure has multiple actuator and sensor pairs of different types at the same location, since if they were at different locations the structure would be modelled and controlled as separate SISO systems.

If the inverse in Equation (4.15) exists, then this compensator is independent of the disturbance spectrum Φ_{dd}. From Equations (4.3) and (4.4), the compensator K is related to H by

$$K = -H(I + GH)^{-1} \tag{4.16}$$

so finally,

$$K_{opt} = (G^{\sim})^{-1} \tag{4.17}$$

This compensator extracts the maximum possible power from the structure at every frequency.

This result is not new; it corresponds to the impedance matching condition found, for example, in [10]. The maximum energy dissipation is obtained if the impedance of the compensator is the complex conjugate of the impedance of the load, which in this case is the rest of the structure.

In general, however, the compensator in Equation (4.17) is noncausal, and cannot be implemented in real time, since it requires knowledge of future information. The dereverberated mobility $G(s)$ must be both stable and causal, and is therefore

right half plane analytic (RHPA). Since it is strictly positive real, it must also be minimum phase, and thus the optimal compensator in Equation (4.17) will be left half plane analytic (LHPA). So every pole of the compensator is in the right half plane. This does not necessarily imply that the compensator is unstable. A right half plane pole corresponds to a unique transfer function, but there are two time domain systems with this transfer function. One is causal and unstable, so that the impulse response is zero for negative time, and increases with increasing positive time. The other is noncausal and stable, with its impulse response zero for positive time, and decreasing to zero as time decreases to minus infinity.

One can determine which of these two systems applies in this case from a Nyquist plot. Since both the compensator and the plant are strictly positive real, there are no encirclements of the point -1, and thus K must be stable for the closed loop system to be stable. This implies that in general, this compensator is noncausal. K can be stable, causal, and LHPA only if it is a constant, and hence only if the dereverberated mobility is a constant. One such case is that of a uniform rod in compression, with a collocated force actuator and velocity sensor at one end. In this case, Equation (4.17) corresponds exactly to the matched termination for the rod.

Some understanding of why the optimal compensator is almost always noncausal can be found from root locus arguments. For a point λ to be on the root locus of the plant $P(s)$, the compensator $K(s)$ must satisfy

$$1 + P(\lambda)K(\lambda) = 0 \tag{4.18}$$

In order to place the structural poles far into the left half plane, the relevant plant $P(s)$ is the structure as it appears from far into the left half plane.

For a lightly damped structure with a large number of closely spaced poles and zeroes, one can divide the complex plane into three regions. Near the $j\omega$ axis, and close to the poles and zeroes, the transfer function varies significantly from its maxima to its minima, and the phase varies between $+90°$ and $-90°$. If one looks at

47

the structure from farther into the right half plane, the effect of individual poles and zeroes becomes smeared out, and the transfer function approaches the smoothed, or dereverberated transfer function $G(s)$. The phase of G in some frequency region will be the average phase of the original transfer function near that region, and the magnitude will be the logarithmic mean of the magnitude of the original transfer function near that region. This behaviour is shown graphically in Figure 3.3.

In the left half plane, however, the structure's transfer function is not $G(s)$. To determine the phase contribution of each pole and zero, the contour to consider must now be to the left of every pole and zero, and so each phase change has opposite sign. The result is that in the left half plane, the structural transfer function approaches $-G(-s)$. Therefore, to move the poles far into the left half plane, $K(s)$ must satisfy

$$1 - G(-s)K(s) = 0 \qquad (4.19)$$

or

$$K(s) = 1/G(-s) \qquad (4.20)$$

as given in Equation (4.17).

If this compensator could be implemented, all of the structural poles could be moved arbitrarily far into the left half plane. Instead, the best causal compensator must be found.

4.2 Causal Optimum

The wave model of Miller et al. [28] can also be put in a form similar to that of Equation (4.1), though only for structures composed of waveguides. As discussed earlier, Miller et al. performed an $\mathcal{H}_2$ optimization of the power flow, which did not guarantee dissipation at all frequencies, and thus did not guarantee closed loop stability. A more appropriate optimization to guarantee stability is to minimize the worst case power dissipation, hence a minimax optimization of the power flow into

48

the structure. As will be shown shortly, this can be cast as an $\mathcal{H}_\infty$ minimization problem. In order for this to make sense, though, the disturbance input d should be normalized to provide the same amount of power available to be dissipated at each frequency. This provides the designer with complete control over the relative importance of one frequency range to another, by removing any inherent frequency weighting from the problem.

With the optimal noncausal compensator derived in the previous section, Equation (4.17), the closed loop power flow into the structure is given by Equations (4.10) and (4.15) as

$$P = -d^\sim (G + G^\sim)^{-1} d \tag{4.21}$$

Represent the disturbance d as

$$d = G_0 w \tag{4.22}$$

Then if the input w has unit magnitude at a certain frequency, the optimal noncausal compensator will dissipate unit power at this frequency, provided that the transfer function G_0 is the co-spectral factor of $G + G^\sim$, given by

$$G_0 \widetilde{G_0} = G + G^\sim \tag{4.23}$$

The block diagram for this system is shown in Figure 4.2, and the system (Equation (4.1)) becomes

$$y(s) = G(s)u(s) + G_0(s)w(s) \tag{4.24}$$

Now, consider the problem of finding a causal compensator that will minimize the worst case power flow in Equation (4.8). This quantity represents the power flow into the structure, which will hopefully be negative. The goal is to find a compensator K that results in

$$\min_u \max_w \left\{ u^H(j\omega)y(j\omega) + y^H(j\omega)u(j\omega) \right\} \tag{4.25}$$

This minimax problem can be solved directly, using the approach of [34]. Alternatively, it can be reformulated as an $\mathcal{H}_\infty$ problem, for which software to find K
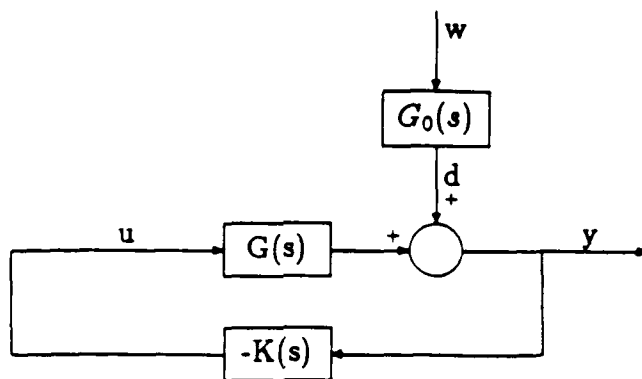
Figure 4.2: System Block Diagram II

exists. In order to cast this as an $\mathcal{H}_\infty$ optimization, however, the performance index must be positive definite. Note, though, that the best causal compensator can dissipate no more power than the unconstrained, noncausal optimum. Thus if the disturbance power $w^\sim w$ is added to the cost, positive definiteness will be assured.

The cost at each frequency is therefore

$$\text{Cost}(\omega) = w^\sim w + u^\sim y + y^\sim u \tag{4.26}$$

$$= w^\sim w + u^\sim(Gu + G_0 w) + (Gu + G_0 w)^\sim u \tag{4.27}$$

$$= \left\{ \begin{array}{c} u \\ w \end{array} \right\}^\sim \left[\begin{array}{cc} G + G^\sim & G_0 \\ G_0^\sim & I \end{array} \right] \left\{ \begin{array}{c} u \\ w \end{array} \right\} \tag{4.28}$$

$$= |G_0^\sim u + w|^2 \tag{4.29}$$

From this, the relevant output that should be minimized is

$$z = G_0^\sim u + w \tag{4.30}$$

Combining this with the system equation (4.24), the result can be written as a four block problem (compare with Figure 2.1):

$$\left\{ \begin{array}{c} z \\ y \end{array} \right\} = \left[\begin{array}{cc} I & G_0^\sim \\ G_0 & G \end{array} \right] \left\{ \begin{array}{c} w \\ u \end{array} \right\} \tag{4.31}$$

The compensator from y to u that minimizes the $\mathcal{H}_\infty$ norm of the transfer function from w to z will minimize the maximum power flow into the structure.

For computation, however, the unstable (1,2) block in Equation (4.31) is unacceptable. Any allowable compensator must stabilize this block, while the only important stability constraint is on the output y. Recall from Chapter 2, however, that the norm of z is unchanged by multiplication by an inner function. Define $\Delta(\cdot)$ to be the characteristic polynomial of the transfer function $(\cdot)$, and define the inner function

$$G_1(s) = \frac{\Delta(G_0^\sim(s))}{\Delta(G_0(s))} \tag{4.32}$$

Then redefine z to be

$$z = G_1 G_0^\sim u + G_1 w \tag{4.33}$$

so that the four-block problem (4.31) becomes

$$\left\{ \begin{array}{c} z \\ y \end{array} \right\} = \left[\begin{array}{cc} G_1 I & G_1 G_0^\sim \\ G_0 & G \end{array} \right] \left\{ \begin{array}{c} w \\ u \end{array} \right\} \tag{4.34}$$

which is stable.

In general, it may be desirable to weight some frequency ranges more heavily than others, while still requiring that power be removed at all frequencies. This could be because there is a known disturbance source in a certain range, because structural modes are ' :s well damped within this range, or because the performance requirements put more emphasis on this range. Similarly, there will usually be some frequency beyond which performance is not required, and the weighting can also be chosen to reflect this.

The manner in which the weighting is introduced into the problem must be such that if power is added to the structure somewhere, the resulting cost will be worse than the open-loop cost. Hence, rather than weighting the sum of the disturbance input power and the power input by the control, as in Equation (4.26), define the

cost to be the sum of the disturbance power and some frequency weighted control power, as

$$\text{Cost}(\omega) = w^\sim w + W_1^\sim(u^\sim y + y^\sim u)W_1 \qquad (4.35)$$

which can be manipulated into the form

$$\text{Cost} = \left| \begin{array}{c} W_1(G_0^\sim u + w) \\ W_2 w \end{array} \right|^2 \qquad (4.36)$$

where W_1 is the selected frequency weighting, and W_2 is defined by the relationship

$$|W_1|^2 + |W_2|^2 = 1 \qquad (4.37)$$

The output z of the four block problem is then

$$z = \left\{ \begin{array}{c} W_1(G_0^\sim u + w) \\ W_2 w \end{array} \right\} \qquad (4.38)$$

Note that as desired, the open loop cost is unity everywhere, and the cost is greater than unity at any frequency where power is added to the structure. Thus as before, a closed loop cost of less than unity guarantees stability.

The only constraint on W_1 is that its magnitude be less than or equal to unity at all frequencies. Without this constraint, there is no guarantee that the cost be positive definite, and the minimization could fail. Where W_1 is small, a greater amount of control effort is required to reduce the cost than before, and thus there is more power removed. Hence, in order to emphasize some frequency range more heavily, the weighting function W_1 should be chosen to be smaller within that region.

Recall from Chapter 2 that one of the properties of $\mathcal{H}_\infty$ compensators is that at the optimum, the closed loop transfer function being minimized is a constant function of frequency, equal to some number γ [15]. From this, and Equation (4.35), the closed loop power absorbed by the compensator can be related to γ and the weighting function. This is expressed as a fraction of the power absorbed by the

unconstrained optimal compensator:

$$P(\omega) = \frac{1 - \gamma^2}{|W_1|^2} \qquad (4.39)$$

This provides some insight into how to select W_1.

The cost in Equation (4.26) or (4.35) can also be modified to include a penalty on the control effort, $\rho u^\sim u$. The four block problem (4.34) is modified to include an additional output in the vector z, corresponding to $\sqrt{\rho} u$. This allows a trade-off between performance and control, and also guarantees a proper compensator. Similarly, it is straightforward to modify the four block problem (4.34) to include sensor noise. An additional disturbance input is included in the vector w which affects only the sensor output y.

The final result of this approach is a positive real compensator, which is guaranteed to be stabilizing for any positive real plant. However, if there are any time delays, actuator or sensor dynamics, or if the actuator and sensor are not truly collocated and dual, then the structure will not be positive real at all frequencies. Stability can still be guaranteed if the complementary sensitivity is bounded above by the inverse of the difference of the true structure from positivity, as noted by Slater [37].

This constraint can be represented as a constraint on the $\mathcal{H}_\infty$-norm of an appropriate transfer function. If the error bound is given as in Equation (1.3) for the difference from positivity, then stability can be guaranteed if the compensator is positive real and, as in Equation (1.2),

$$\left\| GK(I + GK)^{-1} L_m \right\|_\infty \leq 1 \qquad (4.40)$$

The compensator is positive real if power is dissipated at all frequencies, or

$$\|z\|_\infty \leq 1 \qquad (4.41)$$

with z being given by Equation (4.30) or (4.38). Thus this problem is one of minimizing the $\mathcal{H}_\infty$ norm of one transfer function (Equation (4.41)), with a constraint on the $\mathcal{H}_\infty$ norm of another transfer function (Equation (4.40)).

4.3 State Space Computation

The calculation of the optimal compensator for the four-block problem is most easily performed in state space, since software exists to solve the state space $\mathcal{H}_\infty$ four-block problem. The first step then is to obtain a state space representation for the plant $G(s)$ and the desired weighting function $W_1(s)$. From these, state space representations for $W_2(s)$, $G_0(s)$, and $G_1(s)$ must be calculated. These problems can be formulated as spectral factorization problems, and solved by methods similar to those discussed in Section 2.2.

4.3.1 Calculation of G_0

G_0 is a co-spectral factor of $M = G + G^\sim$, and thus can be calculated with the standard algorithm. The algorithm is restricted to systems G with a non-zero direct feedthrough term D. This is not a serious restriction, however. No finite-dimensional model is valid at all frequencies, nor does it need to be. This merely implies that rather than rolling off at high frequencies, $G(\infty)$ should be a constant.

First, define the state space representation of G as

$$G = \left[\begin{array}{c|c} A & B_2 \\ \hline C_2 & D_{22} \end{array} \right] = C_2 \left(sI - A \right)^{-1} B_2 + D_{22} \tag{4.42}$$

The reason for the selection of the subscripts on B, C, and D is that G is the (2,2) block of the four block problem.

G_0 can be represented as

$$G_0 = \left[\begin{array}{c|c} A & B_1 \\ \hline C_2 & D_{21} \end{array} \right] \tag{4.43}$$

where

$$D = D_{22} + D_{22}^T \tag{4.44}$$

$$A^{\times}_{M^T} = \begin{bmatrix} A^T & 0 \\ 0 & -A \end{bmatrix} - \begin{bmatrix} C_2 \\ -B_2^T \end{bmatrix} D^{-1} \begin{bmatrix} B_2 & C_2^T \end{bmatrix} \tag{4.45}$$

$$X_1 = Ric\left\{A^{\times}_{M^T}\right\} \tag{4.46}$$

$$B_1 = (B_2 + X_1 C_2^T) D^{-1/2} \tag{4.47}$$

$$D_{21} = D^{1/2} \tag{4.48}$$

From Chapter 2, Definition 5, the conditions required for this spectral factorization to be valid are:

(i) $M = M^{\sim}$,

(ii) M and M^{-1} are proper,

(iii) M and M^{-1} have no poles on the $j\omega$ axis, (or alternatively, M have no poles or zeroes on the $j\omega$ axis),

(iv) $M(\infty) > 0$.

The first condition is clearly satisfied, as is the second, since M and M^{-1} are proper with non-zero D_{22}. If G is a dereverberated mobility, then it has no imaginary poles, and thus neither does M. Furthermore, G is strictly positive real. This implies that $G(j\omega) + G^{\sim}(j\omega) > 0$, and thus that M has no zeroes on the $j\omega$ axis. This also implies that $M(\infty) > 0$.

4.3.2 Calculation of G_1

The (1,2) block of the four-block problem (4.34) is $G_1 G_0^{\sim}$. This has the stable poles, but the non-minimum phase zeroes of $M = G + G^{\sim}$. The state space algorithm for computing this is related to the spectral factorization algorithm found in [15], or Section 2.2, and only the differences between the two will be indicated here.

Given G as in Equation (4.42), then

$$M = G + G^{\sim} = \left[\begin{array}{cc|c} A & 0 & B_2 \\ 0 & -A^T & -C_2^T \\ \hline C_2 & B_2^T & D_{22} + D_{22}^T \end{array}\right] = \left[\begin{array}{c|c} A_M & B_M \\ \hline C_M & D \end{array}\right] \quad (4.49)$$

and

$$A_M^{\times} = \left[\begin{array}{cc} A & 0 \\ 0 & -A^T \end{array}\right] - \left[\begin{array}{c} B_2 \\ -C_2^T \end{array}\right] D^{-1} \left[\begin{array}{cc} C_2 & B_2^T \end{array}\right] \quad (4.50)$$

The spectral factorization algorithm in Section 2.2 relies on finding the modal spaces $\mathbf{X}_-(A_M^{\times})$ and $\mathbf{X}_+(A_M)$ corresponding to the left half-plane zeroes of M and the right half plane poles respectively. Instead, now find $\mathbf{X}_+(A_M^{\times})$ and $\mathbf{X}_+(A_M)$, corresponding to right half plane zeroes and right half plane poles. If these two spaces are complementary, then the required factorization exists.

Since the unstable poles of any matrix A are the stable poles of $-A$,

$$\mathbf{X}_+(A_M^{\times}) = \mathbf{X}_-(-A_M^{\times}) \quad (4.51)$$

Thus the desired factorization exists if $\mathbf{X}_-(-A_M^{\times})$ and $\mathbf{X}_+(A_M)$ are complementary. Since $A_M^{\times}$ is a Hamiltonian matrix, $-A_M^{\times}$ is as well. Thus, there exists a matrix

$$X_2 = Ric\left\{-A_M^{\times}\right\} \quad (4.52)$$

such that

$$\mathbf{X}_-(-A_M^{\times}) = \operatorname{Im}\left[\begin{array}{c} I \\ X_2 \end{array}\right] \quad (4.53)$$

and this is complementary to $\mathbf{X}_+(A_M)$, given by Equation (2.21). Given this, the remainder of the derivation follows Francis [15] or Section 2.2 exactly, so that

$$G_1(s)G_0(s) = \left[\begin{array}{c|c} A & B_2 \\ \hline D^{-1/2}(C_2 + B_2^T X_2) & D^{1/2} \end{array}\right] \quad (4.54)$$

$$= \left[\begin{array}{c|c} A & B_2 \\ \hline C_1 & D_{12} \end{array}\right] \quad (4.55)$$

Thus,

$$C_1 = D^{-1/2}(C_2 + B_2^T X_2) \tag{4.56}$$

$$D_{12} = D^{1/2} \tag{4.57}$$

Since the remaining (1,1) block $G_1 I$ of the four block problem is inner, it must be true that

$$D_{11} = 1 \tag{4.58}$$

Then the four block problem in Equation (4.34) is completely specified.

4.3.3 Calculation of W_2

The computation of the weighting function W_2 in Equation (4.37) from W_1 can also be represented in terms of a spectral factorization. First, represent W_1 in state space as

$$W_1 = \left[\begin{array}{c|c} A_w & B_w \\ \hline C_w & D_w \end{array} \right] \tag{4.59}$$

Then

$$W_1^{\sim} = \left[\begin{array}{c|c} -A_w^T & -C_w^T \\ \hline B_w^T & D_w^T \end{array} \right] \tag{4.60}$$

Combining these gives

$$W_1 W_1^{\sim} = \left[\begin{array}{cc|c} A_w & 0 & B_w \\ -C_w^T C_w & -A_w^T & -C_w^T D_w \\ \hline -D_w^T C_w & -B_w^T & -D_w^T D_w \end{array} \right] \tag{4.61}$$

The A matrix of this system is a Hamiltonian matrix, with the (1,2) block equal to zero. Thus the modal spaces are given by Equations (2.24) and (2.25). Hence define the similarity transformation

$$T = \left[\begin{array}{cc} I & 0 \\ X_w & I \end{array} \right] \tag{4.62}$$

where X_w satisfies the Lyapunov equation

$$A_w^T X_w + X_w A_w + C_w^T C_w = 0 \tag{4.63}$$

and use this to transform the system, Equation (4.61). This gives

$$W_1 W_1^\sim = \left[\begin{array}{cc|c} A_w & 0 & B_w \\ 0 & -A_w^T & -C_w^{\prime T} \\ \hline C_w' & -B_w^T & -D_w^T D_w \end{array} \right] \tag{4.64}$$

where

$$C_w' = B_w^T X_w + D_w^T C_w \tag{4.65}$$

Then W_2 is a spectral factor of

$$I - W_1 W_1^\sim = \left[\begin{array}{cc|c} A_w & 0 & B_w \\ 0 & -A_w^T & C_w^{\prime T} \\ \hline -C_w' & -B_w^T & I - D_w^T D_w \end{array} \right] \tag{4.66}$$

This is now in the form of a standard spectral factorization. In order to apply the algorithm, W_1 must satisfy

$$1 - D_w^T D_w > 0 \tag{4.67}$$

or $W_1(\infty) < 1$. This is not a limitation at all, since multiplying the weighting function everywhere by a constant will not change the resulting compensator. The other conditions specified in the definition of the spectral factorization are also satisfied. Note that if the magnitude of W_1 is less than one at all frequencies, then $1 - W_1 W_1^\sim$ can have no imaginary zeroes, nor can it have any imaginary poles.

4.3.4 Four Block Problem

Having determined how to compute all of its elements, the complete four-block problem can be written in state space form as

$$\left[\begin{array}{c|cc} A & B_1 & B_2 \\ \hline C_1 & D_{11} & D_{12} \\ C_2 & D_{21} & D_{22} \end{array} \right] \tag{4.68}$$

58

where

$$\mathcal{A} = \begin{bmatrix} A & 0 & 0 \\ B_w C_1 & A_w & 0 \\ 0 & 0 & A_w \end{bmatrix} \quad \mathcal{B}_1 = \begin{bmatrix} B_1 \\ B_w D_{11} \\ B_{w_2} \end{bmatrix} \quad \mathcal{B}_2 = \begin{bmatrix} B_2 \\ B_w D_{12} \\ 0 \end{bmatrix}$$

$$\mathcal{C}_1 = \begin{bmatrix} D_w C_1 & C_w & 0 \\ 0 & 0 & C_{w_2} \end{bmatrix} \quad \mathcal{D}_{11} = \begin{bmatrix} D_w D_{11} \\ D_{w_2} \end{bmatrix} \quad \mathcal{D}_{12} = \begin{bmatrix} D_w D_{12} \\ 0 \end{bmatrix} \qquad (4.69)$$

$$\mathcal{C}_2 = \begin{bmatrix} C_2 & 0 & 0 \end{bmatrix} \qquad \mathcal{D}_{21} = \begin{bmatrix} D_{21} \end{bmatrix} \qquad \mathcal{D}_{22} = \begin{bmatrix} D_{22} \end{bmatrix}$$

The compensator is then found from the Riccati equations given in [16].

Chapter 5

Examples

5.1   Example 1: Free-Free Bernoulli-Euler Beam

As an example of the approach developed in the previous chapters, consider a free-free Bernoulli-Euler beam with a collocated force actuator and velocity sensor at one end, as shown in Figure 5.1. The dereverberated mobility for this system was calculated previously in Section 3.2. It is the transfer function of a semi-infinite beam, which can be found, for example, from the wave approach discussed in Section 2.3:

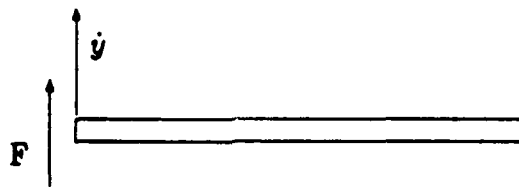$$G(s) = \frac{\sqrt{2}}{(\rho A)^{3/4}(EI)^{1/4}} \cdot \frac{1}{\sqrt{s}} \tag{5.1}$$

Figure 5.1: Bernoulli-Euler Free-Free Beam

For simplicity, assume the mass per unit length ρA and the bending stiffness EI are such that

$$G(s) = \frac{1}{\sqrt{s}} \qquad (5.2)$$

This can be done without loss of generality, as it requires only a scaling of the plant.

First, consider the unconstrained optimal compensator that extracts the maximum possible energy. From Equation (4.17),

$$K(s) = \sqrt{-s} \qquad (5.3)$$

This compensator has a slope of 10 db/decade, and a phase of $-45°$ at all frequencies. Note that this is the same compensator as that obtained by the unconstrained optimization in Miller *et al.* [28], though the derivation differs, and in Flotow and Schäfer [40], by setting the reflection coefficient corresponding to the creation of outgoing travelling waves from incoming travelling waves to zero. As expected, the unconstrained optimal compensator is noncausal and cannot be implemented. That it is noncausal could be determined by finding a rational approximation to $\sqrt{-s}$, which would have right half plane poles, or from the knowledge that $\sqrt{s}$ is stable and causal, since it is the transfer function of a stable structure (see Example 2 in the next section.) Since $\sqrt{s}$ is right half plane analytic, $\sqrt{-s}$ must be left half plane analytic, and therefore if it is stable, it must be noncausal.

Now, find the compensator that minimizes the maximum power flow into the structure. An analytical solution to this is given in Appendix A. With equal weighting at each frequency, $(W_1 = 1)$ the optimal causal compensator is

$$K(s) = \sqrt{s} \qquad (5.4)$$

Thi   similar to the noncausal solution, Equation (5.3), with the same magnitude everywhere, but a phase of $+45°$ instead. This is the "best" causal approximation to Equation (5.3), and dissipates exactly half of the incoming power at all frequencies.
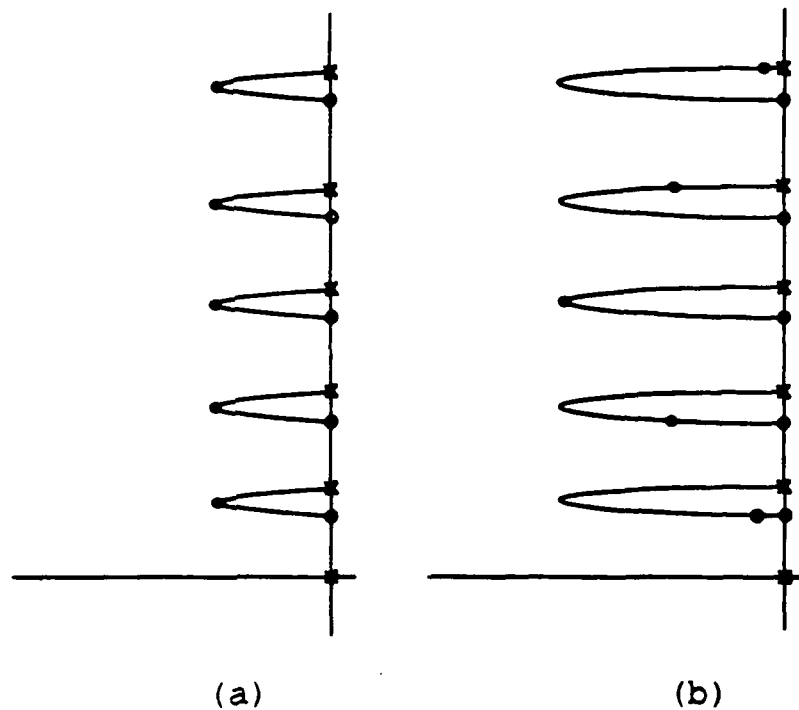
Figure 5.2: Schematic root locus with $\mathcal{H}_\infty$ design (a) and with velocity feedback (b).

Further insight into the nature of this control can be found from the root locus, shown schematically in Figure 5.2. With velocity feedback, an appropriate choice of gain will add significant damping to a given mode, and those nearby, but it is not possible to add significant damping to all of the modes at the same time. Thus the gain in velocity feedback must be optimized to provide damping at a certain frequency. Far enough away from this frequency, the gain is either too low to have much affect, or too high so that the closed loop poles lie near the open loop zeroes, which are undamped. With the optimal causal compensator $\sqrt{s}$, the locus is not as far into the left half plane, but now every pole can be placed at the leftmost part of its locus simultaneously. Ideally, one would like the root locus to be arbitrarily far into the left half plane, and place each pole at the leftmost part of its locus. This is the behavior obtained by the unconstrained optimal compensator $\sqrt{-s}$, which of

course cannot be implemented.

Now consider including a weighting function to increase the importance of a certain frequency range, say in a narrow band near 1 rad/sec. So select W_1 to have unit magnitude far from 1, and less than unit magnitude near 1 rad/sec. Recall that more importance is placed where the weighting function is smaller. An analytic solution here would be difficult. However, the plant in Equation (5.2) can be approximated adequately over a wide frequency range with a finite number of alternating poles and zeroes on the real axis, with equal logarithmic spacing. The state space methods described in Section 4.3 can then be used to obtain an approximate compensator. The resulting compensator is plotted in Figure 5.3, along with the optimal compensator with unity weighting from Equation (5.4), and the unconstrained optimum from Equation (5.3). Note that the magnitudes of these last two compensators are the same. Equation (5.2) in this case was approximated by 9 poles and 9 zeroes with frequencies from 10^{-4} to 10^4 rad/sec. The weighting function W_1 had zeroes at $\frac{1}{\sqrt{2}}$ and $\sqrt{2}$, and poles at $\frac{1}{2\sqrt{2}}$ and $2\sqrt{2}$. Far from the region that was selected as important, the compensator still has a $\sqrt{s}$ behavior, though with less magnitude than the unweighted optimum in Equation (5.4), resulting in poorer performance. Near 1 rad/sec, though, the slope of the compensator is now -10 db/decade, and the phase is closer to $-45°$. At 1 rad/sec, the compensator has exactly the same magnitude, and almost the same phase as the noncausal optimum, and thus it absorbs almost all of the incoming power possible. The net power flow absorbed by this compensator is plotted in Figure 5.4, expressed as a fraction of the disturbance input power. For comparison, the power absorbed by velocity feedback and the unweighted optimum are also plotted in the same figure. The comparison between the two $\mathcal{H}_\infty$ designs illustrates the trade-off in the choice of the weighting function. The power flow can be increased in one frequency region, but at the expense of decreasing the power dissipation at all other frequencies.

If this control law is now applied to a finite beam, the closed loop performance

can be examined. The transfer function between force and velocity at the far (uncontrolled) end of the beam can be calculated using the phase closure approach of [27], discussed in Section 2.3. The beam length was chosen so that the fifth mode of the beam was at the center frequency of the weighted region. The result is plotted in Figure 5.5, and the envelope of the transfer function for any length beam is also plotted. As expected, the modal peaks in the region where W_1 is smallest are more heavily damped. Note that because the compensator in Figure 5.3 is positive real, it will not destabilize the beam at any length. (Nor will it destabilize any positive real structure.) Furthermore, for any length beam, there will be some damping achieved everywhere, and greater damping in the region of interest, as indicated by the envelope of possible transfer functions.

From Equation (4.39), the closed loop power flow can be related to the weighting function W_1. If the damping in a mode could be related to the power absorbed at the frequency of that mode, then the achieved damping could be predicted from knowledge of W_1 and the achievable $\mathcal{H}_\infty$ norm γ. For a simple beam, an approximation to this is relatively straightforward; the procedure is presented in Appendix B. With a unity weighting function W_1, the result is

$$\varsigma_i = -\frac{\log(\gamma)}{\ell c_0 \sqrt{\omega_i}} \tag{5.5}$$

This can be compared with actual eigenvalue calculations, and while the result is not exact, the approximation is reasonable. Thus in this case, not only can the closed loop power flow be predicted without actually designing the compensator, the closed loop damping can also be predicted, provided one can give a reasonable estimate of γ. This would be useful for determining how to modify the weighting function to produce the desired behaviour.

It is worth comparing the results of this approach with those for other control design techniques. Methods such as LQG are difficult to compare due to the lack of a suitable basis for comparison. An LQG compensator will certainly give a better $\mathcal{H}_2$ norm of the quantity minimized than the $\mathcal{H}_\infty$ design approach for the

nominal model. For a sufficiently large perturbation in the plant, however, the LQG design may destabilize the system, as it has poor robustness to parametric model error. Another design technique which is more suitable for comparison is collocated velocity feedback. Rate feedback is also positive real, and thus guaranteed to be stabilizing, but the performance is expected to be worse, being suboptimal. A comparison of the power dissipated by rate feedback and by two $\mathcal{H}_\infty$ designs has already been shown in Figure 5.4. For a given structure, velocity feedback dissipates power with a specific frequency distribution, with the gain as the only parameter to vary. The gain changes only the center frequency of the distribution, and not its shape. The $\mathcal{H}_\infty$ design, on the other hand, allows much more freedom in the characteristics of the power dissipation with frequency. Greater dissipation at a single frequency is possible than with rate feedback, and broader band power dissipation is also achievable. The envelope of possible closed loop transfer functions on the free-free beam is shown in Figure 5.6 for several different gains of rate feedback, and for the unweighted $\mathcal{H}_\infty$ compensator described earlier. Once again, this illustrates the same point. Velocity feedback is stabilizing, but in general, it is suboptimal.

5.2 Example 2: Pinned-Free Beam

As a slightly more complicated example, consider again a finite beam, but this time with one end pinned, with a moment actuator and collocated angular rate sensor at this end. Also include some finite rotational inertia J at this end, as indicated in Figure 5.7. The theoretical dereverberated transfer function for this beam can be found once again using the wave approach of Section 2.3. For this structure, the boundary conditions at the pinned end are given by the matrices

$$ B_u \;=\; \begin{bmatrix} 1 & 0 \\ 0 & \frac{JEI}{\rho A} k^4 \end{bmatrix} \tag{5.6} $$

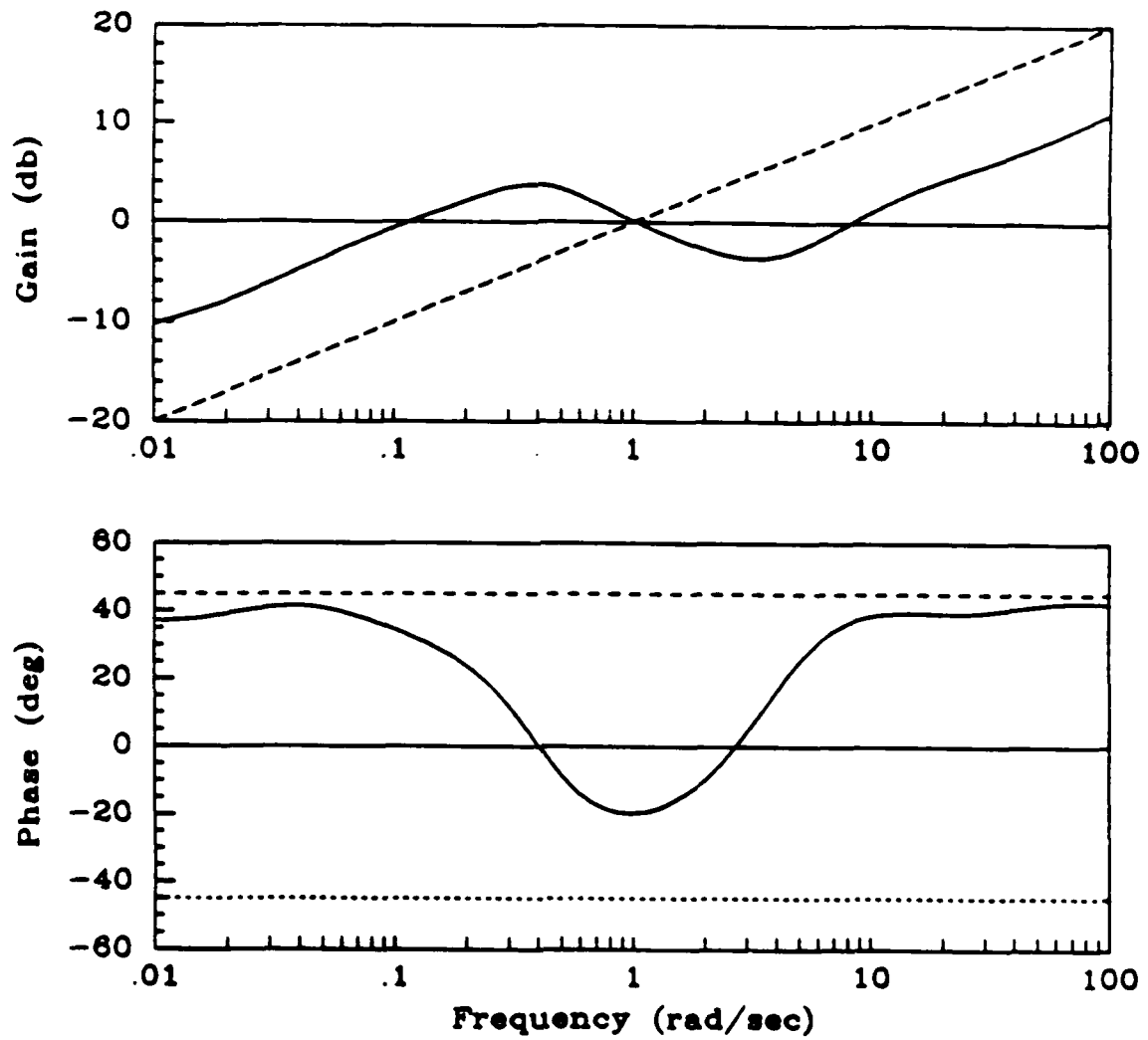Figure 5.3: Optimal compensator for example 1 with weighting at 1 rad/sec (solid), with no weighting (dashed), and unconstrained (dotted).
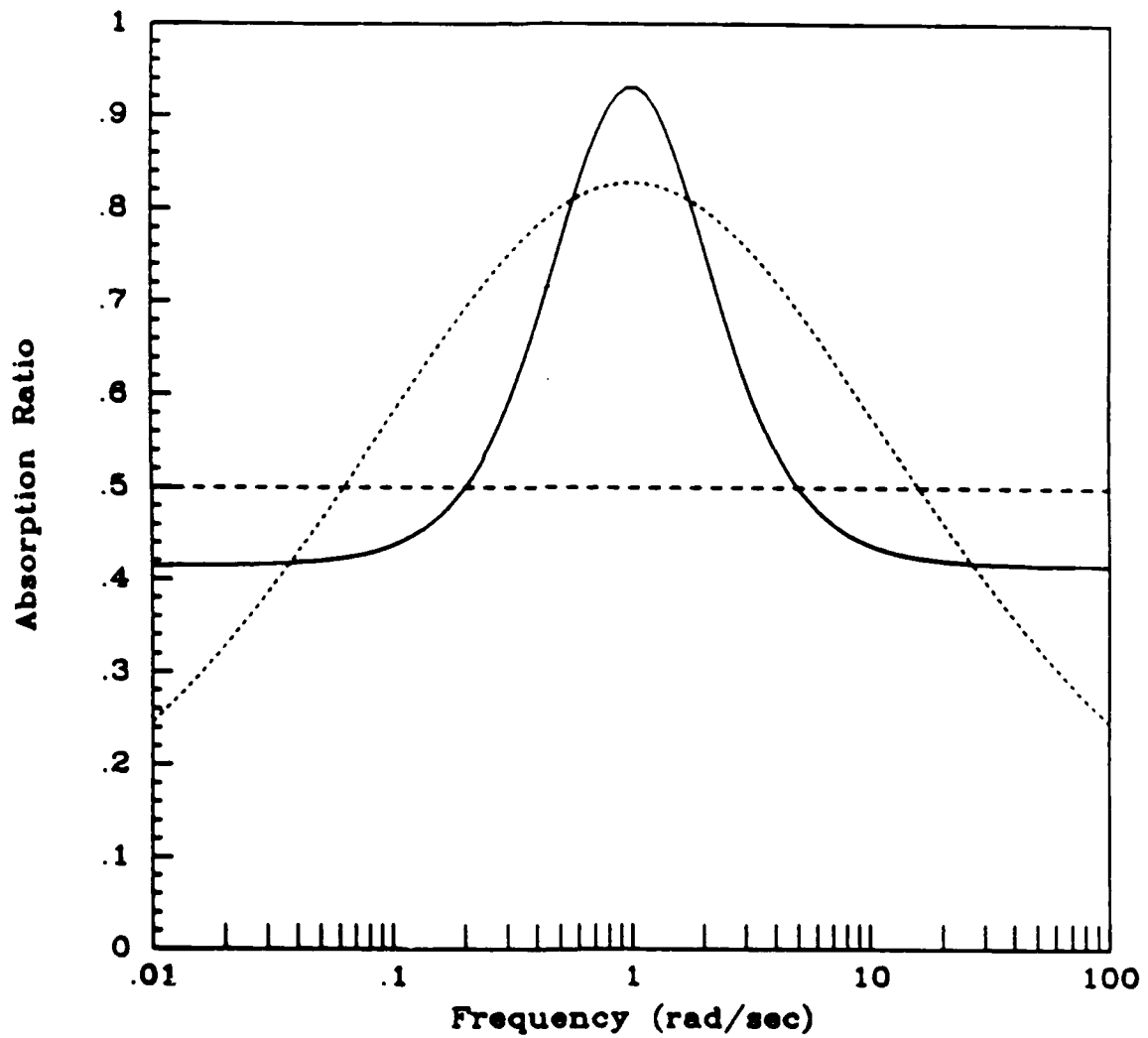
Figure 5.4: Power absorption for weighted $\mathcal{H}_\infty$ design (solid), velocity feedback (dotted), and unweighted $\mathcal{H}_\infty$ design (dashed).

Figure 5.5: Closed loop transfer function at far end of beam (solid) and envelope of possible closed loop transfer functions (dotted).

Figure 5.6: Envelope of   sible closed loop transfer functions at far
end of beam with different gains of rate feedback (dot-
ted) and with unweighted $\mathcal{H}_\infty$ design (solid).

Figure 5.7: Bernoulli-Euler Pinned-Free Beam

$$B_f = \begin{bmatrix} 0 & 0 \\ 0 & 1 \end{bmatrix} \tag{5.7}$$

The wave number k is defined from Equation (2.52). So from Equations (2.40), (2.41), and (2.50),

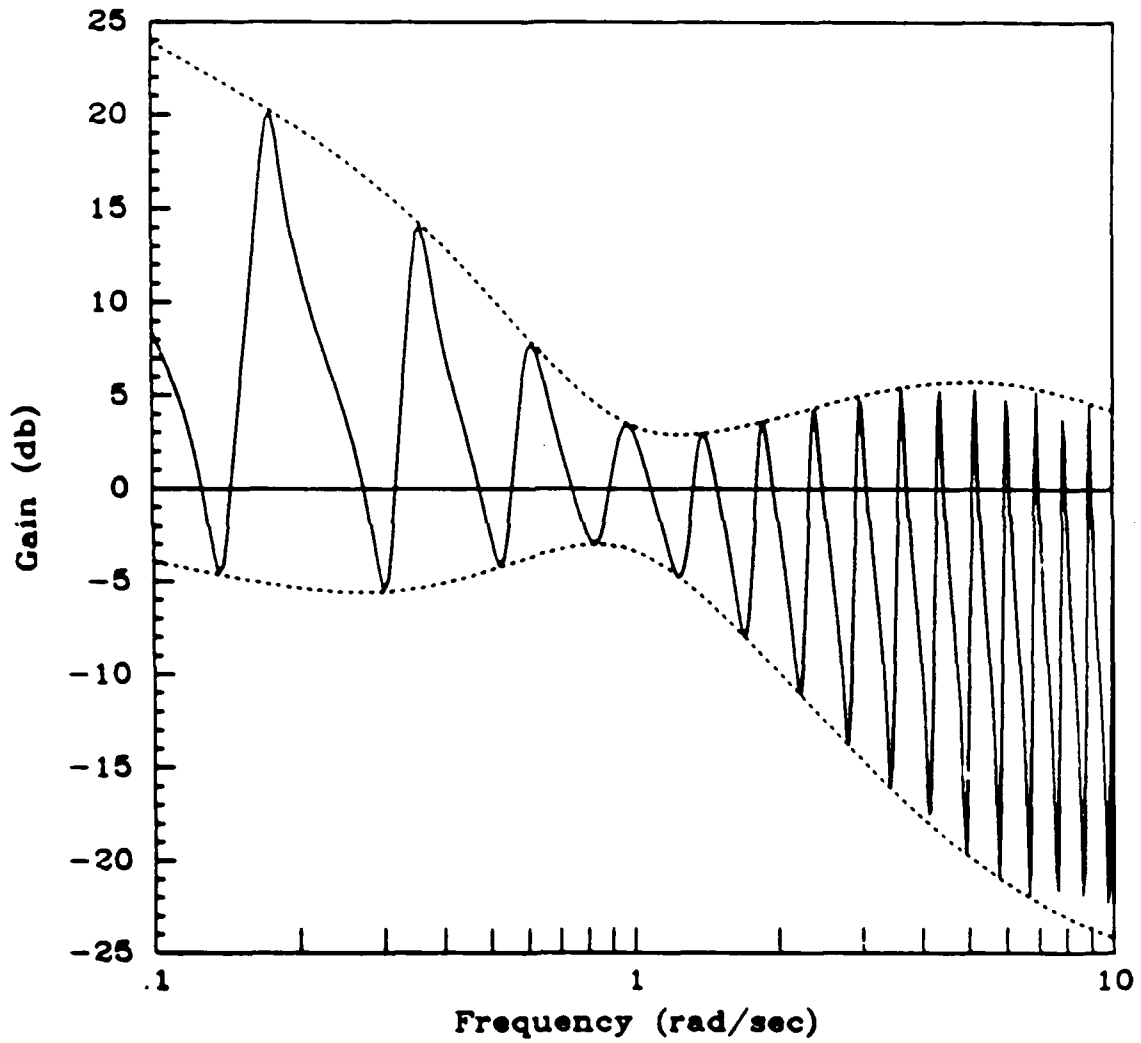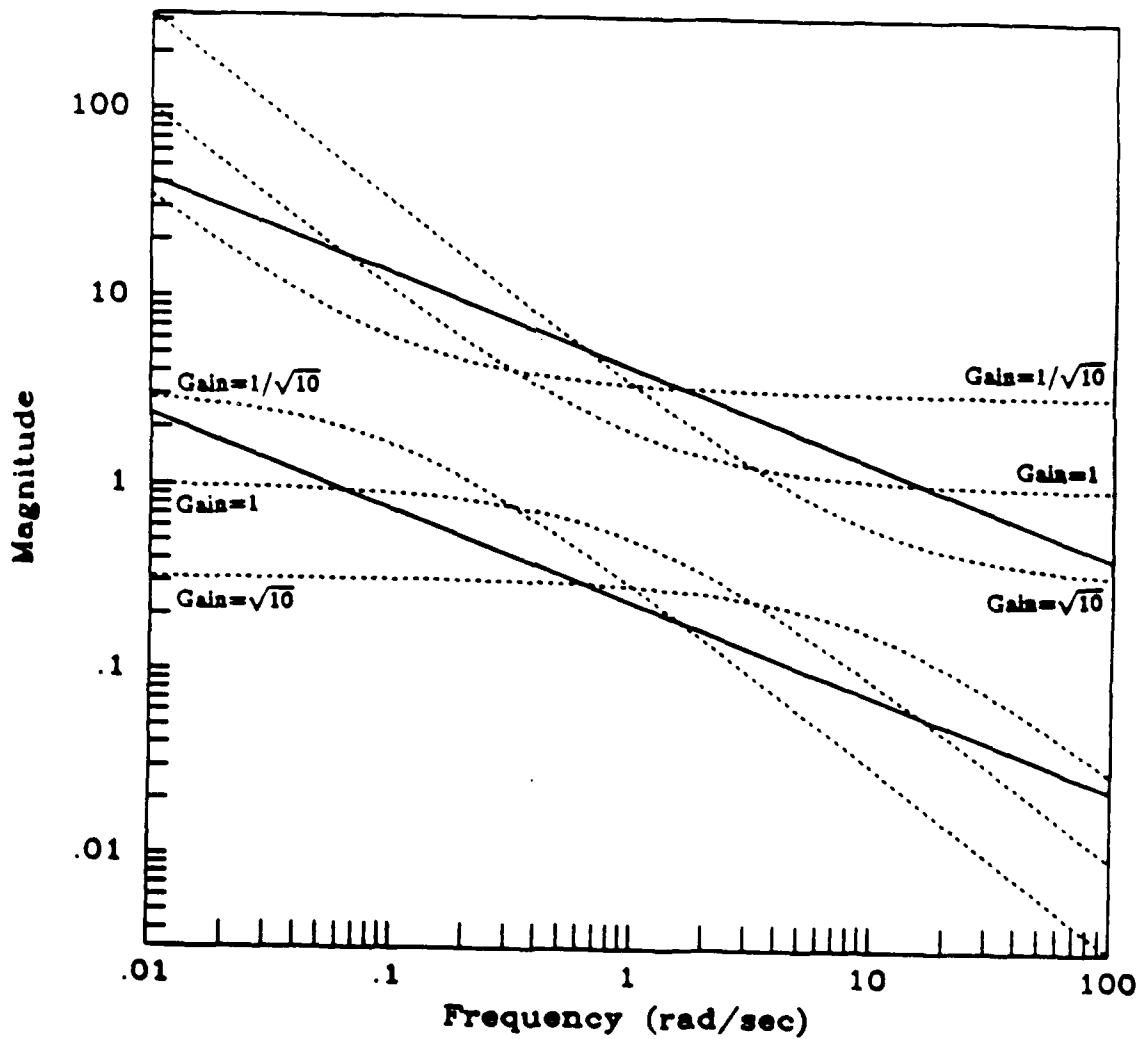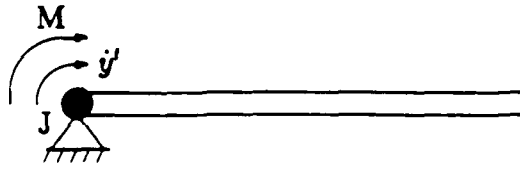$$\frac{\ddot{y}'}{M} = \frac{s}{\sqrt{2}(\rho A)^{1/4}(EI)^{3/4}\sqrt{s} + Js^2} \tag{5.8}$$

If there were no rotational inertia J, then the transfer function would be

$$G(s) = \frac{\sqrt{s}}{\sqrt{2}(\rho A)^{1/4}(EI)^{3/4}} \tag{5.9}$$

The unconstrained optimal compensator would therefore be

$$K(s) = \frac{\sqrt{2}(\rho A)^{1/4}(EI)^{3/4}}{\sqrt{-s}} \tag{5.10}$$

This has a phase of 45°. If the weighting function W_1 was unity at all frequencies, then the causal optimum found from the $\mathcal{H}_\infty$ approach would be

$$K(s) = \frac{\sqrt{2}(\rho A)^{1/4}(EI)^{3/4}}{\sqrt{s}} \tag{5.11}$$

This has the same magnitude as the unconstrained optimum, but a phase of -45°. The calculations required to obtain these compensators are essentially the same as for the free-free beam in the previous example.

With $J \neq 0$, then at low frequencies, the behavior is similar to that of Equation (5.9). At high frequencies, the transfer function is dominated by the rotational

70

inertia, and rolls off at 20 db/decade. From the far end of the beam, the controlled end then behaves as if it were clamped, and regardless of the control, all disturbances are reflected back. Thus, power flow beyond the rolloff frequency of Equation (5.8) should be unimportant, and the weighting function here should be much larger than elsewhere. Also, assume again that some specific frequency range near 1 rad/sec is more important. Note that while in practice it would be difficult to extract power at high frequencies, the theory still allows power to be dissipated, due the presence of G_0. At high frequencies, $G \sim \frac{1}{J_s}$, and hence $G_0 \to \infty$. Thus the disturbance spectrum is increased indefinitely to allow the same amount of power dissipation at all frequencies with the unconstrained compensator.

For computation, $EI = \frac{1}{\sqrt{2}}$ and $\rho A = \frac{1}{\sqrt{2}}$, so that the low frequency behavior is exactly $\sqrt{s}$. The rotational inertia J was selected to be 10^{-3}, to place the rolloff frequency at 100 rad/sec, at a slightly higher frequency than that considered to be important. Again, the system was approximated with a rational transfer function which is accurate over the frequency range of interest, from 10^{-4} to 10^4 rad/sec.

The compensator for this case is shown in Figure 5.8. At low frequencies, the compensator is similar to the $\frac{1}{\sqrt{s}}$ that would be optimal with no rotary inertia and no weighting. Where the weighting function decreases near 1 rad/sec, the phase jumps towards the noncausal optimum phase of 45°, and thus absorbs close to the maximum power possible. At high frequencies, as desired, the compensator gives up and does not attempt to absorb incoming power, though it does remain positive real. Thus again, the closed loop system is stable for any length beam, and for any boundary condition at the far end. The open and closed loop transfer function from moment to slope rate at the controlled end of the beam is given in Figure 5.9. This transfer function shows the rolloff at 100 rad/sec, beyond which the poles and zeroes are essentially undamped, but almost cancel each other. The poles are more heavily damped near 1 rad/sec, but none of the zeroes are affected. Also plotted is the dereverberated mobility (Equation (5.8)), and the upper bound of the envelope

of possible transfer functions for any length of beam.

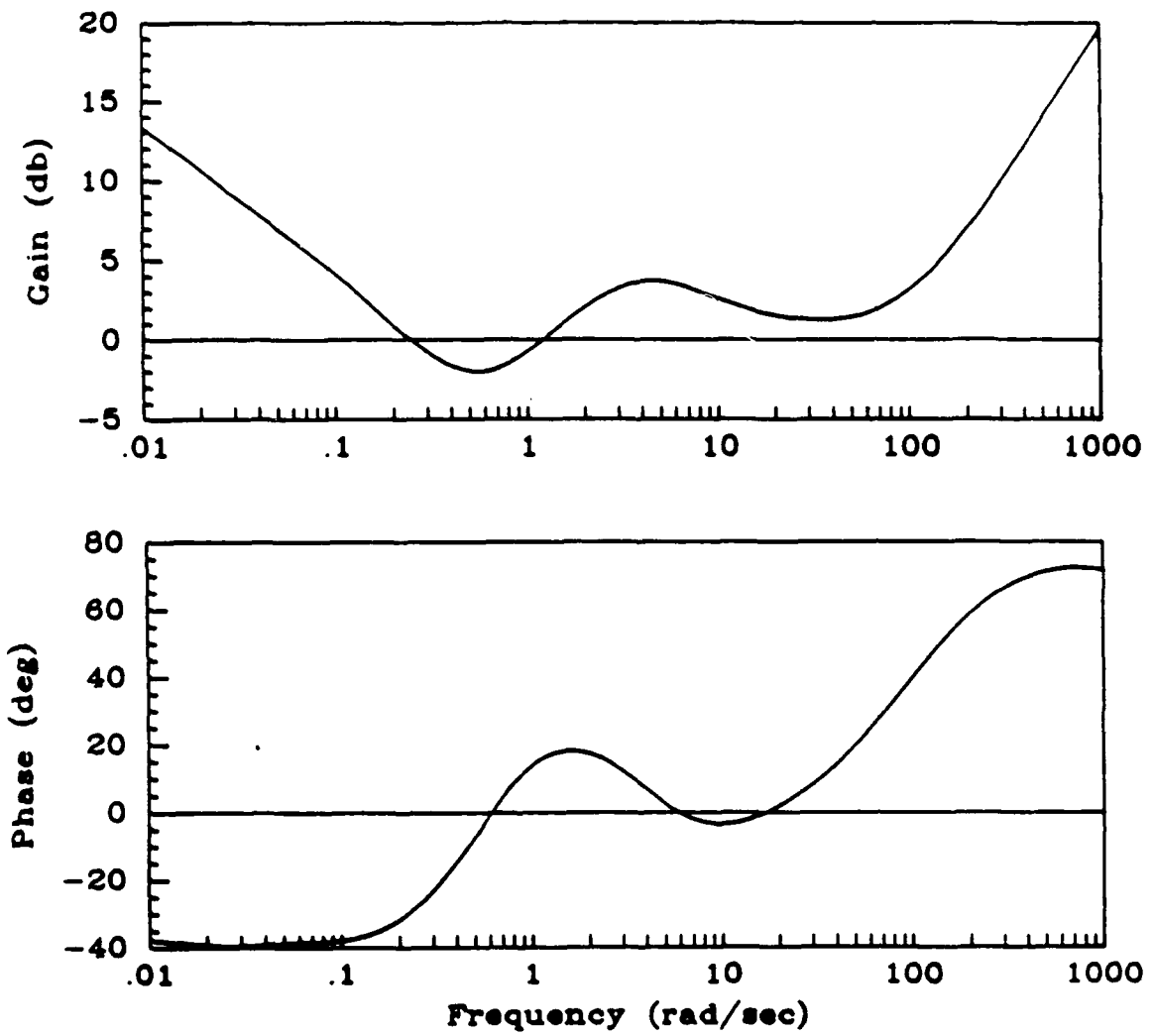Figure 5.8: Optimal compensator for Example 2; pinned-free beam
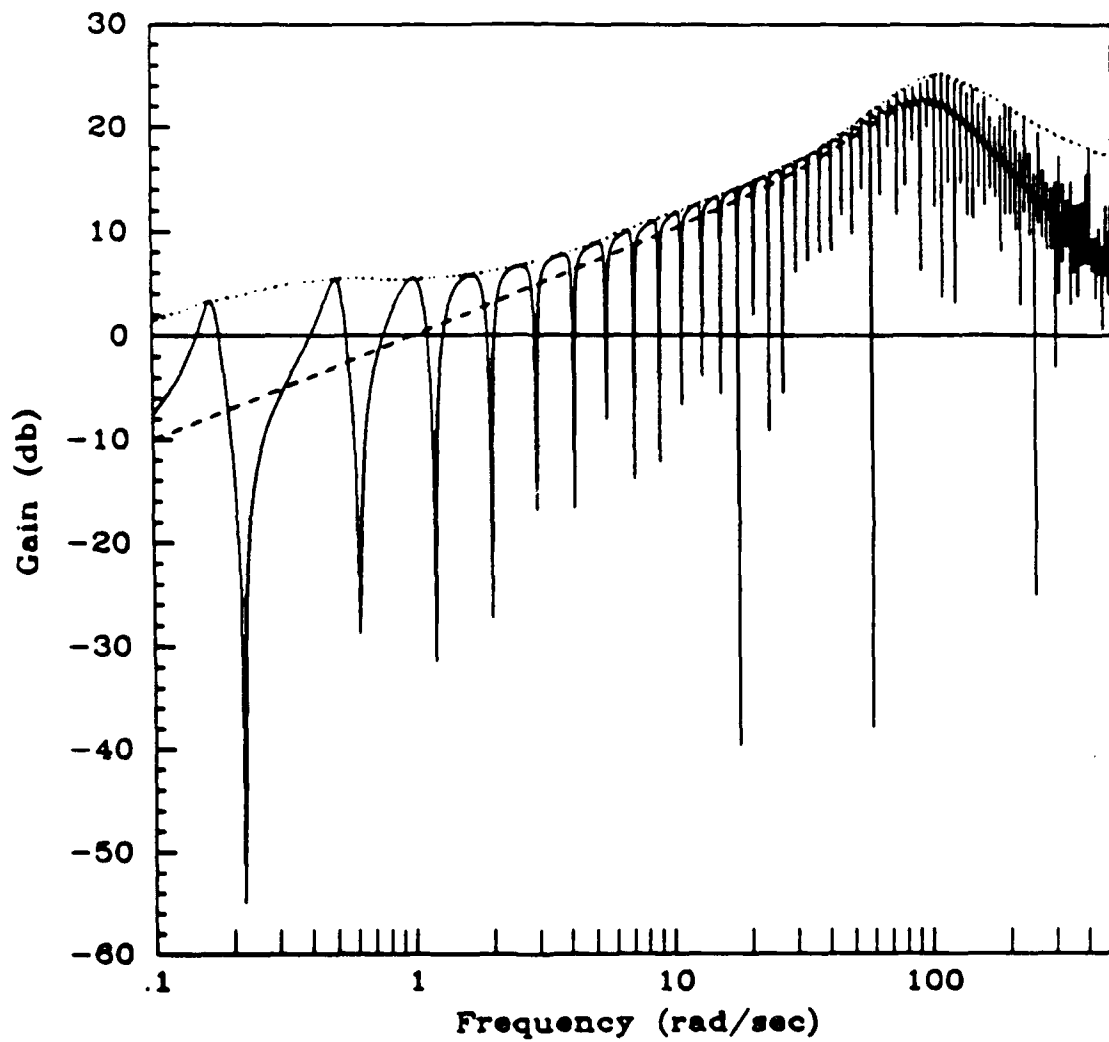
73

Figure 5.9: Closed loop transfer function at controlled end of pinned-free beam (solid), dereverberated mobility (dashed), and envelope of possible transfer functions (dotted).

74

Chapter 6

Experimental Results

While theoretical results are valuable of themselves, they must ultimately be tested in an experiment. This verifies the theoretical results, and indicates problems in their application. In addition to demonstrating the usefulness of the work, the experiment points out limitations, and appropriate directions for further research.

The approach described in Chapters 3 and 4 was tested on a brass beam suspended in the Space Engineering Research Center laboratory at M.I.T. Previous experiments with this beam [26,29] include collocated rate feedback and $\mathcal{H}_2$ optimal wave control, and these provide a basis for comparison with the $\mathcal{H}_\infty$ compensator.

6.1 Experimental Setup

The setup is shown schematically in Figure 6.1. For complete details on the setup, see reference [29]. The beam is suspended horizontally in the lab, with actuation and sensing such that the bending vibration can be controlled. One end is effectively pinned, while the other is free. The properties and dimensions of the beam are summarized in Table 6.1. The open-loop damping of the first 17 modes (up to a frequency of 27.7 Hz) averaged about 0.3%.

Control is applied through a torque motor at the pinned end, and sensing is
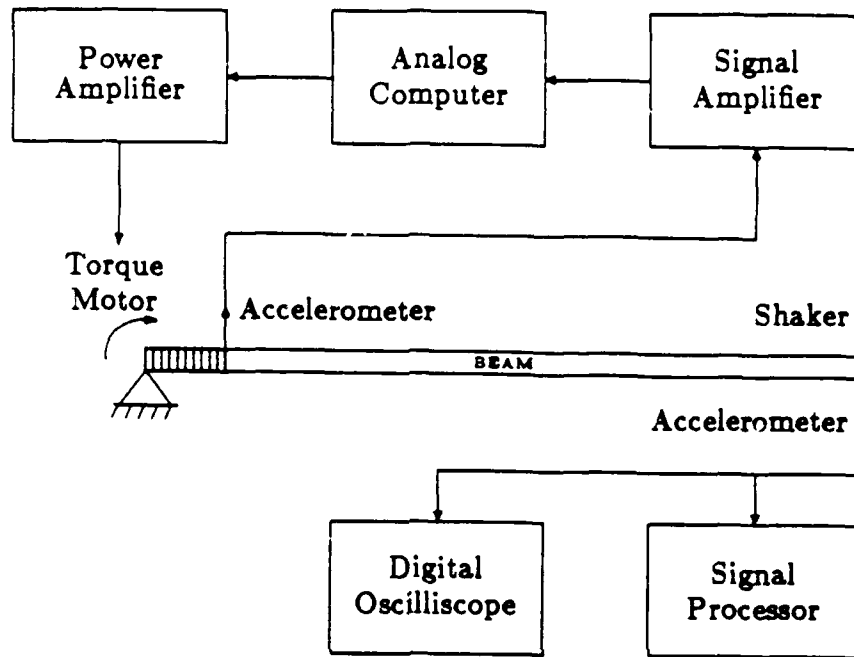
75

Figure 6.1: Schematic of Experimental Setup

Length	7.32 m
Width	0.102 m
Thickness	3.175 mm
EI	31.1 Nm^2
ρA	2.85 kg/m

Table 6.1: Beam Dimensions and Properties

provided by a linear accelerometer mounted a short distance from the end. The member connecting the sensor to the tip is assumed to be rigid, such that the sensor provides a rotational acceleration measurement collocated with the moment actuator. In practice, this assumption is not quite valid, though it is reasonable in the frequency range of interest.

In addition to the control actuator and sensor, a shaker and data acquisition accelerometer were mounted at the free end of the beam. The shaker was mounted to provide a force collocated with the acceleration measurement. The closed loop transfer function between these two was used as an indication of the performance achieved.

The signal from the accelerometer at the controlled end was fed through a signal amplifier into an analog computer which contained the compensator program. The output of this was fed through a power amplifier into the moment actuator. The accelerometer signal from the uncontrolled end was fed into a Signology SP-20 Signal Processing Peripheral to record and analyze the response data, and obtain frequency domain information. This signal was also fed into an oscilliscope so that any instabilities could be quickly identified, and their frequencies determined.

6.2   Compensator Design

A detailed model of the beam is not necessary for the experiment; it is sufficient to just take the transfer function from the control actuator to the control sensor. This transfer function is shown in Figure 6.2. The dereverberated mobility is that of Example 2, given in Equation (5.8) with the rotational inertia at the tip corresponding to the inertia of that part of the actuator armature and sensor that is fixed to the beam. From the measured transfer function, the effect of this inertia was at a frequency higher than the region of interest, so for the control design, the tip rotational inertia was assumed to be zero. The dereverberated mobility based

on this assumption is also shown in Figure 6.2.

The optimal compensator with unity weighting is proportional to $\frac{1}{\sqrt{s}}$, given in Equation (5.11). This compensator can also be derived from previous wave approaches, and had been implemented on this beam in [29]. In order to test the $\mathcal{H}_\infty$ approach, a weighting function was selected to emphasize a narrow frequency band near 35 rad/sec. This corresponds approximately to the frequency of the 7th mode of the beam. The minimum value of W_1 in this region was approximately 0.65, and the weighting increased to near unity a factor of $\sqrt{2}$ above and below this frequency, as shown in Figure 6.3. The optimal compensator from slope rate to moment for this case was found to be well approximated by the product of the unweighted optimum, $\frac{1}{\sqrt{s}}$, and a two pole, two zero lag-lead network. This network provided the phase lead that is required so that at the center of the weighted region, the phase approaches the unconstrained optimal phase of 45° (from Equation (5.10)), allowing the compensator to dissipate more power. The optimum poles and zeroes of this network are symmetric about the center frequency of the weighting function W_1, at 35 rad/sec. The two free parameters of this network were optimized to minimize the $\mathcal{H}_\infty$ norm of the cost. This results in the compensator from slope rate to moment being

$$K(s) = 63.4 \cdot \frac{1}{\sqrt{s}} \cdot \left(\frac{s^2 + 38.5s + 466}{s^2 + 100s + 3210} \right) \tag{6.1}$$

The available measurement, however, was proportional to angular acceleration, and thus a further integration was necessary to obtain angular rate. This integrator was rolled off at DC to prevent saturation and drift problems. The second order dynamics were chosen to have a natural frequency of 0.5 Hz, and a damping ratio of 0.5. Finally, an additional gain was necessary to obtain the compensator from the sensor signal to the actuator input. The resulting compensator as implemented was

$$K(s) = 8110 \cdot \frac{1}{\sqrt{s}} \cdot \left(\frac{s^2 + 38.5s + 466}{s^2 + 100s + 3210} \right) \cdot \left(\frac{s}{s^2 + 3.14s + 9.87} \right) \tag{6.2}$$

The implementation of the half integrator $\frac{1}{\sqrt{s}}$ is presented in [26]. The transfer function of the circuit used to approximate this is shown in Figure 6.4. The approximation is excellent in the region of interest, however at higher frequencies, it rolls off too quickly, and there is an associated phase drop, as shown in Figure 6.4. The measured compensator in the experiment is compared with the desired compensator in Figure 6.5. Good agreement is obtained, except at low frequencies where the DC rolloff of the integrator has a noticeable effect, and at frequencies higher than those shown, where the approximation to $\frac{1}{\sqrt{s}}$ is poor. The actual compensator has some additional phase lead at 35 rad/sec, primarily due to the integrator dynamics, which results in increased damping at this frequency at the expense of poorer performance at low frequencies.

6.3 Results

Once the compensator was implemented, the gain was gradually turned from zero towards the optimal value. Because the actuator and sensor were not truly collocated, and had some dynamics, the plant was not actually positive real. Due to this, and because of the additional phase lag of the half integrator at high frequencies, the compensator could not be implemented at full gain without destabilizing high frequency modes of the beam. At 65% of the full gain, there was an instability at 775 Hz. (If a Bernoulli-Euler pinned free beam model were appropriate at this frequency, this would correspond to approximately the 90th mode of the beam.) At 60% of the optimal gain, a significant improvement in the response of the beam was already apparent, as shown in Figure 6.6. This figure compares the open loop with the closed loop transfer function from force at the free end to collocated velocity. The corresponding open and closed loop transfer functions for velocity feedback can be found in [29]. The results for the $\mathcal{H}_\infty$ technique presented here show some improvement over rate feedback already, even though full gain was not used. As

desired, the modes in one particular frequency range are damped more heavily than others. This range is slightly higher in frequency than that desired due to the implementation at less than the optimal gain. Note that the spikes present in the data at 16.4, 19.8, 24.3, and 24.5 Hz correspond to torsional modes of the beam, which are excited by the shaker but are uncontrolled by the moment actuator.

The predicted response based on the implemented compensator is plotted in Figure 6.7. This was calculated from the experimental compensator transfer function using the approach of Section 2.3. Reasonable agreement is obtained between this prediction and the actual transfer function, although the achieved performance is noticeably better than that predicted. A prediction based on the desired, optimal compensator would be poorer due to the significant additional phase lead at 35 rad/sec in the actual compensator.

Further experimentation is still necessary. The implementation of the compensator could be improved at both low and high frequencies, and this might allow better performance to be achieved, at a higher gain. Ideally, the experiment should be done on a structure with truly collocated sensors and actuators. This could be done on this beam by mounting a tachometer on the torque motor. Ultimately, however, in any experiment, the input to output transfer function will not remain positive real for sufficiently high frequencies, and the compensator design should be modified to recognize this fact. This could be done after the $\mathcal{H}_\infty$ approach developed in this thesis has been applied, by including additional roll-off in an *ad hoc* manner. This would reduce the complementary sensitivity at higher frequencies, so that the singular value test of Slater [37] could be passed. Alternatively, and preferentially, the singular value constraint could be embedded in the design process. Thus this experiment has indicated at least one direction that future research into this control design approach should take.
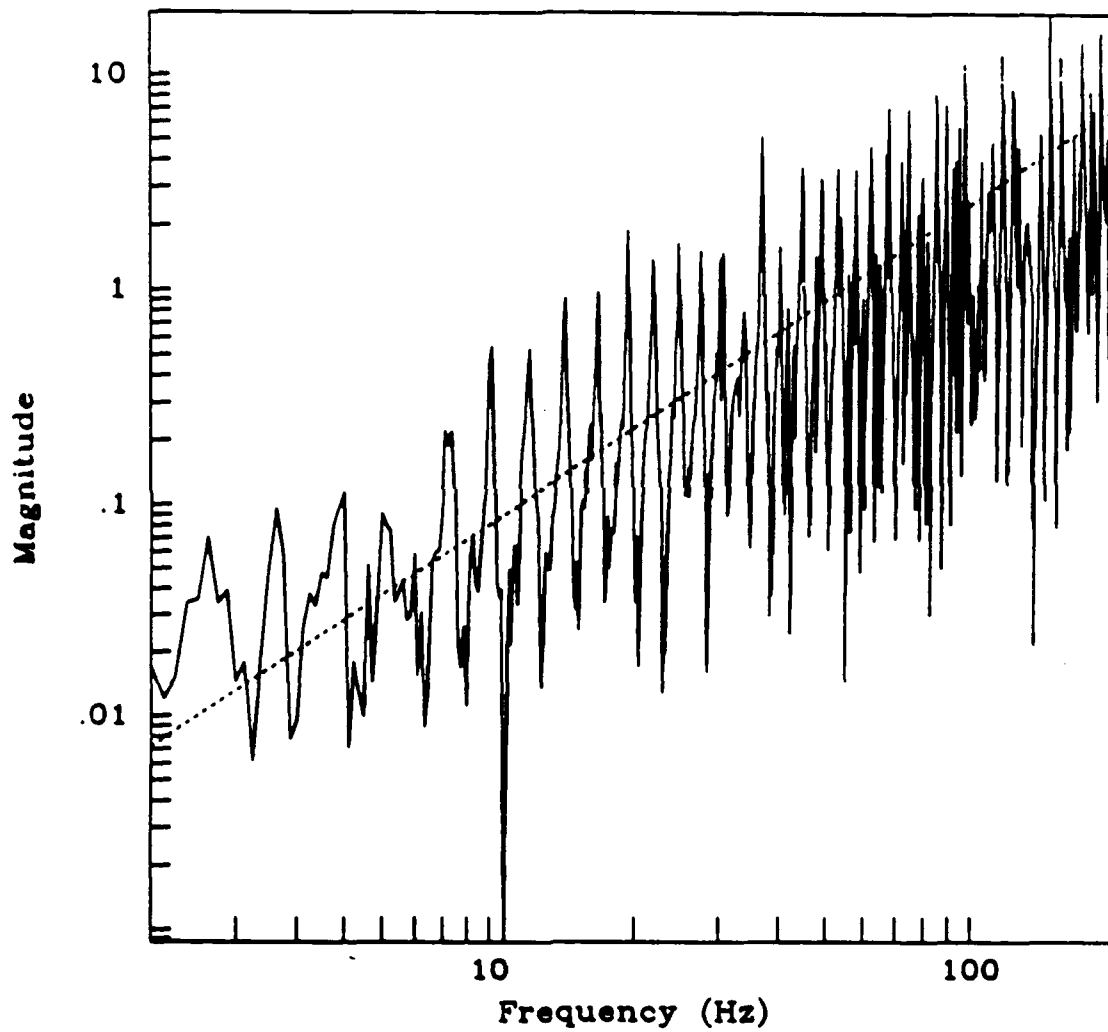
Figure 6.2: Open loop transfer function at controlled end of beam (solid), and dereverberated mobility used for control design (dotted).
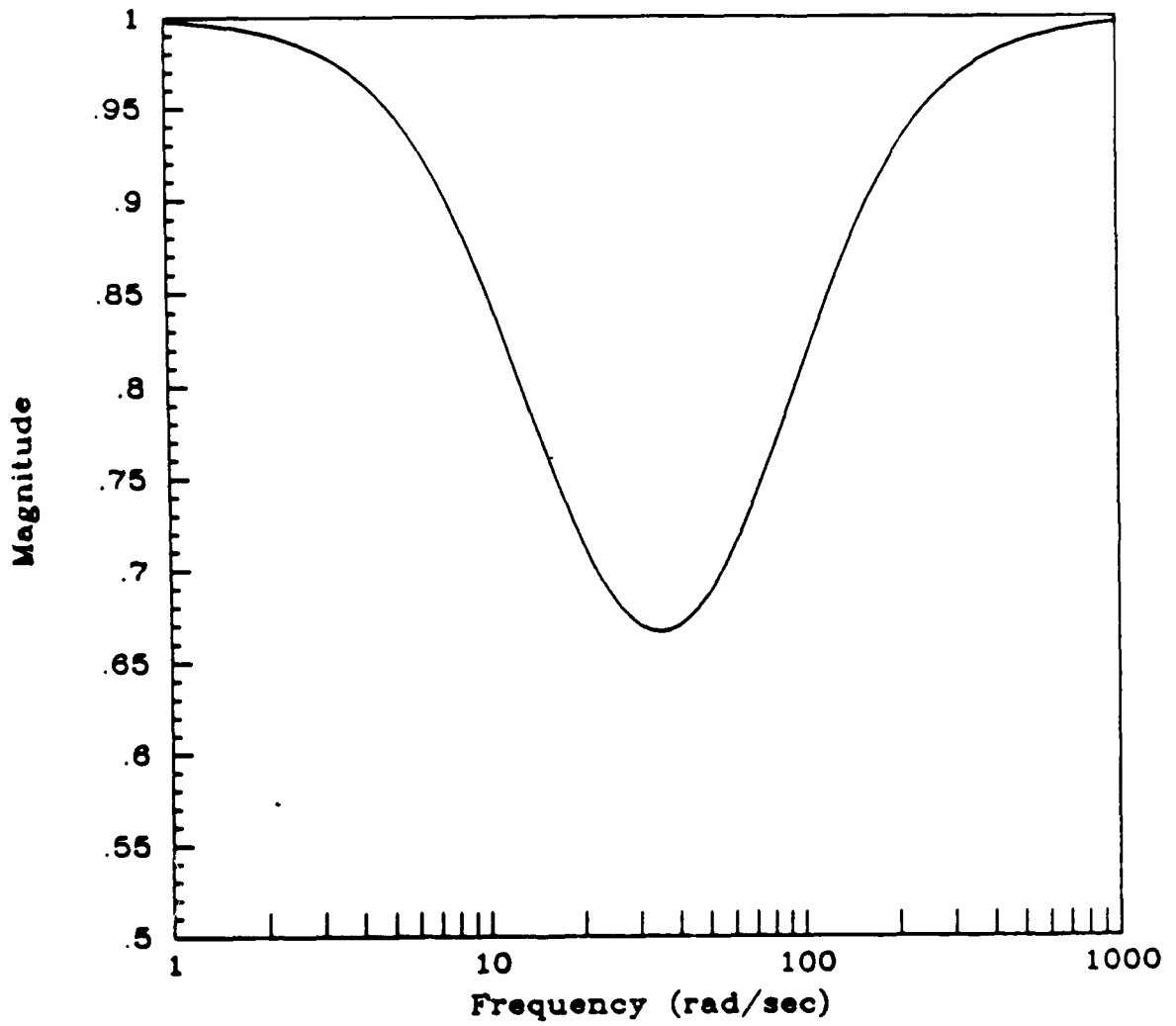
Figure 6.3: Weighting function W_1 used for control design in experiment.
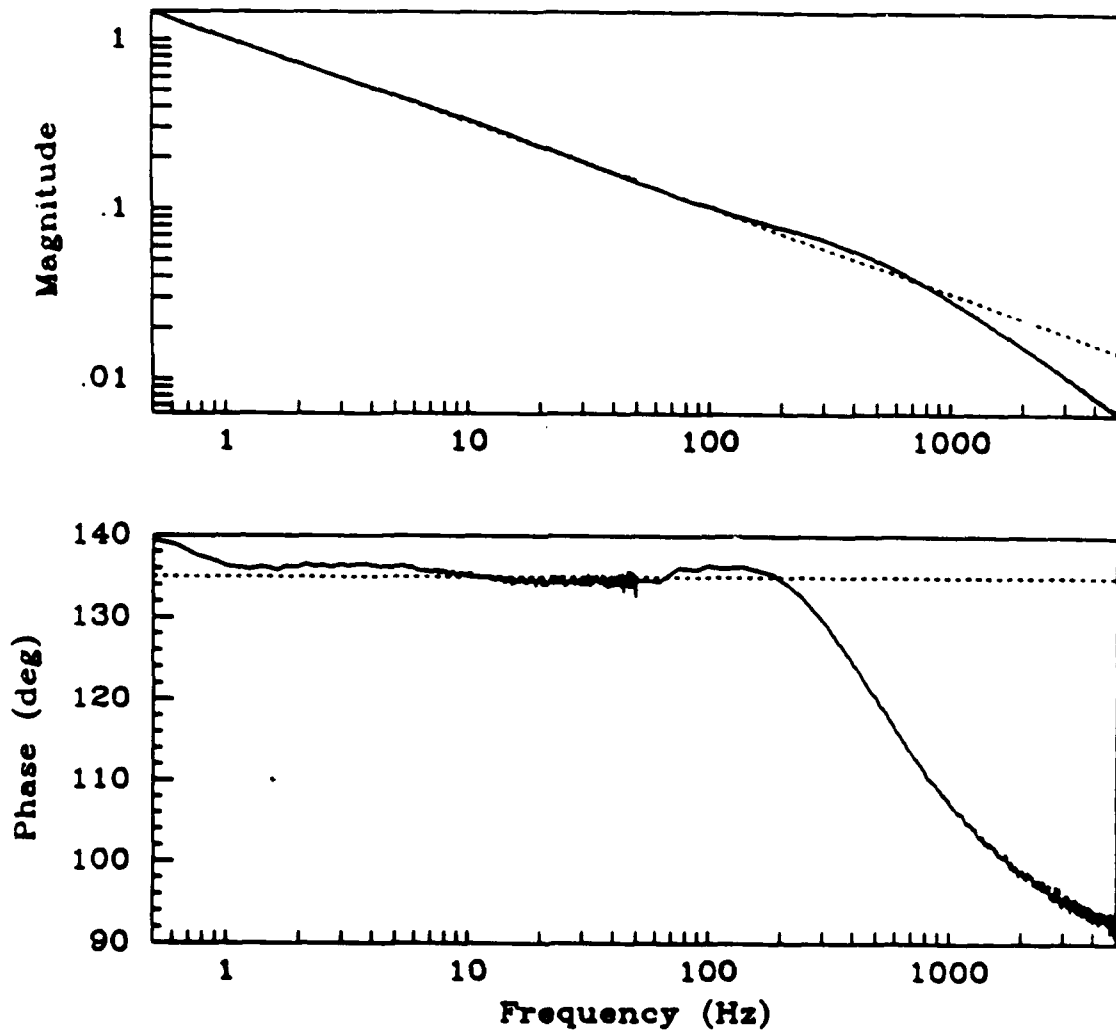
Figure 6.4: Transfer function of half integrator implemented in experiment (solid), and ideal half integrator (dotted).
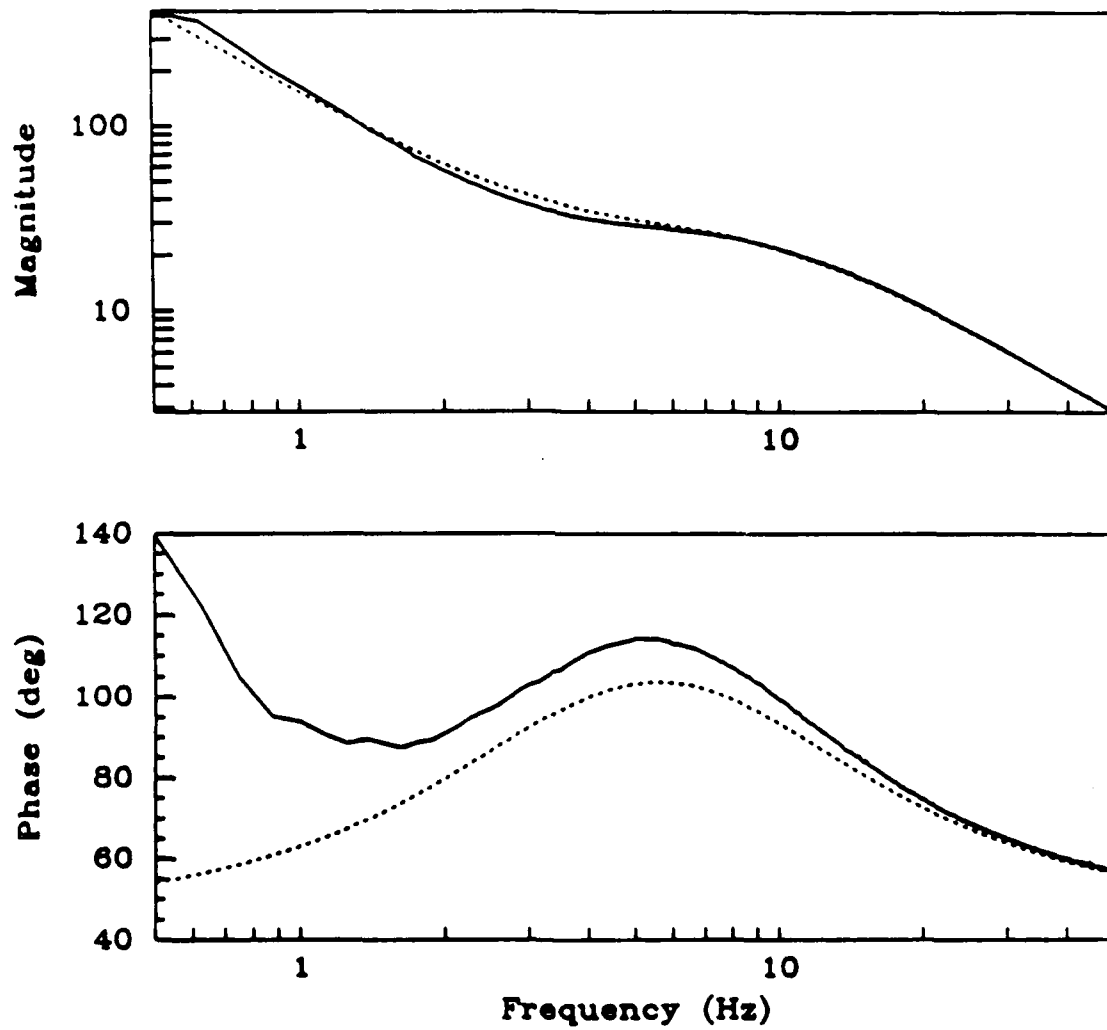
Figure 6.5: Transfer function of compensator implemented in experiment (solid), and desired compensator (dotted).
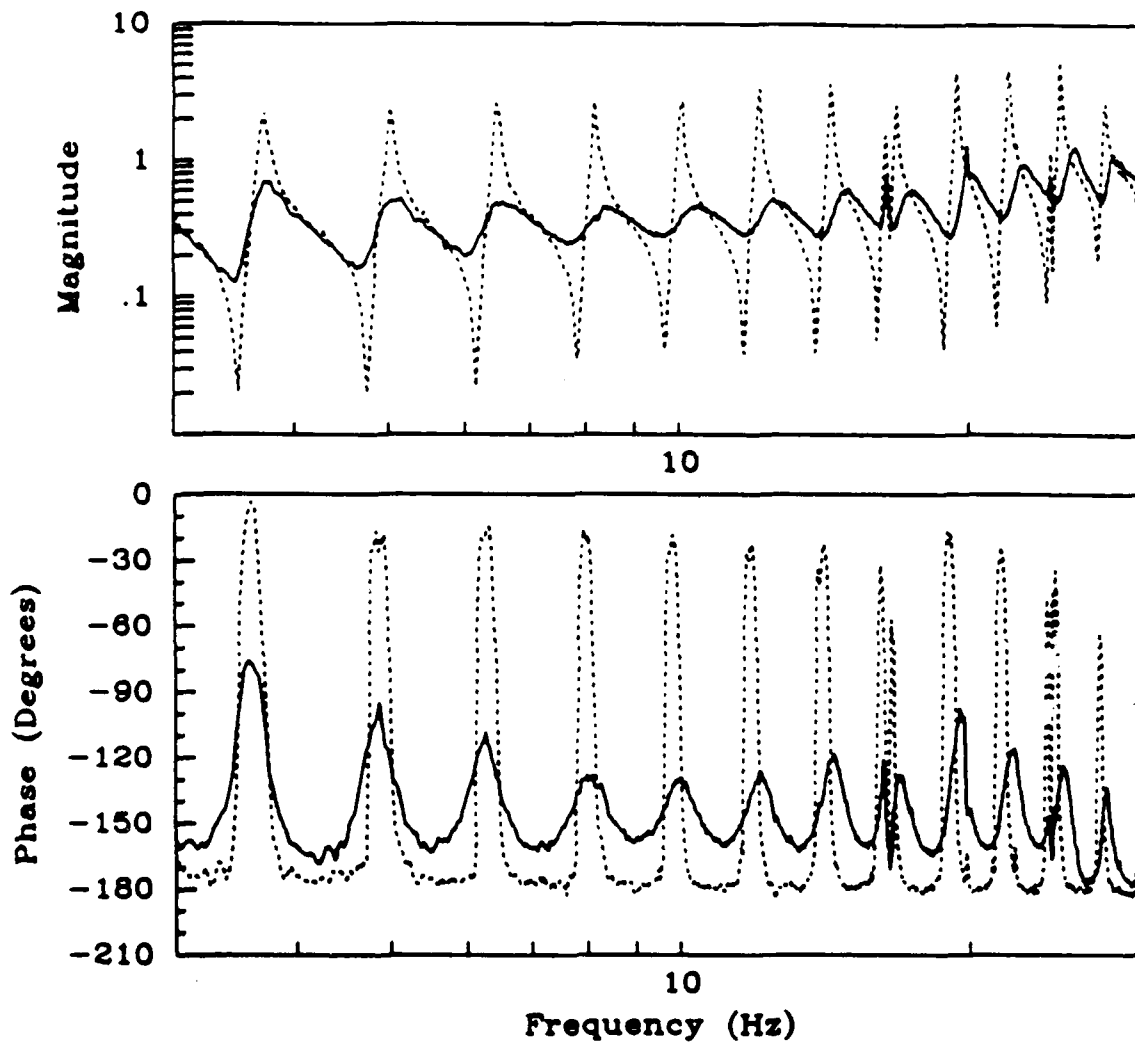
Figure 6.6: Experimental open (dotted) and closed loop (solid) transfer functions.
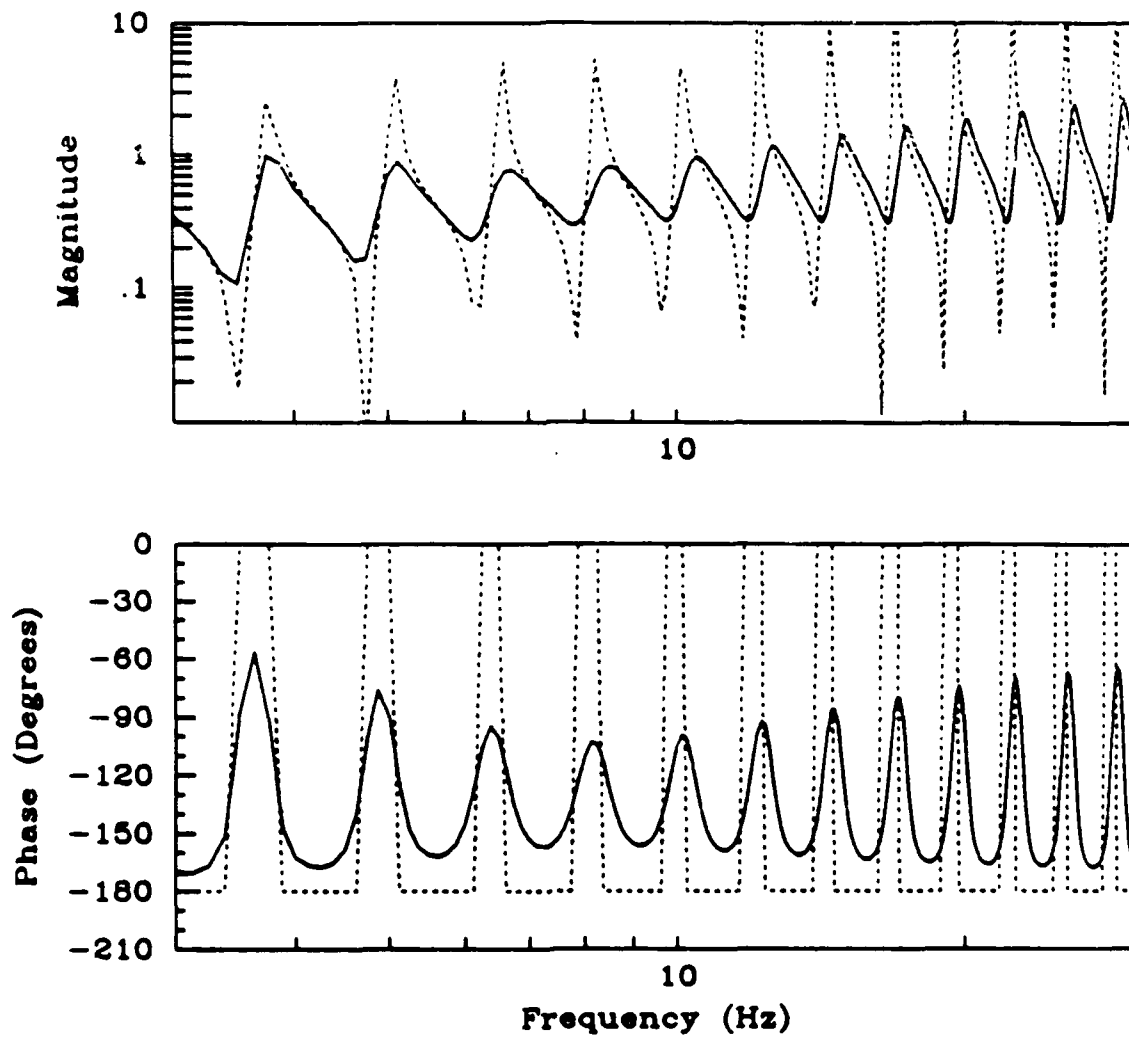
Figure 6.7: Predicted open (dotted) and closed loop (solid) transfer functions.

Chapter 7

Conclusions and Recommendations

7.1 Summary

In this thesis an approach to broadband active damping of modally dense structures with significant uncertainty has been presented. Both modelling and control design issues for this class of problems were investigated. Instead of a wave-based or modal model, the structure is modelled with its dereverberated mobility. The maximum power flow into the structure is minimized by solving an equivalent $\mathcal{H}_\infty$ control problem.

7.2 Contributions and Conclusions

1. A wave based model of the local dynamics of a structure near a collocated and dual sensor and actuator pair is equivalent to a dereverberated model of the structure. The dereverberated model is more general than a local wave model, as it can be easily applied to any structure. This model can be calculated directly from the driving point impedance, by

87

taking its logarithmic average, and can therefore be applied even when only experimental data are available. The dereverberated model retains many of the advantages of wave models. The local information can be determined with less uncertainty than the full structural model, while the global dynamics of the structure can be modified by controlling the local dynamics near an actuator, with a control law based only on this local model.

2. A causal, guaranteed stabilizing, optimal compensator can be obtained by minimizing the maximum power flow into the structure. This results in a positive real controller which dissipates power at all frequencies. This can be compared with several other compensators that could be designed based on the same model. The compensator that dissipates the most power at every frequency is in general noncausal, and cannot be implemented. $\mathcal{H}_2$ optimal power dissipation [28] does not guarantee stability, and simple rate feedback is stabilizing, but not necessarily optimal. The desirable properties of the solution can be retained while increasing the importance of a certain frequency range, through the use of a weighting function.

3. The technique was demonstrated for several simple examples. If a weighting function is chosen to emphasize some frequency range, then at the frequency deemed most important, the optimal compensator is close in both magnitude and phase to the unconstrained optimum. Thus at this frequency, it dissipates almost all of the incoming power possible. The compensator still dissipates some power at all frequencies, and is therefore guaranteed to be stable. The unconstrained optimal compensator thus provides some insight into how one could select the best compensator without requiring the $\mathcal{H}_\infty$ design approach. The transfer function should be chosen to match the unconstrained transfer function as closely

as possible in both magnitude and phase at the frequencies deemed important, while maintaining causality and positive realness.

4. Experimental results indicate that this approach to modelling and control design performs satisfactorily. Significant damping was added to many modes of a laboratory structure, without the large effort in system identification, off-line computation, and compensator complexity that would be required of many control design techniques. Greater damping was achieved than in velocity feedback experiments on the same structure [29]. Difficulties arose, however, for two main reasons. First, the implementation of the compensator was not perfect, particularly at low and high frequencies. Second, and more important, the actuator and sensor were not collocated, and may have had additional dynamics, so that the plant transfer function was not positive real at all frequencies as assumed.

7.3 Recommendations

1. The approach presented in this thesis works for systems which have a positive real transfer function between the sensor and actuator. In real structures, this will never be the case, due to actuator and sensor dynamics, time delays, and noncollocated actuators and sensors. Further work should investigate ways to modify the control design technique to allow for perturbations from the positive real condition, for example using the results of Slater [37]. One approach to doing this was discussed briefly in Chapter 4. Stability can be guaranteed by solving an $\mathcal{H}_\infty$ minimization problem, with a constraint on the $\mathcal{H}_\infty$ norm of a second transfer function. Whether this problem can be easily solved is an open question.

2. Further experimentation is necessary to obtain a better comparison between this technique and existing control design approaches. On the struc-

ture used in the experiment in Chapter 6, this could include a better implementation of the compensator, and either a hardware modification to give a collocated sensor and actuator, or some allowance in the compensator design procedure for non-collocation. Also, the experiment was conducted on a structure which could be easily modelled with a wave approach. Experimental results on a more complex structure for which this is not the case would be valuable in justifying the modelling approach presented in this thesis.

3. There may be a relationship between the modelling and control design approach presented here, and existing approaches, such as MEOP [5] and other optimal wave control methods [28]. These connections should be investigated. In particular, Miller *et al.* [28] solved an $\mathcal{H}_2$ optimal control problem, while this research solved a similar $\mathcal{H}_\infty$ problem. A combination of these two problems would be of interest. Closed loop stability can be guaranteed with an $\mathcal{H}_\infty$ constraint, and an $\mathcal{H}_2$ optimization could then guarantee performance [6,31]. Depending on the value of the constraint, this approach could yield solutions varying from the $\mathcal{H}_\infty$ optimal solution presented here, to the $\mathcal{H}_2$ optimal solution of Miller *et al.* [28].

4. The approach presented in this thesis optimizes the power dissipation associated with the control input, which results in active damping of the structure. However, damping is not necessarily a suitable performance criterion for all structural control problems. The algorithm should be modified to allow for the evaluation and optimization of other performance criteria, such as line-of-sight pointing error.

5. In general, the first few modes of a structure are relatively well known, and the uncertainty increases with frequency. A compensator which discards this information is suboptimal. An additional modification to the

approach should be to incorporate some knowledge of the lowest modes of the structure.

References

[1] Anderson, B.D.O., "A System Theory Criterion For Positive Real Matrices," *SIAM Journal of Control*, Vol. 5, No. 2, 1967, pp. 171-182.

[2] Aubrun, J-N., "Theory of the Control of Structures by Low-Authority Controllers," *AIAA Journal of Guidance and Control*, Vol. 3, No. 5, Sept-Oct 1980, pp. 444-451.

[3] Balas, M.J., "Feedback Control of Flexible Systems," *IEEE Transactions on Automatic Control*, Vol. AC-23, No. 4, Aug. 1978.

[4] Balas, M.J., "Trends in Large Space Structure Control Theory: Fondest Hopes, Wildest Dreams," *IEEE Transactions on Automatic Control*, Vol. AC-27, No. 3, June 1982, pp. 522-535.

[5] Bernstein, D.S. and Hyland, D.C., "Optimal Projection for Uncertain Systems (OPUS): A Unified Theory of Reduced Order, Robust Control Design," in *Large Space Structures: Dynamics and Control*, Atluri and Amos (ed.), Springer-Verlag, 1988.

[6] Bernstein, D.S. and Haddad, W.M. "LQG Control with an $\mathcal{H}_\infty$ Performance Bound: A Riccati Equation Approach," *IEEE Transactions on Automatic Control*, Vol. 34, No 3, March 1989, pp. 293-305.

[7] Blackwood, G.H., Chu, C-C., Fanson, J.L., and Sirlin, S.W., "Uncertainty Modeling for the Control of an Active Structure," to be presented at the ASME 1989 Winter Meeting, San Francisco, CA, Dec. 1989.

[8] Bode, H.W., *Network Analysis and Feedback Amplifier Design*, Van Nostrand, New York, 1945.

[9] Boulahbal, D., *Investigations on Group Delay in Structures and Acoustical Spaces*, 1988 SM Thesis, Department of Mechanical Engineering, M.I.T., Cambridge, MA.

[10] Chen, G-S., Lurie, B.J., and Wada, B.K., "Experimental Studies of Adaptive Structures For Precision Performance," *Proceedings of the 30th Structures, Structural Dynamics and Materials Conference,* Mobile, AL, April 1989, pp. 1462-1472.

[11] Doyle, J.C. and Stein, G., "Multivariable System Design: Concepts for a Classical/Modern Synthesis," *IEEE Transactions on Automatic Control,* Vol. AC-26, No. 1, Feb. 1981, pp. 4-16.

[12] Doyle, J.C., "Analysis of Feedback Systems with Structured Uncertainties," *IEE Proceedings,* Vol. 129, Part D, No. 6, Nov. 1982, pp. 242-250.

[13] Doyle, J.C., Glover, K., Khargonekar, P.P., and Francis, B.A., "State-Space Solutions to Standard $\mathcal{H}_2$ and $\mathcal{H}_\infty$ Control Problems," *IEEE Transactions on Automatic Control,* Vol. 34, No. 8, Aug. 1989, pp. 831-847.

[14] Ewins, D.J., *Modal Testing: Theory and Practice,* John Wiley & Sons, New York, NY, 1986, p. 27.

[15] Francis, B.A., *A Course in $\mathcal{H}_\infty$ Control Theory,* Springer-Verlag 1987.

[16] Glover, K., and Doyle, J.C., "State-Space formulae for all Stabilizing Controllers That Satisfy an $\mathcal{H}_\infty$-Norm Bound and Relations to Risk Sensitivity," *Systems and Control Letters,* 12 (1988) 167-172.

[17] Hagedorn, P., and Schmidt, J.T., "Active Vibration Damping of Flexible Structures Using the Travelling Wave Approach," *Proceedings of the Second International Symposium on Spacecraft Flight Dynamics,* Darmstadt, FR Germany, Oct. 1986, ESA SP-255, Dec. 1986.

[18] Hall, S.R., Crawley, E.F., How, J.P., and Ward, B., "A Hierarchic Control Architecture for Intelligent Structures," submitted to *AIAA Journal of Guidance Control and Dynamics,* (Space Systems Laboratory Report #19-88, M.I.T., Cambridge, MA.)

[19] Hodges, C.H. and Woodhouse, J., "Theories of Noise and Vibration Transmission in Complex Structures," *Reports on Progress in Physics,* 1986 49 pp. 107-170.

[20] How, J.P., *An Analysis of Local Control Designs for a Hierarchic Control Architecture for Intelligent Structures,* 1989 SM Thesis, Department of Aeronautics and Astronautics, M.I.T., Cambridge, MA.

[21] Lyon, R.H., *Statistical Energy Analysis of Dynamical Systems: Theory and Applications,* The MIT Press, Cambridge MA, 1975.

[22] Lyon, R.H., *Machinery Noise and Diagnostics,* Butterworth Publishing, June 1987.

[23] Mace, B.R. "Active Control of Flexural Vibrations," *Journal of Sound and Vibration,* 114, 253-270, 1987.

[24] MacMartin, D.G. and Hall, S.R., "An $\mathcal{H}_\infty$ Power Flow Approach to Control of Uncertain Structures," submitted to *AIAA Journal of Guidance Control and Dynamics,* (Space Systems Laboratory Report #10-89, M.I.T., Cambridge, MA.)

[25] Milich, D.A., *A Methodology for the Synthesis of Robust Feedback Systems,* 1988 PhD Thesis, Department of Mechanical Engineering, M.I.T., Cambridge, MA. (Laboratory for Information and Decision Systems Report LIDS-TH-1748.)

[26] Miller, D.W., *Modelling and Active Modification of Wave Scattering in Structural Networks,* 1988 ScD Thesis, Department of Aeronautics and Astronautics, (Space Systems Laboratory Report #12-88), M.I.T., Cambridge, MA.

[27] Miller, D.W., "Power Flow in Structural Networks," *Journal of Sound and Vibration,* 128, 145-162, 1989.

[28] Miller, D.W., Hall, S.R. and von Flotow, A.H., "Optimal Control of Power Flow at Structural Junctions," *Proceedings of the 1989 American Control Conference,* Pittsburgh, PA, June 1989.

[29] Miller, D.W., and Hall, S.R., "Experimental Results Using Travelling Wave Power Flow Techniques," to be presented at the ASME 1989 Winter Meeting, San Francisco, CA, Dec. 1989.

[30] Mustafa, D., and Glover, K., "Controllers Which Satisfy a Closed-Loop $\mathcal{H}_\infty$-Norm Bound and Maximize an Entropy Integral," *Proceedings IEEE Conference on Decision and Control,* Austin TX, Dec. 1988.

[31] Mustafa, D., "Relations Between Maximum-Entropy/$\mathcal{H}_\infty$ Control and Combined $\mathcal{H}_\infty$/LQG Control," *Systems and Control Letters* 12 (1989) 193-203.

[32] Pines, D.J., and von Flotow, A.H., "Active Control of Bending Wave Propagation at Acoustic Frequencies," *Proceedings of the 1989 American Control Conference,* Pittsburgh, PA, June 1989.

[33] Redman-White, W., Nelson, P.A., and Curtis, A.R.D., "Experiments on the Active Control of Flexural Wave Power Flow," *Journal of Sound and Vibration*, **112**, 187-191, 1987.

[34] Rhee, I., and Speyer, J.L., "A Game Theoretic Controller and Its Relationship to $\mathcal{H}_\infty$ and Linear-Exponential-Gaussian Synthesis," to be presented at the 28th IEEE Conference on Decision and Control, Tampa, Florida, Dec. 1989.

[35] Scheuren, J., "Active Control of Bending Waves in Beams," *Internoise*, Munich, 591-594, Sept. 1985.

[36] Skudrzyk, E. "The mean-value method of predicting the dynamic response of complex vibrators," *Journal of the Acoustical Society of America*, **67**(4), April 1980.

[37] Slater, G.L., Zhang, Q., and Bosse, A., "Robustness with Positive Real Controllers for Large Space Structures," *Proceedings of the 1989 AIAA Guidance, Navigation, and Control Conference*, Boston, MA, August 1989, pp. 932-941.

[38] Tribolet, J.M., and Quatieri, T.F., "Computation of the Complex Cepstrum," in *Programs for Digital Signal Processing*, IEEE Press Book, Ed. by IEEE, ASSP, New York, 1979.

[39] Vaughan, D.R., "Application of Distributed Parameter Concepts to Dynamic Analysis and Control of Bending Vibrations," *Journal of Basic Engineering*, June 1968, pp. 157-166.

[40] von Flotow, A.H., and Shäfer, B., "Wave-Absorbing Controllers for a Flexible Beam," *AIAA Journal of Guidance, Control, and Dynamics*, Vol. 9, No. 6, Nov.-Dec. 1986, pp. 673-680.

[41] von Flotow, A.H., "The Acoustic Limit of Structural Dynamics," in *Large Space Structures: Dynamics and Control*, Atluri and Amos (ed.), Springer-Verlag, 1988.

[42] Zhang, Z., and Freudenberg, J.S., "State-Space Formulas for Inner-Outer Factorization," *Proceedings of the 1989 American Control Conference*, Pittsburgh, PA, June 1989.

Appendix A

Beam $\mathcal{H}_\infty$ Compensator

For a free-free beam with dereverberated mobility $G(s) = \frac{1}{\sqrt{s}}$, the compensator that minimizes the maximum power flow into the structure can be found analytically. From Equation (4.30) the problem is to find a stable, causal compensator that minimizes the $\mathcal{H}_\infty$ norm of the transfer function from w to $G_0^\sim u + w$. From the definition of G_0 (Equation (4.23)),

$$G_0 G_0^\sim = \frac{1}{\sqrt{s}} + \frac{1}{\sqrt{-s}} \tag{A.1}$$

$$= \frac{\sqrt{2}}{\sqrt[4]{s}\sqrt[4]{-s}} \tag{A.2}$$

Or,

$$G_0(s) = \frac{\sqrt[4]{2}}{\sqrt[4]{s}} \tag{A.3}$$

Since $d = G_0 w$, then from Equation (4.4),

$$u = H G_0 w \tag{A.4}$$

The compensator K from y to u will be stable and causal provided H is also stable and causal. Thus the problem is to find H to minimize

$$\| G_0^\sim H G_0 + 1 \|_\infty \tag{A.5}$$

96

The solution to this, using the notation of Francis [15] is

$$\gamma = \min_{H} \|G_0^{\sim} H G_0 + 1\|_{\infty} \qquad (A.6)$$

$$= \min_{H} \left\| \frac{\sqrt[4]{2}}{\sqrt[4]{-s}} H \frac{\sqrt[4]{2}}{\sqrt[4]{s}} + 1 \right\|_{\infty} \qquad (A.7)$$

$$= \min_{H} \left\| \frac{\sqrt{2}}{\sqrt[4]{s}} H + \frac{\sqrt[4]{-s}}{\sqrt[4]{s}} \right\|_{\infty} \qquad (A.8)$$

Equation (A.8) is of the form

$$\gamma = \min_{H} \|R - X\|_{\infty} \qquad (A.9)$$

where

$$R = \frac{\sqrt[4]{-s}}{\sqrt[4]{s}} \qquad (A.10)$$

$$X = -\frac{\sqrt{2}}{\sqrt[4]{s}} H \qquad (A.11)$$

The problem now is to find $X \in \mathcal{H}_{\infty}$ to minimize $\|R - X\|_{\infty}$. From the maximum modulus theorem, only the imaginary axis need be considered, so substitute $s = j\omega$ to give

$$R = \frac{1 - j}{\sqrt{2}} \qquad (A.12)$$

There are three possible options for the behavior of $X(s)$ at the origin. Either X has a pole at zero, in which case $\|R - X\|_{\infty}$ is infinite, X has a zero at the origin, in which case $\|R - X\|_{\infty} \geq 1$, or X is a constant, with either $0°$ or $180°$ phase. In the last case, the smallest value $|R(0) - X(0)|$ can have is $\frac{1}{\sqrt{2}}$, for $X(0) = \frac{1}{\sqrt{2}}$. Thus there cannot exist $X(s)$ for which $\|R - X\|_{\infty} < \frac{1}{\sqrt{2}}$. Since the solution $X(s) = \frac{1}{\sqrt{2}}$ results in $\|R - X\|_{\infty} = \frac{1}{\sqrt{2}}$, this must be an optimal solution. From Equation (A.11),

$$H = -\frac{1}{\sqrt{2}} \cdot \frac{\sqrt[4]{s}}{\sqrt{2}} \qquad (A.13)$$

and from Equation (4.16), the compensator from the output y to u is given by

$$K = \sqrt{s} \qquad (A.14)$$

Appendix B

Damping Prediction from Power Flow

The $\mathcal{H}_\infty$ control design approach described in Chapter 4 yields information about the closed loop power flow achieved, via Equation (4.39). It would be useful to relate this to the closed loop modal damping achieved in the structure. For arbitrary structures, this is extremely difficult. However, for a simple structure such as the free-free beam of Example 1, in Section 5.1, a relationship between power flow and damping can be derived.

To do this, consider a *wave-packet* travelling through the structure. The wave-packet is a spatially localized disturbance, which is also narrowband in frequency, and thus can be approximated as having a single frequency. Though a disturbance that is simultaneously both spatially localized and of a single frequency is not possible, it is an approximation that can lead to reasonable results for sufficiently high frequency. The wave-packet travels at the group velocity v_g of the structure, which is a function of frequency:

$$v_g = \frac{\partial \omega}{\partial k} = \frac{2\sqrt{\omega}}{c_0} \qquad (B.1)$$

where c_0 is defined in Equation (2.52). Therefore, for a beam of length ℓ, in a time

$$t_1 = \frac{2\ell}{v_g} \tag{B.2}$$

the wave-packet has travelled through the beam and back to its original position, with a decrease in amplitude associated with travelling once through the controlled junction.

The compensator absorbs a fraction $\delta(\omega)$ of the total power available. Thus in one cycle, the energy of the wavepacket decreases to

$$E(t_1) = (1 - \delta)E(0) \tag{B.3}$$

and the amplitude, which is proportional to the square root of the energy, decays to

$$A(t_1) = \sqrt{1 - \delta}A(0) \tag{B.4}$$

The modal solution is of the form

$$u(t) = \sum_i a_i \Phi_i(x) e^{(\sigma_i + j\omega_i)t} \tag{B.5}$$

The wave-packet at time t_1 in Equation (B.2) has the same shape as at $t = 0$, and only the amplitude has changed. If the disturbance is approximated to consist of only a single frequency, and if this frequency corresponds to that of mode n, then the amplitude at t_1 is related to the initial amplitude by

$$\frac{u(t_1)}{u(0)} = e^{\sigma_n t_1} \tag{B.6}$$

Comparing this with the wave solution in Equation (B.4), then one finds that the real part of the eigenvalues is given by

$$\sigma_n = \frac{\log(1 - \delta(\omega_n))}{2t_1} \tag{B.7}$$

Combining this with Equation (B.2), then

$$\sigma_n = \frac{\log(1 - \delta(\omega_n))\sqrt{\omega_n}}{2\ell c_0} \tag{B.8}$$

where the power absorbed, $\delta(\omega)$, is given by Equation (4.39) as

$$\delta(\omega) = \frac{1 - \gamma^2}{|W_1|^2} \tag{B.9}$$

In particular, if the weighting function W_1 is unity, then

$$\sigma_n = \frac{\log(\gamma)\sqrt{\omega_n}}{\ell c_0} \tag{B.10}$$

Finally, the modal damping ratio ς_n is related to σ_n by

$$\varsigma_n = \frac{\sigma_n}{\omega_n} \tag{B.11}$$

Thus with equal power absorbed at all frequencies, the time constant of the beam modes increases with frequency, and the modal damping ratio decreases.

OPTIMAL CONTROL OF POWER FLOW AT STRUCTURAL JUNCTIONS

David W. Miller[1], Steven R. Hall[2], Andreas H. von Flotow[2]

Space Engineering Research Center, Department of Aeronautics and Astronautics
Massachusetts Institute of Technology
Cambridge, Massachusetts

ABSTRACT

This paper describes several techniques for deriving optimal feedback compensators for structural waveguides at junctions. A frequency dependent cost functional, composed of power flow and control effort, is minimized. Control of power flow, by modifying junction reflection and transmission properties, enables selective absorption of incoming vibrational power. Noncausal, causal fixed-form and Weiner-Hopf feedback solutions are derived. These solutions, including a positive real approximation to the Weiner-Hopf solution, are illustrated through an extensive example for the free end of a dispersive Bernoulli-Euler beam.

1. INTRODUCTION

For complex structures, modal models can become cumbersome and innaccurate for higher frequency modes. An alternative to a modal description is to retain only a small subset of the modal model, one boundary O.D.E. and descriptions of the members which intersect at that boundary, to generate a wave description of that boundary's reflection and transmission properties. The model is simpler, possibly mathematically exact, and describes important properties of the structure which exist at that boundary (wave junction).

The generic representation of a junction, given in Fig. 1, applies to a number of structural locations. For example, such a location may be a single member end condition (pinned, clamped, free, or attached to a complicated flexible body), an intersection of several members (e.g., the intersection of several truss beams), or an arbitrary location on a uniform member where control hardware is located. A junction description may also include internal dynamics, as long as a consistent input/output relation can be derived.

The basic objective behind wave junction control is to actively alter the wave scattering properties of a junction. Junction control can be used to extract energy from the structure or shunt energy to non-critical locations and therefore has obvious application where vibration suppression and dynamic isolation are required.

Several researchers have approached the problem of controlling elastic structural behavior through the use of wave models [2, 3, 4, 5, 6, 8, 9, 10 and 14]. The technique can pinpoint important disturbance transmission paths and allow analysis of the energetic interaction of disturbance sources with control actuation. Prior work [1, 9, 10 and 14] has shown that, in special cases, compensators designed for active absorption of travelling waves can be very similar to direct velocity feedback. This is due to the common practice of having only one actuator and sensor at a given structural location. As more distinct actuators and sensors are placed at a junction, the compensators become quite different and provide much better performance. Miller, von Flotow and Hall [2] derived feedback compensators which alter reflection and transmission coefficients to minimize power flow. However, the lack of a causality constraint in the formulation resulted in some noncausal compensators. Redman-White [3] minimized narrow band propagating disturbances by a convergent algorithm which measures a quantity indicative of power flow. However, the control is not broadband and an explicit expression for power flow, which includes evanescent effects, would have provided a tool for stability analysis and the

[1]Research Associate
[2]Assistant Professor

derivation of optimal broadband control. Scheuren [4] recognized the ability to shunt or absorb propagating disturbances. In that work, however, evanescent waves were deemed undesirable due to the lack of tools to characterize their contribution to power flow. High performance is predicted but often associated with noncausal compensators. Hagedorn [6] discussed the modelling insensitivity and robustness advantages of local wave control. Temporal expressions for power flow were derived yet did not include the contributions of evanescent behavior. Other approaches [8, 9 and 10] are solely based upon specifying the closed-loop reflection and transmission coefficients.
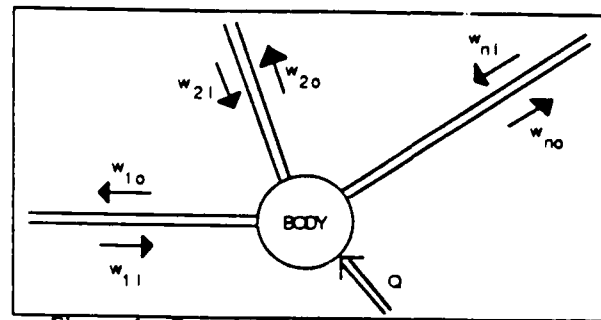

Figure 1 Generic wave junction composed of members and a body.

The motivation for this work lies in the apparent need for a procedure for deriving broadband, optimal, causal wave control compensators which minimize explicit expressions describing the contributions of both propagating and evanescent waves to power flow at structural discontinuities.

This paper discusses the derivation of optimal wave control based upon the minimization of power flow out of a structural junction. This is done by finding that compensator which minimizes a frequency domain cost functional composed of quadratic penalties on power flow and control effort. Power flow was chosen because it provides both a physical and a quadratic quantity for minimization, and yields certain stability information.

2. TRAVELLING WAVE DYNAMICS

This section presents the wave dynamics equations for a structural junction of arbitrary complexity (Fig. 1). The frequency domain derivation of component (member and junction) dynamics was presented by von Flotow [9]. This paper, using slightly different notation, makes extensive use of two of these important relations governing junction dynamics. The members are slender, one-dimensional structural elements. Common spatially continuous examples are beams, rods and cables, while spatially periodic examples include slender trusswork beams [11]. These members are viewed as waveguides along which a set of discrete, decoupled travelling wave modes may propagate at every frequency, ω. These travelling wave modes are coupled to others of the same frequency by scattering at structural junctions. The dynamics of the junction are described by frequency dependent reflection and transmission coefficients. This viewpoint is analogous to that adopted in microwave network analysis.

It is appropriate at this point to clarify the conventions used in this paper. Wave modes in the vicinity of a junction are grouped based upon their *outgoing* or *incoming* nature. Those evanescent modes which decay exponentially away from the junction are grouped with the outgoing waves. In general, wave modes are grouped based upon their causal origin (*i.e.*, outgoing waves are created at the junction and incoming waves are created elsewhere).

Von Flotow [1] uses an assemblage of member transformation matrices to provide a junction transformation matrix which relates complex wave mode amplitudes on all members attached to that junction, at the member/junction interface, to the member cross-sectional quantities: motion and stress, at the same location. This relation has the form

$$y(\omega) = \begin{bmatrix} u \\ f \end{bmatrix} = \begin{bmatrix} Y_{\bullet} & Y_{\bullet\bullet} \\ Y_{f\!i} & Y_{f\bullet} \end{bmatrix} \begin{bmatrix} w_{\bullet} \\ w_{o} \end{bmatrix} = Y(\omega)w(\omega) \tag{1}$$

where $w(\omega)$ is the vector of wave mode amplitudes at each frequency, ω. The partitioning of the wave mode vector is based on propagation direction with respect to the junction: incoming w_i or outgoing w_o. The vector y contains all member motions, u, and stresses, f, at the junction.

Von Flotow [1] gives the junction boundary conditions transformed into wave mode coordinates and arranged in causal, input/output form. Outgoing waves, w_o, result from the scattering of incoming waves, w_i, and the generation by external excitations, Q:

$$w_o(\omega) = S(\omega)w_i(\omega) + \psi(\omega)Q(\omega) \tag{2}$$

In this junction description the matrices S and ψ represent homogeneous and nonhomogeneous wave behavior and are called the scattering and generation matrices, respectively. Both may be complex and frequency dependent. This description contains only local junction dynamics and does not contain information about other portions of the structure. This junction model is valid as long as the boundary condition is an accurate description of the boundary physics and the attached members, for some arbitrarily small length, behave as modelled. In practice, member models can become inaccurate at frequencies where the wavelength divided by the member length becomes rather large or small.

3. JUNCTION POWER FLOW

Travelling waves move elastic and kinetic energy through a structure resulting in a flow of power. The power flow through junctions is a quantity of interest and can be used for response analysis and control design. Power at an arbitrary member cross-section is equal to the product of the deflection velocities and collocated stresses of like type: velocity and force; rotational rate and moment. The power flow at a member cross-section can be expressed in terms of the spectral components of the response variables through the use of the Power Theorem [17], a variation of Parseval's Theorem. Though power is a nonlinear quantity enabling instantaneous interaction between response variables of different frequencies, it is the interaction between identical frequency components that results in steady-state power flow.

Miller and von Flotow [15] show that the power flow through a junction is given by

$$P_{AVG}(\omega) = \begin{bmatrix} w_i(\omega)^H & w_o(\omega)^H \end{bmatrix} P_J(\omega) \begin{bmatrix} w_i(\omega) \\ w_o(\omega) \end{bmatrix} \tag{3}$$

where P_J is the junction power flow matrix, and is given by

$$P_J = i\omega \left[\begin{bmatrix} Y_{\bullet}^{H}Y_{f\!i} & Y_{\bullet}^{H}Y_{f\!o} \\ Y_{\bullet\bullet}^{H}Y_{f\!i} & Y_{\bullet\bullet}^{H}Y_{f\!o} \end{bmatrix} - \begin{bmatrix} Y_{f\!i}^{H}Y_{\bullet} & Y_{f\!i}^{H}Y_{\bullet\bullet} \\ Y_{f\!o}^{H}Y_{\bullet} & Y_{f\!o}^{H}Y_{\bullet\bullet} \end{bmatrix} \right]$$

$$= \begin{bmatrix} P_{\bullet} & P_{\bullet\bullet} \\ P_{\bullet\bullet} & P_{\bullet\bullet} \end{bmatrix} \tag{4}$$

The symbol H denotes the Hermitian or complex conjugate transpose. The matrix P_J is a function only of the dynamics of the members attached to the junction, specifically of the transformation (Eq. 1) from physical coordinates to wave mode coordinates. P_{AVG} is real for any mix of wave modes, since P_J is Hermitian.

In certain applications, such as control or damping design, it is useful to determine how much power is outgoing from a junction as a result of both incoming power and external excitations. When the junction is non-reciprocal due to the action of active control, the formal analysis developed by Miller [15] becomes necessary.

4. JUNCTION CONTROL

The waves incoming to a junction can be thought of as a disturbance to that junction. Conceptually, the disturbance is measured and fed to the actuators at the junction in order to reduce or eliminate the power associated with the resulting outgoing waves. Figure 2 illustrates this control architecture with F as the feedforward compensator and the junction matrices shown. This architecture assumes that measurements of the incoming wave mode amplitudes at the junction interface are available, and that $S(\omega)$ and $\psi(\omega)$ are known.

Since wave mode sensors are not available off the shelf, it is desirable to use cross-sectional variables as feedback measurements. The vector u contains measurable cross-sectional quantities while f contains those cross-sectional quantities that are commanded by the actuators. Equation 1 can be used to express the amplitudes in u in terms of both incoming and outgoing waves. The use of these quantities as measurements results in the feedforward of incoming wave mode amplitudes and the feedback of outgoing wave mode amplitudes as shown in Fig. 3. In this figure, G is the control compensator. If G is causal and physically realizable then the
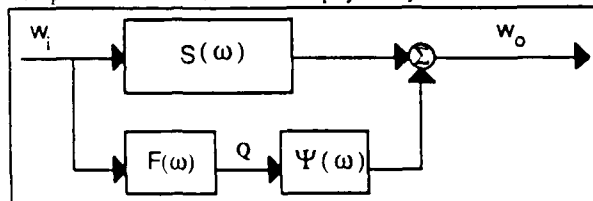
Figure 2 Feedforward of incoming wave modes

actuator commands, Q, are physically realizable because the quantities in u are measurable.

Rearrangement of the block diagram in Fig. 3 yields a structure identical to that in Fig. 2 (see Fig. 4) with a feedback stage in the feedforward path. This illustrates that cross-sectional variables can be used as feedback measurements to mimic the feedforward rejection of incoming wave mode amplitudes.

Figure 3 Feedback of cross-sectional physical measurements

Typically, optimal control is based upon the minimization of some index describing a characteristic of the system being controlled. For this discussion of optimal junction control, a combination of power flow and cont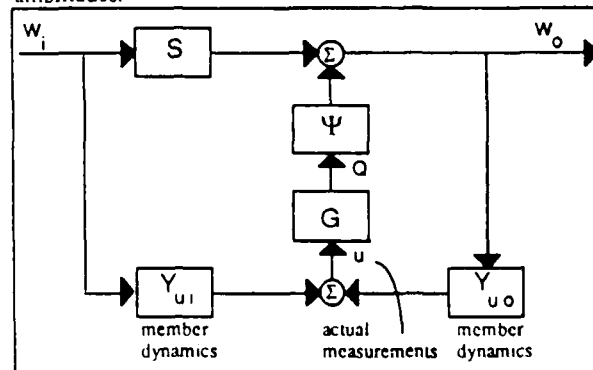rol effort will be the quantity minimized with incoming power defined as negative power flow. If more power arrives at the active junction than departs, the net power flow is negative. Thus, minimization of junction power flow reduces the amount of outgoing power resulting from incoming power. In Section 3, power flow was shown to be a quadratic quantity in terms of the amplitudes of the wave modes incoming to the junction. Since power flow is expressed in terms of its frequency components, a frequency domain formulation is used.
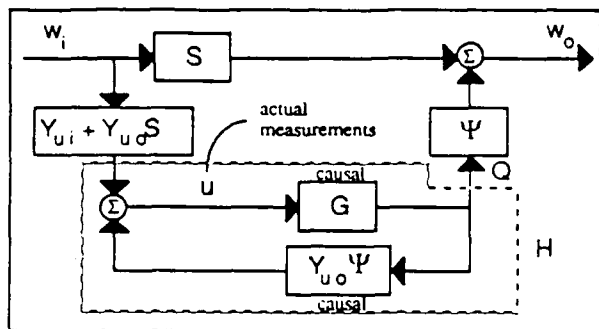

Figure 4 Use of physical measurement feedback to mimic the feedforward of incoming wave mode amplitudes

The control optimization problem becomes the minimization of the expected steady-state power flow plus control effort. Summing over all frequencies yields the total power flow when the structure is undergoing steady-state motion. Adding a quadratic control effort penalty to the power term in Eq. 3 and taking the expected value of the resulting integral relation gives the cost functional as

$$J = \tfrac{1}{2}E\left\{ \int_{-\infty}^{\infty} \left(w^{H} P_j w + Q^{H} R Q \right) d\omega \right\}$$

$$= \tfrac{1}{2}\int_{-\infty}^{\infty} trace \left(E \left(P_j w w^{H} + R Q \Omega^{H} \right) \right) d\omega$$

$$= \tfrac{1}{2}\int_{-\infty}^{\infty} trace \left(P_j(\omega)\Phi_{ww}(\omega) + R(\omega)\Phi_{QQ}(\omega) \right) d\omega \tag{5a}$$

where

$$\Phi_{ww}(\omega) = E(w w^{H}), \quad \Phi_{QQ}(\omega) = E(Q Q^{H}) \tag{5b}$$

The optimal control that minimizes this cost, subject to various constraints, will consist of linear dynamic compensation. The following discussion outlines several procedures for minimizing this specific type of frequency-shaped cost functional.

The next step involves defining the appropriate elements of the feedforward structure shown in Fig. 4. The transfer function from incoming wave modes to cross-sectional coordinates in the absence of junction control is

$$K = Y_{ui} + Y_{uo}S \tag{6}$$

The matrix $Y_{uo}\psi$ in the feedback loop of the feedforward path in Fig. 4 corresponds to the additional junction motions generated by the control inputs.

The portion of the block diagram outlined by the dashed line in Fig. 4 can be condensed into a single transfer function matrix given by

$$H = G(I - Y_{uo}\psi G)^{-1} \tag{7}$$

The transfer function relation from incoming to outgoing wave mode amplitudes is given by

$$w_o = (S + \psi H K)w_i = S_{CL}w_i \tag{8}$$

With these definitions in place, the cost functional given by Eq. 5 can be rewritten in terms of the incoming and outgoing wave mode power spectral densities. Partitioning the vector of junction wave mode amplitudes as

$$w = \begin{bmatrix} w_i \\ w_o \end{bmatrix} \tag{9}$$

gives a cost which can be expressed in terms of the auto- and cross-power spectral density functions for the incoming and outgoing waves:

$$J = \tfrac{1}{2}\int_{-\infty}^{\infty} trace \left(P_j \begin{bmatrix} \Phi_{w_iw_i} & \Phi_{w_iw_o} \\ \Phi_{w_ow_i} & \Phi_{w_ow_o} \end{bmatrix} + RHK\Phi_{w_iw_i}K^{H}H^{H} \right) d\omega \tag{10a}$$

where we have substituted into Eq. 8 the expression

$$\Phi_{QQ} = E(QQ^{H}) = E(HKw_i w_i^{H} K^{H} H^{H}) = HK\Phi_{w_iw_i}K^{H}H^{H} \tag{10b}$$

These power spectral density (PSD) matrices can be expressed in terms of the PSD matrix of the incoming waves by substituting the transfer function relation given in Eq. 8

$$J = \tfrac{1}{2}\int_{-\infty}^{\infty} trace(P_j \begin{bmatrix} \Phi & \Phi(S + \psi H K)^{H} \\ (S + \psi H K)\Phi & (S + \psi H K)\Phi(S + \psi H K)^{H} \end{bmatrix}$$

$$+ RHK\Phi K^{H}H^{H}) d\omega \tag{11}$$

where

$$\Phi = \Phi_{w_iw_i} \tag{12}$$

Optimization involves minimizing the trace of Eq. 11. This is done, using the calculus of variations, by perturbing the feedforward matrix, H, by a frequency dependent perturbation matrix, η, which is scaled by a small parameter, ε

$$H(\omega) \Rightarrow H(\omega) + \varepsilon\eta(\omega) \tag{13}$$

The procedure involves showing that the optimal feedforward compensator matrix, H, when subjected to small "allowable" perturbations, yields a stationary cost. "Allowable" perturbations depend on the constraints imposed upon the optimization problem.

The condition that the optimal compensator matrix must satisfy is found by minimizing the cost with respect to the small parameter ε. The relation governing the optimal compensator matrix, H, is then found by allowing ε to approach zero. The first variation of the cost is

$$\delta J = \tfrac{1}{2}\int_{-\infty}^{\infty} trace (P_j \begin{bmatrix} 0 & \Phi K^{H}\eta^{H}\psi^{H} \\ \psi\eta K\Phi & \psi\eta K\Phi(S + \psi H K)^{H} + (S + \psi H K)\Phi K^{H}\eta^{H}\psi^{H} \end{bmatrix}$$

$$+ R\eta K\Phi K^{H}H^{H} + RHK\Phi K^{H}\eta^{H}) d\omega \tag{14}$$

The expression in Eq. 14 can be simplified by evaluating the trace of the product of the power matrix (P_j) and the matrix quantity shown in brackets. Partitioning the power matrix as shown in Eq. 4 yields an equivalent expression for the first variation of the cost as

$$\delta J = \tfrac{1}{2}\int_{-\infty}^{\infty} trace (P_{oi}\psi\eta K\Phi + P_{io}\Phi K^{H}\eta^{H}\psi^{H}$$

$$+ P_{oo}\psi\eta K\Phi(S + \psi H K)^{H} + P_{oo}(S + \psi H K)\Phi K^{H}\eta^{H}\psi^{H}$$

$$+ R\eta K\Phi K^{H}H^{H} + RHK\Phi K^{H}\eta^{H}) d\omega \tag{15}$$

Using the fact that the trace of the hermitian of a matrix equals the hermitian of the trace of that matrix, Eq. 15 becomes

$$\partial J = \int_{-\infty}^{\infty} \mathrm{Re}(trace(\eta''(\psi''(P_a + P_\infty S)$$
$$+ (\psi^H P_\infty \psi + R)HK)\Phi K''))d\omega \qquad (16)$$

where the real part of the trace is retained.

At this point, the optimization problem can proceed in several directions based upon the perturbations allowed.

<u>5.1 Noncausal Solution</u> For the feedforward gain matrix H to be optimal, it must make the cost stationary for allowable perturbations given by η^H. At present, the optimal noncausal solution is being sought and no constraint is being placed upon H. Therefore, the optimal gain matrix H must make Eq. 16 satisfy

$$\partial J = 0 \qquad (17)$$

for any arbitrary perturbation given by η^H. This indicates that η, and therefore the feedforward compensator H, may contain both right and left half complex plane dynamics. Right half plane dynamics signify that the control must anticipate future information. Of course, such compensators cannot be implemented. ʰ   ;y provide a baseline against which causal compensators ....y oe compared.

Equation 17 is satisfied if

$$HK = -(\psi^H P_\infty \psi + R)^{-1}\psi''[P_a + P_\infty S] = F \qquad (18)$$

This causes Eq. 16 to equal the trace of a zero matrix for arbitrary η^H.

Equation 18 gives the compensator (F in Fig. 2) that relates the amplitudes of the control actuation as a linear function of the incoming wave mode amplitudes at the junction interface. The gain matrix G which feeds cross-sectional junction motions to control inputs, and represents the compensator that is actually implemented in practice, can be found by solving Eq. 18 for H and substituting H into

$$G = (I + HY_\infty \psi)^{-1}H \qquad (19)$$

The frequency dependent compensator G is a function of the junction and attached member dynamics.

The second variation of Eq. 11 with respect to the parameter ε, after allowing ε to approach zero, is given by

$$\psi^H P_\infty \psi + R \qquad (20)$$

P_{oo} is hermitian and positive semidefinite, since outgoing waves propagate energy away from this junction and the resulting power flow has been defined in a positive sense. If R is chosen to make Eq. 20 positive definite, then the control in Eq. 18 satisfies not only the first order but also the second *order necessary conditions.*

Several characteristics are readily visible from the solution in Eq. 18. First, if the term $\psi^H P_{oo}\psi$ is of full rank (invertible) then it is possible to formulate control without a penalty on control effort. Such situations exist when no mechanisms exist to draw power towards the active junction. In other words, the controller must wait for the power to arrive at the junction in order to dissipate it. Since the amount of effort expended is on the order of the incoming power and the arriving power is assumed finite, the control effort is finite even though R=0. Cheap control (R=0) can also occur when only a subset of cross-sectional coordinates are actuated. This results in a reduced ψ matrix in Eq. 18 which might yield an invertible term when R=0.

Situations can arise where the control action can be used to draw power towards the junction rather than waiting for its arrival. As will be shown in Section 5, near and far field evanescent modes interact to propagate power. If

evanescent behavior exists, the controller can create a near field, outgoing evanescent wave with the proper phase so as to draw more power towards the junction. By enlarging the amplitude of the near field, more power can be attracted. Thus, cheap control is not an option in this case, since a zero control effort penalty matrix would result in the controller driving the near field mode to infinite amplitude in order to attract maximum power.

Since there is no constraint on the control compensator, this procedure minimizes power flow at every frequency and provides no guarantee that the compensator will be causal or implementable. Therefore, the next section discusses a technique for finding causal solutions.

<u>5.2 Causal Solution Using Weiner-Hopf Techniques</u> Much of the following discussion on Weiner-Hopf techniques was extracted from Brown [13]. The cost defined in Eq. 5 equals the integral, over all frequency, of the trace of the expected power flow plus control effort. In the following procedure, analytic continuation is employed to enable the various frequency dependent relationships to be valid throughout the complex Laplace plane. In this new domain, the integral in Eq. 5 is evaluated along the infinite extent of the imaginary axis.

The fundamental difference between the free-form causal solution and the free-form noncausal solution presented in Section 5.1 is the definition of "allowable" perturbations. In the noncausal solution, the perturbing matrix, η, was permitted to be arbitrary. In the problem at hand, the optimal feedforward compensator matrix, H, is constrained to be causal and stable. Therefore, it must be analytic in the right half of the complex Laplace plane: it must be right half plane analytic (RHPA). Therefore, the matrix η which perturbs H from its optimal form must itself be causal. In other words, in the search for the optimal, causal compensator, only causal perturbations are permitted. Since η is RHPA, η^H is LHPA. Along the $i\omega$ axis,

$$\eta''(i\omega) = \eta^T(-i\omega) \qquad (21a)$$

Therefore we define

$$\eta''(s) = \eta^T(-s) \qquad (21b)$$

Note that this definition does not equal the Hermitian when s is not on the $i\omega$ axis.

The optimal compensator, H, is that compensator which, for arbitrary LHPA perturbations in η^H, causes

$$\left(\psi''(P_a + P_\infty S) + (\psi^H P_\infty \psi + R)HK\right)\Phi K'' \qquad (22)$$

to be LHPA. If terms which are not analytic in the left half plane do exist in this expression, then the integral in Eq. 16, when the contour is closed about the left half plane, will be nonzero for some RHPA η, and the stationary cost constraint (Eq. 17) will not be satisfied. Therefore, the expression in Eq. 22 must be equal to some LHPA function, so that

$$\psi^H(P_a + P_\infty S)\Phi K^H$$
$$+ (\psi'' P_\infty \psi + R)H_{RHPA}K\Phi K'' = A_{LHPA} \qquad (23)$$

Notice that H_{RHPA} replaces H in the second term. The compensator G being causal is a requirement for real time implementation. From Eq. 7, if G is causal (RHPA) then H is causal. Therefore, the causality constraint is reflected in H being RHPA.

The Wiener-Hopf technique proceeds as follows. First, it is observed that Eq. 23 has the form

$$H_N + H_D H_{RHPA}H_C = A_{LHPA} \qquad (24)$$

Second, the quadratic terms on either side of H_{RHPA} can be spectrally factored into their RHPA and LHPA parts which are

hermitians of each other. Performing this factorization yields

$$H_N + H_{D\ LHPA}H_{D\ RHPA}H_{RHPA}H_{C\ RHPA}H_{C\ LHPA} = A_{LHPA} \quad (25)$$

In the third step, Eq. 25 is pre- and post-multiplied by the inverses of $H_{D\ LHPA}$ and $H_{C\ LHPA}$, respectively, so that

$$H_{D\ LHPA}^{-1}H_N H_{C\ LHPA}^{-1} + H_{D\ RHPA}H_{RHPA}H_{C\ RHPA}$$

$$= H_{D\ LHPA}^{-1}A_{LHPA}H_{C\ LHPA}^{-1} \quad (26)$$

Note that the center term is RHPA whereas the term on the right is LHPA. Therefore, the term on the left must be the sum of LHPA and RHPA parts:

$$H_{D\ LHPA}^{-1}H_N H_{C\ LHPA}^{-1} = NTF\left(H_{D\ LHPA}^{-1}H_N H_{C\ LHPA}^{-1}\right)$$

$$+ PTF\left(H_{D\ LHPA}^{-1}H_N H_{C\ LHPA}^{-1}\right) \quad (27)$$

The LHPA and RHPA terms are transforms of negative (NTF) and positive (PTF) time functions, respectively. The positive time part of a function (H(s)) is given by

$$PTF\ (H\ (s\ )) = \frac{1}{2\pi}\int_0^{\infty}\ \int_{-\infty}^{i\infty} H\ (\xi)e^{\xi}\,d\xi\ e^{-st}\,dt \quad (28)$$

It can be seen in Eq. 26, when the first term is factored as shown in Eq. 27, that two decoupled relations exist: one governing the RHPA functions and one governing the LHPA functions. H_{RHPA} only appears in the RHPA relation. Solving this relation for H_{RHPA} gives

$$H_{RHPA} = -H_{D\ RHPA}^{-1}\left(PTF\left(H_{D\ LHPA}^{-1}H_N H_{C\ LHPA}^{-1}\right)\right)H_{C\ RHPA}^{-1} \quad (29)$$

As desired, H_{RHPA} only contains RHPA functions.

The final step involves evaluating G using H_{RHPA} in Eq. 29 in place of H in Eq. 19.

Several issues should be kept in mind when using these techniques. First, notice that while the noncausal solution was independent of the incoming wave mode statistics Φ, the causal solution is not. Second, it was stated that the term in Eq. 22 must be LHPA to ensure that a contour of integration encircling the left half plane does not enclose any singularities. In addition, the frequency dependence of this term must decay faster than $1/\omega$ in order that the integral along the enclosing contour of infinite radius is zero. Often this may require frequency shaping of Φ. From a physical perspective, one would expect the amplitudes of the incoming waves to have an inverse dependence on frequency to support the fact that the total junction power flow is finite. Third, junction matrices often contain irrational transfer functions. Fourth, the junction model, and therefore the control formulation, contains no information about the rest of the structure. In an attempt to minimize power flow in a certain frequency range, the Wiener-Hopf solution may result in amplification of power in another. The formulation has no knowledge of this problem. However, the finite extent of any structure makes the return of the emanating power an eventuality and an instability can occur. Therefore, an iterative design approach may be required which first solves the Wiener-Hopf problem, then checks junction power flow and repeats the cycle if the first solution proves to be inadequate.

This outlines a Wiener-Hopf approach to the junction wave control problem. Given that future information is not available to the controller, a reduction in performance over the noncausal case might be expected.

5. EXAMPLE

This section presents examples which illustrate the derivation of various junction controllers. The noncausal (part 1), causal fixed-form (part 2), Weiner-Hopf (part 3) and Weiner-Hopf positive real approximation (part 4) solutions are

applied to the left, free end of a dispersive, undamped, Bernoulli-Euler beam (Fig. 5). The governing P.D.E. is

$$EI\ \frac{\partial^4 v}{\partial x^4} + \rho A\ \frac{\partial^2 v}{\partial t^2} = 0 \quad (30)$$

where E, I, ρ and A are the modulus of elasticity, area moment of inertia, volume density of mass and cross-sectional area, respectively, and $v(x,t)$ is the transverse displacement coordinate. From Fig. 5, x=0 at the boundary.

From the dispersion relation, the wave number k will be expressed in terms of the complex Laplace variable, s, as

$$k = \sqrt[4]{\rho A / EI}\ \sqrt{\omega} = c_0\sqrt{s}\ \sqrt[4]{-s} \quad (31a)$$
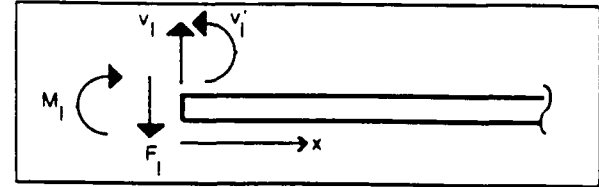
where

$$s = \sigma + i\omega \quad (31b)$$

Figure 5 Free-end of Bernoulli-Euler beam

Notice that the right side of Eq. 31a, k(s), is the analytic continuation, throughout the complex plane, of the function on the left side, k(ω), which is valid on the imaginary axis. Also notice that the substitution of s=iω for positive and negative values of ω yields the principle square root of ω. All roots in Eq. 31a are principle roots. The branch cuts corresponding to the fourth roots in Eq. 31a cut the entire real axis in the complex plane. The portion given by $s^{1/4}$ has its branch cut along the negative real axis and is therefore RHPA and $(-s)^{1/4}$ has its branch cut along the positive real axis and is LHPA.

The motion, as composed of wave modes supported by the partial differential equation in Eq. 30, is given by

$$v\ (x,t\ ) = w_{lp}e^{\pm ikx\ \mp\omega t} + w_{rp}e^{\pm(-ikx)\mp\omega t}$$

$$+ w_{re}e^{-kx\ \mp\omega t} + w_{le}e^{kx\ \mp\omega t} \quad (32)$$

The +/- symbol preserves propagation direction when ω is positive or negative. For brevity, this notation will be abbreviated to include only the upper sign. Except where indicated in the following discussion, +/-i can be substituted for i. Using Eq. 32, the junction transformation (Eq. 1) is

$$\begin{Bmatrix} v \\ v' \\ -EIv'' \\ EIv''' \end{Bmatrix} = \begin{bmatrix} 1 & 1 & 1 & 1 \\ ik & k & -ik & -k \\ iEIk^3 & -EIk^3 & -iEIk^3 & EIk^3 \\ -EIk^2 & EIk^2 & -EIk^2 & EIk^2 \end{bmatrix}\begin{Bmatrix} w_{lp} \\ w_{le} \\ w_{rp} \\ w_{re} \end{Bmatrix} \quad (33)$$

where

w_{lp}	leftward propagating wave modes incoming waves
w_{le}	leftward emanating evanescent wave modes incoming waves
w_{rp}	rightward propagating wave modes outgoing waves
w_{re}	rightward emanating evanescent wave modes outgoing waves

and (') denotes spatial derivative. The scattering matrix [1] for a free boundary condition is

$$S = \begin{bmatrix} -i & 1+i \\ 1-i & i \end{bmatrix} \quad (34)$$

The wave generation matrix is

$$\psi = \frac{1+i}{2EIk^3}\begin{bmatrix} 1 & -k \\ 1 & -ik \end{bmatrix} \quad , \quad \psi_M = -\frac{1+i}{2EIk^2}\begin{Bmatrix} 1 \\ i \end{Bmatrix} \quad (35)$$

where ψ_M is the wave generation matrix with only moment actuation (no force). The K matrix, given by Eq. 6, is

$$K = 2\begin{bmatrix} 1-i & 1+i \\ -(1-i)k & (1-i)k \end{bmatrix} \quad (36)$$

and the junction power matrix is

$$P_j = 4\omega k^3 EI\begin{bmatrix} -1 & 0 & 0 & 0 \\ 0 & 0 & 0 & i \\ 0 & 0 & 1 & 0 \\ 0 & -i & 0 & 0 \end{bmatrix} \quad (37)$$

The term ω arises from the velocity term in the expression for power and is therefore strictly a positive time function (no +/-). Notice that the incoming and outgoing propagating waves propagate power independently and in the negative and positive sense, respectively (entries (1,1) and (3,3) of P_j). The evanescent waves do not propagate power independently (entries (2,2) and (4,4) of P_j) but do propagate power through their interaction (entries (2,4) and (4,2) of P_j).

Part 1. Optimal noncausal control can be derived for the free end of a Bernoulli-Euler beam. If only moment actuation is used, cheap control can be derived (R = 0). The wave mode amplitude feedforward gain matrix (F) found using ψ_M from Eq. 35 in Eq. 18 is

$$F = EIk^2(1 + i)[-1 \quad 1] \quad (38)$$

The equivalent feedback matrix in terms of cross-sectional measurements (Eq. 19) is

$$G = -\tfrac{1}{2}EIk(1 - i)[0 \quad 1] = -\frac{1}{\sqrt{2}}c_0EI\sqrt{-s}[0 \quad 1] \quad (39)$$

This only calls for rotation feedback and does so through a frequency dependent compensator which is similar to a *half differentiator* [2] but with a 90 degree phase shift. The half differentiator exhibits a log/log magnitude slope of 1/2 and a phase shift of 45 degrees: half that of a full differentiator.

The compensator in Eq. 38 results in a closed-loop scattering matrix of

$$S_{CL} = \begin{bmatrix} 0 & 1 \\ -i & 1+i \end{bmatrix} \quad (40)$$

As might be expected, this compensator sets the reflection coefficient from incoming to outgoing propagating wave to zero. The resulting closed-loop junction power matrix is

$$P_{AVG} = 4\omega k^3 EI \; w_i^H \begin{bmatrix} -1 & 1 \\ 1 & -1 \end{bmatrix} w_i = w_i^H P_{CL} w_i \quad (41)$$

This closed-loop power matrix has eigenvalues equal to 0 and $-8\omega k^3 EI$. Therefore, the matrix is negative semidefinite and incoming power is never amplified at the junction. The compensator is optimized frequency by frequency and is therefore independent of the incoming wave mode spectra given by Φ in Eq. 16.

The primary drawback to this solution is that the compensator is noncausal. While a half differentiator can be approximated with relative accuracy over a broad frequency range [16], a ninety degree phase shifter cannot, given the collocated feedback restriction. Therefore, a causal solution is required.

Part 2. This second part illustrates the use of a causal fixed-form parameter optimization technique. The form of the noncausal compensator in Eq. 39 will be used with the exception that the phase is now 45 degrees. A causal H can be found, since Eq. 7 preserves causality, giving the fixed-form with variable gain α as

$$H = \alpha EIk(1 + i)[0 \quad 1] \quad (42)$$

Notice that the compensator G in Eq. 39 with 45 degrees of phase not only provides positive real feedback between rotational velocity and moment, it also causes the closed-loop junction power matrix eigenvalues, as illustrated by Eq. 41, to have the same frequency dependence as those of the open-loop power matrix. This results because the fixed-form compensator was chosen to have the same frequency dependence as the noncausal compensator, which was optimized frequency by frequency, and therefore the impedance of a semi-infinite beam.

Now that a formulation is being used that does not allow optimization frequency by frequency, an appropriate form for the incoming wave mode spectral density Φ must be chosen. It will also be assumed that the propagating and far field evanescent waves exist in equal proportions and that the incoming wave mode amplitudes diminish with frequency above ω_n. As will be seen, the form

$$\Phi = \frac{a^2}{(s-\omega_n)^2}\begin{bmatrix} 1 & 0 \\ 0 & 1 \end{bmatrix}\frac{a^2}{(s+\omega_n)^2} \quad (43)$$

exhibits satisfactory behavior when using contour integration.

Using the compensator form in Eq. 42, Φ from Eq. 43 and the junction matrices gives the trace in Eq. 11 as

$$trace = \frac{(-8\alpha + 16\alpha^2)a^4}{(s^2 - \omega_n^2)^2}$$

$$\frac{\partial trace}{\partial \alpha} = \frac{(-8 + 32\alpha)a^4}{(s^2 - \omega_n^2)^2} = 0 \qquad \alpha = \frac{1}{4} \quad (44)$$

Substituting this minimizing value for α into Eq. 42 and substituting this compensator into Eq. 19 gives

$$G = \frac{EIk}{2}(1 + i)[0 \quad 1] = -\frac{1}{\sqrt{2}}c_0EI\sqrt{s}[0 \quad 1] \quad (45)$$

which has the same gain as the noncausal compensator in Eq. 39. Notice that the optimal value for α is independent of ω_n and therefore independent of the evaluation of the integral in Eq. 11.

The closed-loop scattering matrix for this system is

$$S_{CL} = \frac{1}{2}\begin{bmatrix} 1-i & 1+i \\ 1-i & 1+i \end{bmatrix} \quad (46)$$

and the closed-loop junction power matrix is

$$P_{CL} = \omega k^3 EI\begin{bmatrix} -1 & 1 \\ 1 & -1 \end{bmatrix} \quad (47)$$

Notice that the causal solution does not zero the (1,1) entry of the closed-loop scattering matrix. In addition, while the closed-loop junction power matrix is still negative semidefinite, the eigenvalues are now 0 and $-2\omega k^3 EI$ indicating that, for identical incoming wave mode sets (the eigenvectors are unchanged), the causal control absorbs half as much power as the noncausal control in part one.

Part 3. This third part illustrates the Wiener-Hopf solution to the optimal junction control of the free end of the B-E beam in Fig. 5. Extreme care must be exercised in the solution procedure to ensure that the LHPA and RHPA functions are properly handled.

Each of the terms in Eq. 24 can be evaluated, remembering that A_{LHPA} and H_{RHPA} are as yet unknown. The other three terms are given by

$$H_N = \frac{8 c_0 a^4 s \sqrt[4]{s} \sqrt[4]{-s}}{\left(s^2 - \omega_n^2\right)^2} \left[1 + i \quad - 2 c_0 \sqrt[4]{s} \sqrt[4]{-s}\right] \tag{48}$$

$$H_D = \frac{2 \sqrt[4]{s} \sqrt[4]{-s}}{c_0 EI} \tag{49}$$

$$H_C = \frac{8 a^4}{\left(s^2 - \omega_n^2\right)^2} \begin{bmatrix} 2 & -\sqrt{2} c_0 \sqrt{-s} \\ -\sqrt{2} c_0 \sqrt{s} & 2 c_0^2 \sqrt{s} \sqrt{-s} \end{bmatrix} \tag{50}$$

Eqs. 49 and 50 can be spectrally factored into their LHPA and RHPA terms (Eq. 25) as

$$H_{D\ LHPA} H_{D\ RHPA} = \frac{\sqrt{2} \sqrt[4]{-s}}{\sqrt{c_0 EI}} \frac{\sqrt{2} \sqrt[4]{s}}{\sqrt{c_0 EI}} \tag{51}$$

$$H_{C\ RHPA} H_{C\ LHPA} = \frac{2 \sqrt{2} a^2}{\left(s + \omega_n\right)^2} \begin{bmatrix} -1 & 1 \\ \sqrt{2} c_0 \sqrt{s} & 0 \end{bmatrix} \cdot$$

$$\begin{bmatrix} -1 & \sqrt{2} c_0 \sqrt{-s} \\ 1 & 0 \end{bmatrix} \frac{2 \sqrt{2} a^2}{\left(s - \omega_n\right)^2} \tag{52}$$

The first term in Eq. 26 is given by

$$H_{D\ LHPA}^{-1} H_N H_{C\ LHPA}^{-1} =$$

$$\frac{2 \sqrt{2} c_0 a^2 \sqrt{c_0 EI}}{\left(s + \omega_n\right)^2} \left(-\sqrt{2} \sqrt[4]{s} + \sqrt[4]{-s}\right) s \begin{bmatrix} 1 & 0 \end{bmatrix} \tag{53}$$

Notice that the first term in this expression is RHPA and the second term contains both RHPA and LHPA parts. Using Eq. 28 with Eq. 53 substituted for H(ξ), the positive time part of the expression in Eq. 53 is given by

$$PTF\left(H_{D\ LHPA}^{-1} H_N H_{C\ LHPA}^{-1}\right) = -\frac{2 \sqrt{2} c_0 a^2 \sqrt{c_0 EI}}{\left(s + \omega_n\right)^2}$$

$$\cdot \left(\sqrt{2} s \sqrt[4]{s} - \tfrac{1}{4}(\omega_n + 5s) \sqrt[4]{\omega_n}\right) \begin{bmatrix} 1 & 0 \end{bmatrix} \tag{54}$$

Evaluating Eq. 29 gives H_{RHPA} as

$$H_{RHPA} = \tfrac{1}{2} c_0 EI \left(\sqrt{2} \sqrt[4]{s} - \tfrac{1}{4} \frac{(\omega_n + 5s) \sqrt[4]{\omega_n}}{s^{3/4}}\right) \begin{bmatrix} 0 & 1 \end{bmatrix} \tag{55}$$

The expression for G is found using Eq. 19 to be

$$G = c_0 EI \left(\frac{4 s s^{3/4}}{\sqrt[4]{\omega_n}(5s + \omega_n)} - \frac{\sqrt{s}}{\sqrt{2}}\right) \begin{bmatrix} 0 & 1 \end{bmatrix} \tag{56}$$

Notice that if the compensator in Eq. 56 were altered to represent the feedback of rotational velocity to external moment (G/s), the new compensator would not be positive real at all frequencies. At low frequencies, where the right hand part of the term in parentheses dominates, the compensator would be negative real and lead to the generation

of power at the active junction. If modes of the structure reside in the frequency range where power is generated, instability could occur.

Part 4. The compensator in Eq. 56 can be approximated with the new G/s being positive real for all s=iω. For brevity in the following discussion, a compensator between rotation and moment with phase between 0 and 180 degrees will be referred to as positive real. Figure 6 compares
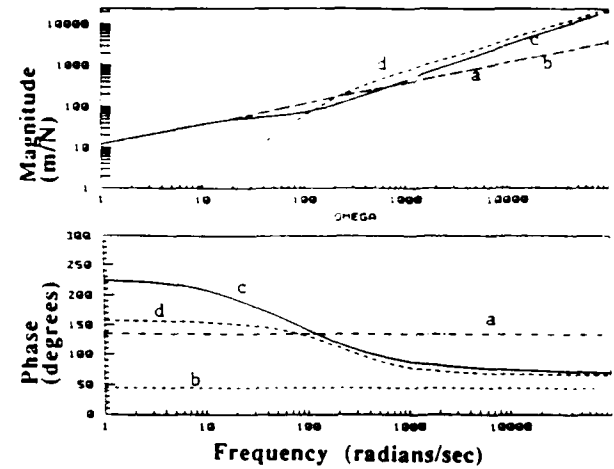

Figure 6 Feedback compensators for noncausal (a), causal fixed-form (b), Weiner-Hopf (c) and approximate (d) formulations.

the transfer functions of the noncausal (dashes and dots (a)), causal fixed-form (widely spaced dashes (b)), Weiner-Hopf (solid (c)) and positive real approximation solutions (closely spaced dashes (d)). Notice that both the noncausal (a) and causal fixed-form (b) solutions have the same $\omega^{1/2}$ magnitude dependence but have phases which differ by 90 degrees; which accounts for their noncausal and causal natures, respectively. For the Weiner-Hopf and Weiner-Hopf approximation solutions, the corner frequency of Φ was chosen as ω_n=100 rad/sec. Near this frequency, the Weiner-Hopf solution (c) has half the magnitude and the same phase as the noncausal solution. This indicates that the Weiner-Hopf solution is better than the causal fixed-form solution at mimicking the noncausal solution near the frequencies of importance (around ω=100 rad/sec). It does not match the noncausal solution in magnitude, however, because incoming waves at frequencies near ω=100 rad/sec also deliver significant incoming power to the active junction. It seems reasonable to suspect that as the Φ matrix becomes more banded around ω_n=100 rad/sec, the magnitude of the Weiner-Hopf solution will approach that of the noncausal solution.

As shown by curves (c) and (d) in Fig. 6, a plausible approximation could have the high frequency behavior of Eq. 56 since the Weiner-Hopf solution is positive real in this regime. However, the approximation should provide phase and gain comparable to the Weiner-Hopf, and therefore the noncausal solution, near ω=100 rad/sec while maintaining a positive real form (i.e., maintain phase between 0 and 180 degrees). The approximation used in this paper, whose transfer function is given by curve (d) in Fig. 6, is

$$G = 4 c_0 EI \frac{s^{3/4}}{5 \sqrt[4]{\omega_n}} \frac{s}{s + 200} \begin{bmatrix} 0 & 1 \end{bmatrix} \tag{57}$$

At low frequencies, the gain has a frequency dependence of $\omega^{7/4}$ which has a phase of 157.5 degrees at low frequencies (less than 180 degrees). The phase equals that of the noncausal compensator (135 degrees) near ω=100 rad/sec.

The junction power flow can be plotted as a function of frequency for each of the compensators (Fig. 7). From Eq. 11, the trace of the integrand gives the power flow as a function of frequency for the chosen incoming wave mode spectrum (Φ). The plotting of *Power*, scaled by frequency (*Power* ω), versus the logarithm of frequency ($d(\log \omega)$) gives the controller cost as the area contained within the curves in Fig. 7. Notice that the noncausal solution (a) has, by definition, minimum cost. The causal fixed-form solution (b) has the worst performance and highest cost due to the low performance near $\omega=100$ rad/sec. As expected, the Weiner-Hopf solution (c) and the noncausal solution have similar cost associated near $\omega=100$ rad/sec. As desired, the Weiner-Hopf approximation (d) has only slightly higher cost. The Weiner-Hopf solution has positive cost below 30 rad/sec, in Fig. 7,
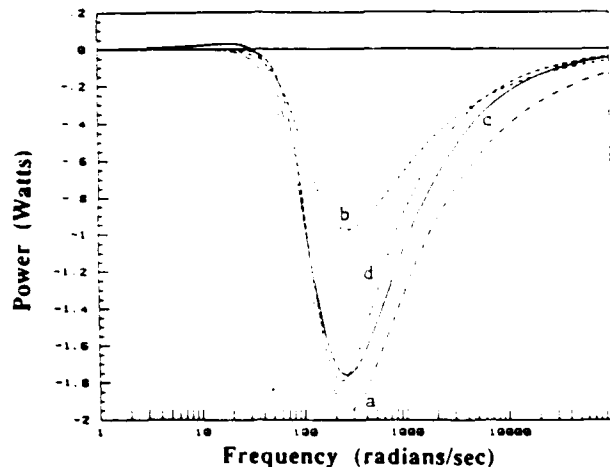

Figure 7 Closed-loop power flow for noncausal (a), causal fixed-form (b), Weiner-Hopf (c) and approximate (d) formulations.

due to its negative real nature at these frequencies. The Weiner-Hopf formulation tolerates positive cost in this region in order to achieve lower total cost. Despite this positive cost, the cost associated with the Weiner-Hopf solution, given by the integral over frequency, is the lowest for all causal compensators.

Using the phase closure principle described by Miller and von Flotow [15], a transfer function was derived between force and transverse displacement at the far end of the beam with that end modelled as a free boundary. The beam properties were EI = 31.1 Nm^2, ρA = 2.85 Kg/m and length = 7.32m. Figure 8 compares the open-loop magnitude and phase characteristics (a) with that obtained using the causal fixed-form compensator (b) and the noncausal compensator (c). The noncausal compensator reflects no incoming propagating waves as outgoing propagating waves. This feature essentially eliminates resonant behavior and the beam behaves as a semi-infinite beam.

Figure 9 compares the open-loop transfer function (a) with that obtained using the Weiner-Hopf approximation (b) and the noncausal compensator (c). Notice that the approximation causes significant increases in damping near ω = 100 rad/sec, as would be achieved using the Weiner-Hopf solution, while maintaining stability in the low frequency modes below 30 rad/sec, which would be destabilized by the Weiner-Hopf compensator.
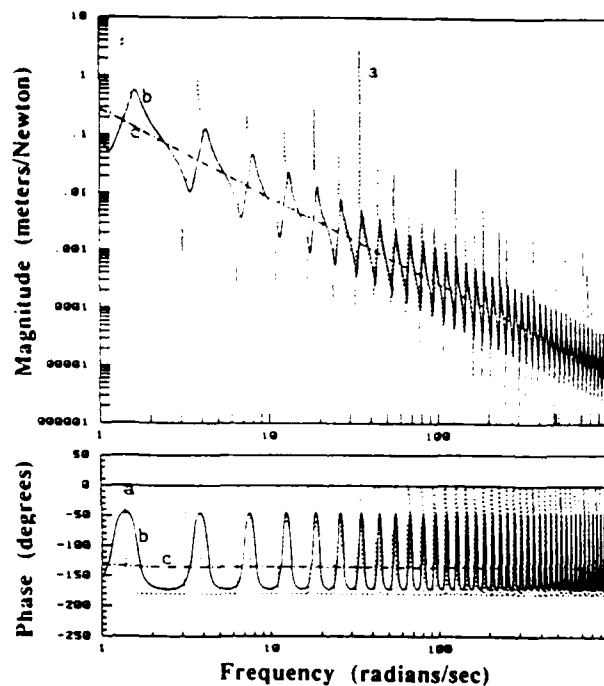

Figure 8 Transfer function for open-loop (a), causal fixed-form (b) and noncausal (c) compensators.
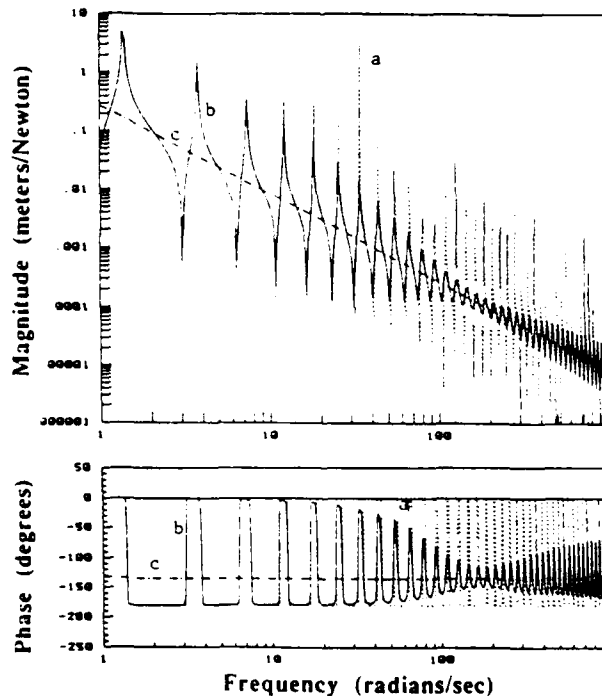

Figure 9 Transfer function for open-loop (a), Weiner-Hopf positive real approximation (b) and noncausal compensator (c).

6. SUMMARY

Several fundamental differences between modal and wave model based control have been illustrated. Wave models place attention on the control of all frequency waves which traverse a structure as opposed to singling out those frequencies which correspond to modes. Though this is a an artifact of using local models incapable of capturing global resonant behavior, it provides several unique insights. First, wave models explicitly describe the finite speeds with which energy propagates through a structure and illustrates the fact that once a disturbance is imparted to a structure, it is not too late to isolate performance critical locations. Second, modal models tend to be large and lead to state estimators which dominate the real time processing effort. This is due to the number of mathematical degrees of freedom required to describe each mode. Wave models model the impedance behavior of structural materials and boundary dynamics which tend to be much more benign (smooth) functions of frequency. As a result, fewer controller degrees of freedom are required to implement the control. Third, while it is difficult to exactly model a complex structure with ordinary and partial differential equations and extract optimal LQR or LQC control algorithms, mathematically exact models can often be employed in the derivation of wave control. Fourth, the wave formulation uses all cross-sectional coordinates to perform control enabling dramatic improvements in performance. Finally, the techniques presented here are strictly limited to the achievement of performance objectives which can be posed in terms of local behavior.

Two important performance objectives which can be posed in terms of local behavior are vibration suppression and dynamic isolation. For some structural geometries, wave controllers can not only suppress but eliminate resonant behavior. This is accomplished by absorbing all impinging energy thus preventing waves from circumnavigating the structure and constructively interfering (resonance). This also implies, as recognized by Hagedorn [6], that energy is extracted by the control in finite time: a result which is not typical of the LQR formulation.

Noncausal optimal control, though globally optimal, does not guarantee causality. Therefore, two causal solutions are presented. The manner in which the Weiner-Hopf approach is constrained guarantees a causal solution but does not guarantee that the junction behaves as a power sink at all frequencies.

7. ACKNOWLEDGEMENTS

8. REFERENCES

1. von Flotow, A. H., "Disturbance Propagation in Structural Networks," J. Sound and Vibration, 106, 433-450, 1986.

2. Miller, D. W., von Flotow, A. H., Hall, S. R., "Active Modification of Wave Reflection and Transmission in Flexible Structures," Proceedings American Control Conference, Minneapolis, 2, 1318-1324, June 1987.

3. Redman-White, W., "Experiments on the Active Control of Flexural Wave Power Flow," J. Sound and Vibration, 112, 187-191, 1987.

4. Scheuren, J., "Active Control of Bending Waves in Beams," Internoise, Munich, 591-594, Sept. 1985

5. Mace, B.R., "Active Control of Flexural Vibrations," Journal of Sound and Vibration, 114, 253-270, 1987.

6. Hagedorn, P., Schmidt, J. T., "Active Vibration Damping of Flexible Structures Using the Travelling Wave Approach," Proceedings of the Second International Symposium on Spacecraft Flight Dynamics, Darmstadt, FR Germany, Oct. 1986, ESA SP-255, Dec. 1986.

7. Piche, R., "Boundary Control of Undamped Beam Using Square-Root Velocity," Presented at the 1987 ACC, Minneapolis, MN, 1314-1317, June 1987.

8. Pines, D.J., "Active Control of Bending Waves at Acoustic Frequencies," 1988 SM Thesis, M. I. T., Cambridge, Ma.

9. von Flotow, A. H., "Traveling Wave Control for Large Spacecraft Structures," J. Guidance, Control, and Dynamics, 9, 462, July- Aug 1986.

10. von Flotow, A. H., Schafer, B., "Wave-Absorbing Controllers for a Flexible Beam," J. Guidance, Control, and Dynamics, 9, 673, Nov-Dec 1986.

11 Signorelli, J., von Flotow, A.H., "Wave Propagation, Power Flow, and Resonance in a Truss Beam," J. Sound and Vibration, 126, 127-144, Nov. 1988.

12. Gupta, N.K., "Frequency-Shaped Cost Functionals: Extension of Linear-Quadratic-Gaussian Design Methods," J. Guidance and Control, 3, 529-535, Nov.-Dec. 1980.

13. Brown, R.G., Introduction to Random Signal Analysis and Kalman Filtering, John Wiley & Sons, New York, N.Y., 1983.

14. Miller, D. W., "Modelling and Active Modification of Wave Scattering in Structural Networks," 1988 ScD Thesis (Space Systems Laboratory Report #12-88), M.I.T., Cambridge, MA.

15. Miller, D. W., "Power Flow in Structural Networks," Journal of Sound and Vibration, 128, 145-162, 1989.

16. Carlson, G. E., Halijak, C. A., "Approximation of Fractional Capacitors $(1/s)^{1/n}$ by a Regular Newton Process," IEEE Transactions on Circuit Theory, 210-213, June 1964.

EXPERIMENTAL RESULTS USING TRAVELLING WAVE POWER FLOW TECHNIQUES

David W. Miller[1], Steven R. Hall[2]

Space Engineering Research Center
Massachusetts Institute of Technology
Cambridge, Massachusetts

ABSTRACT

This paper describes a series of active structural control experiments on a twenty-four foot pinned-free beam. The feedback compensators are derived using a travelling wave approach. A compensator is derived which absorbs all impinging power and therefore eliminates resonant behavior. Since this compensator is noncausal, a causal solution is derived and experimentally implemented which mimics the noncausal compensator in a select frequency range. Experimental damping results obtained using this compensator far exceed that obtainable using rate feedback.

INTRODUCTION

A wave model can be used to describe local reflection and transmission (scattering) properties at a structural cross-section (junction). This model is not a complete model of the structure and therefore does not capture resonant behavior. The model is equivalent to the dereverberated impedance of the structure. "Dereverberated" refers to the impedance that would be revealed if the energy departing the junction never returned.

Minimization of junction power flow corresponds to matching this impedance as closely as possible given the available control degrees of freedom. Achievable performance increases as more distinct actuators and sensors are used. If the impedance is matched, modes which depend entirely on energy traversing the controlled junction will cease to exist.

This paper derives the compensator which maximizes energy absorption when using a moment actuator at a pinned beam end. This compensator is noncausal and therefore not implementable. The analysis and experimental implementation of several causal compensators is presented and compared to the performance obtained through rate feedback.

The following discussion uses experimental results to verify wave control performance. Implementation issues which limit performance are identified. Wave dynamics, power flow and the control formulation are covered in more detail by Miller et al [1].

TRAVELLING WAVE DYNAMICS

This section reviews the wave dynamic equations for a structural junction of arbitrary complexity (Fig. 1). The frequency domain derivation of component (member and junction) dynamics was presented by von Flotow [2]. Von Flotow [3] uses an assemblage of member transformation matrices to derive a junction transformation

matrix which relates complex wave mode amplitudes on all members attached to that junction to the member's cross-sectional quantities. This relation has the form

$$y(\omega) = \begin{bmatrix} u \\ f \end{bmatrix} = \begin{bmatrix} Y_u & Y_{uo} \\ Y_{fi} & Y_{fo} \end{bmatrix} \begin{bmatrix} w_i \\ w_o \end{bmatrix} = Y(\omega)w(\omega) \tag{1}$$

where $w(\omega)$ is the vector of wave mode amplitudes. This vector is partitioned into incoming, w_i, and outgoing, w_o, waves. The vector y contains all member motions, u, and stresses, f, at the junction.
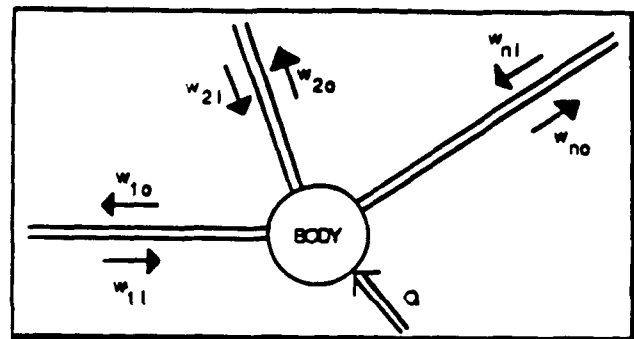

Figure 1   Generic wave junction.

Junction boundary conditions can be transformed into wave mode coordinates and arranged in a causal, input/output form. Outgoing waves, w_o, result from the homogeneous scattering of incoming waves, w_i, and the nonhomogeneous generation by external excitations, Q;

$$w_o(\omega) = S(\omega)w_i(\omega) + \psi(\omega)Q(\omega) \tag{2}$$

This description contains only local junction dynamics and does not contain information about other portions of the structure.

JUNCTION POWER FLOW

Travelling waves transport energy through a structure. This results in a flow of power. Power at an arbitrary member cross-section is equal to the product of the deflection velocities and collocated stresses of like type (e.g., rotational rate and moment). The steady-state power flow at a member cross-section can be expressed in terms of the spectral components of the response variables through the use of the Power Theorem, a variation of Parseval's Theorem.

Miller and von Flotow [4] show that the power flow through a junction has the form

$$P_{AVG}(\omega) = \left[w_i(\omega)^H \quad w_o(\omega)^H\right] P_j(\omega) \begin{bmatrix} w_i(\omega) \\ w_o(\omega) \end{bmatrix} \qquad (3)$$

where

$$P_j = \begin{bmatrix} P_{ii} & P_{io} \\ P_{oi} & P_{oo} \end{bmatrix} \qquad (4)$$

P_j is the junction power flow matrix. P_{AVG} is real for any mix of wave modes since P_j is Hermitian.

JUNCTION CONTROL

The waves incoming to a junction can be thought of as a disturbance to that junction. Conceptually, the disturbance is measured and fed to the actuators in order to reduce the power associated with the resulting outgoing waves (Fig. 2). This architecture assumes that measurements of the incoming wave mode amplitudes are available.
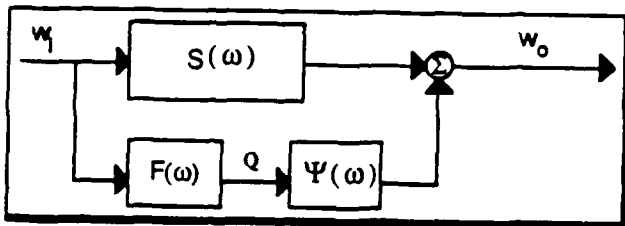

Figure 2 Feedforward of incoming wave modes

It is desirable to use cross-sectional variables as feedback measurements. The vector u contains measurable cross-sectional quantities while f contains those cross-sectional quantities that are commanded by the actuators. Equation 1 can be used to express the amplitudes in u in terms of both incoming and outgoing waves. This results in the feedforward of incoming and the feedback of outgoing wave mode amplitudes (Fig. 3). The control compensator, G, must be causal for real time implementation.

Rearrangement of the block diagram in Fig. 3 yields a structure identical to that in Fig. 2 (see Fig. 4). This illustrates that
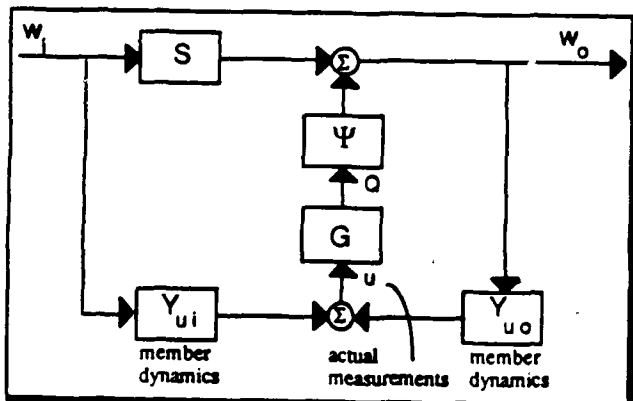

Figure 3 Feedback of cross-sectional measurements

cross-sectional variables can be used as feedback measurements to mimic the feedforward of incoming wave mode amplitudes.

For control purposes, a combination of power flow and control effort will be minimized. Incoming power is defined as negatively flowing. Since power flow is expressed in terms of its frequency components, a frequency domain formulation is used.
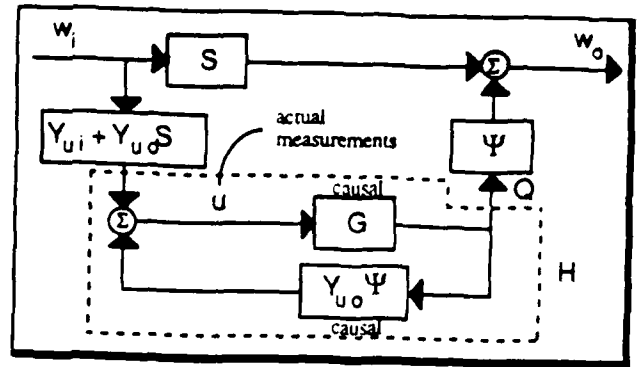

Figure 4 Measurement feedback to mimicking the feedforward of incoming wave amplitudes

Adding a quadratic control effort penalty, R, to the power term in Eq. 3 and taking the expected value of the resulting integral relation gives the cost functional as

$$J = \tfrac{1}{2}E\left\{\int_{-\infty}^{\infty}\left(w^H P_j w + Q^H R Q\right)d\omega\right\}$$

$$= \tfrac{1}{2}\int_{-\infty}^{\infty} trace\left(E\left(P_j w w^H + R Q Q^H\right)\right)d\omega$$

$$= \tfrac{1}{2}\int_{-\infty}^{\infty} trace\left(P_j(\omega)\Phi_{ww}(\omega) + R(\omega)\Phi_{QQ}(\omega)\right)d\omega \qquad (5a)$$

where the assumed power spectral densities of the wave modes and control effort are given by

$$\Phi_{ww}(\omega) = E(w w^H), \quad \Phi_{QQ}(\omega) = E(QQ^H) \qquad (5b)$$

The trace of Eq. 5 can be minimized upon substitution of

$$K = Y_{ui} + Y_{uo}S \qquad (6)$$

$$\Phi_{QQ} = E(QQ^H) = E(HKw_i w_i^H K^H H^H) = HK\Phi_{w_i w_i} K^H H^H \qquad (7)$$

$$\Phi = \Phi_{w_i w_i} \qquad (8)$$

This is done, using the calculus of variations, by perturbing the feedforward matrix, H, by a perturbation matrix, η, scaled by a small parameter, ε

$$H(\omega) \Rightarrow H(\omega) + \varepsilon\eta(\omega) \qquad (9)$$

The condition that the optimal compensator matrix must satisfy is found by minimizing the cost with respect to the small parameter ε. The relation governing the optimal compensator matrix, H, is then found by allowing ε to approach zero. The first variation of the cost is

$$\partial J = \int_{-\infty}^{\infty} Re(trace(\eta^H(\psi^H(P_{oi} + P_{oo}S)$$

$$+ (\psi^H P_{oo}\psi + R)HK)\Phi K^H))d\omega \qquad (10)$$

where the real part of the trace is retained. At this point, the optimization problem can proceed in several directions based upon the perturbations allowed.

Noncausal Solution

Since the optimal noncausal solution is sought, no constraint is placed upon H. Therefore, the optimal gain matrix H must make Eq. 10 satisfy

$$\partial J = 0 \qquad (11)$$

for any arbitrary perturbation given by η^H. This indicates that η, and therefore the feedforward compensator H, may contain both right and left half complex plane dynamics.

Equation 11 is satisfied if

$$HK = - \left(\psi^H P_{\infty} \psi + R \right)^{-1} \psi^H [P_a + P_{\infty} S] = F \qquad (12)$$

Equation 12 gives the compensator (F in Fig. 2) that feeds the incoming wave mode amplitudes to the control actuators. The gain matrix G in Fig. 4 which feeds cross-sectional junction motions to control inputs, and represents the implemented compensator, can be found by solving Eq. 12 for H and substituting into

$$G = (I + HY_{\infty} \psi)^{-1} H \qquad (13)$$

This procedure minimizes power flow frequency by frequency and provides no guarantee that the compensator will be causal or implementable. Therefore, the next section discusses a technique for finding a causal solution.

Causal, Fixed-Form Parameter Optimization

The first step in the solution procedure is to select a causal compensator form with variable gain

$$H (s) = \alpha \ h(s) \qquad (14)$$

This form is then substituted into Eq. 5 and the trace is minimized with respect to the variable gain, α. The compensator G(s) is found using Eq. 13. The effectiveness of the resulting compensator is entirely dependent upon the insight of the designer in the selection of h(s).

Causal Solution Using Wiener-Hopf Techniques

The following discussion on the Wiener-Hopf (W-H) technique is summarized from Miller et al [1]. The fundamental difference between the free-form causal solution and the free-form noncausal solution is the definition of "allowable" perturbations. In the noncausal solution, the perturbing matrix, η, was permitted to be arbitrary. In the problem at hand, G must be causal. Equation 13 guarantees this if the optimal feedforward compensator matrix, H, is constrained to be causal and stable, analytic in the right half of the complex Laplace plane (i.e., right half plane analytic (RHPA)). Therefore, the matrix η which perturbs H from its optimal form must itself be causal. In other words, in the search for the optimal, causal compensator, only causal perturbations are permitted. Since η is RHPA, η^H is LHPA.

The optimal compensator (H_{RHPA}), for arbitrary LHPA perturbations in η^H, must cause

$$\left(\psi^H (P_d + P_{\infty} S) + (\psi^H P_{\infty} \psi + R) H_{RHPA} K \right) \Phi K^H \qquad (15)$$

to be LHPA. If terms which are not analytic in the left half plane do exist in this expression, then the integral in Eq. 10, when the contour is closed about the left half plane, will be nonzero for some RHPA η, and the stationary cost constraint (Eq. 11) will not be satisfied. Therefore, the expression in Eq. 15 must be equal to some LHPA function, so that

$$\psi^H (P_d + P_{\infty} S) \Phi K^H$$
$$+ (\psi^H P_{\infty} \psi + R) H_{RHPA} K \Phi K^H = A_{LHPA} \qquad (16)$$

The W-H technique proceeds as follows. First, it is observed that Eq. 16 has the form

$$H_N + H_D H_{RHPA} H_C = A_{LHPA} \qquad (17)$$

Solving the RHPA part of this relation for H_{RHPA} gives

$$H_{RHPA} = - H_{D \ RHPA}^{-1} \left(PTF \left(H_{D \ LHPA}^{-1} H_N H_{C \ LHPA}^{-1} \right) \right) H_{C \ RHPA}^{-1} \qquad (18)$$

The final step involves evaluating G using H_{RHPA} from Eq. 18 in place of H in Eq. 13.

This outlines a W-H approach to the junction wave control problem. Given that future information is not available to the controller, a reduction in performance over the noncausal case might be expected.

EXPERIMENT CONTROL FORMULATION

This section derives the various junction controllers used in the experiments. The noncausal (part 1), causal fixed-form (part 2), W-H (part 3), W-H positive real approximation (part 4) and rate feedback (part 5) solutions are applied to the left, pinned end of a dispersive, undamped, uniform, Bernoulli-Euler beam (Fig. 5). The governing P.D.E. is

$$EI \ \frac{\partial^4 v}{\partial x^4} + \rho A \ \frac{\partial^2 v}{\partial t^2} = 0 \qquad (19)$$

where E, I, ρ and A are the modulus of elasticity, area moment of inertia, volume density of mass and cross-sectional area, respectively, and v(x,t) is the transverse displacement coordinate. In Fig. 5, x=0 at the pinned end.

From the dispersion relation, the wave number k is expressed in terms of the complex Laplace variable, s, as

$$k = \sqrt[4]{\rho A / EI} \ \sqrt{\omega} = c_0 \sqrt{s} \sqrt[4]{-s} \qquad (20)$$

Notice that the right side of Eq. 20, k(s), is the analytic continuation, throughout the complex plane, of the function on the left side, k(ω), which is valid on the imaginary axis.
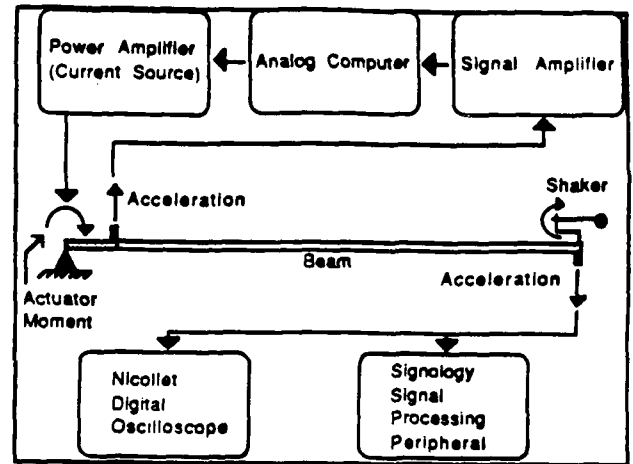

FIGURE 5 Experiment schematic

The motion, as composed of wave modes supported by the partial differential equation in Eq. 19, is given by

$$v (x,t) = w_{lp} e^{\pm ikx \mp \omega t} + w_{rp} e^{\pm(-ikx) \mp \omega t}$$
$$+ w_{re} e^{-kx \mp \omega t} + w_{le} e^{kx \mp \omega t} \qquad (21)$$

The +/- symbol preserves propagation direction when ω is positive or negative. For brevity, this notation will be truncated to include only the upper sign. Using Eq. 21, the junction transformation (Eq. 1) is

$$\begin{Bmatrix} v \\ - EIv''' \\ v \\ EIv'' \end{Bmatrix} = \begin{bmatrix} ik & k & - ik & - k \\ iEIk^3 & - EIk^3 & - iEIk^3 & EIk^3 \\ 1 & 1 & 1 & 1 \\ - EIk^2 & EIk^2 & - EIk^2 & EIk^2 \end{bmatrix} \begin{Bmatrix} w_{lp} \\ w_{le} \\ w_{rp} \\ w_{re} \end{Bmatrix} \qquad (22)$$

where
- w_{lp} leftward propagating, incoming wave
- w_{le} leftward emanating evanescent, incoming wave
- w_{rp} rightward propagating, outgoing wave
- w_{re} rightward emanating evanescent, outgoing wave

The scattering matrix for a pinned boundary condition is

$$S = \begin{bmatrix} - 1 & 0 \\ 0 & - 1 \end{bmatrix} \qquad (23)$$

The wave generation matrix and assumed incoming wave mode spectrum are

$$\psi = \frac{1+i}{2EIk^3}\begin{bmatrix} 1 & -k \\ 1 & -ik \end{bmatrix} \quad , \quad \psi_M = \frac{1}{2EIk^2}\begin{Bmatrix} -1 \\ 1 \end{Bmatrix} \tag{24}$$

$$\Phi = \frac{a^2}{\left(s - \omega_n^2\right)^2}\begin{bmatrix} 1 & 0 \\ 0 & 1 \end{bmatrix}\frac{a^2}{\left(s + \omega_n^2\right)^2} \tag{25}$$

where ψ_M is the wave generation matrix with only moment actuation (no force). The junction power matrix is

$$P_J = 4\omega k^3 EI \begin{bmatrix} -1 & 0 & 0 & 0 \\ 0 & 0 & 0 & i \\ 0 & 0 & 1 & 0 \\ 0 & -i & 0 & 0 \end{bmatrix} \tag{26}$$

Part 1.

If only moment actuation is used, cheap control can be derived ($R = 0$). The noncausal feedback matrix in terms of cross-sectional measurements (Eq. 12 and 13) is

$$M = \sqrt{2}c_0 EI\sqrt{-s}[1\ 0]\begin{Bmatrix} v' \\ -EIv''' \end{Bmatrix} \tag{27}$$

This calls for rotation feedback and does so through a frequency dependent compensator which is similar to a *half differentiator*, but shifted 90 degrees. The compensator is optimized frequency by frequency and is therefore independent of the incoming wave mode spectrum.

The primary drawback to this solution is that the compensator is noncausal. While a half differentiator can be approximated [5], a ninety degree phase shifter cannot. Therefore, a causal solution is required.

Part 2.

This second part illustrates the use of a causal fixed-form parameter optimization technique. The form of the noncausal compensator in Eq. 27, shifted 90 degrees, will be used. Minimizing the cost with respect to a variable gain yields

$$M = \sqrt{2}c_0 EI\sqrt{s}[1\ 0]\begin{Bmatrix} v' \\ -EIv''' \end{Bmatrix} \tag{28}$$

Notice that the gain equals that in Eq. 27.

Part 3.

This third part gives the W-H solution. The expression for G, found using Eqs. 18 and 13, is

$$M = -c_0 EI\left(\sqrt{2}\sqrt{s} - \frac{8s^{7/4}}{(\omega_n + 5s)\sqrt[4]{\omega_n}}\right)[1\ 0]\begin{Bmatrix} v' \\ -EIv''' \end{Bmatrix} \tag{29}$$

Notice that if the compensator in Eq. 29 were altered to represent the feedback of rotational velocity to external moment (G/s), the new compensator would not be positive real at all frequencies. At low frequencies, where the left hand part of the term in parentheses dominates, the compensator would be negative real and lead to the generation of power at the active junction. This could lead to instability.

Figure 6 compares the transfer functions of the noncausal (a), causal fixed-form (b) and W-H (c) solutions. For the W-H solution, the corner frequency of Φ was chosen as ω_n=6.4 Hz. Near this frequency, the W-H solution has half the magnitude and the same phase as the noncausal solution. The W-H solution is better than the causal fixed-form solution at mimicking the noncausal solution near the frequencies of importance, around ω=6.4 Hz. It seems reasonable to suspect that as the Φ matrix becomes more banded around ω_n, the magnitude of the W-H solution will approach that of the noncausal solution.

Part 4.

A positive real approximation to Eq. 29 is required to guarantee stability. This W-H approximation should mimic the W-H solution in the frequency range in which Eq. 29 is positive real (above 2 Hz.). Looking at the right hand term in Eq. 29, the high frequency ($s^{3/4}$) behavior and gain ($8c_0 EI/5\omega_n^{1/4}$) are used in the approximation (Eq. 30). The first order pole in Eq. 30

$$M = \frac{8c_0 EI}{5\sqrt[4]{\omega_n}}\frac{s^2}{s + 92}\frac{1}{\sqrt[4]{s}}[1\ 0]\begin{Bmatrix} v' \\ -EIv''' \end{Bmatrix} \tag{30}$$

maintains the phase between 67.5 and 157.5 degrees (positive real). The corner frequency of 92 rad/sec provides the best match with the W-H phase. The transfer function of Eq. 30 is shown by curve (d) in Fig. 6.
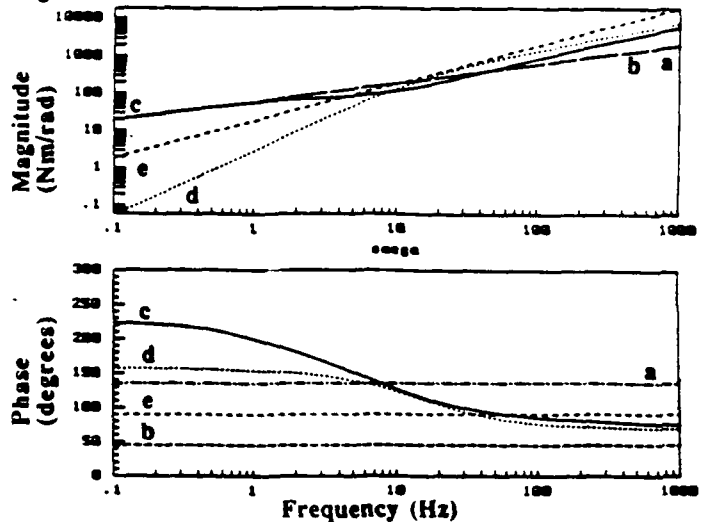

Figure 6 Feedback compensators for noncausal (a), causal fixed-form (b), W-H (c), W-H approximation (d) and rate feedback (e).

This W-H approximation is used, in place of the W-H compensator, for the duration of this paper.

Part 5.

For comparison purposes, rate feedback is analyzed and experimentally implemented. The gain that maximizes damping in a mode at 10 Hz was used. The approximate gain, determined through simulation, is

$$M = 3s[1\ 0]\begin{Bmatrix} v' \\ -EIv''' \end{Bmatrix} \tag{31}$$

The magnitude and phase are given by curve (e) in Fig. 6.

Simulations

Using the phase closure principle described by Miller and von Flotow [4], a transfer function was derived between force and transverse displacement at the opposite, free end of the beam. The beam properties are given in Table 1.

Figure 7 compares the open-loop magnitude characteristics (a) with those obtained using rate feedback (b) and the noncausal compensator (c). For rate feedback, notice that damping is a function of frequency. Below 10 Hz., the gain is lower than optimal. Above 10 Hz., the gain is higher than optimal. The latter leads to clamping of the pinned end. This simulation is provided as a comparison for the performance of the wave control compensators.

The noncausal compensator reflects no incoming propagating waves as outgoing propagating waves. This feature essentially eliminates resonant behavior and the beam behaves as a semi-infinite beam. The achievement of this type of performance is the objective of this work and represents the upper performance bound in these simulations.

Figure 8 shows the magnitude characteristics obtained using the causal fixed-form compensator (b). The selected form of the compensator causes the damping to be independent of frequency. Though the damping performance in the neighborhood of 10 Hz. is less than that obtainable using rate feedback, the damping is more broadband.

Figure 9 shows the transfer function obtained using the W-H approximation (b). Notice the significant increases in damping near $\omega = 10$ Hz.

In general, as more narrowband damping performance is achieved, broadband damping performance is sacrificed. Notice that Fig. 6 shows that the magnitude of the W-H approximation ($s^{3/4}$) increases less rapidly with frequency than rate feedback (s) but more rapidly than the causal, fixed-form compensator ($s^{1/2}$); which maximizes broadband damping. On the other hand, the phase of rate feedback is slightly closer to that of the noncausal compensator at higher frequencies. These observations, in conjunction with the

Figure 7 Transfer function for open-loop (a), rate feedback (b) and noncausal (c) compensators.

TABLE 1 Beam Properties

Length	7.32 m
Width	10.20 cm
Thickness	0.3175 cm
EI	31.1 N m²
ρA	2.85 kg/m
Damping ratio averages 0.30% below 30 Hz.	

simulations, give no indication that rate feedback provides more total damping than the W-H approximation.

Of the three compensators simulated, the W-H approximation provides the best narrowband performance since it provides a better approximation of the noncausal compensator near 10 Hz.

EXPERIMENT SETUP

This section describes the various hardware components used in the conduct of the experiments. These components are 1) the structure, 2) the control hardware, 3) the control computer and 4) the shaker and sensor used to measure the open and closed-loop transfer functions. Finally, the experiment protocol is briefly described. Figure 5 displays the functional elements of the experiment.

Structural Characteristics

The controlled structure is a 24 foot brass beam, suspended from six pairs of wire, with its longitudinal axis horizontal (Table 1). The suspension wires attach to the beam at one seventh length intervals with the two beam ends left free for the attachment of the control and shaker hardware.

Control Hardware Characteristics

The control hardware consists of the control actuator and the sensor used to obtain the feedback measurement. A PMI motor with a low inertia, laser etched armature was chosen. The armature was clamped to the beam with the permanent magnet clamped to the laboratory frame. This replicates the pinned condition used in the model. The specifications for the actuator and sensor are listed in Table 2 and a drawing of the hardware attached to the beam end is shown in Figure 10.

Control Computer

The control computer is a PACE TR-48 analog computer. The two types of fractional elements used in the experiment are a half ($1/s^{1/2}$) [5] and a quarter ($1/s^{1/4}$) [6] integrator. The circuit approximations exhibited good accuracy from 0.1 to 1000 Hz.

Shaker and Sensor Hardware

Shaker and sensor hardware are attached to the other end of the beam for acquisition of transfer function data. The shaker is a pivoting proof-mass actuator [7] and the sensor is a linear accelerometer measuring transverse beam acceleration. The specifications are given in Table 3.
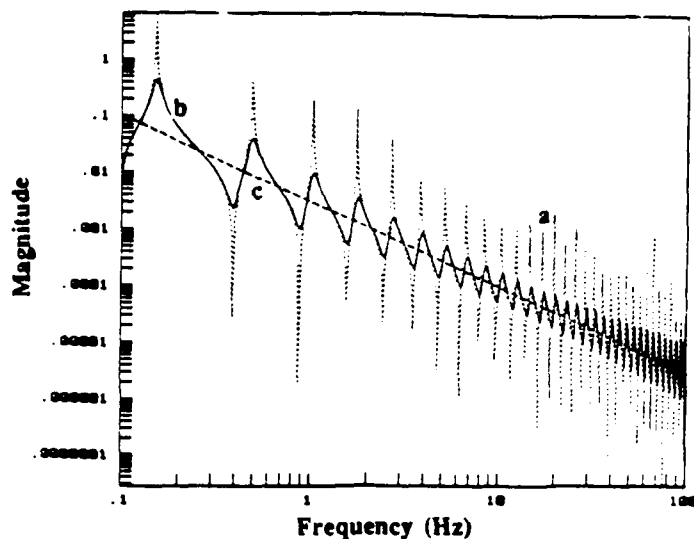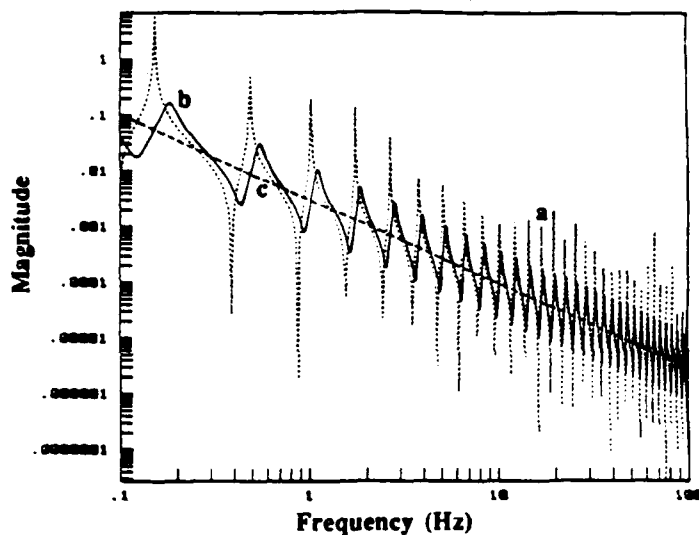

Figure 8 Transfer function for open-loop (a), causal, fixed-form (b) and noncausal (c) compensators.
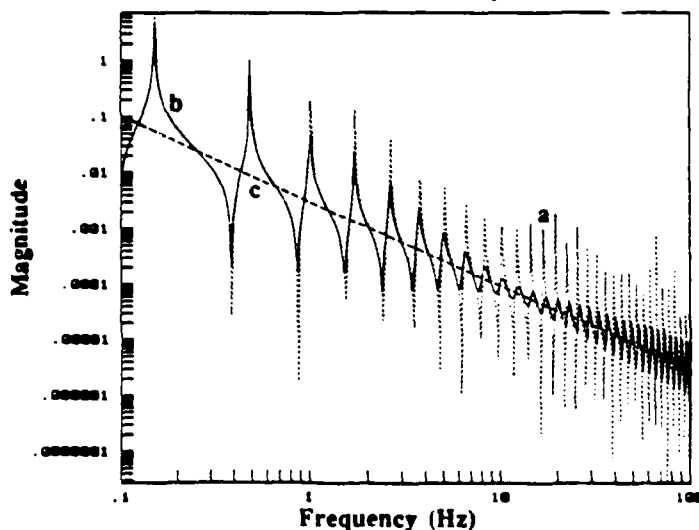

Figure 9 Transfer function for open-loop (a), W-H approximation (b) and noncausal (c) compensators.
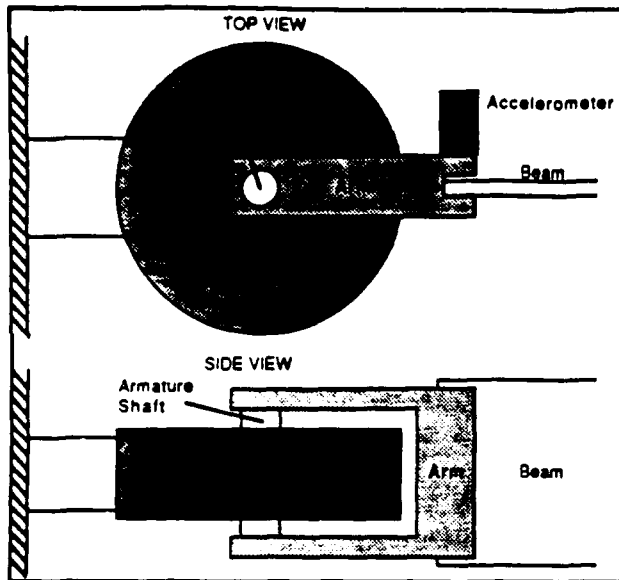
FIGURE 10 Views of control hardware.

TABLE 2 Control hardware specifications

Torque Actuator

Manufacturer/model	PMI U-9
Torque constant	0.0212 N m/amp
Armature plus arm inertia	0.000146 Kg m^2
Motor diameter	0.1048 m
Motor thickness	0.0345 m
Current source	EG&G PA-601
Gain	-2.08 Amps/volt

Piezo Resistive Accelerometer

Manufacturer/model	Endevco 2262-25
Excitation voltage	10.00 volts
Gain with amplifier	2.86 V/m/sec^2
Corner frequency	1200 Hz
Damping	light
Distance from motor pivot	0.062 m

TABLE 3 Shaker and sensor specifications.

Shaker's DC Servo Motor

Manufacturer/model	Pittman 7214
Torque constant	0.0357 N m/amp
Current source	EG&G PA-223
Gain	-1.87 Amps/volt

Piezo Resistive Accelerometer

Manufacturer/model	Endevco 2262-25
Gain	0.378 V/m/sec^2

(see Table 2)

Experiment Protocol

The open-loop transfer function is measured for a frequency range of 0.5 to 50 Hz. Then, for each feedback compensator used, the following iterative procedure is followed. First, a circuit gain, variable between 0 and 1, is increased until the onset of instability or the arrival at the optimal gain. In the event of instability, the cause is identified. Once eliminated, the procedure is repeated. If the optimal gain is reached, or an instability cannot be eliminated, the transfer function of the beam is measured.

EXPERIMENTAL RESULTS

The results of five tests are summarized in this section. The first test consists of obtaining the transfer function of the beam in open loop. The second test uses the causal, fixed-form compensator to control the beam. The third test acquires the same information for the beam controlled using rate feedback. The fourth test involves the

implementation of the W-H approximation. The fifth test involves implementing the highest stable gain using the W-H approximation. In the following discussion, the results of these five tests are compared using measured transfer functions. First, however, the implemented compensators are discussed.

Feedback Compensators

Three different feedback compensators are implemented. In the derivation of the control compensators, feedback from rotational acceleration to moment was assumed. Therefore, the implemented compensators equal the analytical compensators scaled by the frequency squared. Between 0.5 and 50 Hz., Eqs. 32, 33 and 34 have the same gain as the analytical compensators.

The rate feedback compensator is given by

$$\frac{M(s)}{s^2 v'(s)} = 0.31 * \frac{-10s}{s^2 + 0.889 s + 0.394} * \frac{-628}{s + 628} \quad (32)$$

The middle portion is a stabilized integrator with a corner frequency of 0.1 Hz. and a damping ratio of 0.7071. This filters and integrates frequencies below and above 0.1 Hz., respectively. The right portion contains a first order filter to eliminate an instability, at 1180 Hz., caused by the lightly damped feedback accelerometer.

The causal, fixed-form compensator is given by

$$\frac{M(s)}{s^2 v'(s)} = 0.94 * \frac{-10s}{s^2 + 0.889 s + 0.394} * \frac{-2.58}{\sqrt{s}} \quad (33)$$

Again, the middle term is a stabilized integrator while the right term is a 'half integrator.'

The W-H approximation is given by

$$\frac{M(s)}{s^2 v'(s)} = -0.039 * \frac{-92}{s + 92} * \frac{-700}{s + 700} * \frac{-3.348}{\sqrt[4]{s}} \quad (34)$$

The left term is the first order pole shown in Eq. 30. The middle term is a low pass filter and the right term is a 'quarter integrator.'

Random Excitation Tests

Figure 11 shows the measured transfer functions for the five different tests. Figure 12 shows the predicted transfer functions for these same tests. The presentation of the data is ordered starting with the compensator which provides the best broadband damping to the one providing the best narrowband damping. Notice that the model, based on measured values of EI, ρA and length, predict open-loop poles and zeroes within 4% of their measured frequencies.

Figure 11a compares the transfer functions of the beam in open-loop (a) and in closed-loop (b) using the causal, fixed-form compensator at the optimal gain. While this solution exhibits a more broadband affect than the rate feedback, this is achieved by sacrificing narrowband damping performance. Notice that torsional modes appear in the data above 10 Hz. Figure 12a compares the equivalent simulation transfer functions over the same 3 to 30 Hz. frequency range. While the experimental data indicates damping performance that is independent of frequency, the level of damping appears to exceed that predicted. This could result from lower open-loop damping in the simulation model than in the actual beam.
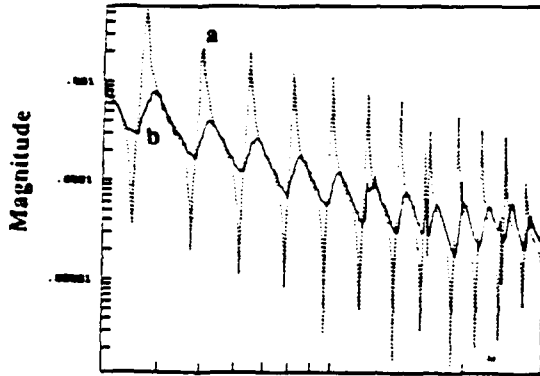
Figure 11b shows the closed-loop transfer function (b) using rate feedback. As supported by the simulation, rate feedback provides better narrow band damping performance than the causal, fixed-form compensator. It is difficult, however, to judge the broadband behavior using this narrow frequency range. Figure 12b shows the simulated transfer function.

Figure 11c shows the closed-loop transfer function using the W-H approximation (b) given in Eq. 34 at the optimal gain. In the frequency range of 10 to 20 Hz., the damping performance exceeds that shown in Figs. 11a and b. Notice that the high frequency decrease in damping is perceptible. Figure 12c displays the simulated transfer function.

Good agreement exists between the experimental and simulated data below 20 Hz. However, the damping in the experimental data above 20 Hz. exceeds that predicted. This could be

a)

b)

c)

d)
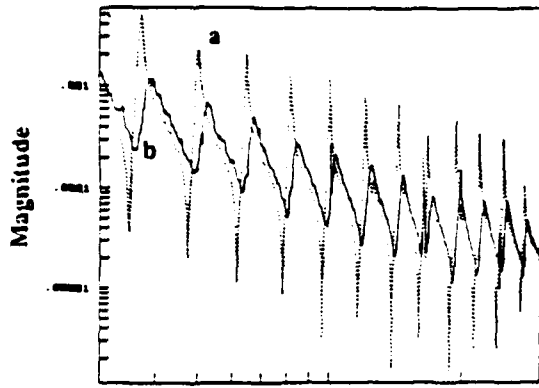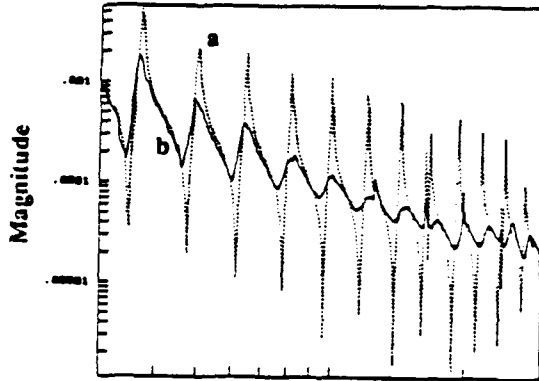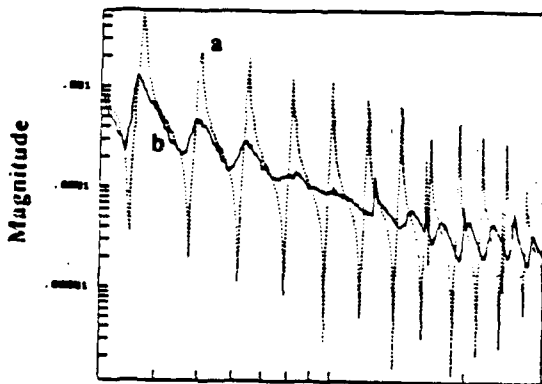
Figure 11. Measured open and closed-loop transfer functions using a) causal fixed-form compensator, b) rate feedback, c) W-H approximation at optimal gain and d) W-H approximation at 1.55 times optimal gain
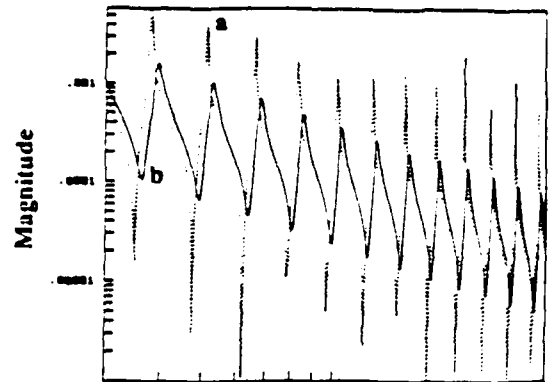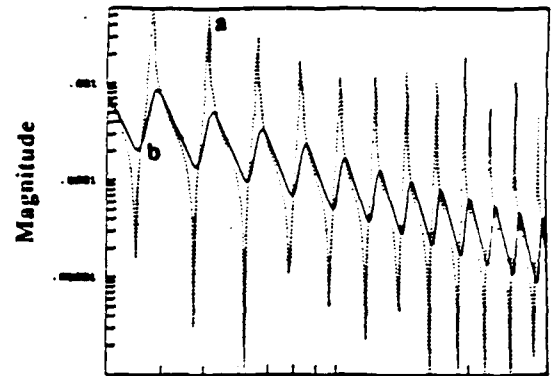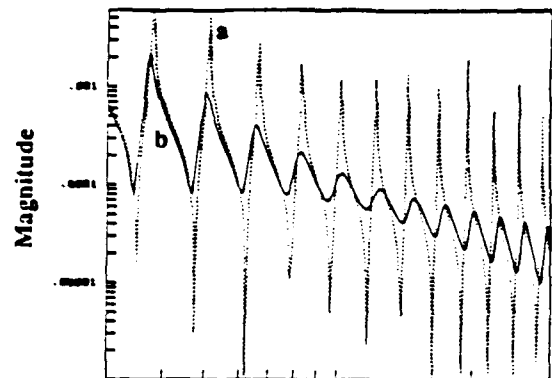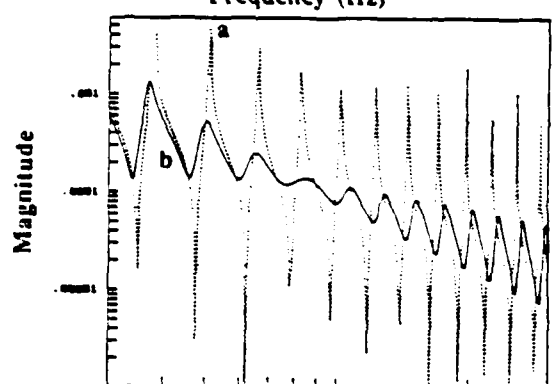
Figure 12. Simulated open and closed-loop transfer functions using a) causal fixed-form compensator, b) rate feedback, c) W-H approximation at optimal gain and d) W-H approximation at 1.55 times optimal gain

caused by the noise floor, or resolution of the accelerometer, limiting the gain at these frequencies. Given an excitation level, increases in gain will eventually clamp the pinned beam at high frequency. This results in lower amplitudes at these frequencies. Eventually, the feedback signal will drop below a noise threshold, resulting in poor signal-to-noise ratio, and limit both the further increase in gain and associated reduction in damping.

Figure 11d shows the closed-loop transfer function using the W-H approximation with a gain that is 1.55 times larger than the optimal gain. As shown in Fig 6, this causes the W-H compensator to better replicate the noncausal compensator. If the optimal gain were doubled, this compensator would have the same gain and phase as the noncausal compensator and the mode near 6.4 Hz. would be eliminated. Between 8 and 10 Hz., the magnitude approaches a line with a slope of -3/2. The simulation (Fig. 12d) at this gain predicts a slightly different behavior. This could result from the small amount of additional lag in the implemented compensator when compared with Eq. 34.

Of the compensators implemented, the W-H approximation provided the most damping in a single mode. This occurred because the causal, fixed-form solution is broadband while rate feedback transitions from damping to clamping with increasing gain, without achieving a gain and phase which equal that of the noncausal compensator.

Performance Limitations

The first encountered instability was caused by the lightly damped feedback accelerometer with a resonance at 1200 Hz. This was suppressed with a first order, low pass filter.

The second encountered instability was due to the flexibility of the angle iron frame to which the actuator's permanent magnet was attached. This flexibility caused the permanent magnet of the torque actuator to undergo rotation. This allowed the feedback sensor to measure acceleration in the absence of armature rotation with respect to the permanent magnet. In other words, the accelerometer and motor were no longer a dual sensor/actuator pair. This instability was suppressed by placing a layer of viscoelastic foam between the frame and laboratory floor.

The third encountered instability was caused by the feedback accelerometer measuring torsional acceleration. This was suppressed by placing the accelerometer closer to the centerline of the beam.

Once these three instabilities were suppressed, the rate feedback, causal fixed-form and W-H compensators were implemented at their optimal gains.

The compensator used to generate curve (b) in Fig. 11d was at the highest stable gain achieved using the W-H approximation. An instability at 773 Hz., believed to be caused by torsional modes, was not suppressed.

CONCLUSIONS

If the control objective is to extract energy from the structure, maximizing power absorption frequency by frequency provides the best solution. As shown, however, there is no guarantee that this compensator will be implementable, raising the need for causal solutions.

Two alternative techniques were illustrated for finding causal compensators under given hardware constraints. The W-H approach was shown to provide better narrowband damping performance than rate feedback without perceptible degradation in broadband damping performance. This was achieved because the W-H technique more closely mimics the magnitude and phase of the noncausal compensator.

The limitation to the W-H procedure is that it does not guarantee that the compensator has a positive real form. Therefore, a positive real approximation to the W-H compensator was derived, using engineering insight. Further work is needed to constrain the W-H formulation to yield a positive real compensator.

This W-H approximation was implemented experimentally and achieved predicted levels of damping. These levels of damping were shown to far exceed the levels of damping that could be achieved through rate feedback. Limitations to performance included the discovery of frequencies above which the sensor and actuator were no longer dual and the inadvertent coupling of the control hardware to unmodelled torsion modes in the structure. The unsuppressed instability occurred at a frequency near the 80th bending mode.

ACKNOWLEDGEMENTS

REFERENCES

1. Miller, D. W., Hall, S. R., von Flotow, A. H., "Optimal Control of Power Flow at Structural Junctions," Automatic Control Conference, pp. 212-220, June 1989.
2. von Flotow, A. H., "Disturbance Propagation in Structural Networks," J. Sound and Vibration, 106, 433-450, 1986.
3. von Flotow, A. H., "Traveling Wave Control for Large Spacecraft Structures," J. Guidance, Control, and Dynamics, 9, 462, July- Aug 1986.
4. Miller, D. W., von Flotow, A. H., "Power Flow in Structural Networks," J. Sound and Vibration, 128, 145-162, 1989.
5. von Flotow, A. H., Schafer, B., "Experimental Comparison of Wave Absorbing and Modal Based Low-Authority Controllers for a Flexible Beam," AIAA Guidance and Control Conference, Snowmass, Co., Aug. 1985.
6. Carlson, G. E., Halijak, C. A., "Approximation of Fractional Capacitors $(1/s)^{1/n}$ by a Regular Newton Process," IEEE Transactions on Circuit Theory, 210-213, June 1964.
7. Miller, D. W., Crawley, E. F., "Experimental Investigations into Passive and Active Control Using Space-Realizable Techniques," AIAA J. Guidance, Control, and Dynamics, Vol. 11, No. 5, pp. 449-458.

An $\mathcal{H}_\infty$ Power Flow Approach to Control of

Uncertain Structures

Douglas G. MacMartin*, Steven R. Hall[†]

Space Engineering Research Center

Massachusetts Institute of Technology

February 7, 1990

*Research Assistant, Department of Aeronautics and Astronautics,

Room 37-367 MIT, Cambridge MA 02139. Student Member AIAA

[†]Boeing Assistant Professor of Aeronautics and Astronautics,

Room 33-103 MIT, Cambridge MA 02139. Member AIAA, IEEE

Abstract

A technique is described for generating guaranteed stable control laws for uncertain, modally dense structures with collocated sensors and actuators. By ignoring the reverberant response created by reflections from other parts of the structure, a dereverberated mobility model can be developed which accurately models the local dynamics of the structure. This is similar in many respects to a wave based model, but can treat more general structures, not only those that can be represented as a collection of waveguides. This model can be determined directly from transfer function data using an analysis technique based on the complex cepstrum. In order to minimize the effect of disturbances propagating through the structure, the power dissipated by the controller is maximized in an $\mathcal{H}_\infty$ sense. This guarantees that the controller is positive real, and thus that the system will remain stable for any uncertainty, provided that the power flow is correctly modelled. The approach is demonstrated for two examples. The resulting controllers are much more effective than simple collocated rate feedback.

Introduction

Broadband active control of flexible structures is difficult for several reasons. Structures tend to be very lightly damped, modally rich, and difficult to model in detail, due to their large sensitivity to parameter variations. It is well known[1] that for many applications, there are likely to be many flexible modes within the desired bandwidth of a structural control system. This is due in part to the anticipated light damping, which implies that many modes can contribute to the performance, as in large space structures, where many problems of interest demand extremely precise pointing. Also, performance requirements may push the bandwidth higher directly, for example in noise control of machinery, where the bandwidth must clearly include acoustic frequencies, and therefore many flexible modes.

One of the problems associated with broadband control of structures is the uncertainty in the plant model. A state space model of a structure must be at best an approximation,

since the true structure is infinite-dimensional. Finite element methods are typically used to model a structure, and are sometimes capable of modelling the lowest modes quite accurately. However, in the region of high modal density, any model is likely to be highly inaccurate. Models of structures with closely spaced modes in particular tend to be extremely sensitive to small parameter changes, in their prediction of natural frequencies, and especially in their prediction of mode shapes. As a result, the actual structure to which the control will eventually be applied may differ significantly from the model for which it was designed. Thus some knowledge about the uncertainty must be taken into account when designing the controllers.

Many approaches to control design for uncertain structures[2,3,4] begin with a large order, detailed nominal model of the structure, and deal with uncertainty by attempting to model it, as well as the nominal plant, in some fashion. However, if the nominal model contains significant error, then the detailed information it contains is meaningless, and has no effect other than to increase the computational burden associated with the control design. Indeed, for broadband control of a modally rich structure, the dimension of the plant required to model each mode may be prohibitive for many control design techniques. Instead, only the information that can be accurately modelled should be included in the description of the plant[3]. With this philosophy, there has been much recent research on the use of wave based models for use in structural control, see for example References 5-12. Here the assumption is that the local dynamics can be accurately modelled, and that an effective control system can be derived based only on this information.

Of particular relevance to this paper is the optimal control approach of Miller et al.[5]. The structure is represented as being composed of one-dimensional waveguides, i.e. structures which support travelling waves along a single dimension, such as beams in bending, or rods in compression. These meet at junctions, and only the junction at which the control acts is modelled. Using Weiner-Hopf techniques to ensure causality, Miller et al. maximize the frequency weighted power dissipation associated with the control. The drawback to this optimization is that it will allow power to be generated at some frequencies in order to achieve greater power dissipation at other frequencies. If there is a mode of the system at

2

such a frequency, it may be destabilized by this compensator. While power generation may be acceptable in a frequency range where the modes are well known, it is not satisfactory if the uncertainty in modal frequency is comparable to the modal spacing. T:..s problem is corrected by approximating the optimal compensator with a positive real form, which is guaranteed to be stabilizing. The final result, then, is suboptimal, because the positive real constraint is applied in a somewhat *ad hoc* manner. Furthermore, arbitrary structures may be difficult to model using this approach because of the difficulty in obtaining an accurate wave description. Thus while this design procedure is attractive, an approach which treats more general structures and provides a guarantee of stability is desired.

This paper describes a new approach to the modelling and control of uncertain structures that will guarantee both stability robustness and some amount of performance robustness. The goal is to provide broadband damping to the structure. This might be used in conjunction with a low order modal-based compensator which could provide good performance on those modes that could be well modelled. Thus this could be used as the low authority controller in a HAC/LAC architecture[13], rather than the rate feedback typically used. Rate feedback is guaranteed to be stable, but it is not necessarily optimal. In general it is possible to add more damping to a structure than can be obtained through rate feedback[6]. Further details on the approach of this paper can be found in Reference 14, and experimental results obtained using this approach are presented in Reference 15.

The model used in this paper is the dereverberated mobility[14,16], which will be described in more detail in the following section. This is calculated between a collocated and dual actuator/sensor pair, which means that the product of the two variables is the power flow into the structure. Only that part of the response which is due to the local dynamics of the structure near the actuator and sensor is retained in the dereverberated mobility model. This can be shown to correspond in the frequency domain to an averaging, or smoothing, of the transfer function. This model bears some relationship to the wave approach of Reference 5, but it is more general, as it allows structures which are not networks of waveguides to be treated. It also has the advantage that it can be derived either from analytical, or from experimental data.

3

Since the driving point mobility of a structure is positive real, stability can be guaranteed by requiring that the compensator be positive real[17]. This is assured by minimizing the maximum value over frequency of the power flow into the structure, which results in power being dissipated at all frequencies. Taking energy as the Lyapunov function shows that the closed loop system must be stable for all plants, provided that the sensors and actuators are not mismodelled. In the presence of actuator and sensor dynamics, time delays, or actuators and sensors that are not quite collocated, stability can still be checked using the results of Slater *et al.*[17]. Extensions to the design procedure to guarantee stability in these cases will be the subject of future work.

Modelling

The intent of this section is to develop a useful model for control design for uncertain modally dense systems. It has been pointed out[7,18] that modes are not useful in this case. The detailed information contained in a modal model is often incorrect, and may also be unimportant. While detailed knowledge of the exact mode shapes and frequencies is unavailable, this does not imply that nothing is known about the structure, or that nothing can be done to control it. In the presence of significant uncertainty, the local dynamics near an actuator can still be well modelled. There is, however, very little information that can be relied upon about the behavior of the structure between an actuator and sensor which are separated by many wavelengths of the disturbance. Thus for broadband control, it is reasonable to require that feedback only be used between collocated sensors and actuators.

For some arbitrary structure, as shown in Figure 1, insight into the nature of the problem can be obtained from a wave perspective. Various disturbances are created at certain points in the structure and propagate through it. At any point in the structure, such as at an actuator, the disturbance will be scattered. In general, each of the resulting outgoing disturbances will eventually affect any global cost criterion. Thus from the perspective of the actuator, without a detailed and accurate description of how each wave propagates, its goal should be to minimize the energy of each of these disturbances. Since the scattering behavior is a function of only the local dynamics, this goal can be achieved with only a

4

local model of the structure. Thus for a sufficiently uncertain structure, a local model contains all the information that can be accurately determined, and also contains enough information for effective control design.

One approach to obtaining such a model is through the use of waves. However, it may be difficult to obtain a useful wave description for many complicated structures, because not all structures can be well represented as a collection of waveguides. An alternative to a wave approach is to represent the structure by its dereverberated driving point mobility[16]. The mobility is the ratio of a generalized velocity and a generalized force, which is the inverse of the mechanical impedance. The driving point mobility is then the transfer function between two variables whose product is the power flow into the structure, thus the sensors and actuators must be both collocated and dual. The response at a point can be considered to be the sum of two parts: a *direct field*, due to the local dynamics; and a *reverberant field*, which is caused by energy reflected back from other parts of the structure. The term "dereverberated" implies that the "reverberant" part of the response has been removed before computing the mobility. It should be possible to model the direct field more easily and accurately than the reverberant field, as it depends only on a few parameters, while the reverberent field depends on the entire structure. For the same reason, it is the reverberant field that contains greater detail, and requires more degrees of freedom to model. Thus by using the dereverberated mobility, a lower order model can be used that is based only on the details of the structure which can be accurately modelled.

The dereverberated mobility may be calculated through the use of the cepstrum[16] of the impulse response. The cepstrum is the inverse Fourier transform of the log of the complex spectrum, and is a function of time. The low time portion corresponds to the direct response, and the high time portions correspond to the reverberant response, with spikes at times corresponding to the return times of the impulse from the rest of the structure. Windowing the cepstrum before the first of these yields the direct response, which can then be transformed back to the frequency domain to yield the dereverberated mobility. This approach is shown schematically in Figure 2 for the transfer function from force to collocated velocity at one end of a free-free beam. The dereverberated mobility

5

and cepstrum in this figure were calculated directly from the exact local model of the structure. The cepstrum of the dereverberated structure is only approximated by the truncated cepstrum of the original reverberant system.

The truncation time to choose can be based on the level of confidence in the impulse response data. This illustrates one of the differences between the dereverberated mobility and a local wave model, that being direct control over how much of the structure is included in the model. By truncating the cepstrum at the appropriate point, some information about the rest of the structure is maintained while the details of it are ignored. Thus the control design is provided with more information, allowing it to do a better job.

The fundamental distinction between this and the wave approach is the ability to treat generic structures. While the concept of direct and reverberant fields is based on wave ideas, there is no requirement to actually identify a local wave model. All that is needed is the input/output behavior at the driving point, which may be found from experimental data, calculated from some nominal model, or found analytically, perhaps even from a wave model. This also indicates another important advantage of this modelling approach – the ability to use experimental data to generate a measurement based model.

The effect of ignoring the reverberant field is to smooth out the transfer function. If no energy returns from beyond some closed surface surrounding the actuator, then this is equivalent to the structure beyond this surface either being infinite in extent, or having perfectly absorbing boundary conditions. This has also been shown[18,19] to be equivalent to replacing the log magnitude of the original transfer function with its mean. This is not surprising, considering that the cepstral analysis approach described earlier is essentially the same as low-pass filtering the logarithmic frequency response. Thus another way to compute the dereverberated mobility is simply to take the logarithmic average of the magnitude of the transfer function, with the phase being determined uniquely from the fact that the dereverberated mobility is positive real. In practice, this method should be adequate. Fitting the result with a rational polynomial gives a model that captures the essential dynamics of the system over a wide frequency range that encompasses many modes, with only a small number of poles and zeroes.

The dereverberated mobility model is not intended to accurately represent the structure – it clearly fails in this regard. However, it is shown in the examples that this can be a useful model for the design of control systems for the structure. Although the local dynamics of the controlled junction are accurately modelled by the dereverberated mobility, the resonant and anti-resonant details of the full reverberant mobility are not explicitly modelled. However, the reverberant field is composed of waves whose behavior is governed by the local dynamics of the controlled junction each time they pass through it. Thus if the local dynamics can be appropriately modified based on a local model, then the complete reverberant field can be controlled.

Control Design

The previous section described the modelling approach used, while this section focuses on the design of the control system for this model. There are two main objectives to be satisfied by the control design. It must be guaranteed to be stabilizing for all possible plants, and it must provide good performance, again for all possible plants. In order to guarantee stability, positive real feedback from velocity to force will be required. One could, for example, select rate feedback, which is guaranteed to be stable, but this does not necessarily give the best performance that could be achieved. The object of this section is to derive the optimal positive real compensator.

The criterion to be used for optimality will be the minimum power flow into the structure. That is, power extracted from the structure will be maximized. Power flow is the appropriate quantity to minimize to provide active damping of the structure, and allows a guarantee of stability by ensuring that the power flowing into the structure due to the control is always negative.

Miller *et al.*[5] minimized the $\mathcal{H}_2$ norm of the power flow. This required some assumptions about the power spectral density of the disturbance entering the junction, which in the actual structure is related to the control through the disturbance that previously departed the junction. In the wave model, however, it was assumed constant and independent

7

of the control, and thus the resulting compensator allowed power to be added at some frequencies. This problem can be avoided by minimizing the power flow in an $\mathcal{H}_\infty$ setting. For an open-loop system, the power removed by the controller is zero, and the closed loop is guaranteed to be no worse. In fact, it is sufficient to place a constraint on the maximum value of the power flow which guarantees it to be negative at all frequencies, and then to use an $\mathcal{H}_2$ optimization[20], which may improve the overall performance.

Define $G(s)$ to be the dereverberated driving point mobility, and assume some disturbance input d to be additive at the output. Then the output y is related to the input u and the disturbance via

$$y(s) = G(s)u(s) + d(s) \tag{1}$$

As yet, no assumptions have been made about the nature of the disturbance.

The disturbance d in Equation (1) can be thought of as originating from two sources: the original disturbance input to the real structure, and the reverberant field ignored in the modelling process. This second source will have significant power at the modal frequencies, and if the closed loop damping is still relatively small, then in steady state this will be much larger than the physical disturbance. Thus the disturbance spectrum in Equation (1) consists of significant power in narrowband but unknown frequency ranges, which are exactly the assumptions indicated in Reference 20 as being appropriate for $\mathcal{H}_\infty$ minimization.

The instantaneous power flow into the structure is the product of the input $u(t)$ and the output $y(t)$, since $G(s)$ is a mobility. The average power flow can be expressed as a time integral of the instantaneous power flow[21], and making use of Parseval's theorem, this can be transformed into the frequency domain:

$$
\begin{aligned}
P_{ave} &= \lim_{T \to \infty} \frac{1}{2T} \int_{-T}^{T} y(t)^T u(t) \mathrm{d}t \\
&= \frac{1}{2} \int_{-\infty}^{\infty} \left(u(j\omega)^H y(j\omega) + y(j\omega)^H u(j\omega) \right) \frac{\mathrm{d}\omega}{2\pi}
\end{aligned} \tag{2}
$$

The integrand of the right hand side of Equation (2) represents the steady state, or average, power flow into the structure as a function of frequency[21]. For convenience, the average

8

power flow at each frequency can be defined without the factor of $\frac{1}{2}$ as

$$P(\omega) = u(j\omega)^H y(j\omega) + y(j\omega)^H u(j\omega) \tag{3}$$

where $(\cdot)^H$ indicates Hermitian, or complex conjugate transpose.

The control law is assumed to be of the form

$$u(s) = -K(s)y(s) \tag{4}$$

Solving for the control in terms of the disturbance from Equation (1) gives

$$u = -(I + KG)^{-1}Kd \tag{5}$$

$$= Hd \tag{6}$$

where the explicit dependence on the Laplace transform variable has been dropped. Then the output can also be represented in terms of the disturbance as

$$y = (I + GH)d \tag{7}$$

Substituting these expressions for u and y into Equation (3) yields that the average power flow at each frequency is

$$P(\omega) = d^H \left\{ H^H(I + GH) + (I + GH)^H H \right\} d \tag{8}$$

Since the power flow is a scalar, it is equal to its trace. The expected value of the power flow at each complex frequency can then be written in terms of the power spectral density of the disturbance, $\Phi_{dd} = E\left[dd^H\right]$, as

$$E(P(\omega)) = \text{Trace}\left\{ \Phi_{dd}\left[H^H(I + GH) + (I + GH)^H H \right] \right\} \tag{9}$$

Unconstrained Optimum

Before finding a compensator which minimizes the worst case power flow, consider finding the compensator which minimizes the power flow at each value of the Laplace transform variable s. Equation (9) is only valid on the $j\omega$ axis, and must first be extended

analytically to the remainder of the complex plane. The analytic continuation of the Hermitian operator is the *parahermitian conjugate*[22], denoted $(\cdot)^{\sim}$, and defined as

$$F^{\sim}(s) = F(-s)^T \tag{10}$$

With this substitution for the Hermitian, then optimizing Equation (9) at each point in the complex plane with respect to H yields

$$H_{opt} = -(G + G^{\sim})^{-1} \tag{11}$$

which is independent of the disturbance spectrum Φ_{dd}. This is the optimal disturbance feedforward control law. The equivalent feedback from the velocity is related to this from Equations (5) and (6), by

$$K = -H(I + GH)^{-1} \tag{12}$$

So finally,

$$K_{opt} = (G^{\sim})^{-1} \tag{13}$$

This compensator extracts the maximum possible power from the structure at every frequency. This result is not new; it corresponds to the impedance matching condition found, for example, in Reference 23. The maximum energy dissipation is obtained if the impedance of the compensator is the complex conjugate of the impedance of the load, which in this case is the rest of the structure. Also note that although Equation (13) was obtained using the dereverberated mobility, it is also optimal for the actual structure. The dereverberated mobility accurately models the local dynamics of the structure, and the power flow is a function of only the local dynamics. Thus the compensator that dissipates the maximum power from the dereverberated structure will also dissipate the maximum power from the actual reverberant structure.

In general, however, the compensator in Equation (13) is noncausal, and cannot be implemented. The dereverberated mobility $G(s)$ must be both stable and causal, and is therefore right half plane analytic (RHPA). Since it is strictly positive real, it must also be minimum phase, and thus the optimal compensator in Equation (13) will be left half plane analytic (LHPA). Because both the compensator and the plant are strictly positive real,

10

then in the Nyquist plot there are no encirclements of -1, and K must be stable for the closed loop system to be stable. This implies that unless the dereverberated mobility is a constant, this compensator is noncausal. One case for which the dereverberated mobility is constant is that of a uniform rod in compression, for which Equation (13) corresponds exactly to the matched termination.

Some understanding of why the optimal compensator is almost always noncausal can be found from root locus arguments. For a point λ to be on the root locus of the plant $P(s)$, the compensator $K(s)$ must satisfy $1 + P(\lambda)K(\lambda) = 0$. In order to place the structural poles far into the left half plane, the relevant plant $P(s)$ is the structural transfer function evaluated for values of the Laplace variable s far into the left half plane.

For a lightly damped structure with a large number of closely spaced poles and zeroes, one can divide the complex plane into three regions. Near the $j\omega$ axis, and close to the poles and zeroes, the transfer function varies significantly from its maxima to its minima, and the phase varies between $+90°$ and $-90°$. If one looks at the transfer function evaluated farther into the right half plane, the effect of individual poles and zeroes becomes smeared out, and the transfer function approaches the smoothed, or dereverberated transfer function $G(s)$. The phase of G in some frequency region will be the average phase of the original transfer function near that region.

In the left half plane, however, the structure's transfer function is not $G(s)$. To determine the phase contribution of each pole and zero, the contour to consider must now be to the left of every pole and zero, and so each phase change has opposite sign. The result is that in the left half plane, the structural transfer function approaches $-G(-s)$. Therefore, to move the poles far into the left half plane, $K(s)$ must satisfy $1 - G(-s)K(s) = 0$, or $K(s) = 1/G(-s)$, as given in Equation (13).

If this compensator could be implemented, all the poles could be moved arbitrarily far into the left half plane. Instead, the best causal compensator must be found.

Causal Optimum

The wave model of Miller *et al.*[5] can also be put in a form similar to that of Equation (1), though only for structures composed of waveguides. As discussed earlier, Miller *et al.* performed an $\mathcal{H}_2$ optimization of the power flow, which did not guarantee dissipation at all frequencies, and thus did not guarantee closed loop stability. A more appropriate optimization to guarantee stability is to minimize the worst case power dissipation, hence a minimax optimization of the power flow into the structure. As will be shown shortly, this can be cast as an $\mathcal{H}_\infty$ minimization problem. In order for this to make sense, though, the disturbance input d should be normalized to provide the same amount of power available to be dissipated at each frequency. This provides the designer with complete control over the relative importance of one frequency range to another, by removing any inherent frequency weighting from the problem.

With the optimal noncausal compensator derived in the previous subsection, Equation (13), the closed loop power flow into the structure is given by Equations (8) and (11) as

$$P = -d^H (G + G^H)^{-1} d \qquad (14)$$

Introduce a scaled disturbance w related to the original disturbance d via

$$d = G_0 w \qquad (15)$$

Then if the input w has unit magnitude at a certain frequency, the optimal noncausal compensator will dissipate unit power at this frequency, provided that the transfer function G_0 is the co-spectral factor of $G + G^\sim$, given by

$$G_0 G_0^\sim = G + G^\sim \qquad (16)$$

The block diagram for this system is shown in Figure 3, and the system (Equation (1)) becomes

$$y(s) = G(s)u(s) + G_0(s)w(s) \qquad (17)$$

Now, consider the problem of finding a causal compensator that will minimize the worst case power flow in Equation (3). This quantity represents the power flow into the

12

structure, which will hopefully be negative. In order to cast this as an $\mathcal{H}_\infty$ optimization, however, the performance index must be positive definite. This problem can be solved by considering that the best causal compensator can dissipate no more power than the noncausal optimum. Thus if the disturbance power $w^\sim w$ is added to the cost, positive definiteness will be assured.

Thus the cost at each frequency is

$$\text{Cost}(\omega) = w^\sim w + u^\sim y + y^\sim u \tag{18}$$

$$= w^\sim w + u^\sim(Gu + G_0 w) + (Gu + G_0 w)^\sim u \tag{19}$$

$$= \left\{ \begin{array}{c} u \\ w \end{array} \right\}^\sim \left[\begin{array}{cc} G + G^\sim & G_0 \\ G_0^\sim & I \end{array} \right] \left\{ \begin{array}{c} u \\ w \end{array} \right\} \tag{20}$$

$$= |G_0^\sim u + w|^2 \tag{21}$$

From this, we have that the relevant output that should be minimized is

$$z = G_0^\sim u + w \tag{22}$$

Combining this with the system equation (17), the result can be written as a four block problem[24,25]:

$$\left\{ \begin{array}{c} z \\ y \end{array} \right\} = \left[\begin{array}{cc} I & G_0^\sim \\ G_0 & G \end{array} \right] \left\{ \begin{array}{c} w \\ u \end{array} \right\} \tag{23}$$

The compensator from y to u that minimizes the $\mathcal{H}_\infty$ norm of the transfer function from w to z will minimize the maximum power flow into the structure.

For computation, however, the unstable (1,2) block in Equation (23) is unacceptable. Any allowable compensator must stabilize this block, while the only important stability constraint is on the output y. Note, however, that the norm of z is unchanged by multiplication by an inner function. An inner function is one which is stable, purely non-minimum phase, and has unit magnitude at all frequencies[24]. Define $\Delta(\cdot)$ to be the characteristic polynomial of the transfer function $(\cdot)$, and define the inner function

$$G_1(s) = \frac{\Delta(G_0^\sim(s))}{\Delta(G_0(s))} \tag{24}$$

13

Then redefine z to be

$$z = G_1 G_0^\sim u + G_1 w \qquad (25)$$

so that the four-block problem (23) becomes

$$\left\{ \begin{array}{c} z \\ y \end{array} \right\} = \left[\begin{array}{cc} G_1 I & G_1 G_0^\sim \\ G_0 & G \end{array} \right] \left\{ \begin{array}{c} w \\ u \end{array} \right\} \qquad (26)$$

which is stable.

In general, it may be desirable to weight some frequency ranges more heavily than others, while still requiring that power be removed at all frequencies. This could be because there is a known disturbance source in a certain range, because structural modes are less well damped within this range, or because the performance requirements put more emphasis on this range. Similarly, there will usually be some frequency beyond which performance is not required, and the weighting can also be chosen to reflect this.

The manner in which the weighting is introduced into the problem must be such that if power is added to the structure somewhere, the resulting cost will be worse than the open-loop cost. Hence, rather than weighting the sum of the disturbance input power and the power input by the control, as in Equation (18), define the cost to be the sum of the disturbance power and some frequency weighted control power, as

$$\text{Cost}(\omega) = w^\sim w + W_1^\sim (u^\sim y + y^\sim u) W_1 \qquad (27)$$

which can be manipulated into the form

$$\text{Cost} = \left| \begin{array}{c} W_1(G_0^\sim u + w) \\ W_2 w \end{array} \right|^2 \qquad (28)$$

where W_1 is the selected frequency weighting, and W_2 is defined by the relationship

$$|W_1|^2 + |W_2|^2 = 1 \qquad (29)$$

Note that as desired, the open loop cost is unity everywhere, and the cost is greater than unity at any frequency where power is added to the structure. Thus as before, a closed loop cost of less than unity guarantees stability.

14

The only constraint on W_1 is that its magnitude be less than or equal to unity at all frequencies. Without this constraint, there is no guarantee that the cost be positive definite, and the minimization could fail. Where W_1 is small, a greater amount of control effort is required to reduce the cost than before, and thus there is more power removed. Hence, in order to emphasize some frequency range more heavily, the weighting function W_1 should be chosen to be smaller within that region.

One of the properties of $\mathcal{H}_\infty$ compensators is that at the optimum, the closed loop transfer function being minimized is a constant function of frequency, equal to some number γ (see Reference 24). From this, and Equation (27), the closed loop power absorbed by the compensator can be related to γ and the weighting function as

$$P(\omega) = \frac{1 - \gamma^2}{|W_1|^2} \tag{30}$$

This provides some insight into how to select W_1.

The cost in Equation (18) or (27) can also be modified to include a penalty on the control effort, $\rho u^\sim u$. The four block problem (26) is modified to include an additional output in the vector z, corresponding to $\sqrt{\rho} u$. This allows a tradeoff between performance and control, and also guarantees a proper compensator. Similarly, it is straightforward to modify the four block problem (26) to include sensor noise. An additional disturbance input is included in the vector w which affects only the sensor output y.

Because of the form of the cost in Equations (18) and (27), the final result of this approach is a compensator which dissipates power at all frequencies, provided that the optimal $\mathcal{H}_\infty$ cost γ is less than unity. From Equation (8), power is dissipated provided that $\left[H^H(I + GH) + (I + GH)^H H\right]$ is negative definite. Using Equation (12), this is equivalent to $\left[H^H(K^{-1} + K^{-1^H})H\right]$ being positive definite, or $K^{-1}(j\omega) + K^{-1^H}(j\omega) > 0$ for all ω. This is precisely the requirement that K^{-1}, and therefore K be positive real[17]. Hence the approach generates a positive real compensator, which is guaranteed to be stabilizing for any positive real plant. From a mathematical perspective, the approach has replaced a phase constraint – that the compensator be positive real – with an equivalent magnitude constraint on another transfer function. The $\mathcal{H}_\infty$ approach guarantees satisfaction of the latter magnitude constraint, and therefore of the original phase constraint.

If there are any time delays, actuator or sensor dynamics, or if the actuator and sensor are not truly collocated and dual, then the structure will not be positive real at all frequencies. Stability can still be guaranteed if the complementary sensitivity is bounded above by the inverse of the difference of the true structure from the positive real condition as noted by Slater et al.[17].

State Space Computation

The calculation of the optimal compensator for the four-block problem is most easily performed in state space, using the formulae given in Reference 25. The first step then is to obtain a state space representation for the plant $G(s)$ and the desired weighting function $W_1(s)$. In general, the dereverberated mobility $G(s)$ will not be rational, and a rational approximation that is valid in the frequency range of interest must be found. This approximation can also be denoted $G(s)$ without confusion since only the approximation can be used in state space calculations.

From $W_1(s)$ and $G(s)$, state space representations for $W_2(s)$, $G_0(s)$, and $G_1(s)$ must be calculated. These problems can be formulated as spectral factorization problems, and solved by methods similar to those presented in Francis[24] or in Fuhrmann[22].

G_0 is a co-spectral factor of $M = G + G^\sim$, and thus can be calculated with the standard algorithm in Reference 24. The algorithm is restricted to systems G with a non-zero direct feedthrough term D. This is not a serious restriction, however. No finite-dimensional model is valid at all frequencies, nor does it need to be. This merely implies that rather than rolling off at high frequencies, $G(\infty)$ should be a constant.

First, define the state space representation of G as

$$G = \left[\begin{array}{c|c} A & B_2 \\ \hline C_2 & D_{22} \end{array} \right] = C_2 \left(sI - A \right)^{-1} B_2 + D_{22} \tag{31}$$

The reason for the selection of the subscripts on B, C, and D is that G is the (2,2) block of the four block problem.

16

G_0 can be represented as

$$G_0 = \left[\begin{array}{c|c} A & B_1 \\ \hline C_2 & D_{21} \end{array} \right] \qquad (32)$$

where

$$D = D_{22} + D_{22}^T \qquad (33)$$

$$A_{M^T}^\times = \left[\begin{array}{cc} A^T & 0 \\ 0 & -A \end{array} \right] - \left[\begin{array}{c} C_2 \\ -B_2^T \end{array} \right] D^{-1} \left[\begin{array}{cc} B_2 & C_2^T \end{array} \right] \qquad (34)$$

$$X_1 = Ric\left\{ A_{M^T}^\times \right\} \qquad (35)$$

$$B_1 = (B_2 + X_1 C_2^T) D^{-1/2} \qquad (36)$$

$$D_{21} = D^{1/2} \qquad (37)$$

The notation $X = Ric\{P\}$ indicates that X is the solution of the Riccati equation corresponding to the Hamiltonian matrix[24] P. That is, if

$$P = \left[\begin{array}{cc} A & -R \\ -Q & -A^T \end{array} \right] \qquad (38)$$

then $X = Ric\{P\}$ is the positive definite solution to

$$A^T X + XA + Q - XRX = 0 \qquad (39)$$

The conditions required for this spectral factorization to be valid are that $M = M^\sim$, which is clearly satisfied, that M and M^{-1} are proper, which is satisfied with non-zero D_{22}, that M have no poles or zeroes on the $j\omega$ axis, and that $M(\infty) > 0$. If G is dereverberated, then G has no imaginary poles, and thus M also has no imaginary poles. The remaining conditions are satisfied if G is strictly positive real, as is the case for the dereverberated driving point mobility of any structure.

The (1,2) block of the four-block problem (26) is $G_1 G_0^\sim$. This has the stable poles, but the non-minimum phase zeroes of $M = G + G^\sim$. This is a factorization of M, but it is not in the standard form. A modification to the standard algorithm is required, which is given in Appendix A. The result is

$$G_1(s)G_0(s) = \left[\begin{array}{c|c} A & B_2 \\ \hline C_1 & D_{12} \end{array} \right] \qquad (40)$$

17

where

$$A_M^\times = \begin{bmatrix} A & 0 \\ 0 & -A^T \end{bmatrix} - \begin{bmatrix} B_2 \\ -C_2^T \end{bmatrix} D^{-1} \begin{bmatrix} C_2 & B_2^T \end{bmatrix} \qquad (41)$$

$$X_2 = Ric\left\{-A_M^\times\right\} \qquad (42)$$

$$C_1 = D^{-1/2}(C_2 + B_2^T X_2) \qquad (43)$$

$$D_{12} = D^{1/2} \qquad (44)$$

Since the remaining (1,1) block $G_1 I$ of the four block problem is inner, it must be true that

$$D_{11} = 1 \qquad (45)$$

Then the four block problem (26) is completely specified.

The computation of the weighting function W_2 in Equation (29) from W_1 can also be represented in terms of a spectral factorization. This derivation is presented in Appendix B.

Examples

Bernoulli-Euler Beam

As an example of this approach, consider a free-free Bernoulli-Euler beam with a collocated force actuator and velocity sensor at one end. The dereverberated mobility for this system is simply that of a semi-infinite beam, which can be found for example from the wave approach of Reference 5:

$$G(s) = \frac{\sqrt{2}}{(\rho A)^{3/4}(EI)^{1/4}} \cdot \frac{1}{\sqrt{s}} \qquad (46)$$

For simplicity, assume the mass per unit length ρA and the bending stiffness EI are such that

$$G(s) = \frac{1}{\sqrt{s}} \qquad (47)$$

This can be done without loss of generality, as it requires only a scaling of the plant.

First, consider the unconstrained optimal compensator that extracts the maximum possible energy. From Equation (13),

$$K(s) = \sqrt{-s} \tag{48}$$

This compensator has a slope of 10 db/decade, and a phase of $-45°$ at all frequencies. As expected, it is noncausal and cannot be implemented. Note that this is the same compensator as that obtained by the unconstrained optimization in Reference 5, though the derivation differs, and in Flotow and Schäfer[8], by setting the reflection coefficient to zero.

Now, find the compensator that minimizes the maximum power flow into the structure. This can be done analytically, the solution is given in Reference 14. With equal weighting at each frequency, $(W_1 = 1)$ the optimal causal compensator is

$$K(s) = \sqrt{s} \tag{49}$$

This is similar to the noncausal solution, Equation (48), with the same magnitude everywhere, but a phase of $+45°$ instead. This is the "best" causal approximation to Equation (48), and extracts exactly half the power at all frequencies.

With velocity feedback, an appropriate choice of gain will add significant damping to a given mode, and those nearby, but it is not possible to add significant damping to all of the modes at the same time. Thus the gain in velocity feedback must be optimized to provide damping at a certain frequency. Far enough away from this frequency, the gain is either too low to have much affect, or too high so that the closed loop poles lie near the open loop zeroes, which are undamped. With the optimal causal compensator $\sqrt{s}$, although no poles are damped as heavily as the best pole with velocity feedback, every pole is given some damping.

Now consider including a weighting function to increase the importance of a certain frequency range, say in a narrow band near 1 rad/sec. So select the weighting function W_1 to have poles at $\frac{1}{2\sqrt{2}}$ and $2\sqrt{2}$, zeroes at $\frac{1}{\sqrt{2}}$ and $\sqrt{2}$, and unit magnitude far from 1 rad/sec, giving it less than unit magnitude near 1 rad/sec. Recall that more importance

is placed where the weighting function is smaller. An analytic solution here would be difficult. However, the plant in Equation (47) can be approximated adequately over a wide frequency range with a finite number of alternating poles and zeroes on the real axis, with equal logarithmic spacing. The state space methods described earlier can then be used to obtain an approximate compensator. For this example, Equation (47) was approximated by 9 poles and 9 zeroes on the negative real axis, between 10^{-4} and 10^4 rad/sec. The transfer function of this approximation matches the exact dereverberated mobility to within 2 degrees of phase and 0.25 db magnitude for 3 decades above and below the center frequency of the weighting function.

The resulting compensator is plotted in Figure 4, along with the optimal compensator with $W_1 = 1$ from Equation (49), and the unconstrained optimum from Equation (48). Far from the region that was selected as important, the compensator still has a $\sqrt{s}$ behavior, though with less magnitude than the unweighted optimum in Equation (49) resulting in poorer performance. Near 1 rad/sec, though, the slope of the compensator is now -10 db/decade, and the phase is closer to $-45°$. At 1 rad/sec, the compensator has exactly the same magnitude, and almost the same phase as the noncausal optimum, and thus it absorbs almost all the incoming power possible. The power flow absorbed by this compensator is plotted in Figure 5, expressed as a fraction of the available incoming power at each frequency. For comparison, the power absorbed by velocity feedback and the unweighted optimum are also plotted in the same figure.

If this control law is now applied to a finite beam, the closed loop performance can be examined. The transfer function between force and velocity at the far (uncontrolled) end of the beam can be calculated using the phase closure approach of Reference 21. The beam length was chosen so that the fifth mode of the beam was at the center frequency of the weighted region. The result is plotted in Figure 6, and the envelope of the transfer function for any length beam is also plotted. As expected, the modal peaks in the region where W_1 is smallest are more heavily damped. Note that because the compensator in Figure 4 is positive real, it will not destabilize the beam at any length. (Nor will it destabilize any positive real structure.) Furthermore, the performance is insensitive to the length of

the beam. For any length beam, there will be some damping achieved at all frequencies, and greater damping in the region of interest, as indicated by the envelope of possible transfer functions. Also note that although the modal information is not contained in the dereverberated mobility model of the structure, significant damping can still be added to the modes with a controller designed for this model.

Example 2: Pinned-Free Beam

As a slightly more complicated example, consider again a finite beam, but this time with one end pinned, with a moment actuator and collocated angular rate sensor at this end. Also include some finite rotational inertia J at this end. The theoretical dereverberated transfer function for this beam can be found in a straightforward manner using the wave approach of Reference 5 to be

$$\frac{\dot{y}'}{M} = \frac{s}{\sqrt{2}(\rho A)^{1/4}(EI)^{3/4}\sqrt{s} + Js^2} \tag{50}$$

At low frequencies, the behavior is the $\sqrt{s}$ behavior that would be the transfer function if there were no lumped rotational inertia. At high frequencies, the transfer function is dominated by the rotational inertia, and rolls off at 20 db/decade. From the far end of the beam, the controlled end then behaves as if it were clamped, and regardless of the control, all disturbances are reflected back. Thus, power flow beyond the rolloff frequency of Equation (50) should be unimportant, and the weighting function here should be much larger than elsewhere. Also, assume again that some specific frequency range near 1 rad/sec is more important.

For computation, $EI = \frac{1}{\sqrt{2}}$ and $\rho A = \frac{1}{\sqrt{2}}$, so that the low frequency behavior is $\sqrt{s}$, and $J = 10^{-3}$ to place the rolloff frequency at 100 rad/sec, at a slightly higher frequency than that considered to be important. Again, the system is approximated with a rational transfer function which is accurate over the frequency range of interest, from 10^{-4} to 10^4 rad/sec.

The $\mathcal{H}_\infty$ and unconstrained optimal compensators for this case are shown in Figure 7. At low frequencies, the $\mathcal{H}_\infty$ compensator is similar to the $\frac{1}{\sqrt{s}}$ that would be optimal with no

rotary inertia and no weighting. Where the weighting function decreases near 1 rad/sec, the phase jumps towards the unconstrained optimum phase of 45°, and thus absorbs close to the maximum power possible. At high frequencies, as desired, the compensator gives up and does not attempt to absorb incoming power, though it does remain positive real. Thus again, the closed loop system is stable for any length beam, and for any boundary condition at the far end. The open and closed loop transfer function from moment to slope rate at the controlled end of the beam is given in Figure 8. This transfer function shows the rolloff at 100 rad/sec, beyond which the poles and zeroes are essentially undamped, but almost cancel each other. The poles are more heavily damped near 1 rad/sec, but none of the zeroes are affected. Also plotted is the dereverberated mobility (Equation (50)), and the upper bound of the envelope of possible transfer functions for any length of beam.

Conclusions

In this paper an approach to broadband active damping of modally dense structures with significant uncertainty has been presented. A modal model for such a structure would be both inaccurate and unnecessarily large. Instead, the structure is modelled with its dereverberated mobility. For simple structures, this is equivalent to a local wave model, and can be calculated from such a model. For general structures, the dereverberated mobility can be calculated from an experimental or analytic transfer function using cepstral analysis, or by taking the logarithmic average of the transfer function. Ideally, a compensator that dissipates the most power possible at every frequency is desired. This compensator is in general noncausal, and cannot be implemented. A causal, guaranteed stabilizing, optimal compensator can be obtained by minimizing the maximum power flow into the structure. This problem is solved by reformulating it as an equivalent $\mathcal{H}_\infty$ control problem. This results in a positive real controller which dissipates power at all frequencies. The importance of a certain frequency range can be increased through use of a weighting function. The technique was demonstrated for several simple examples. At the frequency deemed most important, the compensator is close to the noncausal optimum, and dissipates almost all incoming power. It is expected that this approach to modelling and control

design will allow significant damping to be added to many modes of a structure, without the large effort in system identification, off-line computation, and compensator complexity that would be required of many control design techniques.

Appendix A: Modified Spectral Factorizations

A state space method is desired for calculating $G_1 G_0^{\sim}$, which has the stable poles, but the non-minimum phase zeroes of $M = G + G^{\sim}$. This is related to the spectral factorization algorithm found in Reference 24, and only the differences between the two will be indicated here.

Given G as Equation (31), then

$$M = G + G^{\sim} = \left[\begin{array}{cc|c} A & 0 & B_2 \\ 0 & -A^T & -C_2^T \\ \hline C_2 & B_2^T & D_{22} + D_{22}^T \end{array} \right] = \left[\begin{array}{c|c} A_M & B_M \\ \hline C_M & D \end{array} \right] \tag{51}$$

The spectral factorization algorithm in Reference 24 relies on finding the modal spaces $\mathbf{X}_-(A_M^{\times})$ and $\mathbf{X}_+(A_M)$ corresponding to the left half-plane zeroes of M and the right half plane poles respectively. Instead, now find $\mathbf{X}_+(A_M^{\times})$ and $\mathbf{X}_+(A_M)$, corresponding to right half plane zeroes and right half plane poles. If these two spaces are complementary, then the required factorization exists.

Since the unstable poles of any matrix A are the stable poles of $-A$,

$$\mathbf{X}_+(A_M^{\times}) = \mathbf{X}_-(-A_M^{\times}) \tag{52}$$

Thus the desired factorization exists if $\mathbf{X}_-(-A_M^{\times})$ and $\mathbf{X}_+(A_M)$ are complementary.

Since $A_M^{\times}$ is a Hamiltonian matrix, $-A_M^{\times}$ is as well. Thus, there exists a matrix

$$X_2 = Ric\left\{ -A_M^{\times} \right\} \tag{53}$$

such that

$$\mathbf{X}_-(-A_M^{\times}) = \text{Im} \left[\begin{array}{c} I \\ X_2 \end{array} \right] \tag{54}$$

23

and this is complementary to $\mathbf{X}_+(A_M)$. Given this, the remainder of the derivation follows Francis exactly, so that

$$G_1(s)G_0(s) = \left[\begin{array}{c|c} A & B_2 \\ \hline D^{-1/2}(C_2 + B_2^T X_2) & D^{1/2} \end{array} \right] \tag{55}$$

Appendix B: Calculation of W_2

As noted earlier, the computation of the weighting function W_2 in Equation (29) from W_1 can also be represented in terms of a spectral factorization. First, represent W_1 in state space as

$$W_1 = \left[\begin{array}{c|c} A_w & B_w \\ \hline C_w & D_w \end{array} \right] \tag{56}$$

Then

$$W_1^{\sim} = \left[\begin{array}{c|c} -A_w^T & -C_w^T \\ \hline B_w^T & D_w^T \end{array} \right] \tag{57}$$

Combining these gives

$$W_1 W_1^{\sim} = \left[\begin{array}{cc|c} A_w & 0 & B_w \\ -C_w^T C_w & -A_w^T & -C_w^T D_w \\ \hline -D_w^T C_w & -B_w^T & -D_w^T D_w \end{array} \right] \tag{58}$$

Define the similarity transformation

$$T = \left[\begin{array}{cc} I & 0 \\ X_w & I \end{array} \right] \tag{59}$$

where X_w satisfies the Lyapunov equation

$$A_w^T X_w + X_w A_w + C_w^T C_w = 0 \tag{60}$$

and use this to transform the system, Equation (58). This gives

$$W_1 W_1^{\sim} = \left[\begin{array}{cc|c} A_w & 0 & B_w \\ 0 & -A_w^T & -\overline{C}_w^T \\ \hline \overline{C}_w & -B_w^T & -D_w^T D_w \end{array} \right] \tag{61}$$

24

where

$$\overline{C}_w = B_w^T X_w + D_w^T C_w \tag{62}$$

Then W_2 is a spectral factor of

$$I - W_1 W_1^{\sim} = \left[\begin{array}{cc|c} A_w & 0 & B_w \\ 0 & -A_w^T & \overline{C}_w^T \\ \hline -\overline{C}_w & -B_w^T & I - D_w^T D_w \end{array} \right] \tag{63}$$

This is now in the form of a standard spectral factorization. In order to apply the algorithm, W_1 must satisfy

$$1 - D_w^T D_w > 0 \tag{64}$$

or $W_1(\infty) < 1$. This is not a limitation at all, since multiplying the weighting function everywhere by a constant will not change the resulting compensator. The other conditions specified in the definition of the spectral factorization are also satisfied, provided W_1 has no imaginary poles. Note that if the magnitude of W_1 is less than one at all frequencies, then $1 - W_1 W_1^{\sim}$ can have no imaginary zeroes.

Acknowledgements

References

[1] Balas, M. J., "Trends in Large Space Structure Control Theory: Fondest Hopes, Wildest Dreams," *IEEE Transactions on Automatic Control,* Vol. AC-27, No. 3, June 1982, pp. 522-535.

[2] Doyle, J. C. and Stein, G., "Multivariable System Design: Concepts for a Classical/Modern Synthesis," *IEEE Transactions on Automatic Control,* Vol. AC-26, No. 1, Feb. 1981, pp. 4-16.

[3] Bernstein, D. S. and Hyland, D. C., "Optimal Projection for Uncertain Systems (OPUS): A Unified Theory of Reduced Order, Robust Control Design," in *Large Space Structures: Dynamics and Control*, Atluri and Amos (ed.), Springer-Verlag, 1988, pp. 263-302.

[4] Doyle, J. C., "Analysis of Feedback Systems with Structured Uncertainties," *IEE Proceedings*, Vol. 129, Part D, No. 6, Nov. 1982, pp. 242-250.

[5] Miller, D. W., Hall, S. R. and von Flotow, A. H., "Optimal Control of Power Flow at Structural Junctions," *Proceedings of the 1989 American Control Conference*, Pittsburgh, PA, June 1989.

[6] Miller, D. W., and Hall, S. R., "Experimental Results Using Travelling Wave Power Flow Techniques," *Proceedings of the Winter Annual Meeting of the ASME*, AD-Vol. 15, San Francisco, CA, Dec. 1989, pp. 35-42.

[7] von Flotow, A. H., "The Acoustic Limit of Structural Dynamics," in *Large Space Structures: Dynamics and Control*, Atluri and Amos (ed.), Springer-Verlag, 1988, pp. 213-238.

[8] von Flotow, A. H., and Shäfer, B., "Wave-Absorbing Controllers for a Flexible Beam," *Journal of Guidance, Control, and Dynamics*, Vol. 9, No. 6, Nov.-Dec. 1986, pp. 673-680.

[9] Mace, B. R. "Active Control of Flexural Vibrations," *Journal of Sound and Vibration*, Vol. 114, 1987, pp. 253-270.

[10] Hagedorn, P., and Schmidt, J. T., "Active Vibration Damping of Flexible Structures Using the Travelling Wave Approach," *Proceedings of the Second International Symposium on Spacecraft Flight Dynamics*, Darmstadt, FR Germany, Oct. 1986, see also ESA SP-255, Dec. 1986.

[11] Redman-White, W., "Experiments on the Active Control of Flexural Wave Power Flow," *Journal of Sound and Vibration*, Vol. 112, 1987, pp. 187-191.

[12] Scheuren, J., "Active Control of Bending Waves in Beams," *Internoise,* Munich, Sept. 1985, pp. 591-594.

[13] Aubrun, J-N., "Theory of the Control of Structures by Low-Authority Controllers," *Journal of Guidance and Control,* Vol. 3, No. 5, Sept-Oct 1980, pp. 444-451.

[14] MacMartin, D. G., *An $\mathcal{H}_\infty$ Power Flow Approach to Control of Uncertain Structures,* S.M. Thesis, Department of Aeronautics and Astronautics, M.I.T., Cambridge, MA, Feb. 1990.

[15] MacMartin, D. G., and Hall, S. R., "Structural Control Experiments Using an $\mathcal{H}_\infty$ Power Flow Approach," submitted to *1990 AIAA Guidance Navigation and Control Conference.*

[16] Lyon, R. H., *Machinery Noise and Diagnostics,* Butterworth Publishing, June 1987.

[17] Slater, G. L., Zhang, Q., and Bosse, A., "Robustness with Positive Real Controllers for Large Space Structures," *Proceedings of the 1989 AIAA Guidance, Navigation, and Control Conference,* Boston, MA, August 1989, pp. 932-941.

[18] Hodges, C. H. and Woodhouse, J., "Theories of Noise and Vibration Transmission in Complex Structures," *Reports on Progress in Physics,* Vol. 49, 1986, pp. 107-170.

[19] Skudrzyk, E. "The Mean-value Method of Predicting the Dynamic Response of Complex Vibrators," *Journal of the Acoustical Society of America,* Vol. 67, No. 4, April 1980, pp. 1105-1135.

[20] Bernstein, D. S. and Haddad, W. M. "LQG Control with an $\mathcal{H}_\infty$ Performance Bound: A Riccati Equation Approach," *IEEE Transactions on Automatic Control,* Vol. 34, No 3, March 1989, pp. 293-305.

[21] Miller, D. W., "Power Flow in Structural Networks," *Journal of Sound and Vibration,* Vol. 128, 1989, pp. 145-162.

22 Fuhrmann, P. A., "Elements of Factorization Theory From a Polynomial Point of View," in *Three Decades of Mathematical System Theory*, Nijmeijer and Schumacher (ed.), Springer-Verlag, 1989, pp. 148-178.

23 Van Valkenburg, M. E., and Kinariwala, B. K., *Linear Circuits*, Prentice-Hall, 1982, pp. 297-298.

24 Francis, B. A., *A Course in $\mathcal{H}_\infty$ Control Theory*, Springer-Verlag, 1987.

25 Doyle, J. C., Glover, K., Khargonekar, P. P., and Francis, B. A., "State-Space Solutions to Standard $\mathcal{H}_2$ and $\mathcal{H}_\infty$ Control Problems," *IEEE Transactions on Automatic Control*, Vol. 34, No. 8, Aug. 1989, pp. 831-847.

Figure 1: Arbitrary structure

Figure 2: Calculation of dereverberated admittance from complex cepstrum.
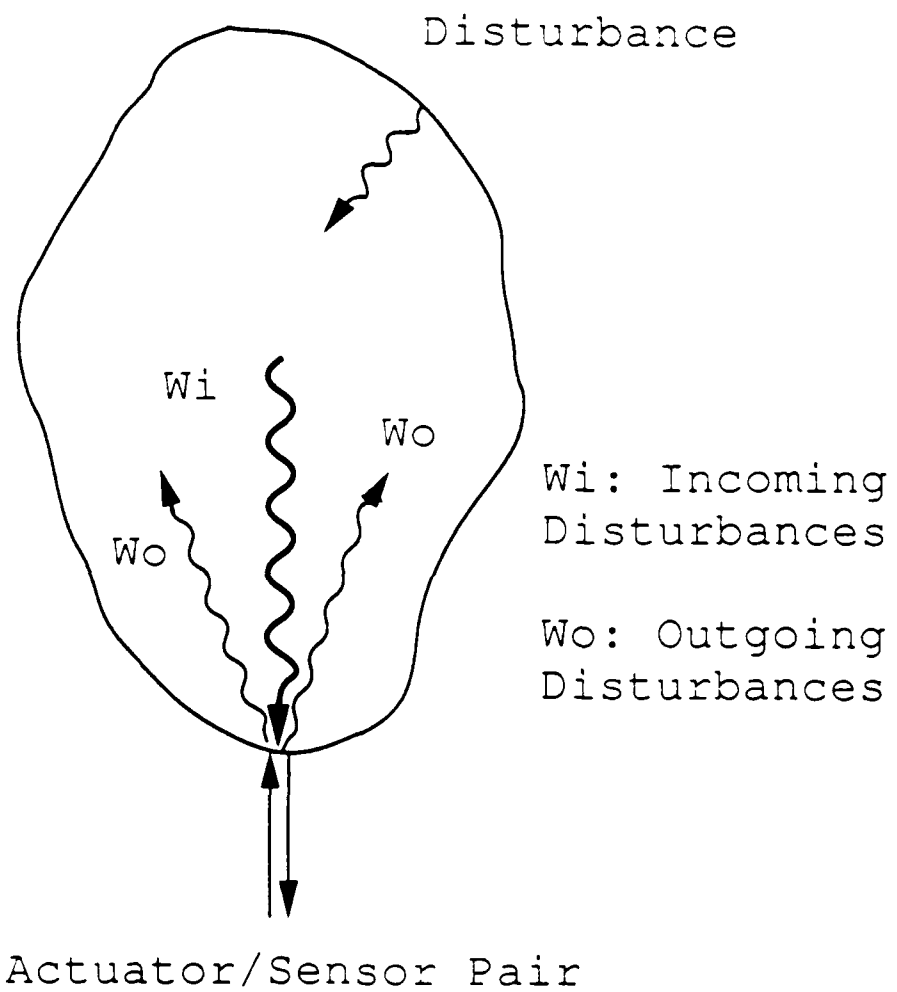
Figure 3: System block diagram.

Figure 4: Optimal compensator for Example 1 with weighting at 1 rad/sec (a), with no weighting (b), and unconstrained (c).

Figure 5: Power absorption for unconstrained optimum (a), velocity feedback (b), unweighted $\mathcal{H}_\infty$ design (c), and weighted $\mathcal{H}_\infty$ design (d).
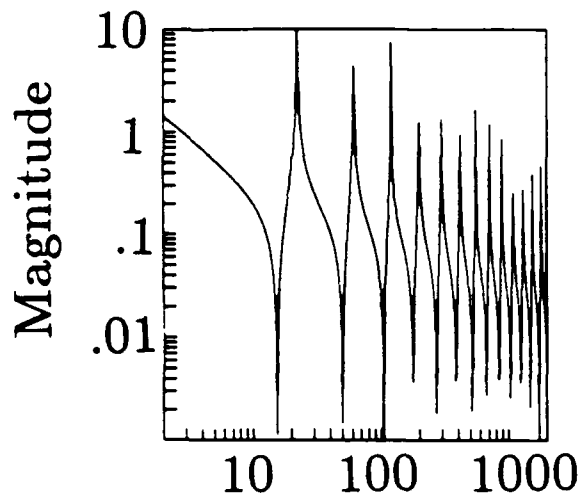
Figure 6: Closed loop transfer function at far end of free-free beam.

Figure 7: Optimal compensator for Example 2 with $\mathcal{H}_\infty$ design (a) and unconstrained (b).
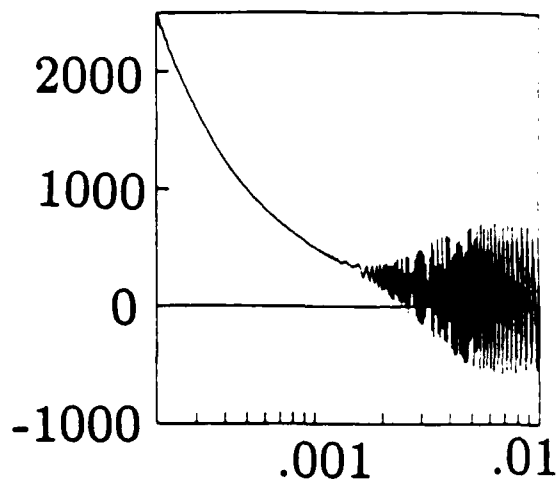
Figure 8: Closed loop transfer function at controlled end of pinned-free beam (a), dereverberated admittance (b), and envelope of possible transfer functions (c).
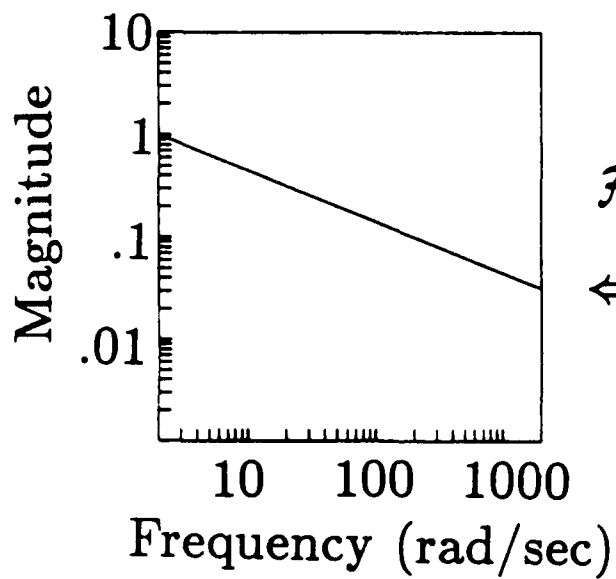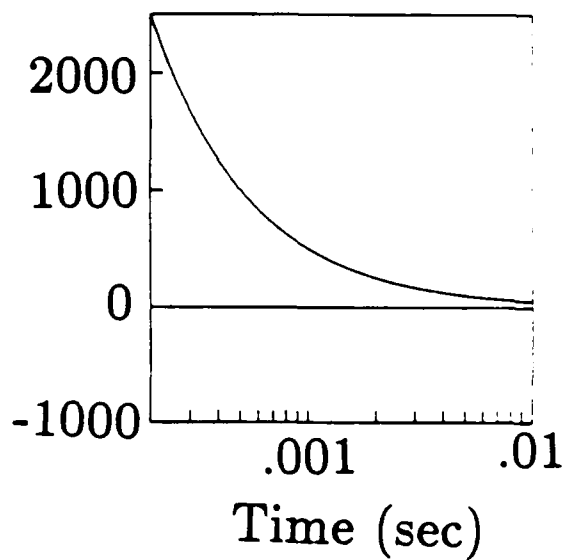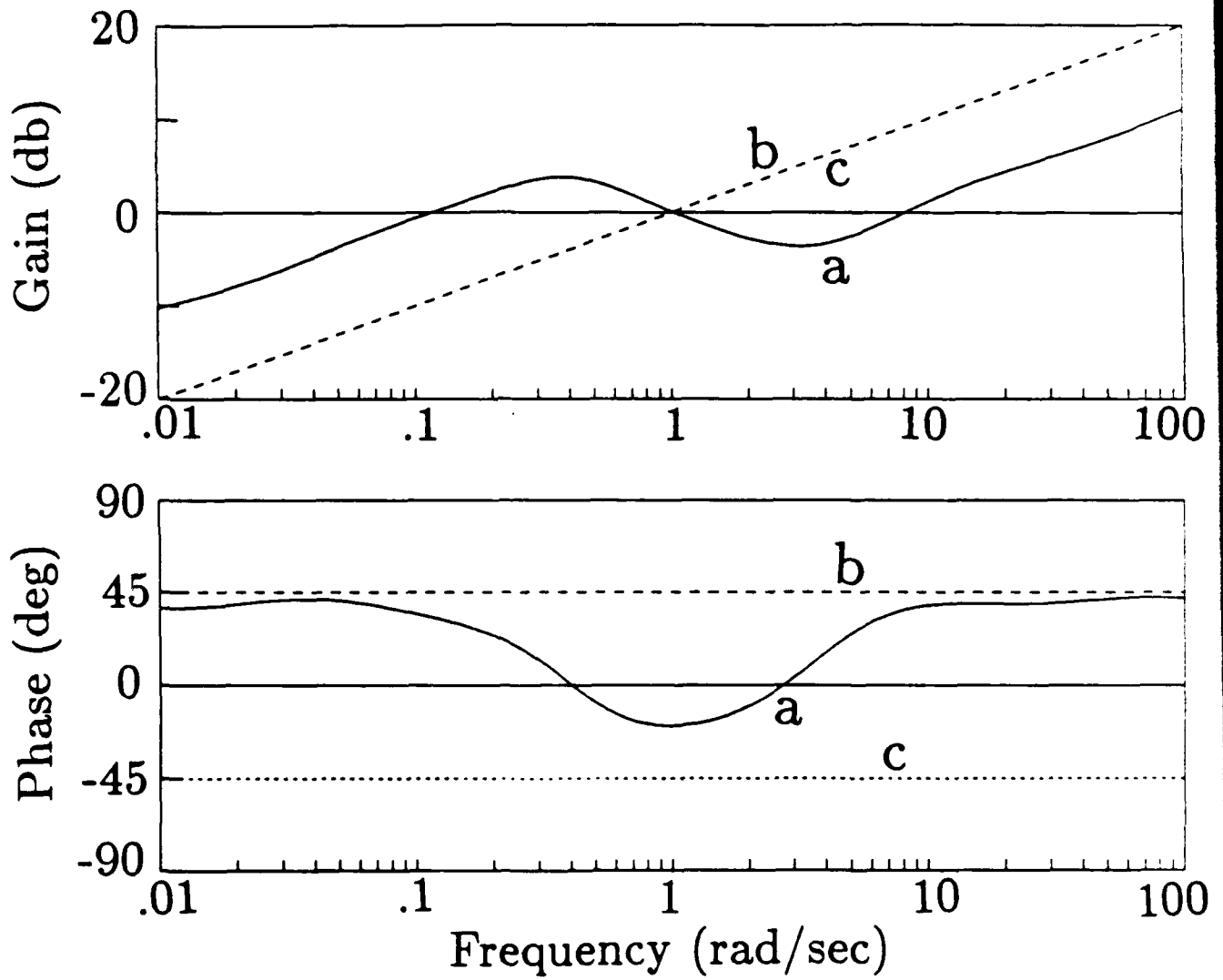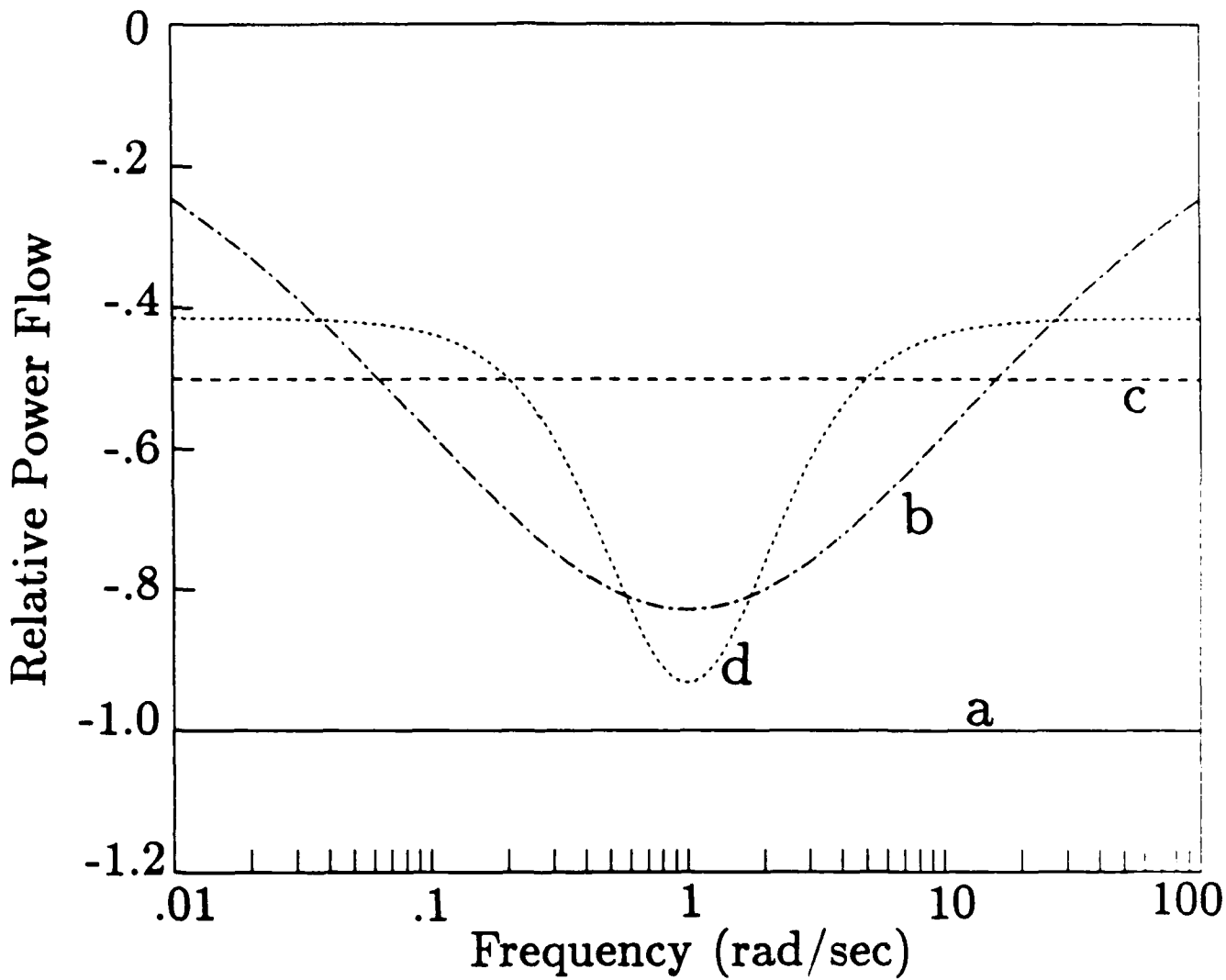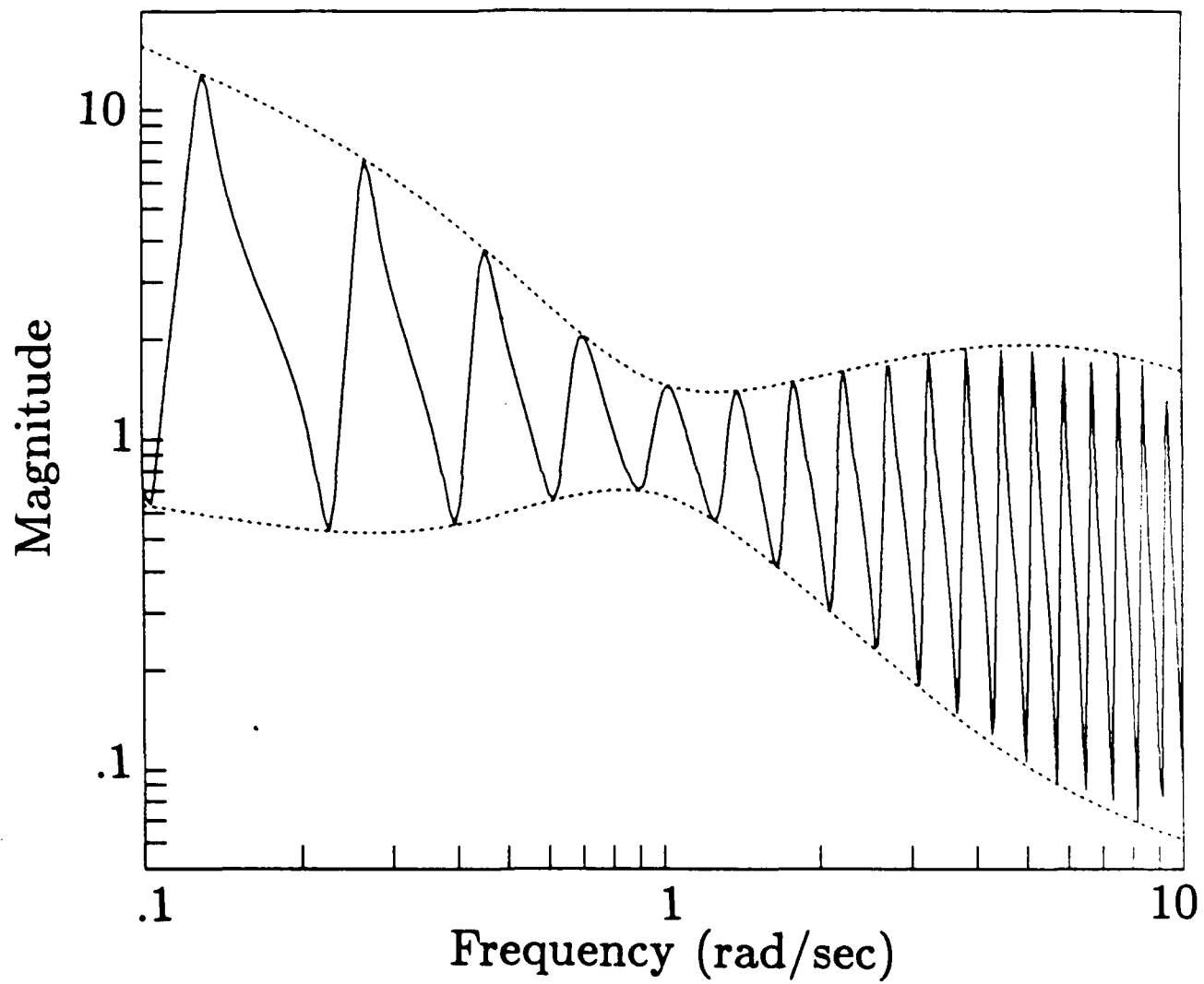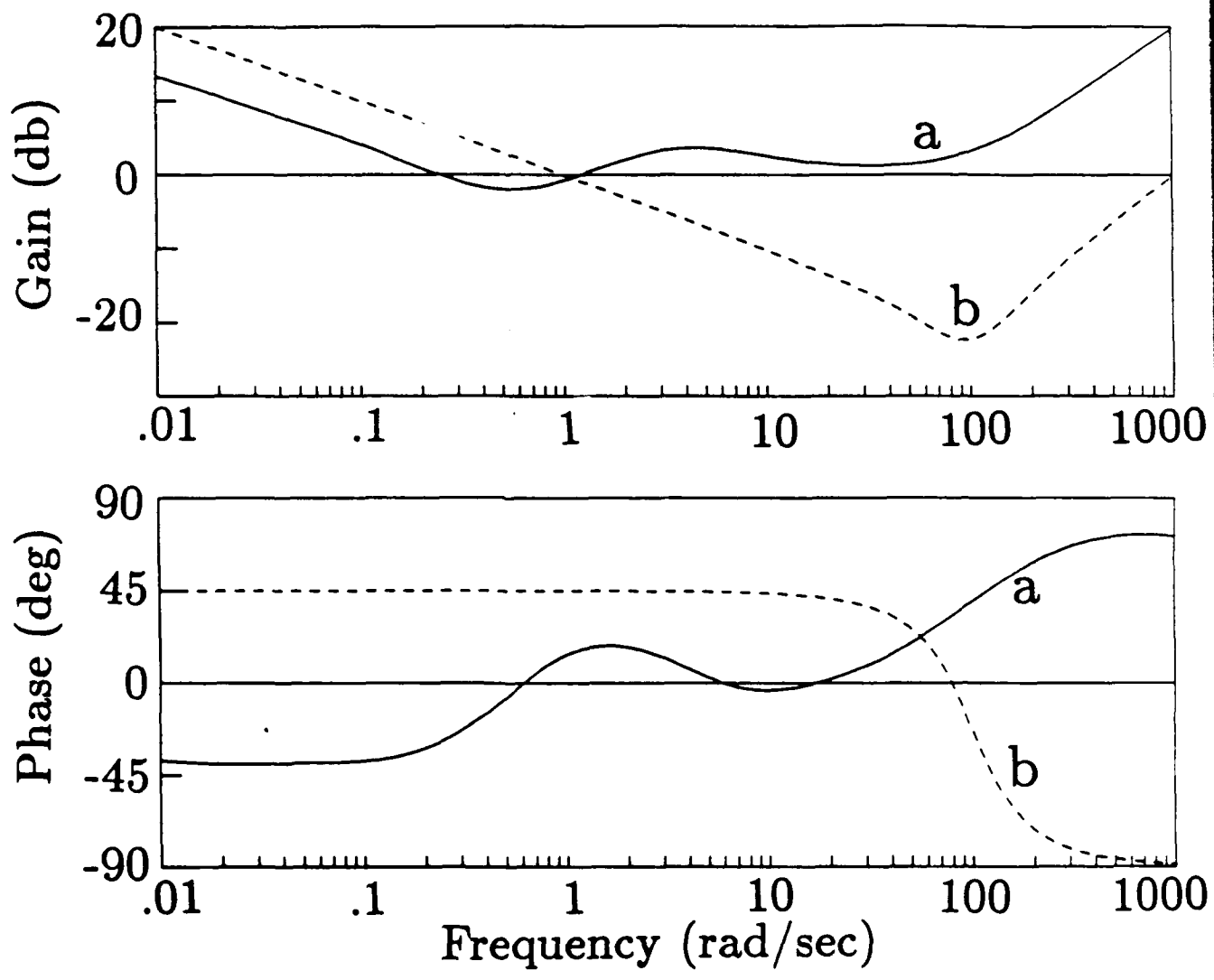
Disturbance

Wi

Wo

Wo

Wi: Incoming
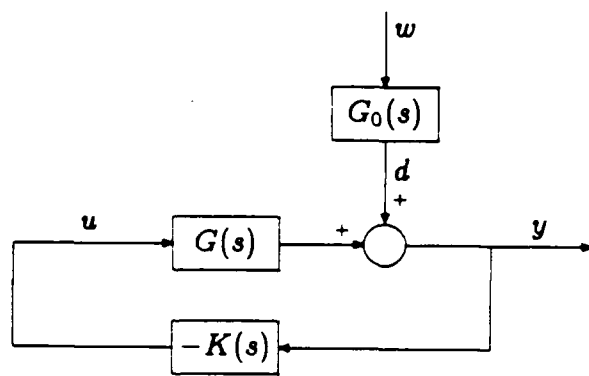Disturbances

Wo: Outgoing
Disturbances

Actuator/Sensor Pair

Magnitude

$\mathcal{F}^{-1}$
$\Rightarrow$

10

1

.1

.01

10   100   1000

$\Downarrow$ Direct Field

2000

1000

0

-1000

.001   .01

Magnitude

10

1

.1

.01

10   100   1000

Frequency (rad/sec)

$\mathcal{F}$
$\Leftarrow$

2000

1000

0

-1000

.001   .01

Time (sec)
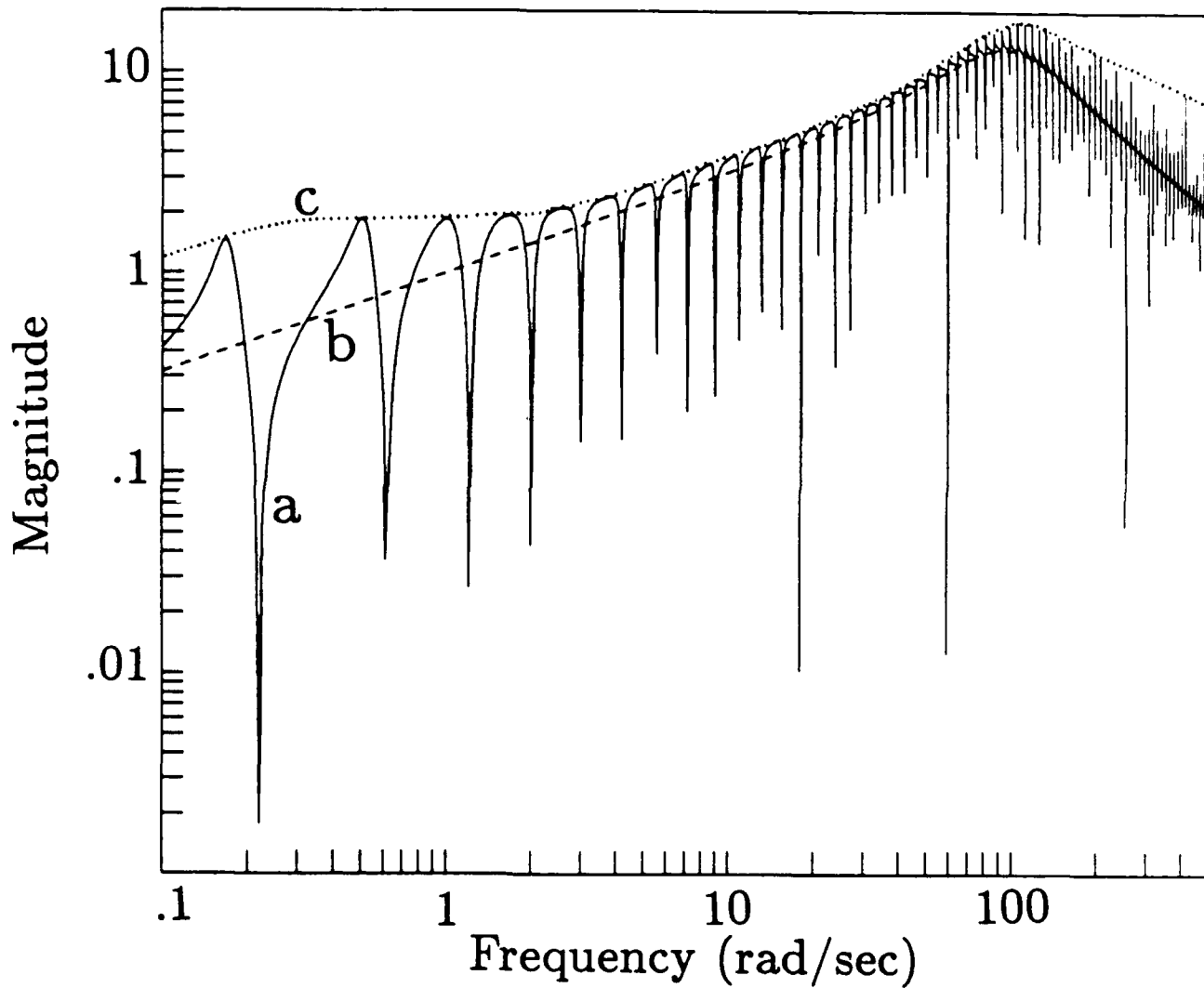
Structural Control Experiments Using An $\mathcal{H}_\infty$ Power Flow Approach

Douglas G. MacMartin,* Steven R. Hall[†]
Space Engineering Research Center
Department of Aeronautics and Astronautics
Massachusetts Institute of Technology

Abstract

Experimental results are presented comparing velocity feedback with a new technique for designing guaranteed stable control laws for uncertain, modally dense structures with collocated sensors and actuators. A dereverberated mobility model is used, which is similar in many respects to a wave based model, but can treat more general structures. The power dissipated by the controller can be maximized in either an $\mathcal{H}_2$ or an $\mathcal{H}_\infty$ sense. The $\mathcal{H}_\infty$ approach guarantees that the controller is positive real, and thus that the system will remain stable for any uncertainty, provided that the power flow is correctly modelled. The experimental results indicate that the controllers designed with this approach are much more effective than simple collocated rate feedback.

Introduction

Broadband active control of flexible structures is difficult for several reasons. Structures tend to be very lightly damped, modally rich, and difficult to model in detail, due to their large sensitivity to parameter variations. For many applications, there are likely to be many flexible modes within the desired bandwidth of a structural control system,[1] and these modes are likely to be poorly known. Models of structures with closely spaced modes in particular tend to be extremely sensitive to small parameter changes, in their prediction of natural frequencies, and especially in their prediction of mode shapes.

Typically, structural modelling is done with state space based methods, which were originally applicable only for structures with a few flexible modes in the bandwidth. Various tools have been developed in an attempt to increase both the number of modes within the bandwidth, and the extent of uncertainty that the control design techniques are capable of dealing with. Alternatively, an acoustic approach, suitable

for modally dense structures could be used. With this philosophy, there has been much research on the use of wave based models for use in structural control, see for example References 2,3,4,5, and the references therein. Here the assumption is that the local dynamics can be accurately modelled, and that an effective control system can be derived based only on this information. A more general approach with similar philosophy is to use the dereverberated driving point mobility of the structure.[6,7] Only that part of the response which is due to the local dynamics is retained in the model. This model will be discussed briefly in the next section.

The control design approach must be suitable for the local model being used. Of particular relevance here are the optimal control approaches of Miller *et al.*,[2] and of MacMartin and Hall.[6,7] Using Wiener-Hopf techniques to ensure causality, Miller *et al.* maximize the frequency weighted power dissipation associated with the control. The drawback to this approach is that it will allow power to be generated at some frequencies in order to achieve greater power dissipation at other frequencies, potentially destabilizing the structure. Since the driving point mobility of a structure is positive real, stability can be guaranteed by requiring that the compensator be positive real. Approximating the optimal compensator with a positive real form thus guarantees a stable closed loop, but is suboptimal, because the positive real constraint is applied in a somewhat *ad hoc* manner. MacMartin and Hall[6] minimise the maximum value over frequency of the power flow into the structure, resulting in power dissipation at all frequencies, and a positive real compensator. This approach will be summarized in Section 3, and parallels with the technique of Reference 2 will be illustrated. Indeed, it is possible to solve the frequency weighted power dissipation problem of Reference 2 in state space, using some of the results developed in Reference 6.

Experiments were performed on a pinned free beam in bending, using a torque motor and collocated angular rate sensor at the pinned end of the beam. The experimental results verify the performance that can be achieved by modelling the structure with its dereverberated mobility, and minimizing the worst case

*Research Assistant. Room 37-367, MIT, Cambridge, MA 02139. Student Member AIAA.
[†]Boeing Assistant Professor of Aeronautics and Astronautics. Room 33-103, MIT, Cambridge, MA 02139. Member AIAA.

power flow. Several compensators are designed with this approach, and their performance is compared with that of velocity feedback. Previous experiments on the same structure have demonstrated the $\mathcal{H}_2$ wave approach of Miller et al.[3]

Modelling

This section reviews the dereverberated mobility model for control design for uncertain modally dense systems.[6] A modal model may not be useful in this case, since the detailed information it contains is often incorrect, and may also be unimportant. In the presence of significant uncertainty, the modal information may be uncertain, but the local dynamics near an actuator can still be well modelled. The dynamics of the structure between an actuator and sensor which are separated by many wavelengths of the disturbance are, however, unknown due to the uncertain phase. Thus for broadband control, it is reasonable to require that feedback only be used between collocated sensors and actuators.

For some arbitrary structure, as shown in Figure 1, insight into the nature of the problem can be obtained from a wave perspective. Various disturbances are created at certain points in the structure and propagate through it. At any point in the structure, such as at an actuator, the disturbance will be scattered. In general, each of the resulting outgoing disturbances will eventually affect any global cost criterion. Thus from the perspective of the actuator, without a detailed and accurate description of how each wave propagates, its goal should be to minimize the energy of each of these outgoing disturbances. Since the scattering behavior is a function of only the local dynamics, this goal can be achieved with only a local model of the structure.

One approach to obtaining such a model is through the use of waves. However, it may be difficult to obtain a useful wave description for many complicated structures. An alternative to the wave approach for obtaining a local model is to represent the structure by its dereverberated driving point mobility.[8] The driving point mobility is the transfer function between two variables whose product is the power flow into the structure. The response at a point can be considered to be the sum of two parts: a *direct field*, due to the local dynamics; and a *reverberant field*, which is caused by energy reflected back from other parts of the structure. The term "dereverberated" implies that the "reverberant" part of the response has been removed before computing the mobility.

One method by which the dereverberated mobility may be approximated is through the use of the cepstrum[8] of the impulse response. This procedure involves taking the inverse Fourier transform of the log of the complex spectrum, windowing this to remove the reverberant part, and transforming back to the
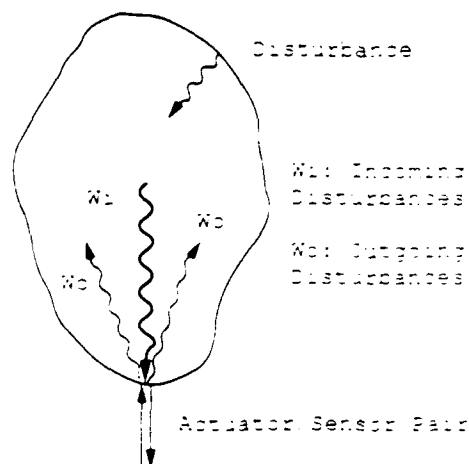

Figure 1: Wave behavior in an arbitrary structure

frequency domain to yield the dereverberated impulse response. A simpler approach is based on the observation that neglecting the reverberant field is equivalent to replacing the log magnitude of the original transfer function with its mean.[9,10] Thus another way to compute the dereverberated mobility is simply to take a logarithmic average of the transfer function, with the phase being determined uniquely from the fact that the dereverberated driving point mobility is positive real. In practice, this method should be adequate. Fitting the result with a rational polynomial gives a model that captures the essential dynamics of the system over a wide frequency range that encompasses many modes, with only a small number of poles and zeroes.

This approach can be easily applied to arbitrarily complex structures, since all that is needed is the input/output behavior at the driving point, which may be found from experimental data, calculated from some nominal model, or found analytically, perhaps even from a wave model. Indeed, for simple structures such as the beam in bending used in the experiment, the resulting model is equivalent to the local wave model of Reference 2.

Control Design

The previous section summarized the modelling approach used, while this section examines the design of the control system for this model. All of the techniques that will be examined rely on an optimization of the power flow, maximizing in an appropriate sense the dissipation associated with the control system. For a lightly damped system, the power flow gives a measure of both the performance achieved, and the degree of stability.

Miller et al.[2] minimized the $\mathcal{H}_2$ norm of the power flow, using a Wiener-Hopf procedure. The same problem can be solved in state space using a Linear-Quadratic-Gaussian (LQG) algorithm. In either case,

some assumptions are required about the power spectral density of the disturbance entering the junction. In the actual structure, this is related to the control action through the disturbance that previously departed the junction. With only a local model, however, it is assumed constant and independent of the control, and thus the resulting compensator may allow power to be added at some frequencies. This problem can be avoided by minimizing the power flow in an $\mathcal{H}_\infty$ setting. For the open-loop system, the power removed by the controller at each frequency is zero, and the closed loop is guaranteed to be no worse.

Define $G(s)$ to be the dereverberated driving point mobility, and assume some disturbance input d to be additive at the output. Then the output y is related to the input u and the disturbance via

$$y(s) = G(s)u(s) + d(s) \qquad (1)$$

The disturbance d in this equation can be thought of as originating from two sources: the original disturbance input to the real structure, and the reverberant field ignored in the modelling process.

The instantaneous power flow into the structure is the product of the input $u(t)$ and the output $y(t)$, since $G(s)$ is a mobility. The average power flow can be expressed as a time integral of the instantaneous power flow,[11] and making use of Parseval's theorem, this can be transformed into the frequency domain:

$$P_{ave} = \lim_{T \to \infty} \frac{1}{2T} \int_{-T}^{T} y(t)^T u(t)\, dt \qquad (2)$$

$$= \frac{1}{2} \int_{-\infty}^{\infty} \left(u(j\omega)^H y(j\omega) + y(j\omega)^H u(j\omega) \right) \frac{d\omega}{2\pi} \qquad (3)$$

The integrand in Equation (3) represents the steady state, or average, power flow into the structure as a function of frequency.[11] For convenience, the average power flow at each frequency can be defined without the factor of $\frac{1}{2}$ as

$$\mathbb{P}(\omega) = u(j\omega)^H y(j\omega) + y(j\omega)^H u(j\omega) \qquad (4)$$

The control law is assumed to be of the form

$$u(s) = -K(s)y(s) \qquad (5)$$

Solving for the control in terms of the disturbance from Equation (1) gives

$$u = -(I + KG)^{-1} K d \qquad (6)$$
$$= H d \qquad (7)$$

where the explicit dependence on the Laplace transform variable has been dropped. From these equations, the equivalent feedback K is related to the disturbance feedforward H via

$$K = -H(I + GH)^{-1} \qquad (8)$$

Using Equations (1), (6) and (7), then Equation (4) yields that the average power flow at each frequency is

$$\mathbb{P}(\omega) = d^H \left\{ H^H(I + GH) + (I + GH)^H H \right\} d \qquad (9)$$

Since the power flow is a scalar, it is equal to its trace. The expected value of the power flow at each complex frequency can then be written in terms of the power spectral density of the disturbance, $\Phi_{dd} = \mathrm{E}\left[dd^H\right]$, as

$$\mathrm{E}(\mathbb{P}(\omega)) = \mathrm{Tr}\left\{ \Phi_{dd} \left[H^H(I + GH) + (I + GH)^H H \right] \right\} \qquad (10)$$

Unconstrained Optimum

The simplest optimization approach is to minimize the power flow at each value of the Laplace transform variable s. Equation (10) is only valid on the $j\omega$ axis, and must first be extended analytically to the remainder of the complex plane. The analytic continuation of the Hermitian operator is the *parahermitian conjugate*,[12] denoted $(\cdot)^\sim$, and defined as

$$F^\sim(s) = F(-s)^T \qquad (11)$$

Since $F^\sim(j\omega) = F^H(j\omega)$, this notation will be used in place of the Hamiltonian operator throughout the rest of the paper. Optimizing the expected power flow at each point in the complex plane yields

$$K_{opt} = (G^\sim)^{-1} \qquad (12)$$

which is independent of the disturbance spectrum Φ_{dd}.

This compensator extracts the maximum possible power from the structure at every frequency. This result is not new; it corresponds to the impedance matching condition found, for example, in Reference 13. The maximum energy dissipation is obtained if the impedance of the compensator is the complex conjugate of the impedance of the load, which in this case is the rest of the structure.

Unless the dereverberated mobility is a constant, however, the compensator in Equation (12) is non-causal, and cannot be implemented. If this compensator could be implemented, all the poles could be moved arbitrarily far into the left half plane. Instead, the best causal compensator must be found.

Causal Optimum – $\mathcal{H}_\infty$ Approach

To guarantee dissipation at all frequencies, the worst case power dissipation will be minimized over the set of causal compensators, hence a minimax optimization of the power flow into the structure. This can be cast as an $\mathcal{H}_\infty$ minimisation problem. First, however, the disturbance should be normalised to provide the same amount of power available to be dissipated at each frequency. This provides the designer with complete control over the relative importance of one frequency
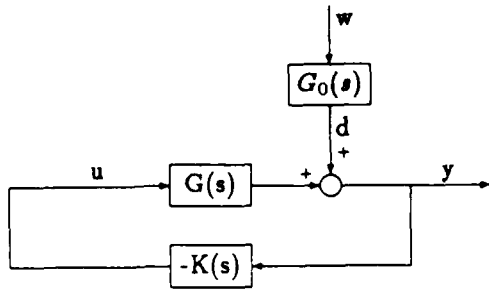
Figure 2: System block diagram

range to another, by removing any inherent frequency weighting from the problem.

With the optimal noncausal compensator from Equation (12), the closed loop power flow into the structure is

$$\mathbb{P} = -d^{\sim}(G + G^{\sim})^{-1}d \qquad (13)$$

Introduce a scaled disturbance w related to the original disturbance d via

$$d = G_0 w \qquad (14)$$

Then if the input w has unit magnitude at a certain frequency, the optimal noncausal compensator will dissipate unit power at this frequency, provided that the transfer function G_0 is the co-spectral factor of $G + G^{\sim}$, given by

$$G_0 G_0^{\sim} = G + G^{\sim} \qquad (15)$$

The block diagram for the resulting system is shown in Figure 2, and the system (Equation (1)) becomes

$$y(s) = G(s)u(s) + G_0(s)w(s) \qquad (16)$$

Now, consider the problem of finding a causal compensator that will minimize the worst case power flow in Equation (4). This quantity represents the power flow into the structure, which will be negative for any stabilizing (energy absorbing) controller. In order to cast this as an $\mathcal{H}_\infty$ optimization, however, the performance index must be positive definite. Since the best causal compensator can dissipate no more power than the noncausal optimum, positive definiteness will be assured if the disturbance power $w^{\sim}w$ is added to the cost. Thus the cost at each frequency is

$$\begin{aligned}\mathrm{Cost}(\omega) &= w^{\sim}w + u^{\sim}y + y^{\sim}u \qquad (17)\\ &= |G_0^{\sim}u + w|^2\\ &= |G_1 G_0^{\sim}u + G_1 w|^2 \qquad (18)\end{aligned}$$

where

$$G_1(s) = \frac{\Delta(G_0^{\sim}(s))}{\Delta(G_0(s))} \qquad (19)$$

and $\Delta(\cdot)$ is the characteristic polynomial of the transfer function $(\cdot)$. The inner function G_1 does not change

the cost, and is included to give a representation of the cost in terms of stable transfer functions.

From Equation (18), the relevant output that should be minimized is

$$z = G_1 G_0^{\sim}u + G_1 w \qquad (20)$$

Combining this with the system equation (16), the result can be written as a standard $\mathcal{H}_\infty$ problem:[14]

$$\left\{ \begin{array}{c} z \\ y \end{array} \right\} = \left[\begin{array}{cc} G_1 I & G_1 G_0^{\sim} \\ G_0 & G \end{array} \right] \left\{ \begin{array}{c} w \\ u \end{array} \right\} \qquad (21)$$

The compensator from y to u that minimizes the $\mathcal{H}_\infty$ norm of the transfer function from w to z will minimize the maximum power flow into the structure.

In general, it may be desirable to weight some frequency ranges more heavily than others, while still requiring that power be removed at all frequencies. This could be because there is a known disturbance source in a certain range, because structural modes are less well damped within this range, or because the performance requirements put more emphasis on this range. Similarly, there will usually be some frequency beyond which performance is not required, and the weighting can also be chosen to reflect this. Rather than weighting the sum of the disturbance input power and the power input by the control, as in Equation (17), the cost is defined to be the sum of the disturbance power and some frequency weighted control input power, as

$$\mathrm{Cost}(\omega) = w^{\sim}w + W_1^{\sim}(u^{\sim}y + y^{\sim}u)W_1 \qquad (22)$$

This can again be factored as $\mathrm{Cost}(\omega) = |z|^2$ and therefore written as a standard $\mathcal{H}_\infty$ problem.[6]

The calculation of the optimal compensator for the $\mathcal{H}_\infty$ problem is most easily performed in state space.[15] The algorithms for computing G_0, $G_1 G_0^{\sim}$, and W_2 are given in References 6 and 7. Each of these problems is related to a spectral factorization, the solution to which can be found from a Riccati or Lyapunov equation.[14]

Causal Optimum – $\mathcal{H}_2$ Approach

For structures for which the local wave model of Miller et al.[2] can be identified, this model can be represented in the form of Equation (1). The $\mathcal{H}_2$ power flow minimization in Reference 2 was constrained to be causal using a Wiener-Hopf[16] approach. A similar Wiener-Hopf solution can be found in the current framework.

First, introduce the notation

$$\begin{aligned}\Phi &= \Phi_R \Phi_L \qquad (23)\\ \Phi &= \Phi_+ + \Phi_- \qquad (24)\end{aligned}$$

for the right half plane analytic and left half plane analytic factors of Φ, and the positive and negative time

parts of Φ respectively. Both of these types of spectral factorisations can be solved in state space with the solution to a Riccati or Lyapunov equation.[14]

With disturbance feedforward $u = Hd$, the frequency weighted power flow being minimized is given by Equation (10) as

$$J = \int_{-\infty}^{\infty} \{\Phi_{dd}[H^\sim(I + GH) + (I + GH)^\sim H]\}\, d\omega \tag{25}$$

The first order variation in J with respect to H is

$$\delta J = 2 \int_{-\infty}^{\infty} \delta H^\sim ((G + G^\sim)H + I)\, \Phi_{dd}\, d\omega \tag{26}$$

This should be zero for all admissible variations $\delta H^\sim$. To insure causality, δH must be right half plane analytic (RHPA), and then Equation (26) is zero provided that

$$((G + G^\sim)H + I)\, \Phi_{dd} = a_L \tag{27}$$

for some arbitrary left half plane analytic (LHPA) function a_L. Solving for the RHPA compensator that satisfies Equation (27) yields the optimal disturbance feedforward compensator as

$$H = -(G + G^\sim)_R^{-1} \left[(G + G^\sim)_L^{-1} (\Phi_{dd})_R\right]_+ (\Phi_{dd})_R^{-1} \tag{28}$$

from which the feedback law $u = -Ky$ can be determined via Equation (8). Note that the quantity $(G + G^\sim)_R$ in this equation is precisely G_0 from Equation (15).

Miller et al.[2] specify the power spectral density of the incoming wave modes, while this solution requires the power spectral density of the disturbance d. The disturbance d is the disturbance in the generalized velocity caused by both the incoming and outgoing wave modes. Thus

$$d = (j\omega)T(Y_{ui} + Y_{uo}S)w_i \tag{29}$$

Y_{ui} and Y_{uo} are partitions of the transformation matrix from wave mode variables to physical variables, with Y_{ui} relating the displacement vector u to the incoming wave mode vector w_i, and Y_{uo} relating u to the outgoing wave modes w_o. S is the scattering matrix of the junction relating outgoing wave modes to incoming wave modes. The matrix T is present to select the appropriate elements of the displacement vector u corresponding to each element of the disturbance d, and the factor of $j\omega$ is required since d is a velocity and u is a displacement. The power spectral density of d can be easily related to that of the incoming wave modes w_i from this equation.

The Wiener-Hopf optimisation problem is also equivalent to a standard LQG problem.[16] Using the results of the previous subsection, the $\mathcal{H}_2$ problem can be solved more easily using this approach. The cost J

is proportional to the $\mathcal{H}_2$ norm of the power flow,

$$J = \int_{-\infty}^{\infty} (u^\sim y + y^\sim u)\, d\omega \tag{30}$$

and as in Equation (17), the addition of the constant $w^\sim w$ to the integrand does not change the problem, so

$$J = \int_{-\infty}^{\infty} (z^\sim z)\, d\omega = \|z\|_2^2 \tag{31}$$

with z given by Equation (20). Hence, the $\mathcal{H}_2$ optimal compensator is that which minimizes the $\mathcal{H}_2$ norm of the transfer function from w to z in the standard problem (21). This is very similar to the $\mathcal{H}_\infty$ approach; the norm used in the optimization has changed, and the deterministic (but unknown) finite power noise w has been replaced by a stochastic process, but the setup is otherwise identical.

The power spectral density of $w = G_0^{-1}d$ can be related to that of d, and therefore to that of the incoming wave modes w_i by Equation (29). This PSD can also be used to introduce frequency weighting into the problem; more importance is attached to a certain frequency range by increasing the power available to be dissipated in that range.

As was noted in Reference 2, the $\mathcal{H}_2$ approach suffers from the fact that it does not guarantee a stabilising compensator. That the state space LQG method presented here yields the same results as the Wiener-Hopf approach in Reference 2 will be demonstrated in the next section.

Example

The approach described in the previous sections can be demonstrated in the design of compensators for a pinned-free Bernoulli-Euler beam with a moment actuator at the pinned end. This structure is chosen to represent that of the experiment described in the next section; as a result the beam properties used in this example will be those of the experiment, given in Table 1. This example also allows a comparison to be made of the $\mathcal{H}_2$ and $\mathcal{H}_\infty$ compensators, and demonstrates that the LQG based $\mathcal{H}_2$ method presented here is equivalent to the Wiener-Hopf method of Reference 2.

The dereverberated mobility can be found analytically as the transfer function of the "infinitely extended" system. Using a wave approach, the transfer function of a semi-infinite pinned Bernoulli-Euler beam between collocated tip moment and slope rate is

$$G(s) = \frac{\sqrt{s}}{\sqrt{2}(\rho A)^{1/4}(EI)^{3/4}} \tag{32}$$

With no causality constraint, the compensator that dissipates the maximum possible power at all frequencies is, from Equation (12),

$$K(s) = \frac{\sqrt{2}(\rho A)^{1/4}(EI)^{3/4}}{\sqrt{-s}} \tag{33}$$

This is the ideal compensator for the structure, but cannot be implemented. Instead, a number of other compensators can be designed.

Velocity feedback is the simplest of these, and was chosen to compare the optimal designs with a similar existing design approach. To achieve maximum power dissipation at a frequency ω_0, the gain should be as close as possible to the unconstrained compensator at this frequency, so

$$K_1(s) = \frac{\sqrt{2}(\rho A)^{1/4}(EI)^{3/4}}{\sqrt{\omega_0}} \qquad (34)$$

The second compensator is the $\mathcal{H}_\infty$-optimal compensator with unity weighting at all frequencies, given by

$$K_2(s) = \frac{\sqrt{2}(\rho A)^{1/4}(EI)^{3/4}}{\sqrt{s}} \qquad (35)$$

The analytic derivation of this compensator is similar to that for a free end of a beam, presented in References 6 and 7. The magnitude is the same as that of the unconstrained optimal compensator, but the phase is $-45°$, rather than $+45°$. This compensator was also derived and implemented by Miller,[3] as the fixed form optimal compensator.

In order to further test the $\mathcal{H}_\infty$ approach, a weighting function was selected to emphasise a narrow frequency band near 35 rad/sec. This corresponds approximately to the frequency of the 7th mode of this beam. The minimum value of W_1 in this region was approximately 0.65, and the weighting increased to near unity a factor of $\sqrt{2}$ above and below this frequency. An analytic solution for the compensator in this case would be difficult. However, the plant in Equation (32) can be approximated adequately over a wide frequency range with a finite number of alternating poles and zeroes on the real axis, with equal logarithmic spacing. State space methods can then be used to obtain an approximate compensator. For this example, Equation (32) was approximated by 9 poles and 9 zeroes on the negative real axis, between 3.5×10^{-3} and 3.5×10^5 rad/sec. The transfer function of this approximation matches the assumed dereverberated mobility to within 2 degrees of phase and 0.25 db magnitude for 3 decades above and below the center frequency of the weighting function.

The optimal compensator from slope rate to moment was found to be well approximated by the product of the unweighted optimum in Equation (35), and a two pole, two zero network. This network provided the phase lead that is required so that at the center of the weighted region, the phase approaches the unconstrained optimal phase of 45° (from Equation (33)), allowing the compensator to dissipate more power. The optimal poles and zeroes of this network are symmetric about the center frequency of the weighting function W_1, at 35 rad/sec. The two free parameters of this

network were optimised to minimise the $\mathcal{H}_\infty$ norm of the cost. This results in the compensator from slope rate to moment being

$$K_3(s) = 2.62\frac{\sqrt{2}(\rho A)^{1/4}(EI)^{3/4}}{\sqrt{s}}\left(\frac{s^2 + 38.5s + 466}{s^2 + 100s + 3210}\right) \qquad (36)$$

For comparison with these designs, an $\mathcal{H}_2$ optimal solution can also be computed using the same model, as the solution of an LQG problem. For comparison with the results of Miller et al.,[3] the power spectral density $\Phi_{w_i w_i}$ is chosen to be the same as in Reference 3;

$$\Phi_{w_i w_i} = \frac{a^2}{(s - \omega_n^2)^2}\begin{bmatrix} 1 & 0 \\ 0 & 1 \end{bmatrix}\frac{a^2}{(s + \omega_n^2)^2} \qquad (37)$$

Using Equation (29) and the definitions for Y_{wi}, Y_{wo}, and S for the pinned beam from Reference 3, the tip slope rate can be related to the incoming wave modes by

$$d = 2j\omega\left(\frac{\rho A}{EI}\right)^{1/4}\begin{bmatrix} j\sqrt{\omega} & \sqrt{\omega} \end{bmatrix}w_i \qquad (38)$$

The normalized disturbance w is related to d by Equation (29). Using these equations, the power spectral density of w is

$$\Phi_{ww} = \frac{b^2\omega^{5/2}}{(s - \omega_n^2)^2(s + \omega_n^2)^2} \qquad (39)$$

for some constant b. This is proportional to $\omega^{2.5}$ at low frequencies, and to $\omega^{-1.5}$ at high frequencies, with a maximum at ω_n, selected to be 40 rad/sec. Thus one would expect the most damping near this frequency, and a much sharper drop in damping for lower frequencies than for higher frequencies.

The $\mathcal{H}_2$, weighted $\mathcal{H}_\infty$, unweighted $\mathcal{H}_\infty$, and unconstrained optimal compensators are plotted in Figure 3, as is the velocity feedback compensator. Note that at the frequency weighted most heavily, the $\mathcal{H}_\infty$ solution achieves the magnitude of the unconstrained optimal compensator, but not quite the phase, while the $\mathcal{H}_2$ optimal solution achieves the phase, but not the magnitude. The $\mathcal{H}_2$ compensator calculated by Miller et al. in Reference 3 by a wave approach and Wiener-Hopf methods is also plotted for comparison with the $\mathcal{H}_2$ compensator calculated here with the LQG method. The agreement indicates that the two approaches are equivalent; the discrepancy at high frequencies is due to the inclusion of a small penalty on control effort in the LQG solution.

The power input to the structure by these compensators is plotted in Figure 4, expressed as a fraction of the available incoming power at each frequency. Thus a value of -1 indicates that the maximum possible power is being dissipated, a value of zero means that the compensator does nothing at this frequency,
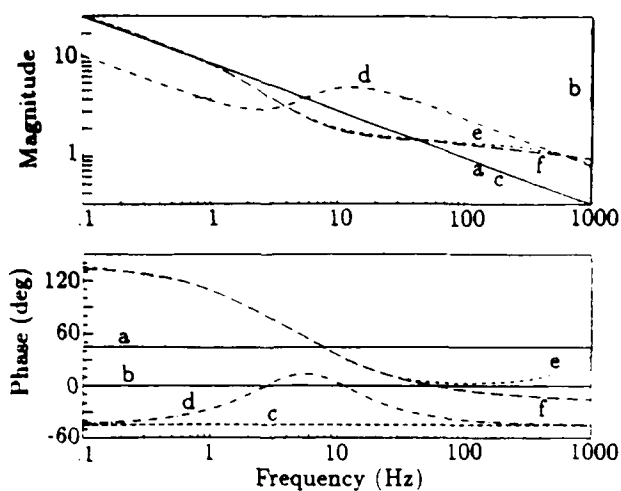
Figure 3: Comparison of compensators. Unconstrained optimum (a), velocity feedback (b), unweighted $\mathcal{H}_\infty$ design (c), weighted $\mathcal{H}_\infty$ design (d), LQG $\mathcal{H}_2$ design (e) and Wiener-Hopf $\mathcal{H}_2$ design (f).
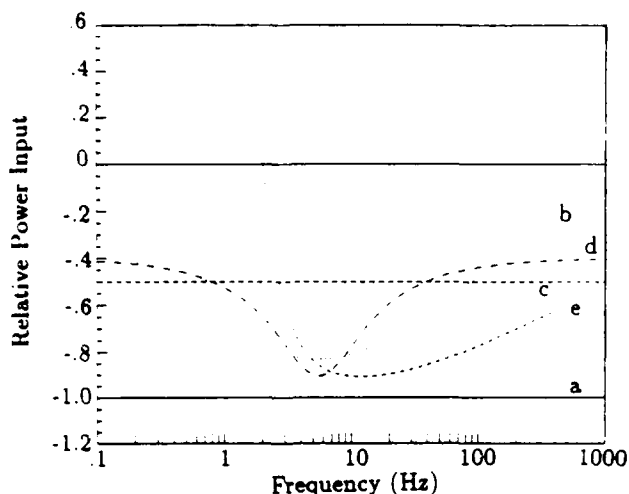

Figure 4: Power absorption for unconstrained optimum (a), velocity feedback (b), unweighted $\mathcal{H}_\infty$ design (c), weighted $\mathcal{H}_\infty$ design (d), and $\mathcal{H}_2$ design (e).

and values larger than zero indicate that power is being added to the structure, which could lead to instabilities. Note that the $\mathcal{H}_2$ solution adds power to the structure at certain frequencies, while the $\mathcal{H}_\infty$ solutions do not. Furthermore, as expected from the weighting function chosen, the $\mathcal{H}_2$ solution treats higher frequencies with more importance than lower, while the $\mathcal{H}_\infty$ solution treats both equally.

Both of the $\mathcal{H}_\infty$ compensators absorb some power, and thus provide some damping at all frequencies, whereas velocity feedback is ineffective at sufficiently
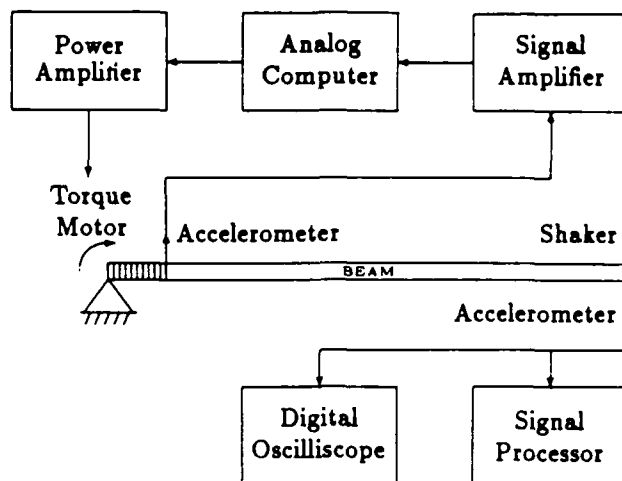

Figure 5: Schematic of experimental setup

Length	7.32 m
Width	0.102 m
Thickness	3.175 mm
EI	31.1 Nm^2
ρA	2.85 kg/m

Table 1: Beam dimensions and properties

high and low frequencies. The weighted $\mathcal{H}_\infty$ design will also provide better narrowband damping than velocity feedback, and only slightly worse broadband damping than the unweighted $\mathcal{H}_\infty$ design.

Experiment

The $\mathcal{H}_\infty$ and velocity feedback compensators designed in the previous section were implemented on a brass beam suspended in the Space Engineering Research Center laboratory at M.I.T. Previous experiments with this beam include collocated rate feedback and $\mathcal{H}_2$ optimal wave control.[3]

Setup

The setup is shown schematically in Figure 5. The beam is suspended horizontally in the lab, with actuation and sensing such that the bending vibration can be controlled. One end is effectively pinned, while the other is free. The properties and dimensions of the beam are summarized in Table 1. The open-loop damping of the first 17 modes, up to a frequency of approximately 30 Hz, averaged about 0.3%.

Control is applied through a torque motor at the pinned end, and sensing is provided by a linear accelerometer mounted a short distance from this end. The member connecting the sensor to the tip is as-
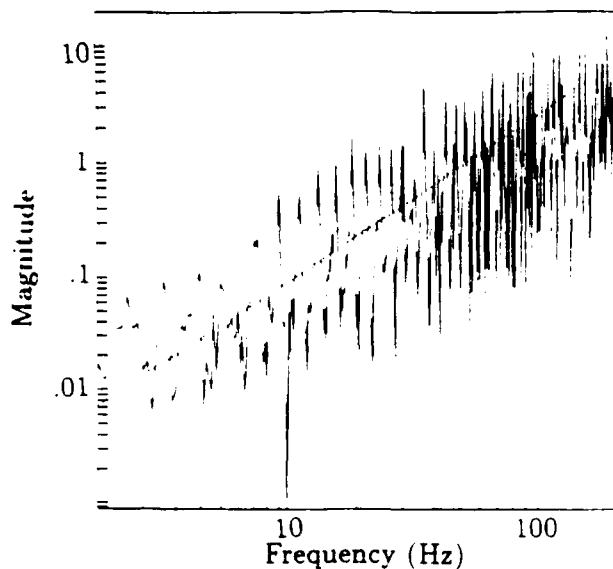
Figure 6: Open loop transfer function at controlled end of beam (solid), and dereverberated mobility used for control design (dotted).

sumed to be rigid, so that the sensor provides a rotational acceleration measurement collocated with the moment actuator. In practice, this assumption is not quite valid, although it is reasonable in the frequency range of interest.

In addition to the control actuator and sensor, a shaker and data acquisition accelerometer were mounted at the free end of the beam. The shaker was mounted to provide a force collocated with the acceleration measurement. The closed loop transfer function between these two was used as an indication of the performance achieved.

The signal from the accelerometer at the controlled end was fed through a signal amplifier into an analog computer which contained the compensator program. The output of this was fed through a power amplifier into the moment actuator. The accelerometer signal from the uncontrolled end was fed into a Signology SP-20 Signal Processing Peripheral to record and analyze the response data, and obtain frequency domain information. An oscilliscope was used to monitor the accelerometer signal so that any instabilities could be quickly identified, and their frequencies determined. Detailed information on the characteristics of the sensors and actuators can be found in Reference 3.

Compensator Implementation

A detailed model of the beam is not necessary for the experiment; it is sufficient to examine the transfer function from the control actuator to the control sensor. This transfer function is shown in Figure 6. The dereverberated mobility could be calculated from this transfer function through cepstral analysis, or by

averaging. Alternatively, it can be approximated by the theoretical dereverberated mobility for a pinned end of a beam, given by Equation (32). This transfer function is also plotted in Figure 6, and closely approximates the logarithmic average of the measured transfer function in the region of interest. The presence of a rotational inertia at the tip, corresponding to the inertia of that part of the actuator armature and sensor that is fixed to the beam, introduces a roll-off into the transfer function at high frequencies. However, the effect of this inertia was at a sufficiently high frequency so that for the control design, it was assumed to be zero and not modelled. As a result, the previously designed compensators can be used here.

The velocity feedback, unweighted $\mathcal{H}_\infty$, and the weighted $\mathcal{H}_\infty$ compensator designs are all positive real, and thus guaranteed to be stable for any positive real structure. The transfer function from the actuator to the sensor of this beam, however, was not positive real at high frequencies. This is due to the noncollocatedness of the sensor and actuator, the additional dynamics of the sensor and actuator, and any time delays in the system. The system can still be guaranteed to be stable if the complementary sensitivity is bounded above by the inverse of this difference from positivity.[17] So, to be stable, the complementary sensitivity, and therefore the compensator, must roll off at high frequency. Ideally, the compensator design procedure would result in this behavior automatically. Since it does not, the additional roll off required must be added in an *ad hoc* manner. Low-pass filters were therefore added to all three designs, with poles at 500 rad/sec.

The available measurement in the experiment was proportional to angular acceleration, and thus a further integration was necessary to obtain angular rate. This integrator was rolled off at DC to prevent saturation and drift problems. The second order dynamics were chosen to have a natural frequency of 1 rad/sec, and a damping ratio of 0.7071. Finally, a high-pass filter was included to remove the DC offset of the accelerometer.

With the two $\mathcal{H}_\infty$ compensators at their optimal gains, a small amount of passive damping was found to be required in order to maintain closed loop stability of modes of the system above 1000 Hz. A constrained layer of foam rubber was added to a short section of the beam, which did not appreciably increase the open loop damping in any of the modes below about 300 Hz, corresponding to about the 55th bending mode of the beam. This, however, was not sufficient to implement the velocity feedback compensator at its optimal gain without destabilising high frequency modes. Indeed, a second lowpass filter was necessary to achieve stability at even 40% of the optimal gain, at which level data was taken. This implemented velocity feedback compensator provides its maximum damping at
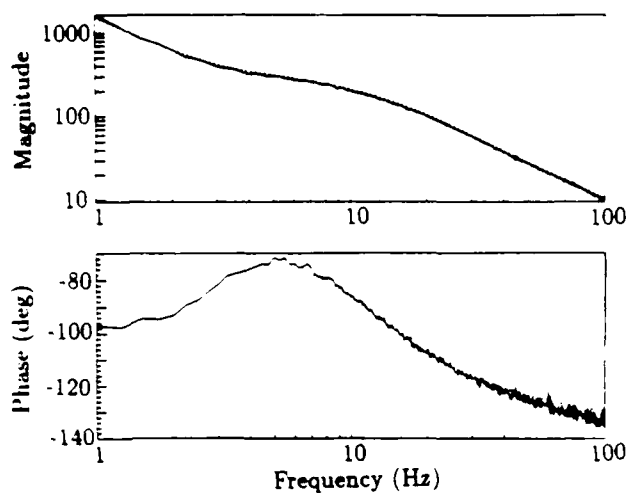
Figure 7: Transfer function of compensator implemented in experiment (solid), and desired compensator (dotted).

about 35 Hz.

The low-pass and high-pass filters and integrator dynamics are combined into the filter

$$F(s) = \left(\frac{s}{s^2 + 1.41s + 1} \right) \left(\frac{500}{s + 500} \right) \left(\frac{s}{s + 1} \right) \quad (40)$$

The implemented compensators between moment and angular acceleration are then

$$K_1(s) = 1.64 \left(\frac{500}{s + 500} \right) \cdot F(s) \quad (41)$$

$$K_2(s) = 24.2 \frac{1}{\sqrt{s}} \cdot F(s) \quad (42)$$

$$K_3(s) = 63.4 \frac{1}{\sqrt{s}} \left(\frac{s^2 + 38.5s + 466}{s^2 + 100s + 3210} \right) \cdot F(s) \quad (43)$$

The circuit used to implement the half integrator $\frac{1}{\sqrt{s}}$ is based on that presented in Reference 5. The approximation is excellent up to about 700 Hz, well above the region of interest. The measured compensator for the weighted $\mathcal{H}_\infty$ design is compared with the desired compensator in Figure 7. Good agreement is obtained, except at low frequencies where the dynamics of the integrator and the high-pass filter have a noticeable effect, and at frequencies higher than those shown, where the low-pass filter was added. Similar agreement exists between the measured and desired compensators for the other two cases.

Results

The closed loop transfer functions from force at the free end to collocated velocity with the three compensators are compared with the open loop response in Figure 8. Note that the spikes present in the data

at 16.4, 19.8, and 24.5 Hz correspond to torsional modes of the beam, which are excited by the shaker but are uncontrolled by the moment actuator. The corresponding predicted responses appear in Figure 9. These were calculated from the compensator transfer function using the phase closure approach of Reference 11. Reasonable agreement is obtained between this prediction and the actual transfer function, although the achieved performance is noticeably better than that predicted. Similar experimental and predicted transfer functions with $\mathcal{H}_2$ optimal compensators can be found in Reference 3.

These results confirm the expected advantages of each technique. The unweighted $\mathcal{H}_\infty$ design achieves damping in a broadband region. This is obtained by sacrificing some of the narrowband damping achieved by velocity feedback. The lowest modes present in the frequency range plotted are damped more heavily by the unweighted $\mathcal{H}_\infty$ than by velocity feedback, one would expect that this would also be true of modes at a sufficiently high frequency. The unweighted $\mathcal{H}_\infty$ design achieves excellent narrowband damping in the desired frequency-range, while maintaining some damping everywhere. This is a result of the exact match in magnitude, and close match in phase, with the unconstrained optimal compensator that absorbs all of the incoming power at each frequency. In fact, the modes near 6 Hz can be virtually eliminated if the phase of the compensator is boosted still closer to the unconstrained noncausal optimum, at the expense of performance at other frequencies.

Conclusions

The dereverberated driving point mobility is a simple but useful model for control design of uncertain, modally dense structures. For simple structures, such as the beam used in this experiment, this is equivalent to a local wave model, but the approach is capable of modelling much more general structures, as it can be determined directly from an experimental transfer function.

The compensator that dissipates the most power possible at every frequency is in general noncausal, and cannot be implemented. Two approaches were examined for obtaining a causal compensator that dissipates power. The $\mathcal{H}_2$-optimal solution can be found using either Wiener-Hopf or LQG techniques. However, this compensator may allow power to be generated at certain frequencies. Another approach is to find the $\mathcal{H}_\infty$-optimal solution which minimises the maximum power flow into the structure. This compensator dissipates power at all frequencies, and is therefore guaranteed to be stabilising.

Experimental results demonstrate that the damping that can be achieved with the $\mathcal{H}_\infty$ approach is much greater than that achievable with rate feedback. With
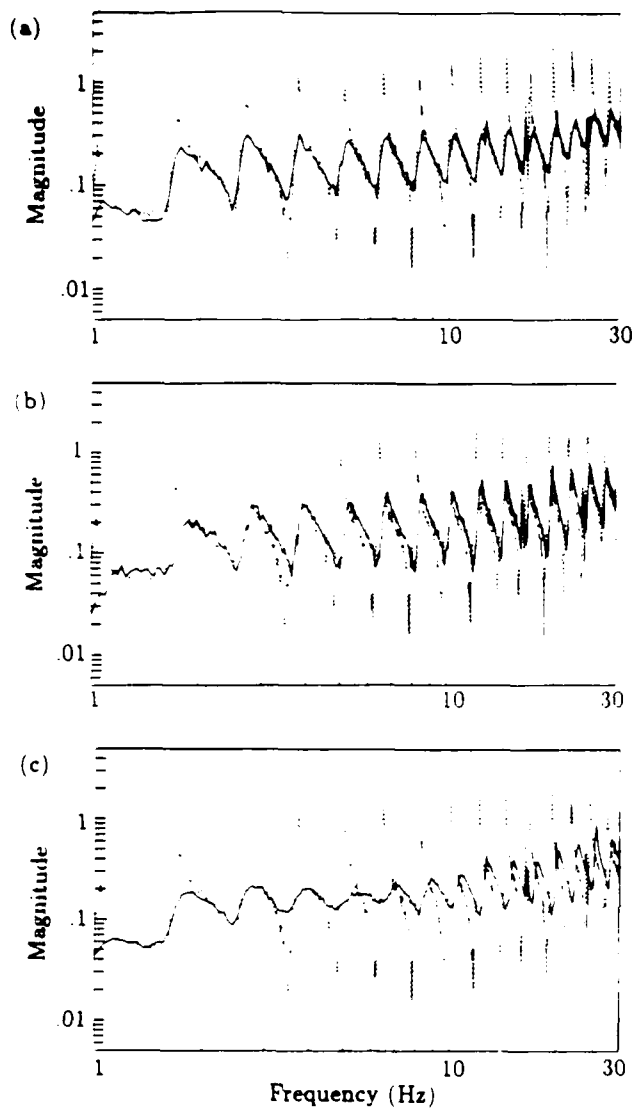
Figure 8: Experimental open (dotted) and closed loop (solid) transfer functions using (a) velocity feedback, (b) unweighted $\mathcal{H}_\infty$ design, and (c) weighted $\mathcal{H}_\infty$ design.

Figure 9: Predicted open (dotted) and closed loop (solid) transfer functions using (a) velocity feedback, (b) unweighted $\mathcal{H}_\infty$ design, and (c) weighted $\mathcal{H}_\infty$ design.

no frequency weighting, good broadband damping can be obtained. With a frequency weighting, excellent narrowband performance can be achieved while some broadband damping is maintained. At the frequency where the best performance is obtained, the compensator closely matches the unconstrained (noncausal) optimum in both magnitude and phase.

One difficulty with the approach is that it does not enforce rolloff that is necessary to deal with high frequency sensor and actuator dynamics, or noncollocatedness. The required roll-off must be added on an *ad hoc* basis. Having done this, this approach to modelling and control design successfully added significant damping to many modes of a laboratory structure,
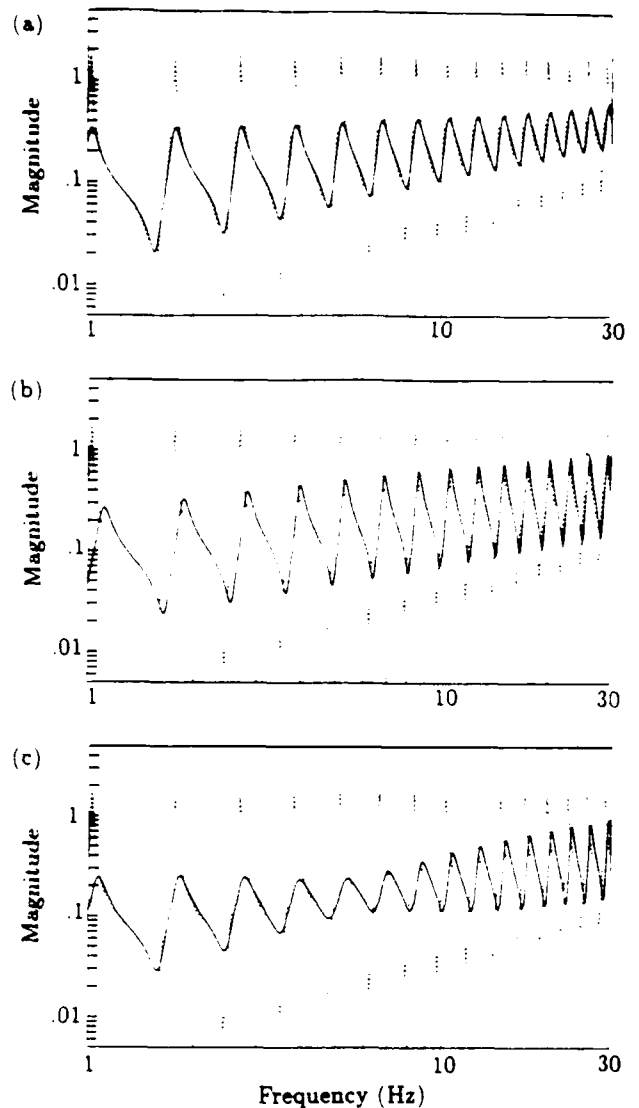
without the large effort in system identification, off-line computation, and compensator complexity that would be required of many control design techniques.

Acknowledgements

References

[1] Balas, M. J., "Trends in Large Space Structure Control Theory: Fondest Hopes, Wildest Dreams," *IEEE Trans. Auto. Control*, Vol. AC-27, No. 3, June 1982, pp. 522-535.

[2] Miller, D. W., Hall, S. R. and von Flotow, A. H., "Optimal Control of Power Flow at Structural Junctions," *J. of Sound and Vibration*, Vol. 140, No. 2, 1990.

[3] Miller, D. W., and Hall, S. R., "Experimental Results Using Travelling Wave Power Flow Techniques," *Proc. ASME Winter Annual Meeting*, AD-Vol. 15, San Francisco, CA, Dec. 1989, pp. 35-42, to appear in *AIAA J. of Guidance, Control, and Dynamics*.

[4] von Flotow, A. H., "The Acoustic Limit of Structural Dynamics," in *Large Space Structures: Dynamics and Control*, Atluri and Amos (ed.), Springer-Verlag, 1988, pp. 213-238.

[5] von Flotow, A. H., and Shäfer, B., "Wave-Absorbing Controllers for a Flexible Beam," *AIAA J. Guidance, Control, and Dynamics*, Vol. 9, No. 6, Nov.-Dec. 1986, pp. 673-680.

[6] MacMartin, D. G. and Hall, S. R., "An $\mathcal{H}_\infty$ Power Flow Approach to Control of Uncertain Structures," *Proceedings of the 1990 American Control Conference*, San Diego, CA, May 1990, pp. 3073-3080, to appear in *AIAA J. of Guidance, Control, and Dynamics*.

[7] MacMartin, D. G., *An $\mathcal{H}_\infty$ Power Flow Approach to Control of Uncertain Structures*, S.M. Thesis, Department of Aeronautics and Astronautics, M.I.T., Cambridge, MA, Feb. 1990.

[8] Lyon, R. H., *Machinery Noise and Diagnostics*, Butterworth Publishing, June 1987.

[9] Hodges, C. H. and Woodhouse, J., "Theories of Noise and Vibration Transmission in Complex Structures," *Reports on Progress in Physics*, Vol. 49, 1986, pp. 107-170.

[10] Skudrzyk, E. "The Mean-value Method of Predicting the Dynamic Response of Complex Vibrators," *Journal of the Acoustical Society of America*, Vol. 67, No. 4, April 1980, pp. 1105-1135.

[11] Miller, D. W., "Power Flow in Structural Networks," *J. of Sound and Vibration*, Vol. 128, 1989, pp. 145-162.

[12] Fuhrmann, P. A., "Elements of Factorisation Theory From a Polynomial Point of View," in *Three Decades of Mathematical System Theory*, Nijmeijer and Schumacher (ed.), Springer-Verlag, 1989, pp. 148-178.

[13] Van Valkenburg, M. E., and Kinariwala, B. K., *Linear Circuits*, Prentice-Hall, 1982, pp. 297-298.

[14] Francis, B. A., *A Course in $\mathcal{H}_\infty$ Control Theory*, Springer-Verlag, 1987.

[15] Doyle, J. C., Glover, K., Khargonekar, P. P., and Francis, B. A., "State-Space Solutions to Standard $\mathcal{H}_2$ and $\mathcal{H}_\infty$ Control Problems," *IEEE Trans. Auto. Control*, Vol. 34, No. 8, Aug. 1989, pp. 831-847.

[16] Kailath, T., *Lectures on Wiener and Kalman Filtering*, Springer-Verlag, 1981.

[17] Slater, G. L., Zhang, Q., and Bosse, A., "Robustness with Positive Real Controllers for Large Space Structures," *Proc. 1989 AIAA Guidance, Navigation, and Control Conference*, Boston, MA, Aug. 1989, pp. 932-941.

DEVELOPMENT OF SPATIALLY CONVOLVING SENSORS FOR STRUCTURAL CONTROL APPLICATIONS

D. W. Miller,[*] S. A. Collins[**] and S. P. Peltzman[†]

Space Engineering Research Center
Massachusetts Institute of Technology
Cambridge, Massachusetts

ABSTRACT

This work explores a class of structural sensors which convolve measurements, distributed along a structure, into a single temporal signal. The manner in which this information is convolved is determined by the geometry of the sensor.

Particular types of geometries are developed which make this class of sensors attractive for structural control applications. The objective is to develop a sensor, using piezoelectric film, whose geometry filters the spatial harmonics of the structure's shape to achieve rolloff without exhibiting phase lag. Such a sensor would facilitate gain stabilization without the risk of sacrificing phase margin.

Various analytical examples are derived, several of which are verified experimentally. These sensors may be beneficial at structural frequencies where the dynamics are modally dense and poorly modelled.

INTRODUCTION

Motivation

There are many examples of structural control applications where desired objectives could be achieved if it were possible to implement noncausal compensators in real time. For example, Refs. [1-5] illustrate that resonances in a beam could be eliminated using one actuator and its dual sensor if it were possible to implement $(-s)^{1/2}$. Other applications involve sensor dynamics where typical sensor rolloff introduces phase lag. This phase lag reduces phase margin, often to the point of creating an unstable system [6]. Sensors which 'l off without this phase lag would be extremely useful, as they could be used it facilitate gain

---

[*] Research Associate, Member AIAA
[**] Research Assistant, Student Member AIAA
[†] Undergraduate Researcher

stabilization without concerns for loss of phase margin.

The basic problem associated with noncausal compensators is that some portion of their singularities lies in the right half of the Laplace plane. Singularities in the right half plane indicate one of two situations. Either the dynamics are affiliated with a system which is stable in negative time and therefore anticipates future information, or they are affiliated with a system that is unstable in positive time. The latter yields a sensor signal which is unstable and therefore unusable.

The former situation is more relevant to this discussion. Noncausal compensators anticipate future information which is otherwise unavailable. Viewed from a travelling wave perspective, however, it becomes clear that the spatial Fourier components, which will sum to create a future motion at a particular structural cross-section, are presently propagating towards that cross-section. Similarly, components which created a cross-sectional motion in the past are presently propagating away from that cross-section. In other words, future and past information about the response of a cross-section can be obtained by sensing upstream and downstream.

Upstream and downstream in a structure are not distinguishable based upon location because they can correspond to the same physical region. Rather, they are distinguished by the direction in which the energy is travelling with respect to the original cross-section (Fig. 1). Measurement of this upstream and downstream information should enable the reconstruction of both past and future cross-sectional motion.

The convolution of spatially distributed measurements can be performed in two basic ways. In the first, a finite array of discrete point sensors can be distributed along the spatial extent of the structure to measure the deflection pattern at discrete locations. The products of
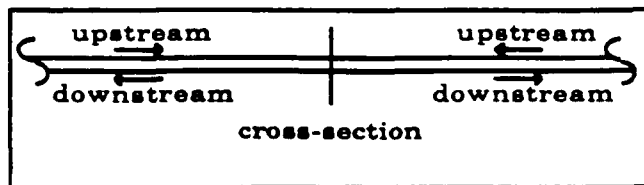
Figure 1. Illustration of the concept of energy upstream and downstream of a cross-section.

these measurements, with discrete values of the weighting function, create the output signal.

In the second, a single distributed sensor is used. The spatial weighting function is achieved by creating the appropriate sensor geometry. Rather than having numerous discrete point sensors dispersed along the structure, the single continuously distributed sensor acquires measurements from the entire domain over which it is attached.

In practice, the array has the advantage of a wide range of available sensors (strain, position, etc. and associated rates) whereas the single distributed sensor may be restricted to strain- (and strain-rate-) sensing piezoelectric polymers. While distributed point sensors have a higher per-unit sensor cost, application to complex structural geometries may be easier. The weighting function can also be easily altered because it is implemented in software.

Use of a single, continuous sensor reduces the computational burden, and associated time delays, by 'realizing' the convolution in the mechanical geometry of the sensor. In addition, while both suffer from truncation effects due to the restriction of a finite sensor domain, the use of point sensors also suffers from spatial aliasing associated with the finite-length gaps between the individual point sensors.

An example of this second type of spatially convolving sensor is a modal sensor. Realized by cutting piezoelectric polymer film [6] in the shape of a particular modal strain distribution, it is attached to the structure in the appropriate orientation [7]. The work in this paper expands upon this concept by using the same type of sensor to achieve other desirable signal characteristics.

Prior Research

Spatially distributed sensors and actuators were initially studied in order to apply distributed-parameter control theory to distrib-

uted-parameter systems such as beams [8,9]. It was found that these sensors could also perform as point sensors, with the added advantage that, because of the effective spatial integration, the distributed sensors were not as sensitive to placement errors [10].

The weighting on the contribution of various modes can be adjusted through the use of a spatially-varying sensor distribution. For example, a modal sensor is shaped such that the weighting is zero for all modes except one [10]. Several experimental investigations using piezo film sensors, the width of which was proportional to the modal strain distribution [7, 11, 12], have verified the behavior of modal sensors. Lee *et al.* have noted that these sensors are a realization of the modal-filtering concept [13], but they can also be thought of as very narrow bandpass filters centered on the frequency of the mode to be sensed. In regions of travelling waves, this corresponds to convolving the measurements at a single wavenumber, namely that of the mode of interest.

The following sections describe how a spatially convolving sensor was developed and experimentally implemented. The dispersion equation relates the behavior of a structural medium in time and space. It reveals how spatial weighting functions can be used to achieve desirable temporal behavior. This concept is analytically demonstrated for several types of spatially convolving sensors. The structural medium and sensor are assumed to be of infinite, one-dimensional extent. An infinite domain, wave analysis is used to obtain these solutions. Since actual structures and sensors must be of finite length, a discussion of truncation effects is given. Finite sensor length requires that some of the spatial weighting function be absent during actual implementation. This loss of information causes a deviation in performance from that predicted by the infinite domain solution. The manufacture of the sensors, experimental setup and experimental results are described.

INFINITE DOMAIN ANALYSIS

An infinite domain analysis is used to demonstrate the acquisition of desirable temporal domain characteristics through the implementation of an appropriate spatially distributed sensor. A wave analysis is used to

analyze the rod and the Bernoulli-Euler beam examples.

Rod Example

Exponential and sinc weighting functions are analyzed for the rod. The objective of the exponential weighting function is to create a sensor which has a second order rolloff without phase lag. The purpose of the sinc weighting function is to achieve infinite order rolloff without phase lag.

Substituting the wave solution

$$u(x,t) = Ue^{ikx + i\omega t} \quad (1)$$

into the governing partial differential equation for a rod

$$EA\frac{\partial^2 u(x,t)}{\partial x^2} - \rho A\frac{\partial^2 u(x,t)}{\partial t^2} = 0 \quad (2)$$

yields the rod dispersion relation as

$$k^2 = \frac{\rho}{E}\omega^2 \quad or \quad p^2 = \frac{\rho}{E}s^2 = c_0^2 s^2 \quad (3)$$

The symbols k and ω are the spatial and temporal Fourier variables, respectively, and p and s are the spatial and temporal Laplace variables, respectively. The quantities E, A and ρ are the modulus of elasticity, cross-sectional area and mass per unit volume, respectively. The roots of the dispersion relation indicate that the rod supports two wave modes at each frequency, leftward and rightward propagating, given by

$$u(x,\omega) = u_l(\omega)e^{ikx} + u_r(\omega)e^{-ikx} \quad (4)$$

Exponential Sensor. As discussed in the previous section, it is desirable to develop a sensor which rolls off without the classic phase lag which plagues control systems. Therefore, the sought-after temporal transfer function is a sensor with rolloff but no associated phase lag. This sensor has the following form

$$y(0,s) = \frac{\omega_n}{s + \omega_n}\frac{-\omega_n}{s - \omega_n}u(0,s) \quad (5)$$

where $y(0,s)$ is the temporal Laplace transform of the desired sensor signal at the position $x=0$, $u(0,s)$ is the transform of a particular structural degree of freedom at the same location and ω_n is the corner frequency of the sensor. Since the sensor characteristics are dependent upon the dispersion relation, the appropriate spatial weighting function will be dependent upon the structural medium on which the weighting function is implemented.

Substituting the dispersion relation, Eq. (3), for the Laplace variable in Eq. (5) yields

$$y(0,s) = \frac{c_0\omega_n}{p + c_0\omega_n}\frac{-c_0\omega_n}{p - c_0\omega_n}u(p,0) \quad (6)$$

The spatial weighting functions are exponential, one decaying in the positive x-direction and one decaying in the negative x-direction, with a scale length equal to $1/c_0\omega_n$.

The convolution of these spatial weighting functions, with the wave solution (Eq. 4), is

$$y = \frac{\alpha}{2}\left(\int_{-\infty}^{0} u(x,\omega)e^{\alpha x}dx + \int_{0}^{\infty} u(x,\omega)e^{-\alpha x}dx\right)$$

$$= \frac{-\alpha^2/c_0^2}{(s + \alpha/c_0)(s - \alpha/c_0)}(u_l(\omega) + u_r(\omega)) \quad (7)$$

This equals the motion at the location $x = 0$

$$u(0,\omega) = u_l(\omega) + u_r(\omega) \quad (8)$$

with a second order rolloff but without phase lag.

Sinc Function Sensor. The sinc function

$$W(x) = \frac{\sin(\Delta x)}{\Delta x} \quad (9)$$

was chosen as a plausible sensor geometry because the transform of a spatial sinc function is a step function in the wavenumber domain. This indicates that an infinite order rolloff in the sensor's response can occur at a particular wavenumber (Δ), and corresponding frequency, without associated phase lag.

Convolving the sinc function with the wave solution, Eq. (4), gives

$$y = \int_{-\infty}^{\infty}\left(u_l(\omega)e^{ikx} + u_r(\omega)e^{-ikx}\right)\frac{\sin(\Delta x)}{2\pi r} \quad (10)$$

If the rightward and leftward travelling wave mode amplitudes are equal, $u_l = u_r = u(\omega)$, the output of the sensor becomes

$$y = \frac{1}{2}u(\omega)(1 - sign(k - \Delta)) \quad (11)$$

This geometry of sensor results in a flat response for wavenumbers below the characteristic wavelength Δ of the sinc function and no response above Δ. This sensor exhibits no phase lag. Such a sensor characteristic would be extremely valuable in a structural control

3

application. However, performance degradation due to sensor truncation must be considered.

Beam Example

One spatial geometry of strain sensor is studied for the infinite extent Bernoulli-Euler beam. This spatial weighting function is an exponential function that will result in a first order temporal rolloff.

The partial differential equation for a Bernoulli-Euler beam

$$EI \frac{\partial^4 v}{\partial x^4} + \rho A \frac{\partial^2 v}{\partial t^2} = 0 \qquad (12)$$

has the dispersion relation

$$k^4 = \frac{\rho A}{EI}\omega^2 \quad or \quad p^4 = -\frac{\rho A}{EI}s^2 \qquad (13)$$

which supports four wave modes

$$v = (w_{lp}e^{ikx} + w_{le}e^{kx} + w_{rp}e^{-ikx} + w_{re}e^{-kx}) \qquad (14)$$

The quantity I is the area moment of inertia and the wave mode amplitudes (w) are functions of frequency.

The sensor that will be used in the beam experiments senses strain. This is proportional to the curvature in the beam, given by

$$\frac{\partial^2 v}{\partial x^2} = k^2(-w_{lp}e^{ikx} + w_{le}e^{kx}$$
$$- w_{rp}e^{-ikx} + w_{re}e^{-kx}) \qquad (15)$$

Exponential Sensor. The output of the exponential sensor is found by convolving an exponential weighting function with the curvature in the beam, Eq. (15), to give the convolution

$$y = \frac{\alpha}{2}\left(\int_{-\infty}^{0} \frac{\partial^2 v}{\partial x^2}e^{\alpha x}dx + \int_{0}^{\infty} \frac{\partial^2 v}{\partial x^2}e^{-\alpha x}dx\right) \qquad (16)$$

This yields

$$y = \frac{-\alpha^2 k^2}{k^4 - \alpha^4}\Big[(k^2 - \alpha^2)(w_{lp} + w_{rp})$$
$$+ (k^2 + \alpha^2)(w_{le} + w_{re})\Big] \qquad (17)$$

Notice that at wavenumbers much larger than α (*i.e.*, high frequencies) the sensor magnitude rolls off as $1/k^2$ with respect to the point curvature measurement

$$\frac{\partial^2 v_c}{\partial x^2} = k^2(-w_{lp} + w_{le} - w_{rp} + w_{re}) \qquad (18)$$

at the center of the exponential sensor $(x=0)$.

Assuming that no evanescent waves exist $(w_{le} = w_{re} = 0)$, substituting the dispersion relation, Eq. (13), for k in Eq. (17) gives the transfer function from curvature at the center of the exponential sensor to the output of the exponential sensor as

$$\frac{y_c}{\left(\dfrac{\partial^2 v_c}{\partial x^2}\right)} = \frac{\alpha^2/c_0^2}{\left(\sqrt{s} + i\dfrac{\alpha}{c_0}\right)\left(\sqrt{-s} - i\dfrac{\alpha}{c_0}\right)} \qquad (19)$$

The exponential weighting function creates a second order rolloff for the rod because the rod's dispersion relation linearly relates frequency to wavenumber (Eq. 3). The exponential weighting function for the Bernoulli-Euler beam creates a first order rolloff since the wavenumber is proportional, through the dispersion relation (Eq. 13), to the square root of the frequency.

While these examples indicate what is theoretically possible using these spatial weighting functions, the truncation effects associated with finite length sensors must be considered.

TRUNCATION EFFECTS

Any realistic application of these types of sensors will involve truncation in order to confine the sensor to some finite region of the structure. This will result in the loss of measurement information and therefore a deviation of performance from that predicted by the infinite domain analysis.

Rod Example

The first step in quantifying the truncation effect is to evaluate the point measurement of the motion variable at the center of the convolving sensor. This measurement can then be compared to the measurement from the convolving sensor to quantify its behavior.

Figure 2 shows a finite length, free-free rod with a forcing excitation at the left end. The length is $l = 1.0$ m, the axial stiffness is $EA = 1.0$ N and the mass per unit length is $\rho A = 1.0$ kg/m The point sensor and the center of the convolving sensor will be located at the midpoint of the rod

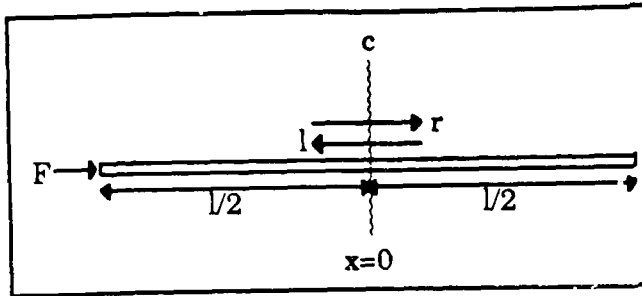(at $x=0$). Displacement is the measured variable in all of the rod examples.

Figure 2. Free-free rod with forcing at left end.

The displacement at position c, $x = 0$, is

$$u_c = \frac{1}{ikEA}\frac{\xi}{1-\xi^2}F \quad where \quad \xi = e^{-ikl/2} \quad (20)$$

The poles of the system are given by the roots of the denominator $1-\xi^2$. The displacement as a function of position is given by

$$u(x) = \frac{F}{ikEA}\frac{\xi}{1-\xi^4}\left(\xi^2 e^{ikx} + e^{-ikx}\right) \quad (21)$$

The modal, exponential and sinc spatial weighting functions are analyzed for the rod.

Modal Sensor. A modal sensor is one type of convolving sensor. It simply convolves the distributed measurements with the mode shape. The mode shapes for a free-free rod are

$$\phi(x) = A\cos(\frac{2m\pi}{l}x)$$
$$\phi(x) = B\sin(\frac{(2n+1)\pi}{l}x) \quad (22)$$

Selecting a cosine shape, the modal sensor is evaluated by

$$y = \int_{-l/2}^{l/2} u(x)\cos(k_0 x)dx$$
$$= \int_{-l/2}^{l/2} u(x)\frac{1}{2}\left(e^{ik_0 x} + e^{-ik_0 x}\right)dx \quad (23)$$

The transfer function from left end forcing to the modal sensor signal is

$$y = \frac{F}{ikEA}\frac{\xi}{1-\xi^2}\left\{\left[\frac{\sin(k+k_0)\delta}{k+k_0}\right] + \left[\frac{\sin(k-k_0)\delta}{k-k_0}\right]\right\} \quad (24)$$

Choosing $m = 4$ in Eq. (22) gives $k_0 = 8\pi/l$. The transfer function from the displacement at the center to the output of the modal sensor is

$$\frac{y}{u_c} = \frac{2k}{k^2 - \left(\frac{8\pi}{l}\right)^2}\sin\left(\frac{kl}{2}\right) \quad (25)$$

The sine function is zero at all wave numbers corresponding to a mode. However, the denominator equals zero at the wavenumber corresponding to the mode for which the sensor was designed, such that the value of Eq. (25) becomes $l/2$ for that mode.

Figure 3 shows the magnitudes of the transfer functions from force at the left end to displacement at the center of the rod (dotted curve), to the output of the modal sensor (dashed curve) and from the displacement at the center to the output of the modal sensor (solid curve [dashed divided by dotted]). Notice that the solid curve shows a zero at the same frequencies as the resonances (dotted) with the exception of the resonance for which the sensor was designed. The net result is that the modal sensor only 'sees' one mode in the rod (dashed curve). As might be expected from Fig. 3 an imperfect modal sensor will exhibit near pole-zero cancellation of the other modes.
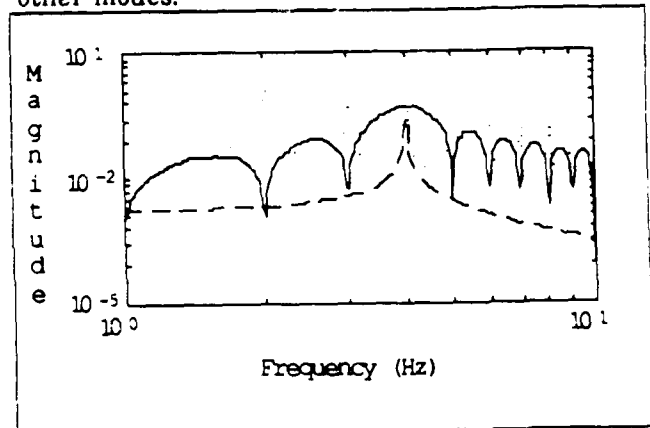

Figure 3. Transfer functions from force to displacement (dotted), to modal sensor (dashed) and from displacement to modal sensor (solid). EA=1.0 N, ρA=1.0 kg/m, l=1.0 m and k₀=8π m⁻¹

Exponential Sensor. The output of an exponential sensor is evaluated in the following manner

$$y = \frac{\alpha}{2(1 - e^{-\alpha\delta})}\left(\int_{-\delta}^{0} u(x)e^{\alpha x}dx + \int_{0}^{\delta} u(x)e^{-\alpha x}dx \right) \quad (26)$$

Notice that rather than evaluating the convolution across an infinite extent, the convolution is now evaluated across a finite length 2δ. The purpose of the constant in front of the integrals is to provide the same gain as the point sensor at low frequencies. The transfer function is given by

$$\frac{y}{F} = \frac{1}{ikEA}\frac{\xi}{1 - \xi^2}\left(\frac{\alpha}{k^2 + \alpha^2}\right)$$
$$\left[\frac{\alpha - e^{-\alpha\delta}\{\alpha\cos(k\delta) + k\sin(k\delta)\}}{1 - e^{-\alpha\delta}}\right] \quad (27)$$

Figure 4 shows the magnitude and phase of the transfer functions from the point measurement at the center of the rod to the output of the exponential sensor for three different lengths. In all three cases, α was selected to give a 10 Hz corner frequency (α = 62.83 Hz, c_O=1). The solid curve is for a sensor which covers the entire length of the rod (δ = 0.5m), the dashed curve is for a sensor which covers 10% of the rod resulting in a sensor of three scale lengths in extent (δ = 0.05m) and the dotted curve is for a sensor which covers 6% of the rod resulting in a sensor of less than two scale lengths in extent (δ = 0.^3m). Notice that the sensor which covers the entire rod has a clearly visible second order rolloff. This rolloff occurs without phase lag. The other sensors exhibit significant truncation effects between 10 and 100 Hz. The lower the number of scale lengths used in the sensor, the more significant the truncation effects at lower frequencies.

For wavenumbers much larger than α (high frequencies) Eq. (27) becomes

$$y = -\frac{F}{ikEA}\frac{\xi}{1 - \xi^2}\frac{\alpha}{k}\frac{e^{-\alpha\delta}\sin(k\delta)}{1 - e^{-\alpha\delta}} \quad (28)$$
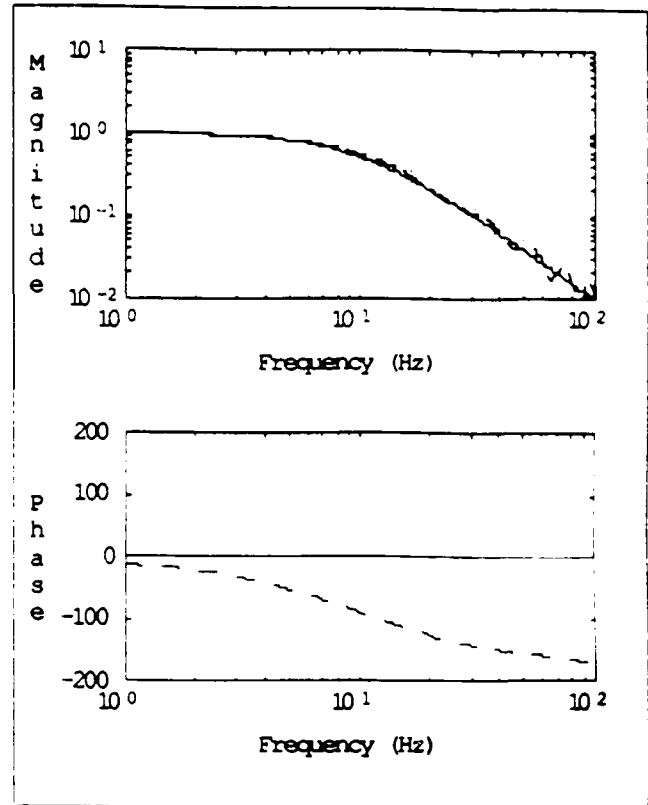
Figure 4. Transfer functions from displacement to exponential sensor output for lengths of sensors of δ=0.5 m (solid), δ=0.05 m (dashed), δ=0.03 m (dotted) and to the output of a double, real pole temporal filter (dash-dot). α=62.83 m^{-1}, EA=1.0 N, ρA=1.0 kg/m and l=1 m

Remembering that frequency and wavenumber are linearly related in the dispersion relation for the rod, Eq. (3), the truncation effects cause the second order rolloff to degrade to a first order temporal rolloff. The frequency at which this transition occurs is determined by the exponential term in Eq. (27). The larger the product $\alpha\delta$, the more scale lengths that are used in the sensor and the higher the frequency at which the truncation effects become important. Also notice that the shortest sensor exhibits a sign change, causing a 180 degree phase reversal just below 100 Hz. This illustrates the need for providing a reasonable length sensor.

The dash-dot curve in Fig. 4 shows the magnitude and phase of a temporal sensor with the same second order rolloff. Notice that this sensor starts reducing phase margin at a much lower frequency (above 1 Hz).
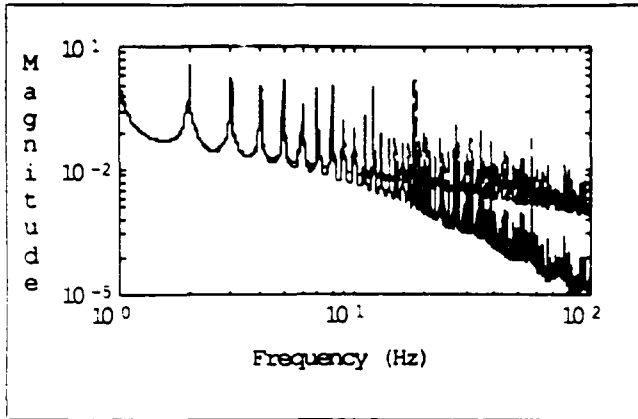
6

Figure 5. Transfer functions from end force to displacement (dashed curve) and to the output of the exponential sensor (solid, lower curve). δ=0.05 m

Figure 5 shows the magnitude of the transfer functions from end force to the displacement at the center of the rod (dashed curve) and to the output of the exponential sensor (solid, lower curve) for δ =0.05m. Notice that below 10 Hz the outputs have the same gain. However, above 10 Hz the exponential sensor exhibits a second order rolloff without phase lag (Fig. 4). The sensor truncation effects cause the waviness in the transfer function of the exponential sensor above 30 Hz.

Sinc Function. The transfer function from end forcing to the output of a truncated sinc function is found by evaluating

$$\frac{y}{F} = \frac{1}{ikEA}\frac{\Delta}{2\pi}\left(\frac{\xi}{1-\xi^4}\right)$$

$$\int_{-\delta}^{\delta}\left(\xi^2 e^{ikx} + e^{-ikx}\right)\frac{\sin(\Delta x)}{\Delta x}dx \quad (29)$$

Since the solution to this convolution is an infinite series, the integral was evaluated numerically.

Figure 6 shows the magnitude and phase of the transfer functions from the center motion to output of the truncated sinc function sensor (solid) and to the ideal, infinite extent sinc function sensor (dashed).
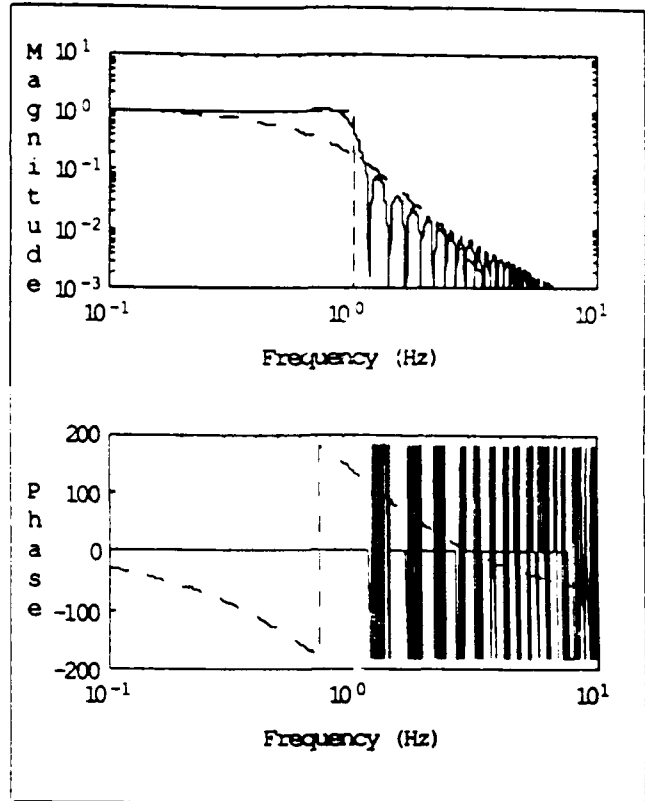

Figure 6. Transfer functions from center motion to the sinc function sensor (solid), to the infinite extent sinc function sensor (dashed) and to a fifth order temporal filter (dash-dot). EA=1.0 N, ρA=1.0 kg/m, l=16π m, Δ=1.0 m⁻¹, δ=4π m

The dash-dot curves in Fig. 6 show the transfer function of a temporal sensor which achieves a fifth order rolloff, like the sinc function between 0.8 and 1.2 Hz, using five identical poles at s = -62.83rad/sec. Notice that no phase shift occurs until the gain has attenuated one decade. The rolloff becomes sharper as more characteristic wavelengths Δ are included in the sensor.

Beam Example

This section studies the truncation effects of various sensors on a Bernoulli-Euler beam. The beam is pinned-pinned with a length of l = 7.32 m, a bending stiffness of EI = 31.1 Nm² and a mass per unit length of ρA = 2.85 kg/m (Figure 7). These values correspond to the beam used in the experiment.
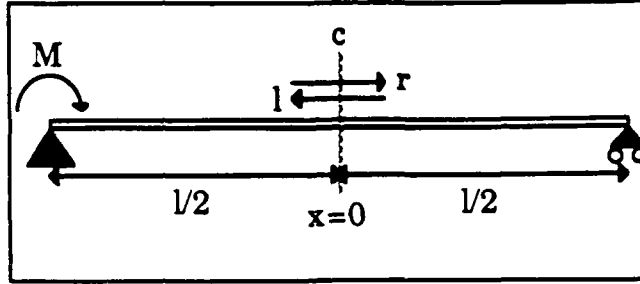
7

Figure 7. Pinned-pinned Bernoulli-Euler beam with a moment input at the left end.

The steady-state curvature at the center of the beam ($x=0$) is given by

$$\frac{\partial^2 v_c}{\partial x^2} = \frac{M}{EI} \frac{\xi_p\left(1+\xi_e^2\right) + \xi_e\left(1+\xi_p^2\right)}{\left(1+\xi_p^2\right)\left(1+\xi_e^2\right)} \quad (30)$$

where

$$\xi_p = e^{-ikl/2} \quad and \quad \xi_e = e^{-kl/2} \quad (31)$$

To perform the convolutions, the curvature as a function of position (x) is required. This is given by

$$\frac{\partial^2 v(x)}{\partial x^2} = \frac{M}{EI}\left\{ \frac{\xi_p\left(e^{-ikx} - \xi_p^2 e^{ikx}\right)}{\left(1-\xi_p^4\right)} \right.$$
$$\left. + \frac{\xi_e\left(e^{-kx} - \xi_e^2 e^{kx}\right)}{\left(1-\xi_e^4\right)} \right\} \quad (32)$$

which was obtained using the phase closure principle discussed in Ref. [3]. The one sensor studied for the beam is an exponential sensor used to create a first order temporal rolloff.

Exponential Sensor. The exponential sensor spatially convolves with the distributed curvature in the following manner

$$y = \frac{\alpha}{1-e^{-\alpha\delta}}\left\{ \int_{-\delta}^{0} \frac{\partial^2 v(x)}{\partial x^2}e^{\alpha x}dx \right.$$
$$\left. + \int_{0}^{\delta} \frac{\partial^2 v(x)}{\partial x^2}e^{-\alpha x}dx \right\} \quad (33)$$

This gives the steady-state sensor output as a function of the applied moment (M) at the left end of the beam as

$$y = \frac{M}{EI}\frac{1}{\left(1+\xi_p^2\right)\left(1+\xi_e^2\right)}\frac{\chi_1+\chi_2}{\alpha^4-k^4}\frac{\alpha}{1-e^{-\alpha\delta}} \quad (34)$$

where

$$\chi_1 = \xi_p\left(1+\xi_e^2\right)\left(\alpha^2-k^2\right)$$
$$\left[\alpha - e^{-\alpha\delta}\left(\alpha\cos(k\delta) - k\sin(k\delta)\right)\right] \quad (35)$$

and

$$\chi_2 = \xi_e\left(1+\xi_p^2\right)\left(\alpha^2+k^2\right)$$
$$\left[\alpha - e^{-\alpha\delta}\left(\alpha\cosh(k\delta) + k\sinh(k\delta)\right)\right] \quad (36)$$

Figure 8 shows the magnitude and phase of the transfer function from the point curvature sensor to the output of the exponential sensor for three different sensor lengths (δ). The value of $\alpha = 6.7$ m^{-1} places the temporal corner frequency near 23.0 Hz. Notice that the magnitude starts to roll off, with a corner frequency of 23 Hz, at a logarithmic slope of negative one. However, the phase does not exhibit the typical 90 degree phase lag associated with a first order rolloff (dash-dot curve in Fig. 8). This occurs because the first order rolloff is obtained by using both right and left half plane singularities whose logarithmic magnitudes add and whose phase contributions cancel. Notice in Fig. 8 that the temporal filter exhibits 90 degrees of lag one and a half decades before the $\delta = 0.3556$ m sensor exhibits its first phase shift.

The growing sinusoid at higher frequencies is an artifact of the truncation of the exponential sensor. Notice in Eq. (35) that χ_1 has a term which becomes larger as a linear function of wavenumber, k. For k much larger than α, this transfer function becomes

$$y\Big|_{k\to\infty} = \frac{M}{EI}\frac{e^{-\alpha\delta}}{\left(1+\xi_p^2\right)}\frac{\xi_p\sin(k\delta)}{k} \quad (37)$$

Due to the truncation of the exponential sensor, the first order rolloff predicted by the infinite domain analysis degrades to a half order temporal rolloff ($1/k$) at higher frequencies. The half order rolloff is determined by the logarithmic slope of a line connecting the peaks of the truncation induced sinusoid in the magnitude plot. The effect of the truncation manifests itself at a frequency which is determined by the exponential in the second term of Eq. (35). The product $\alpha\delta$ equals the number of spatial scale lengths encompassed by the sensor.
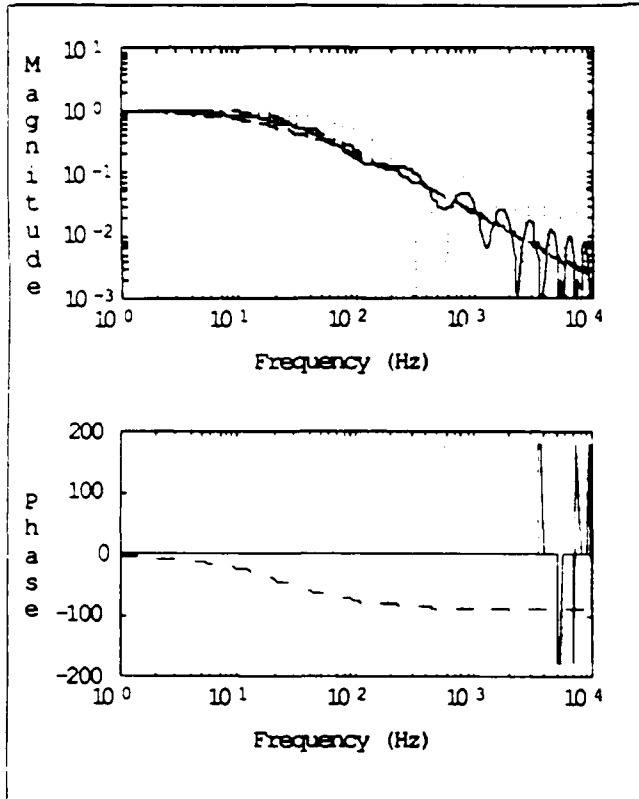
8

Figure 8. The transfer function from the point curvature sensor to the output of the exponential sensor for δ =0.71 m (dashed), δ=0.36 m (solid) and δ =0.18 m (dotted) and the transfer function for a first order temporal filter (dash-dot). EI=31.1Nm^2, ρA=2.85kg/m, l=7.3m & α=6.7m^{-1}

Notice in Eq. (37) that the sine term eventually causes the transfer function to shift 180 degrees and to continue to do so periodically. These sharp phase transitions can have implications for control. The onset of these transitions can be delayed in frequency, while the magnitude drops, by increasing the length of the sensor (2δ) to encompass more spatial scale lengths. Hopefully, gain stabilization can be achieved prior to the onset of these 180 degree phase reversals.

Figure 9 shows the magnitudes of the transfer functions from applied moment at the left end of the beam to the point curvature sensor (dashed) and to the output of the exponential sensor (solid).
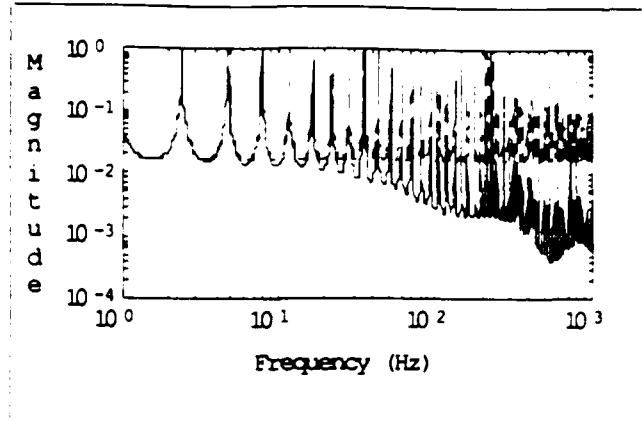

Figure 9. Magnitudes of the transfer functions from moment to the point curvature sensor (dashed) and to the exponential sensor (solid). δ=0.3556 m

Notice both the rolloff, with a corner frequency at 23.0 Hz, associated with the exponential sensor and the onset of the truncation effects near 100 Hz.

SENSOR FABRICATION

This section describes the methods used to fabricate the exponential and sinc function sensors for a beam. Sensor fabrication consisted of creating Mylar templates in the shape of the specific sensors, using these to mask the piezo polymer film during etching, and then attaching the piezo film to the beam. The final product consisted of connected sensor segments with an etched pattern on one side and a completely intact electrode on the other, an example of which is shown in Fig. 10.

Piezo Film

The Pennwalt Corporation's KYNAR Piezo Film was used. KYNAR Piezo Film is polyvinylidene flouride (PVDF) coated on both sides with conductive metal electrodes. PVDF is a long chain semi-crystalline polymer of the repeat unit CH_2-CF_2. The film produces charge per electrode area across the thickness of the polymer, due to the stress applied along the transverse axis.

The film is composed of three layers (Fig. 11): a pair of electrodes surrounding the PVDF. Vacuum deposition results in an electrode thickness of less than 0.1 μm. A
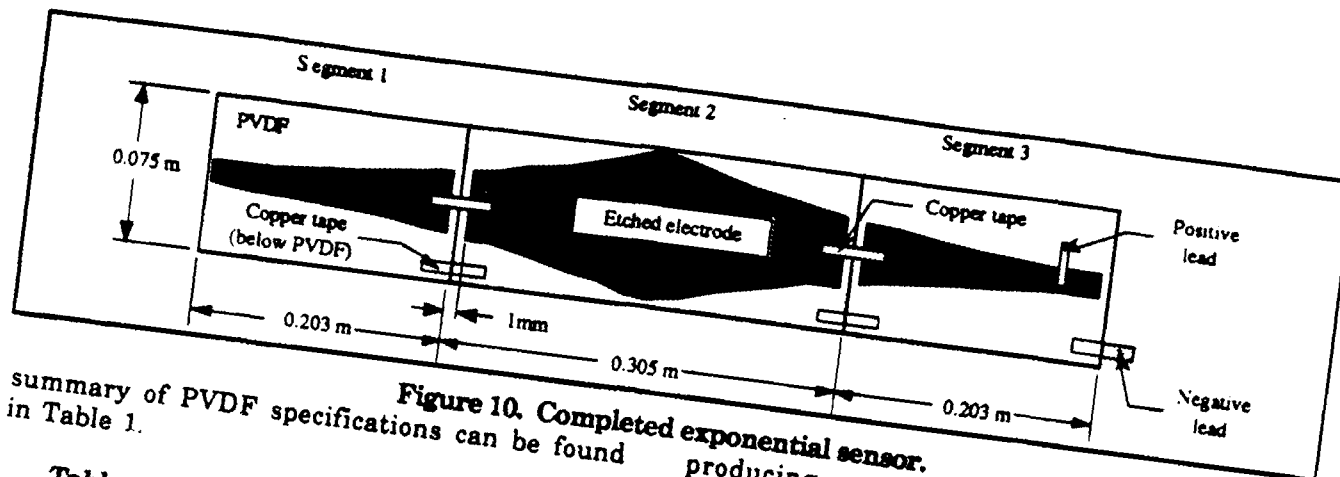
9

Figure 10. Completed exponential sensor.

Table 1. KYNAR Piezo Film Properties.

Thickness (Total)	52 μm
Thickness (Electrode)	<0.1 μm
Piezo Strain Constant (d$_{31}$)	23 x 10^{-12} C/N
Capacitance	205 x 10^{-12} F/cm^2
Electrical Impedance	78 Ω/cm^2
Density	1780 kg/m^3

Templates

The patterns were first plotted to actual size on paper. Since the total length of the sensor was greater than a standard PVDF sheet, several pieces were connected together to form the sensor. A millimeter was left between the etched pattern and the edge of the piezo film sheet (Fig. 10). This was done to prevent any possibility of shorting the electrodes when leads were added to connect the pieces. This pattern was then transferred onto a clear plastic sheet.

Thin sheets of Mylar (0.03 mm) backed on one side with acrylic adhesive were used for three purposes: as a mask to shield specific patterns from being etched away on the sensor, to provide an electrical insulator (if needed), and to attach the sensor to the beam. The Mylar masks were cut from the plastic templates.
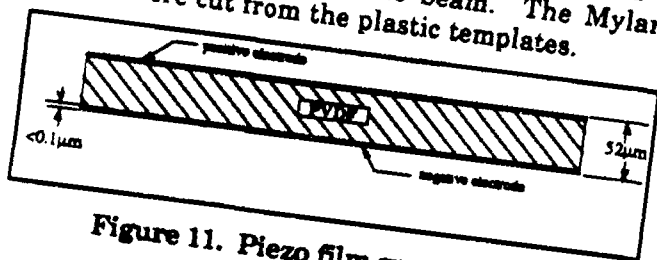

Figure 11. Piezo film cross-section.

Etching

Ferric chloride etching solution, obtained from a printed circuit-board etching kit, was used to etch the electrodes. When producing connecting pieces of film, it is imperative to ensure that all the etching is done on the same side with respect to polarity, be it positive or negative. "Negative segments," needed for the sinc sensor, were obtained by etching the negative side of the film and mounting these segments negative-side up, rather than the usual positive-side up arrangement.

The backing of the Mylar pattern was peeled off, exposing the adhesive, and stuck on the film. Using a paper towel slightly dampened with the ferric chloride etching solution, the exposed metal was "wiped away" from the sheet. A towel dampened with isopropanol solution served to neutralize the etching solution and clean the film. The electrode on the reverse side was kept completely intact.

Mounting

Once the sensor had been etched, it was ready to be attached to the beam, using Mylar as an electrical insulator and an adhesive layer. Rectangular Mylar pieces, larger than the sensor, were used to ensure complete adhesion. After cleaning the beam, the uncoated side of the Mylar was lightly covered with a spray adhesive and secured to the beam. The backing of the Mylar was then removed, exposing the adhesive.

A lead between the segments of the sensor must be applied to both surfaces of the piezo film to connect them electrically (Fig. 10). Copper tape with conductive adhesive was placed sticky side up between the Mylar and the sensor to connect the lower surfaces of the pieces of piezo film and to provide a negative lead. After applying the tape, the sensor sections were applied to the beam (Fig. 12). To provide the positive lead connecting sections of the sensor on the upper surface, copper tape was used again, this time sticky side down.
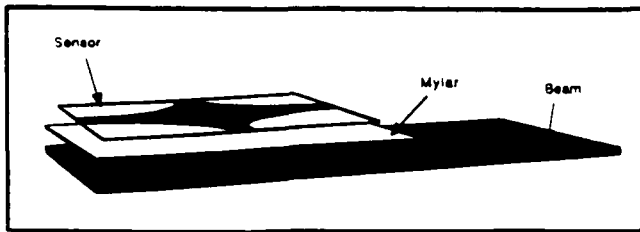
Figure 12. Sensor mounting.

Strain Gage

A strain gage was used to provide a point measurement for comparison with the piezo film signal. It was attached to the opposite side of the beam at the center point of the sensor. The gage resistance was 120 Ω and gage factor was 2.050.

Sensor Details

Two piezo film sensors were fabricated with electrode widths proportional to an exponential function and to a sinc function. All patterns were symmetric with respect to both a horizontal and a vertical centerline (Fig. 13). The exponential and sinc sensors were both mounted on the centerline of the beam. Further details can be found in Table 2.

The segment length was constrained by the size of the piezo film sheets (0.15 x 0.30 m). The width of the exponential and the sinc sensors was scaled to be half the width of a sheet.

Table 2. Sensor details.

Sensor	Exponential	Sinc function
Electrode pattern	$e^{\alpha x}, x<0$ $e^{-\alpha x}, x>0$	$[\sin(\Delta x)]/(\Delta x)$
	$\alpha = 6.7 \text{ m}^{-1}$	$\Delta = 27.1 \text{ m}^{-1}$
Corner freq.	23 Hz	386 Hz
Width at $x =0$	0.075 m	0.075 m
Length	0.71 m	1.16 m
Segments	3	9
Distance from free end of beam to $x =0$	1.35 m	2.46 m

BEAM EXPERIMENT

Set-Up

The sensors were mounted on a 7.32 m brass beam, composed of four 1.8 m sections bolted end to end and suspended by six pairs of cables (Fig. 14). The beam was 0.10 m wide, 3.175 mm thick and had the following properties: $EI = 31.1 \text{ Nm}^2$ and $\rho A = 2.85 \text{ kg/m}$. It can be modelled as a pinned-free Bernoulli-Euler beam up to approximately 1 kHz. A pseudo random noise source from a Tektronix Fourier Analyzer and a power amplifier were used to drive a PMI torque motor. This supplied a moment excitation at the pinned end of the beam.

The strain gage signal was passed through a strain gage conditioner to the Fourier analyzer. A high-impedance amplifier based on a 3140 FET op. amp. was used to lower the corner frequency of the highpass filter introduced by the film's capacitance. The input resistance of the circuit (R_{in} = 66 MΩ) was chosen so as to ensure a uniform signal gain in the frequency range of interest by placing the 1/RC pole at 0.06 Hz.

To help eliminate noise, the sensors were grounded to the beam, as was the shielded cable used for the strain gage.
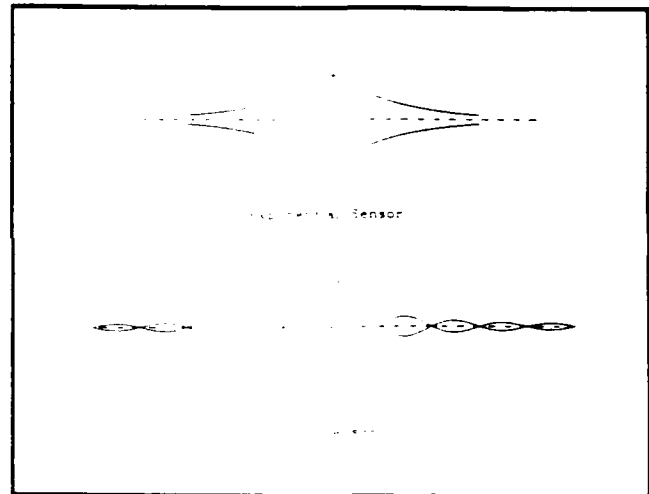
Figure 13. Electrode patterns.

Procedure

Each sensor was tested by exciting the beam with band-limited white noise. The noise source voltage level was such that a root-mean-square torque of 0.0794 Nm was applied to the beam in each test. Three channels of data were collected with the Fourier analyzer: the excitation voltage, the strain gage signal and the sensor signal. Transfer functions were then calculated from moment to strain gage signal, from moment to sensor signal and from strain gage signal to sensor signal. The transfer function data was taken from 1 Hz to 1 kHz. This range was selected so as to show the sensor behavior both before and after the corner frequency.

11

Figure 14. Beam set-up.

EXPERIMENTAL RESULTS

Exponential Sensor

Figure 15 shows the magnitude and phase of the transfer function from the strain gage signal to the exponential sensor signal. Examination of the coherence function (a ratio of cross-power spectra) indicated that the two signals were poorly correlated at the 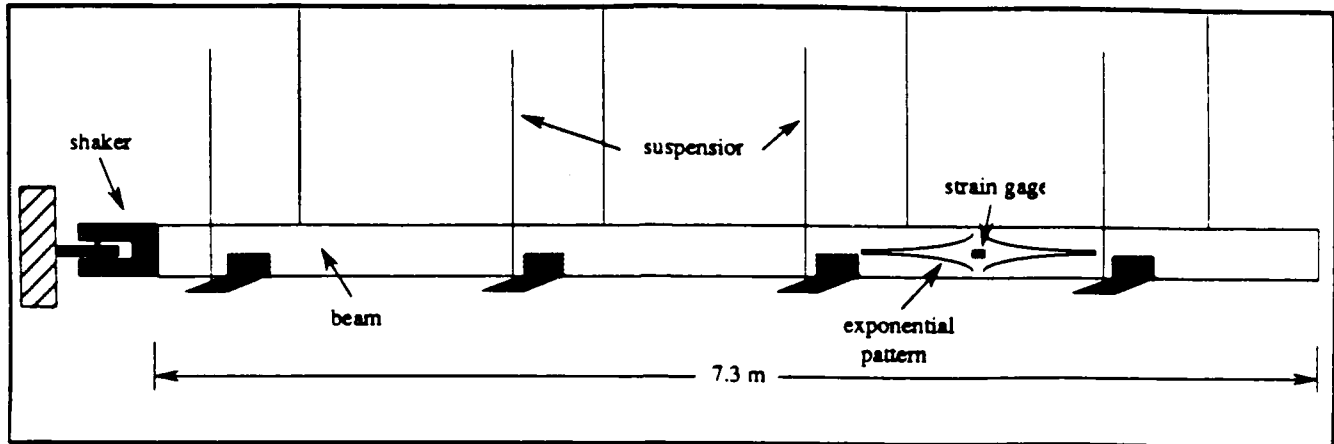sharp peaks in Fig. 15. These correspond to the low level signals obtained at the zeros of the transfer function from moment to either the exponential sensor signal or strain gage signal shown in Fig. 16. In order to highlight the general behavior of the sensor, the experimental transfer function was smoothed by taking a moving average of the experimental data.

Note the overall agreement with theory in Fig. 15. Below 100 Hz, the experimental data exhibits a roughly first order rolloff with a corner frequency of 23 Hz and no phase lag. As predicted in Fig. 8 for δ=0.36m, the truncation effects become evident in the data above 100 Hz. The first significant phase transition, around 250 Hz, occurs after the magnitude has been attenuated by about one decade. Figure 16 shows almost perfect overlay of the two transfer functions below 23 Hz and attenuation of the exponential sensor signal above 23 Hz.

Deviations between the data and theory are of two kinds. The first corresponds to the rapid fluctuation, with frequency, of the magnitude and phase. This could arise from several sources. As stated previously, the coherence was poor at these frequencies. This implies that either the strain gage or exponential sensor signals were below their noise floors.

Alternately, the two sensor gains may not be linear with amplitude, or the assumption of a Bernoulli-Euler beam may be inappropriate at higher frequencies. Nonlinearity in amplitude could cause the two signals to differ significantly near the poles or zeros where the transfer functions are changing rapidly. The introduction of torsion and plate modes in the beam could also affect the two sensors differently.

Two factors indicate that these spikes are of little concern. Detailed inspection of the two transfer functions in Fig. 16 show good agreement between the frequencies of the poles and zeros. In other words, the two sensors appear
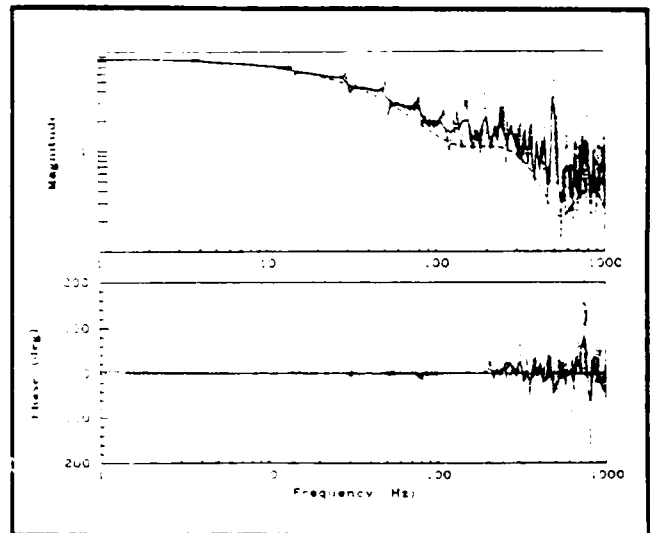

Figure 15. Transfer function between strain gage and exponential sensor signals for three cases: predicted (dashed); actual (dotted); and smoothed (solid).

12

to be observing the same phenomenon. In addition, Fig. 16 verifies that the magnitude of he exponential sensor signal drops and stays below that of the strain gage. Therefore, these spikes most likely result from poor signal to noise ratio near the zeros of the system.

The second kind of deviation corresponds to the observation that the magnitude of the experimental data is greater than that predicted at higher frequencies. This may be the result of a slower rolloff rate than predicted by the dispersion relation. An alternate explanation is that the actual and predicted corner frequencies are different causing the same rolloff as predicted but at higher frequency.
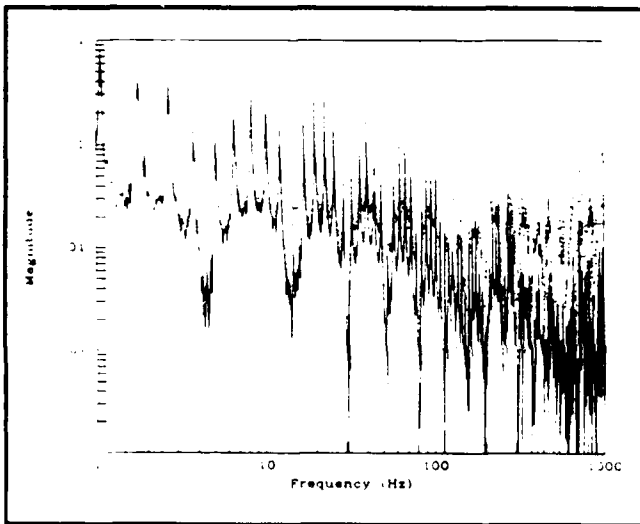

Figure 16. Transfer function from moment to strain gage signal (dotted) and to exponential sensor signal (solid).

Sinc Function Sensor

The data for the sinc sensor is presented in the same format in Figs. 17 and 18. However, the theoretical prediction is not overlayed because the sinc function analysis was performed for the rod. Nonetheless, performance similar to that shown in Fig. 6 would be expected.

Note in Fig. 17 that the magnitude exhibits a roughly fifth order rolloff between 300 and 500 Hz. This is in good agreement with the predicted rolloff near 386 Hz (Table 2). As would be expected from the rod analysis, the first significant phase shift occurs at 500 Hz, after attenuation of one decade, at the first zero caused by the sensor. A couple of the truncation induced

lobes in the magnitude plot are barely visible The two 180 degree phase reversals at 520 Hz and 710 Hz support this observation.

Figure 18 shows almost perfect overlay of the two transfer functions below 300 Hz. Above 300 Hz, the sinc function sensor signal attenuates rapidly with frequency.
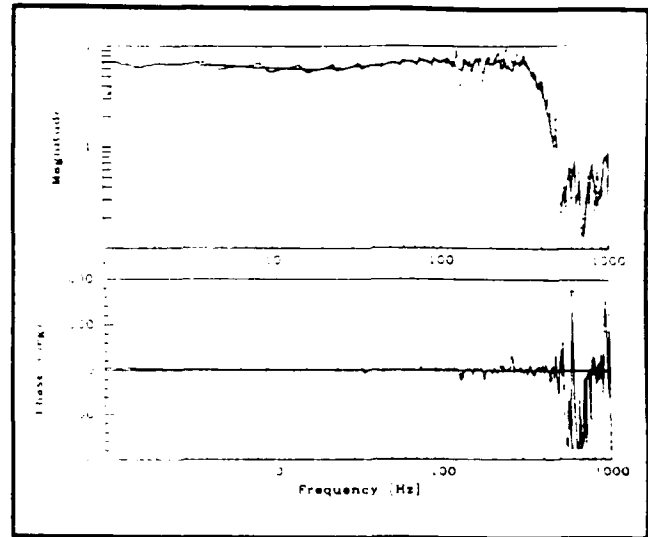

Figure 17. Transfer function between strain gage and sinc function sensor signals for two cases: actual (dotted) and smoothed (solid).
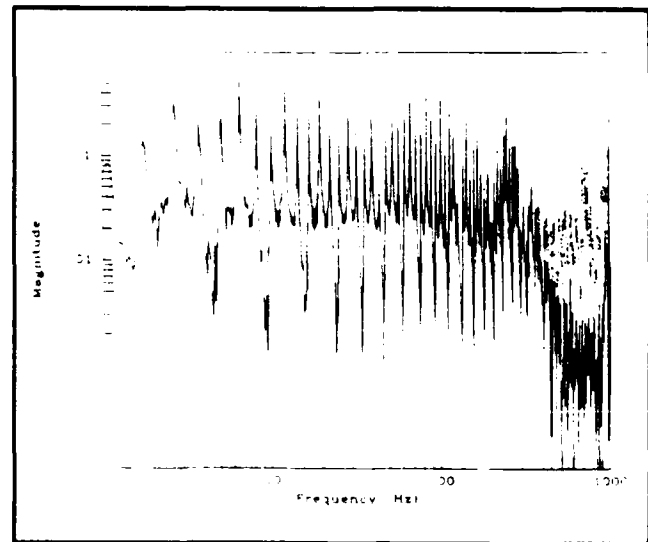

Figure 18. Transfer function from moment to strain gage signal (dotted) and to sinc function sensor signal (solid).

Note, when comparing the exponential and sinc function sensor data, that the latter exhibits greater fluctuation in magnitude below the corner frequency of the sensor. This may result from the greater number of zeros in the transfer function of the sinc function sensor (compare Figs. 16 and 18). The two sensor transfer functions have different zeros because they are located at different positions on the beam. This indicates that a sensor located at the center would provide the best coherence because it has no zeros in its transfer function.

SUMMARY

Measurement of a structure's spatial deflection pattern can be used to generate sensor signals which possess dynamic characteristics that are beneficial to real-time structural control applications. By convolving the sensor shape with the distributed measurements, the sensor filters the spatial harmonics of the deflection pattern. Since these harmonics are uniquely related to temporal frequencies, through that structural medium's dispersion relation, the resulting sensor signal becomes dynamically compensated. Since causality is not an issue in the spatial domain, the resulting dynamically compensated sensor signals can possess particular characteristics which are unobtainable through direct dynamic compensation. In particular, it was shown that magnitude rolloff could be achieved with no phase lag.

Several spatially convolving sensors were implemented on a beam. The output closely matched that predicted by the analyses. Since the structural length and amount of material available to construct the sensor were both finite, truncation of the convolved measurements was an issue. These truncation effects were quantified and their minimization, through delaying their manifestation to higher frequencies, was achieved by incorporating more scale lengths into the sensor.

Future work will entail working on several improvements to the sensors. In particular, smoother truncation of the sensor may help to delay, in frequency, the abrupt truncation effects. The objective of this sensor development is to reduce or eliminate the sensitivity of structural control, using point sensors, to short wavelength, high frequency phenomena.

REFERENCES

[1] Miller, D.W. Hall, S.R., "Experimental Results Using Active Control of Travelling Wave Power Flow," presented at the 1989 ASME Winter Meeting, San Francisco, CA, Dec. 11-15, 1989, submitted to *J. Guidance, Control, and Dynamics*.

[2] Miller, D.W., Hall, S.R. and von Flotow, A.H., "Optimal Control of Power Flow at Structural Junctions," *Proc. of the American Control Conference*, Pittsburgh, PA, June 21-23, 1989, pp. 212-220, submitted to *J. Sound and Vibration*.

[3] Miller, D. W. and von Flotow, A.H., "A Travelling Wave Approach to Power Flow in Structural Networks," *J. Sound and Vibration*, 128(1), 1989, pp. 145-162.

[4] MacMartin, D.G. and Hall, S.R., "Structural Control Experiments Using an H_∞ Power Flow Approach, submitted to the 1990 AIAA Guidance, Navigation and Control Conference, San Diego, CA, May, 1990 and to appear in *J. Guidance, Control, and Dynamics*..

[5] MacMartin, D.G. and Hall, S.R., "An H_∞ Power Flow Approach to Control of Uncertain Structures," to be presented at the American Control Conference,

[6] *KYNAR Piezo Film Technical Manual*, Pennwalt Corp., Valley Forge, PA, 1987.

[7] Lee, C.-K., "Piezoelectric Laminates for Torsional and Bending Modal Control: Theory and Experiment," PhD Dissertation, Cornell University, Ithaca, NY, 1987.

[8] de Luis, J., Crawley, E.F. and Hall, S.R., "Design and Implementation of Optimal Controllers for Intelligent Structures Using Infinite Order Structural Models," Space Systems Laboratory Report No. 3-89, M.I.T., Cambridge, MA, 1989.

[9] Bailey, T. and Hubbard, Jr., J.E., "Distributed Piezoelectric-Polymer Active Vibration Control of a Cantilever Beam," *J. Guidance, Control, and Dynamics*, 8(5), Sept.-Oct. 1985, pp. 605-611.

[10] Miller, S.E., Hubbard, J., "Theoretical and Experimental Analysis of Spatially Distributed Sensors on a Bernoulli-Euler Beam," Charles Stark Draper Laboratory Report C-5953, Cambridge, MA, 1987.

[11]   Lee, C.-K., Chiang, W.-W. and
O'Sullivan, T.C., "Piezoelectric Modal Sensors
and Actuators Achieving Critical Damping on a
Cantilever Plate," *Proc. of the
AIAA/ASME/ASCE/AHS/ASC 30th Structures,
Structural Dynamics and Materials
Conference*, Mobile, AL, April 3-5, 1989,
pp. 2018-2026.

[12]   Collins, S.A., Notestine, R.J., Padilla,
C.E., Ramey, M., Schmitz, E. and von Flotow,
A.H., "Design, Manufacture, and Application to
Space Robotics of Distributed Piezoelectric Film
Sensors," to be presented at 31st
AIAA/ASME/ASCE/AHS/ASC Structures,
Structural Dynamics and Materials
Conference, Long Beach, CA, April 2-4, 1990,
Paper No. AIAA-90-0949.

[13]   Meirovitch, L. and Baruh, H., "The
Implementation of Modal Filters for Control of
Structures," *J. Guidance, Control, and
Dynamics*, 8(6), Nov.-Dec. 1985, pp. 707-716.

Development of Wave-mode Observers for Active Wave Control of One-Dimensional Structures

By

Darryll J. Pines and Andreas H. von Flotow
Department of Aeronautics and Astronautics
Massachusetts Institute of Technology, Cambridge, Mass. 02139

ABSTRACT

This paper presents approaches for local observation of wave components which propagate along one-dimensional structural components. In each case, the solution of the partial differential equation which characterizes the dynamics of a one-dimensional structural component is written in terms of travelling waves. This form of the solution is then exploited in the first method to combine a sequence of spatially discrete measurements through a frequency dependent decoupling matrix to yield magnitude and direction of travelling wave components. In the second method a finite difference scheme is employed to estimate local deflections and internal forces at a cross-section in a member. A frequency domain transformation is then applied to this local state information to obtain the decoupled wave components. Because both of these methods require local discretization of the spatial domain, perfect resolution of decoupled wave components will suffer from the effects of spatial aliasing. Noisy measurements and approximate realization of the frequency dependent decoupling matrices also limit the achievable sensor decoupling. This paper addresses these issues and presents techniques for minimization of the effects of these limitations. Experimental results are not presented.

1.0 INTRODUCTION

Active control of structures whose dynamics can be modelled using partial differential equations has been studied extensively in the last two decades. Two applications receiving much attention are Large Space Structures-LSS-[1-3] and Structural Acoustics-[4-6]. Several modelling techniques such as modal analysis, finite element analysis-FEA, statistical energy analysis-SEA, and asymptotic modal analysis-AMA have been used in attempting to predict and control such structural dynamics. More recently, travelling wave descriptions-[4,5,7-11] , have become popular as an analysis tool for doing control design at discrete locations in complex structural networks. Locally the response of the structure is interpreted in terms of the propagation of travelling waves. This leads to local structural models which are exploited for local control.

This approach views one-dimensional structural members essentially as elastic waveguides which propagate signals from one point to the other-(See Figure 1). The response can be described by a superposition of certain wave-modes-(types) which can propagate along a member in the positive or negative direction. Depending upon the order of the mathematical model used to describe the dynamics of a member, only a finite number of wave-modes-(types) can propagate along any member. Representing the dynamics of a member in terms of wave-mode amplitudes is useful because these variables propagate along the member without coupling, and because the boundary conditions, transformed to these variables take on a clear, causal, input/output form. This causal form of the boundary conditions has, to date, formed the basis of all wave control theory-(and practice).

In this paper we develop procedures for extracting wave-mode states from physical measurements along structural members. The procedures utilize causal filtering of discrete sensor signals to extract the evolution of wave-modes propagating along both a rod and a beam. Two approaches are developed, which under appropriate approximation yield identical procedures. Measurements corrupted by noise are also considered from the point of view of optimal resolution of travelling wave components. Here we derive an expression for the spacing which maximizes the rms-(root mean squared) value of a travelling wave signal in the
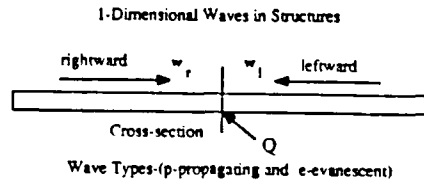
Figure 1 Local member dynamics described in terms of waves

presence of noise. We also discuss issues associated with the transient performance of the observer dynamics and with actual physical realizability.

2.0 TRAVELLING WAVE DYNAMICS AND FEEDFORWARD CONTROL

Following the frequency domain formalism developed in references [7] and [8], the dynamic behavior of each structural member can be obtained by superposing independently propagating travelling wave-modes at every frequency. The wave nature of each member can be exposed by manipulating the governing partial differential equations into a state-space description of member dynamics of the form

$$\frac{d y(x , \omega)}{d x} = A(\omega) y (x , \omega)$$

(1)

where $y(x,\omega)$ represents member deflections and/or internal forces. $A(\omega)$ is a frequency dependent matrix which characterizes member dynamics.

Equation-(1) can be diagonalized to give the following decoupled dynamic description of the spatial evolution of wave-mode variables, $w(x,\omega)$

$$\frac{d w(x , \omega)}{d x} = \Gamma(\omega) w (x , \omega)$$

(2)

where

$$\Gamma(\omega) = Y(\omega)^{-1} A(\omega) Y(\omega) \quad and \quad y (x , \omega) = Y(\omega) w(x , \omega)$$

(3)

The invertible matrix $Y(\omega)$ represents a frequency dependent set of complex eigenvectors which transforms member deflections and internal forces into leftward and rightward travelling wave-modes which propagate along the structure. Each column of this matrix yields the relative magnitude and phase of the physical variables, $y(x,\omega)$, which are present in the corresponding wave type.

Travelling waves, propagating independently along each member, can be scattered or generated at structural discontinuities or at locations where external excitations alter the homogeneous evolution of the member dynamics-(See Figure 2a). Locations at which the scattering or generation of travelling waves occur are referred to as junctions. Junctions are important because they help to describe the dynamics locally in terms of waves which are reflected, transmitted or generated as disturbances travel through a complex structural network. Transforming the junction governing equations(often refereed to as boundary conditions) into wave-mode coordinates, leads to a causal open loop description for outgoing waves, $w_o(x,\omega)$, which arise from the scattering of incoming waves, $w_i(x,\omega)$, and external excitations, $Q(\omega)$, which act at the junction

$$w_o(x , \omega) = S(\omega) w_i(x , \omega) + \Psi(\omega) Q(\omega)$$

(4)

The matrix $S(\omega)$ and $\Psi(\omega)$ are termed the scattering and generation matrix respectively. $Q(\omega)$ is a of vector of external excitations. Equation (4) is used to describe the local open loop plant wave dynamics, and forms the basis for most wave-control design methods.

As in the case of modal control methods full-state information is also desired for wave control implementation. Unfortunately, full knowledge of wave-mode states is complicated by the fact that they are not sensed directly, but must be inferred from physical measurements. This lack of direct accessibility of wave-mode states complicates control procedures based on this approach. Thus, instead of being able to directly cancel the propagation of outgoing waves from a junction by simply inverting the local plant dynamics $S(\omega)$ in a feed-forward control loop, where typically the form of the compensation $K(\omega)$ which generates control forces $Q(\omega)$ is given by(See upper loop in Figure 2b);

$$Q(\omega) = K(\omega) w_i(\omega)$$

$$= - \Psi^{-1}(\omega) S(\omega) w_i(\omega)$$

(5)

we are forced to realize a more complicated form of the compensation to implement most wave control designs(See lower loop in Figure 2c). This modified control loop structure generates the following form for the closed loop compensation
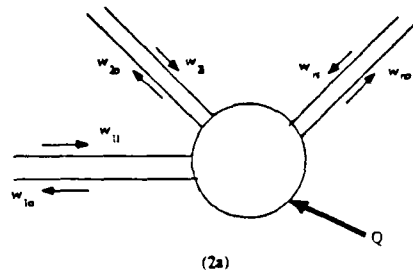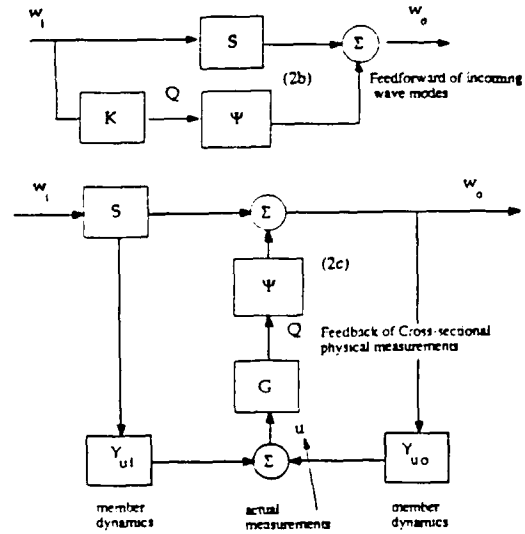
Figure (2a) Generic Scattering Junction for local input/output dynamics. (2b) (Upper Loop) Ideal active control loop is possible only when decoupled wave components can be fed directly to the control vector. (2c) (Lower Loop) Actual closed loop realization where lack of decoupling of wave components leads to feedback of outgoing waves to the control Q.

$$Q(\omega) = G(\omega) u(\omega)$$

$$= G(\omega) Y(\omega) \begin{bmatrix} w_i(\omega) \\ w_o(\omega) \end{bmatrix} = G(\omega) \begin{bmatrix} Y_{ui} & Y_{uo} \end{bmatrix} \begin{bmatrix} w_i(\omega) \\ w_o(\omega) \end{bmatrix} \tag{6}$$

where $u(\omega)$ is a vector of local deflections and internal forces, $Y(\omega)$ is a transformation matrix relating $u(\omega)$ to incoming-(w_i) and outgoing waves-(w_o) at the junction and $G(\omega)$ is the compensation matrix multiplying $u(\omega)$.

Notice that in this equation the compensation generates control forces based on physical measurements $u(\omega)$. However, this form of the compensation leads to the superfluous feedback of outgoing waves-(w_o) back into the control, giving rise to the following loop transfer function

$$H(\omega) = I - \Psi(\omega) G(\omega) Y_{uo}(\omega) \tag{7}$$

where I is the identity matrix.

The problem with this additional loop in the control structure is two-fold: (1) The presence of the loop complicates the design and implementation of $G(\omega)$, and (2) The loop may lead to a local instability. Thus, the difficulties associated with implementation of the form of the compensation given in equation (6) motivates the need for sensors which can directly measure wave components. Knowledge of the magnitude and direction of these wave components would permit implementation of the decoupled form of the compensation given in equation (5).

3.0 WAVE-MODE OBSERVATION

Many sophisticated analytical procedures for control design are based on the assumption that the full-state vector is available for measurement. Wave control is no exception; it would exploit full knowledge of a "local state." In addition wave control methods add more complexity since most wave control designs yield compensators which are not static functions of the local state and are often difficult to realize-[4,5,7-11]. As in most control design methods, performance is limited when the full state of the dynamic system is not available. We are thus faced with the common dilemma of approximating state information from a few measurements. In the work to follow we present two procedures for estimating wave-modes along one-dimensional structures from a limited number of measurements. We label these wave-mode estimates w to explicitly differentiate them from the unknown, actual wave-modes, w.

3.1 SPATIALLY COLLOCATED MEASUREMENTS

The most direct approach to sensing waves propagating along one dimensional members is to infer this information from full-knowledge of the dynamic state of the system at a cross-section. This is done by inverting the wave-mode transformation matrix-(eq'n 3) relating physical cross-sectional measurements to wave-mode coordinates.

$$\begin{bmatrix} w_r(x, \omega) \\ w_l(x, \omega) \end{bmatrix} = \begin{bmatrix} Y(\omega)^{-1} \end{bmatrix} y(x, \omega) \tag{8}$$

where subscripts r and l denote the rightward and leftward wave components respectively. Difficulties with

such an approach are specific to the case at hand. It may be physically impractical to measure all of $y(x,\omega)$ at a single point, (e.g. measurement of the internal shear force in a beam is difficult). Further, the frequency dependence of this matrix is such that temporal filters cannot always be built to implement equation (8); as the theoretical matrix $Y^{-1}(\omega)$ may be non-causal.

Example L1-(Longitudinal Waves in a Rod)
In the case of a longitudinal rod the dynamics are described by the partial differential equation

$$EA\frac{\partial^2 u(x,t)}{\partial x^2} = \rho A\frac{\partial^2 u(x,t)}{\partial t^2}$$

(9)

which has steady-state harmonic solutions of the form

$$u(x,t) = (w_r(0)e^{-jkx} + w_l(0)e^{jkx})e^{j\omega t}$$

(10a)

and the corresponding broadband solution of the form

$$u(x,\omega) = (w_r(0,\omega)e^{-jkx} + w_l(0,\omega)e^{jkx})$$

(10b)

where the subscripts r and l refer to rightward and leftward travelling components respectively. The wavenumber k is given by

$$k = \omega\sqrt{\frac{\rho A}{EA}}$$

Transforming equation (9) into the frequency domain and obtaining a state-space representation of the dynamics in the form of equation (1)-($y(x,\omega)=[u(x,\omega)\ u'(x,\omega)]^T$) leads to the following relation between wave-mode coordinates and physical states at a cross-section

$$\begin{bmatrix} w_r(x,\omega) \\ w_l(x,\omega) \end{bmatrix} = \begin{bmatrix} \dfrac{1}{2} & \dfrac{1}{2j\omega}\sqrt{\dfrac{EA}{\rho A}} \\ \dfrac{1}{2} & -\dfrac{1}{2j\omega}\sqrt{\dfrac{EA}{\rho A}} \end{bmatrix} \begin{bmatrix} u(x,\omega) \\ u'(x,\omega) \end{bmatrix}$$

(11)

where steady-state behavior is not implied.

Estimates for the local right and left-going wave modes are thus available from a linear combination of local deflection, u, and strain, u'. Temporally, only an integration of strain is required. This appears to be a viable technique for obsererving wave components along a rod, although care would be required to avoid integrating a strain gage bias.

Example B1-(Bending waves in a B-E Beam)
The governing partial differential equation describing the dynamics of a Bernoulli-Euler beam is given by

$$EI\frac{\partial^4 u(x,t)}{\partial x^4} + \rho A\frac{\partial^2 u(x,t)}{\partial t^2} = 0$$

(12)

where the Fourier transformed solution in terms of waves can be represented as

$$u(x,\omega) = w_{rp}(0,\omega)e^{-jkx} + w_{re}(0,\omega)e^{-kx} +$$

$$w_{lp}(0,\omega)e^{jkx} + w_{le}(0,\omega)e^{kx}$$

(13)

where the subscripts p,e refer to whether a wave component is a propagating or an evanescent term, and r and l refer to whether it is rightward or leftward going. Inverting the transformation relation between wave-modes and physical member measurements at x we find that

$$\begin{bmatrix} w_{rp}(x,\omega) \\ w_{re}(x,\omega) \\ w_{lp}(x,\omega) \\ w_{le}(x,\omega) \end{bmatrix} = \begin{bmatrix} \dfrac{1}{4} & \dfrac{j}{4k} & \dfrac{j}{4EIk^3} & -\dfrac{1}{4EIk^2} \\ \dfrac{1}{4} & \dfrac{1}{4k} & -\dfrac{1}{4EIk^3} & \dfrac{1}{4EIk^2} \\ \dfrac{1}{4} & -\dfrac{j}{4k} & -\dfrac{j}{4EIk^3} & -\dfrac{1}{4EIk^2} \\ \dfrac{1}{4} & -\dfrac{1}{4k} & \dfrac{1}{4EIk^3} & \dfrac{1}{4EIk^2} \end{bmatrix} \begin{bmatrix} u(x,\omega) \\ u'(x,\omega) \\ -EIu'''(x,\omega) \\ EIu''(x,\omega) \end{bmatrix}$$

(14)

In this expression the wavenumber k for transverse bending motion is given by

$$k = \omega^{\frac{1}{2}}\sqrt[4]{\frac{\rho A}{EI}}$$

Thus equation (14), if implemented as written, would require measurement of lateral deflection, u, slope, u', bending moment M= Elu" and shear force, V=-Elu'''. Measurements of internal shear force V, with a point sensor, may not be practical. These would be combined using temporal filters with gain characteristics of 1, $\omega^{(-1/2)}$, ω^{-1}, $\omega^{(-3/2)}$, - d with various constant phases. Not all are implementable in real time since they are acausal.

However, if we are only interested in observing the propagating components, then rows one and three give

$$
\begin{bmatrix} w_{rp} \\ w_{lp} \end{bmatrix} = \begin{bmatrix} \frac{1}{4} & \frac{e^{-j\frac{\pi}{4}}}{4\sqrt{j\omega}}\sqrt[4]{\frac{EI}{\rho A}} & \frac{e^{j\frac{\pi}{4}}}{4(j\omega)^{\frac{3}{2}}\sqrt[4]{EI(\rho A)^3}} & \frac{e^{-j\frac{\pi}{2}}}{4j\omega\sqrt{EI\rho A}} \\ \frac{1}{4} & \frac{-e^{-j\frac{\pi}{4}}}{4\sqrt{j\omega}}\sqrt[4]{\frac{EI}{\rho A}} & \frac{-e^{j\frac{\pi}{4}}}{4(j\omega)^{\frac{3}{2}}\sqrt[4]{EI(\rho A)^3}} & \frac{e^{-j\frac{\pi}{2}}}{4j\omega\sqrt{EI\rho A}} \end{bmatrix} \begin{bmatrix} u \\ u' \\ -Elu'' \\ Elu'' \end{bmatrix}
$$

(15)

where we have substituted for k and rearranged to illustrate elements having positive and negative phase delays. Notice that elements of the third column are anticipatory; requiring prior knowledge of the internal shear at a point in the beam. This complicates direct observation of w_{rp} and w_{lp} from 4 collocated point sensors. However, several wavelengths removed from structural discontinuities near field terms contribute

negligibly to the response u(x,ω) given in equation (13). Thus, at high frequencies we can interpret the response of the beam in terms of propagating components only. This reduces the number of sensors required for observation to two. One possible causal solution is given by

$$
\begin{bmatrix} \hat{w}_{rp}(x,\omega) \\ \hat{w}_{lp}(x,\omega) \end{bmatrix} = \begin{bmatrix} \frac{e^{-j\frac{\pi}{4}}}{2\sqrt{j\omega}}\sqrt[4]{\frac{EI}{\rho A}} & \frac{e^{-j\frac{\pi}{2}}}{2j\omega\sqrt{EI\rho A}} \\ -\frac{e^{-j\frac{\pi}{4}}}{2\sqrt{j\omega}}\sqrt[4]{\frac{EI}{\rho A}} & \frac{e^{-j\frac{\pi}{2}}}{2j\omega\sqrt{EI\rho A}} \end{bmatrix} \begin{bmatrix} u'(x,\omega) \\ Elu''(x,\omega) \end{bmatrix}
$$

(16)

where measurement of only slope u' and bending moment M=Elu" are required. This expression combines phase delays with temporal filters having gain characteristics of $\omega^{(1/2)}$ and ω. Unfortunately, real time implementation would require approximation of these phase delays which are only valid over some restricted frequency range. Another possible causal choice of measurements might involve the deflection-u and slope-u'.

These two examples have highlighted two difficulties with the simple concept of employing the transformation of y(x,ω) between physical measurements at a point and the wave components at that point. The first is simply the difficulty of measuring all the necessary variables at the cross-section in question. The second difficulty is the impossibility of achieving the needed (acausal) temporal filtering in real time. This requrement for acausal filtering appears to be related to dispersive wave propagation.

3.2 SPATIALLY SEQUENTIAL NON-COLLOCATED MEASUREMENT

In this section we relax a requirement implicitly imposed in the previous section; that all measurements be spatially collocated. Rather we suggest a spatial stencil of point sensors, (implicitly assumed to be strain gages) and discuss possible signal processing approaches to extract wave components from this sensor array. Such techniques are widespread in ocean acoustics and geophysics, where the domain is three-dimensional and the wave propagation is essentially non-dispersive. Real-time implementation is not an issue in these fields, since active control is not contemplated. Acausal signal processing is thus not ruled out in these fields.

3.2.1 Exploiting Phase Delays

One approach might involve a sequence of similar measurements at multiple locations along a member(See Figure 3). This implies that waves propagating without attenuation along the member will only have relative phase leads or lag between spatially discrete points and that a signal processing scheme might exploit this known phase relation to identify the wave component of interest.

Example L2-(Longitudinal Waves in a Rod)
Consider again the longitudinal rod with successive axial strain measurements given by

$$
u'\left(-\frac{\Delta}{2},\omega\right) = jk\left(-w_r(0,\omega)e^{jk\frac{\Delta}{2}} + w_l(0,\omega)e^{-jk\frac{\Delta}{2}}\right)
$$

(17)

and

$$u' \left(\frac{\Delta}{2}, \omega \right) = jk \left(- w_r(0, \omega) e^{-jk\frac{\Delta}{2}} + w_l(0, \omega) e^{jk\frac{\Delta}{2}} \right)$$

(18)

where Δ is the separation between the two strain gages and $x=0$ is taken to identify a point midway between them. Solving for the rightward and leftward wave-modes leads to an expression (for this non-dispersive example involving both positive and negative delays)

$$\begin{bmatrix} w_r(0, \omega) \\ w_l(0, \omega) \end{bmatrix} = F(\Delta, \omega) \begin{bmatrix} u'(-\frac{\Delta}{2}, \omega) \\ u'(\frac{\Delta}{2}, \omega) \end{bmatrix}$$

$$= \frac{l}{jk(e^{-jk\Delta} - e^{jk\Delta})} \begin{bmatrix} e^{jk\frac{\Delta}{2}} & -e^{-jk\frac{\Delta}{2}} \\ e^{-jk\frac{\Delta}{2}} & -e^{jk\frac{\Delta}{2}} \end{bmatrix} \begin{bmatrix} u'(-\frac{\Delta}{2}, \omega) \\ u'(\frac{\Delta}{2}, \omega) \end{bmatrix}$$

(19)

where $F(\Delta,\omega)$ is referred to as the observation matrix.

If one can assume $k\Delta \ll 1$ (the sensor spacing is much less than a wavelength) some straightforward algebraic manipulation leads to the following first-order form of equation(17):

$$\begin{bmatrix} \hat{w}_r (0, \omega) \\ \hat{w}_l (0, \omega) \end{bmatrix} \equiv \begin{bmatrix} \frac{l}{2 k^2 \Delta} - \frac{l}{4 jk} & -\frac{l}{2 k^2 \Delta} - \frac{l}{4 jk} \\ \frac{l}{2 k^2 \Delta} + \frac{l}{4 jk} & -\frac{l}{2 k^2 \Delta} + \frac{l}{4 jk} \end{bmatrix} \begin{bmatrix} u'(-\frac{\Delta}{2}, \omega) \\ u'(\frac{\Delta}{2}, \omega) \end{bmatrix}$$

(20)

Evaluation of this expression requires up to two causal temporal integrations of each local strain measurement. Sensor bias would need to be dealt with. Figure 4 compares the first-and the infinite-order expressions of the (1,1) and (1,2) terms of this observation matrix. Here we define the non-dimensional amplitude and frequency to be

$$w_{nd} = \frac{w}{\Delta} \quad and \quad \omega_{nd} = \frac{\omega \Delta}{\sqrt{\frac{EA}{\rho A}}}$$
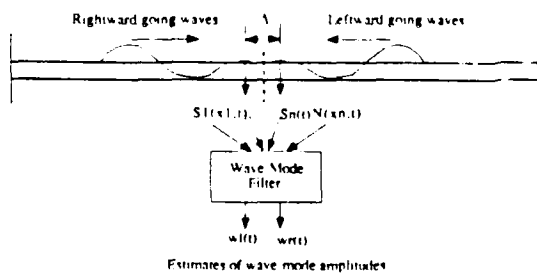
Figure 3 Spatially Sequential Measurement Method for Observation of Travelling Wave Components along a 1-dimensional member.
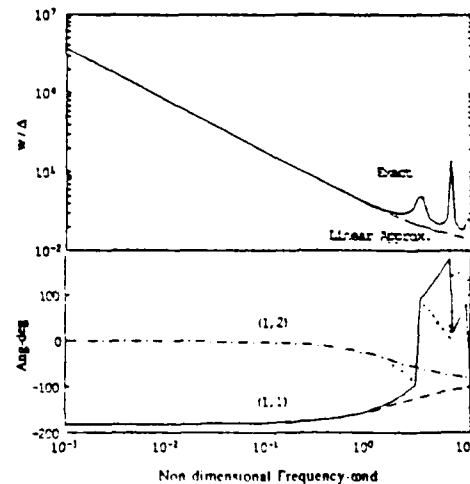
Figure 4 Elements of the observation matrix $F(\Delta,\omega)$ which decouples propagating wave components traversing a longitudinal rod from local strain measurements. Non dimensional magnitude (w/Δ) and phase (deg) are plotted versus non dimensional frequency ($\omega\Delta/(\rho A/EA)^{(1/2)}$) for each element. The linearized approximation of these elements are also shown.

Notice that in this figure there is close agreement between the first-and infinite-order elements up to $\omega_{nd}=1$.

However, as $\omega_{nd} \gg 1$, the phenomenon of spatial aliasing appears in the form of resonance behavior in the magnitude and phase of the infinite-order elements. These resonances arise because spatially discrete measurements are incapable of resolving all possible wavelengths propagating along the member. Therefore, whenever

$$\omega_{nd} > \pi \quad or \quad \omega > (\pi/\Delta)(EA/\rho A)^{(1/2)}$$

there will be ambiguity in determining the true wavelength of a disturbance propagating along a rod.

Example B2·(Bending Waves in a B-E beam)

As in the case of the longitudinal rod, we can infer information about wave-modes from sequential strain measurements at spatially discrete locations along a simple Bernoulli-Euler beam member. Applying the same approach we can write local expressions for bending strains in terms of wave-mode amplitudes as

$$\epsilon_b(x,\omega) = -\frac{t_b}{2}k^2(- w_{rp}(0,\omega)e^{-jkx} + w_{re}(0,\omega)e^{-kx}$$

$$- w_{lp}(0,\omega)e^{jkx} + w_{le}(0,\omega)e^{kx})$$

(21)

where ϵ_b refers to bending strain on the surface of a member of rectangular cross-section, t_h denotes the thickness of the beam, and x takes on four values. If the strain gage stencil is equally spaced about x=0, these values are $(\pm\Delta/2)$, $(\pm3\Delta/2)$, where Δ is the gage spacing.

Solving for the frequency dependent wave-mode amplitudes at x=0 we arrive at the following matrix expression

$$w(0,\omega)_{4\times1} = F(\Delta,\omega)_{4\times4}\,\epsilon_b(\Delta,\omega)_{4\times1}$$

(22)

where each element in $F(\Delta,\omega)$ represents the contribution to the evolution of a particular wave-mode from a discrete local measurement. For the sake of brevity the elements of this matrix are not given, however, the non-dimensional magnitude-(w_{nd}) and phase of elements of a typical row of this matrix are plotted versus non-dimensional square root frequency-(ω_{nd}) in figure 5 where

$$w_{nd} = \frac{wt_b}{\Delta^2} \quad and \quad \omega_{nd} = \frac{\omega^{\frac{1}{2}}}{\Delta}\sqrt[4]{\frac{EI}{\rho A}}$$

Unfortunately, attempts at linearizing the elements of $F(\Delta,\omega)$(for $k\Delta<<1$) causes the matrix to become singular. This singularity occurs because we cannot infer four wave-modes from a strain field which is approximated as locally linear in space. Only two sensors are actually needed to determine this strain field approximation. Hence, the linearized version of matrix $F(\Delta,\omega)$ is no longer of full rank, and we would be forced to higher order-(in $k\Delta$) approximations.
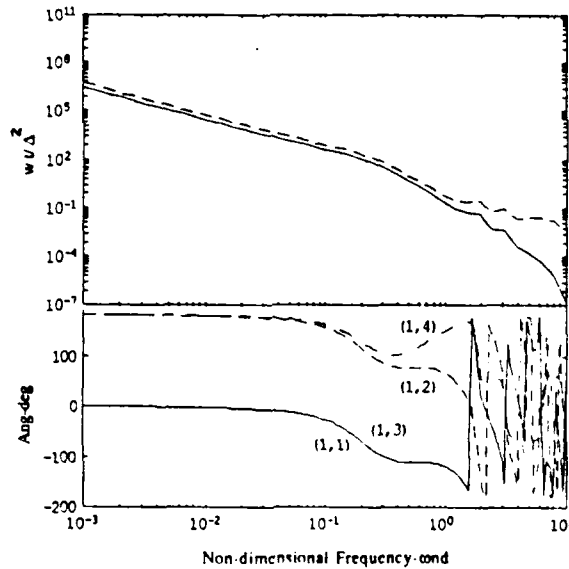
Figure 5 Elements of the observation matrix $F_{4\times4}(\Delta,\omega)$ which decouples travelling wave components traversing a B-E beam from local strain measurements. Non dimensional magnitude (w/Δ) and phase (deg) are plotted versus non dimensional frequency-$(\omega^{1/2}\Delta(EI/\rho A)^{1/4})$ for each element

Several wavelengths removed from structural discontinuities and boundary effects, near field components contribute negligibly to the response of the beam. As a result we can interpret the response of the beam at high frequencies in terms of travelling components only. With this assumption the rightward and leftward travelling wave-mode can be found from an expression which only accounts for the contributions of travelling components;.

$$\begin{bmatrix} \hat{w}_{rp} \ (0,\omega) \\ \hat{w}_{lp} \ (0,\omega) \end{bmatrix} = \frac{2}{k^2 t_b (e^{jk\Delta} - e^{-jk\Delta})} \begin{bmatrix} e^{jk\frac{\Delta}{2}} & -e^{-jk\frac{\Delta}{2}} \\ -e^{-jk\frac{\Delta}{2}} & e^{jk\frac{\Delta}{2}} \end{bmatrix} \begin{bmatrix} \epsilon_b(-\frac{\Delta}{2},\omega) \\ \epsilon_b(\frac{\Delta}{2},\omega) \end{bmatrix}$$

(23)

Linearizing the elements of this matrix for small separation distance leads to the non-causal solution given by

$$\begin{bmatrix} \hat{w}_{rp} \ (0,\omega) \\ \hat{w}_{lp} \ (0,\omega) \end{bmatrix} = \begin{bmatrix} -\frac{1}{jk^3 t_b \Delta} - \frac{1}{2k^2 t_b} & \frac{1}{jk^3 t_b \Delta} - \frac{1}{2k^2 t_b} \\ \frac{1}{jk^3 t_b \Delta} - \frac{1}{2k^2 t_b} & -\frac{1}{jk^3 t_b \Delta} - \frac{1}{2k^2 t_b} \end{bmatrix} \begin{bmatrix} \epsilon_b(-\frac{\Delta}{2},\omega) \\ \epsilon_b(\frac{\Delta}{2},\omega) \end{bmatrix}$$

(24)

The (1,1) and (1,2) elements of equations (23) and(24) are plotted in figure 6. As in the case of the rod this figure shows that there is close agreement between the nonlinear matrix elements and their linearized approximations in both phase and magnitude over a broad frequency range. Note that in this case, linearizing in $k\Delta$ leads to an approximation first-order in $k\Delta$, but not linear in ω. This is because of the form of the dispersion relation. Unfortunately, this filter is not causal. Spatial aliasing is again apparent in the form of resonance behavior in the observation matrix elements whenever

$$\omega_{nd} > \pi, \ (n=1,2,3,...) \quad \text{or} \quad \omega > (\pi)^2 \Delta^2 (\rho A/EI)^{(1/2)}$$

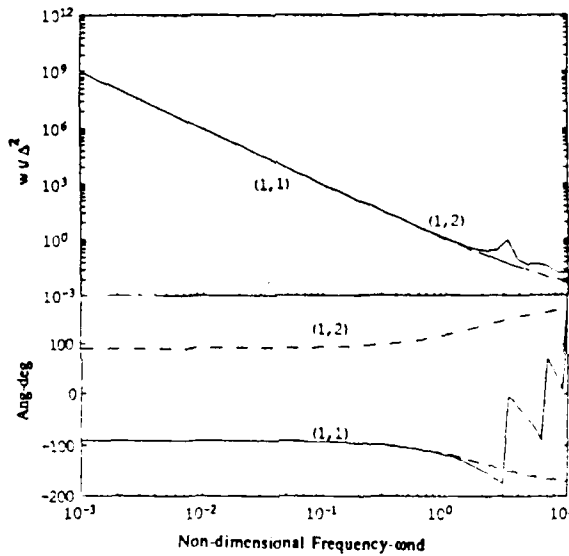Figure 6 Approximate linearized elements (near field components have been assumed to negligible) of the observation matrix $F_{2 \times 2}(\Delta,\omega)$ which decouples propagating wave components traversing a B-E beam from local strain measurements. Non-dimensional magnitude $(\hat{w}/\Delta)$ and phase-(deg) are plotted versus non-dimensional frequency-$(\omega^{(1/2)}\Delta/(EI/\rho A)^{(1/4)})$ for each element.

3.2.2 Finite Difference Approximation of Partial Differential Equation

Strain sensors are the most convenient types of instruments used to infer an element of the physical state vector at spatially discrete points along one-dimensional members. The reason for this is that they are lightweight, thin and inexpensive. More importantly, the sensor contribution to the overall impedance of the structure is negligible. This implies that this type of measuring instrument has very little effect on the propagation and scattering properties of waves as they traverse individual members in a network.

Pavic'-[13,14] also demonstrates that strain sensors can be used to estimate spatial derivatives at locations along a member which are far removed from structural discontinuities. At such locations Pavic' employs a finite difference scheme which he uses to approximate the first and second derivatives of strain for both one and two-dimensional members. He uses this information to determine local inertial acceleration, effectively using a portion of the structure as the accelerometer proof mass. This same approach can be used as an effective way of determining the direction and amplitude of longitudinal and transverse travelling waves.

Example L3-(Longitudinal Waves in a Rod)

Equation (9), presented earlier, describes the dynamics of a rod in compression or tension without distributed loading. The longitudinal strain at any location in the member is given by

$$\epsilon_L(x_i , \omega) = \frac{\partial u(x_i , \omega)}{\partial x} \tag{25}$$

Using this relation in conjunction with the central difference method, the second spatial derivative can be approximated as follows

$$\epsilon'_L(x , \omega) \approx \frac{\epsilon_L(x_i + \frac{\Delta}{2} , \omega) - \epsilon_L(x_i - \frac{\Delta}{2} , \omega)}{\Delta} \tag{26}$$

where Δ is separation between the two strain sensors and the error is on the order of the square of the separation distance (See Figure 7). Following the sign convention shown in this figure the direction and amplitude of wave-modes can be approximated by the following relation

$$\begin{bmatrix} \hat{w}_r (0 , \omega) \\ \hat{w}_l (0 , \omega) \end{bmatrix} \cong \begin{bmatrix} \dfrac{1}{2jk} & -\dfrac{1}{2k^2} \\ -\dfrac{1}{2jk} & -\dfrac{1}{2k^2} \end{bmatrix} \begin{bmatrix} \epsilon_L(0 , \omega) \\ \epsilon'_L(0 , \omega) \end{bmatrix} \tag{27}$$

where $x_i = 0$. This expression is equivalent to the sequential measurement scheme in the approximation $k\Delta \ll 1$(eq'n 20). The two methods are related by the following finite difference transformation

$$\begin{bmatrix} \epsilon_L(0 , \omega) \\ \epsilon'_L(0 , \omega) \end{bmatrix} \cong \begin{bmatrix} \dfrac{1}{2} & \dfrac{1}{2} \\ -\dfrac{1}{\Delta} & \dfrac{1}{\Delta} \end{bmatrix} \begin{bmatrix} \epsilon_L(-\frac{\Delta}{2} , \omega) \\ \epsilon_L(\frac{\Delta}{2} , \omega) \end{bmatrix} \tag{28}$$
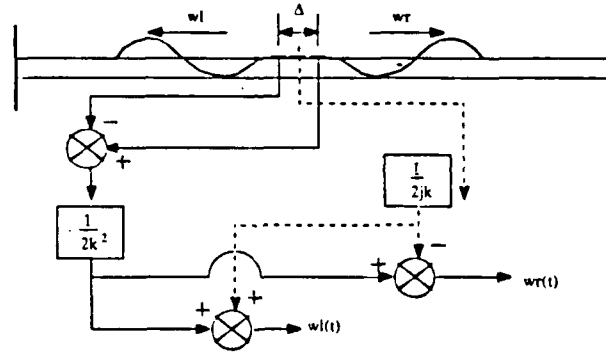
This substitution leads directly to equation-(20).

Figure 7 Illustration of the Spatial Dervative Method for estimating deflections and internal forces to complete the physical state vector at a cross-section. Example of local estimation along a longitudinal rod.

Example B3-(Bending waves in a B-E beam)

Because the second spatial derivative of displacement is related to the curvature of the member, the bending strain corresponding to transverse propagating waves is given by

$$\epsilon_b(x_i , \omega) = -\frac{t_b}{2} \frac{\partial^2 u(x_i , \omega)}{\partial x^2} \tag{29}$$

Again applying the first central difference scheme, the third spatial derivative can be approximated as

$$\epsilon'_b(x_i , \omega) \cong \left\{ \frac{\epsilon_b(x_i + \frac{\Delta}{2} , \omega) - \epsilon_b(x_i - \frac{\Delta}{2} , \omega)}{\Delta} \right\} \cong -\frac{2}{t_b} \frac{\partial^3 u(x_i , \omega)}{\partial x^3} \tag{30}$$

The second derivative of strain yields the fourth derivative of displacement which by equation (12) is related to the local beam acceleration. Applying the central difference method for the second derivative of bending strain, and exploiting equation (12) leads to the following expression for the transverse beam deflection

$$u(0,\omega) \cong \frac{2}{l_b}\frac{EI}{\rho A}\frac{1}{s^2}\left\{\frac{\epsilon_b(\frac{\Delta}{2},\omega) + \epsilon_b(-\frac{\Delta}{2},\omega) - 2\epsilon_b(0,\omega)}{\Delta^2}\right\} \tag{31}$$

where $x_i = 0$ and s is the Laplace variable.

The only element of the physical cross-sectional state vector yet to be accounted for is the local slope. Since the slope represents the rate of change of deflection with respect to position along the member, the deflection at two neighboring points must be found using equation (31) before the slope can be estimated. Applying this method the local slope can be approximated as

$$u'(0,\omega) \cong \frac{u(\frac{\Delta}{2},\omega) - u(-\frac{\Delta}{2},\omega)}{\Delta}$$

$$= \frac{2}{l_b}\frac{EI}{\rho A}\frac{1}{s^2}\left\{\frac{\epsilon_b(\frac{3}{2}\Delta,\omega) - \epsilon_b(-\frac{3}{2}\Delta,\omega) - 3\epsilon_b(\frac{\Delta}{2},\omega) + 3\epsilon_b(-\frac{\Delta}{2},\omega)}{\Delta^3}\right\} \tag{32}$$

The error in this expression is on the order of Δ, the separation between strain sensors.

Equation (32) completes the estimation of elements of the physical state vector at a particular location from only 4 local strain sensors. Combining equations (29-32) with equation (14) we can approximate the evolution of rightward and leftward going wave-modes along a beam member in terms of local strain measurement.

$$
\begin{bmatrix} \hat{w}_{rp}(0,\omega) \\[1em] \hat{w}_{re}(0,\omega) \\[1em] \hat{w}_{lp}(0,\omega) \\[1em] \hat{w}_{le}(0,\omega) \end{bmatrix} = \frac{2}{l_b}
\begin{bmatrix} \frac{1}{4} & \frac{j}{4k} & \frac{j}{4EIk^3} & \frac{-1}{4EIk^2} \\[0.8em] \frac{1}{4} & \frac{-1}{4k} & \frac{1}{4EIk^3} & \frac{1}{4EIk^2} \\[0.8em] \frac{1}{4} & \frac{-j}{4k} & \frac{-j}{4EIk^3} & \frac{-1}{4EIk^2} \\[0.8em] \frac{1}{4} & \frac{1}{4k} & \frac{-1}{4EIk^3} & \frac{1}{4EIk^2} \end{bmatrix}
\begin{bmatrix} \frac{P}{\Delta^2} & \frac{-P}{\Delta^2} & \frac{-P}{\Delta^2} & \frac{P}{\Delta^2} \\[0.8em] \frac{-P}{\Delta^3} & \frac{3P}{\Delta^3} & \frac{-3P}{\Delta^3} & \frac{P}{\Delta^3} \\[0.8em] 0 & \frac{EI}{\Delta} & \frac{-EI}{\Delta} & 0 \\[0.8em] 0 & \frac{-EI}{2} & \frac{-EI}{2} & 0 \end{bmatrix}
\begin{bmatrix} \epsilon_b(-\frac{3}{2}\Delta,\omega) \\[1em] \epsilon_b(-\frac{\Delta}{2},\omega) \\[1em] \epsilon_b(\frac{\Delta}{2},\omega) \\[1em] \epsilon_b(\frac{3}{2}\Delta,\omega) \end{bmatrix}
$$

$$P = \frac{EI}{\rho A s^2} \tag{33}$$

As in the sequential sensor scheme, contributions due to the evanescent terms can be considered negligible when measurements are taken more than a wavelength away from structural discontinuities. This implies that the rightward and leftward propagating components can be found from extracting the 1st and 3rd rows of the matrix given in equation (31). It was pointed out earlier, however, that this expression is not realizable in real-time because the terms in the third column of the matrix in equation (33) are non-causal. However, since the evanescent terms have been considered negligible it is possible to exploit the remaining causal terms in equation (33) to derive an expression which uses only knowledge of local bending strain ϵ_b and slope-u' to estimate the propagating wave components w_{rp} and w_{lp}. Such an approximation would lead to the following equation for the propagating wave components for a beam

$$
\begin{bmatrix} \hat{w}_{rp}(0,\omega) \\[1em] \hat{w}_{lp}(0,\omega) \end{bmatrix} = \frac{2}{l_b}
\begin{bmatrix} \frac{j}{2k} & \frac{-1}{2EIk^2} \\[0.8em] \frac{-j}{2k} & \frac{-1}{2EIk^2} \end{bmatrix}
\begin{bmatrix} \frac{-P}{\Delta^3} & \frac{3P}{\Delta^3} & \frac{-3P}{\Delta^3} & \frac{P}{\Delta^3} \\[0.8em] 0 & \frac{-EI}{2} & \frac{-EI}{2} & 0 \end{bmatrix}
\begin{bmatrix} \epsilon_b(-\frac{3}{2}\Delta,\omega) \\[1em] \epsilon_b(-\frac{\Delta}{2},\omega) \\[1em] \epsilon_b(\frac{\Delta}{2},\omega) \\[1em] \epsilon_b(\frac{3}{2}\Delta,\omega) \end{bmatrix} \tag{34}
$$

Since the local deflection and slope represent a causal pair of physical measurements they can also be used to estimate propagating wave components far away from structural discontinuities. However, such a selection would introduce additional resolution errors associated with inaccuracies in estimating local deflection from four point strain measurements. Other non-realizable pairs include (deflection & strain) and those physical measurements which are combined with an estimate of the internal shear force at a cross-section.

3.2.3 Optimal Sensor Spacing in the Presence of Noise

Up until this point we have ommitted any restrictions imposed by the possibility of noisy strain

measurements. Clearly we will not be able to choose the separation distance Δ arbitrarily small since the difference between strain signals will become very small, potentially smaller than the noise level in the measurement. Further restrictions will be imposed by the occurence of spatial aliasing, limiting the smallest resolvable wavelength that can be accurately detected by this measurement scheme. The optimal spacing between succesive strain sensors will be based on our ability to achieve the maximum rms signal to noise level for each wave component for a given noise spectrum and stencil configuration.

Assuming that the sensors are corrupted with stationary, uncorrelated white noise, the wave sensor observation integral determines the estimated wave components from the following equation.

$$\hat{w}\ (t) = \int_0^t f\ (\Delta, t - \tau)(\epsilon(\tau) + n(\tau))$$

(35)

where $f(\Delta, t-\tau)$ is the convolution kernel associated with the observation matrix-$F(\Delta,\omega)$, $n(\tau)$ is the noise vector and $\epsilon(\tau)$ is vector of discrete strain measurements. This convolution expression permits the covariance matrix-$\phi_{ww}(\tau)$ for the estimated wave components to be computed from

$$\phi_{ww}(\ \tau\ ) = E(\ w(\ t\ )w^T(\ t\ +\ \tau))$$

$$= \int_{-\infty}^{\infty} d\tau_1 \int_{-\infty}^{\infty} d\tau_2 f(\ \Delta, \tau_1\ ) E((\ \epsilon(t-\tau_1)\ +\ n(t-\tau_1))$$

$$\cdot\ (\ \epsilon(t + \tau - \tau_2)\ +\ n(t + \tau - \tau_2))^T\ )f(\ \Delta, \tau_2\ )^T$$

(36)

where $\phi_{\epsilon\epsilon}(\tau)$ and $\phi_{nn}(\tau)$ are the covariance matrices for the deterministic and stochastic part of the measurement. The power spectral density matrix is found by taking the fourier transform of the covariance matrix $\phi_{ww}(\tau)$. This leads to

$$\Phi_{ww}(\ \omega\ ) = F(\ \Delta, s\ ) \left(\begin{bmatrix} \Phi_{\epsilon_1\epsilon_1}(\ \omega\ ) \dots \dots \Phi_{\epsilon_1\epsilon_n}(\ \omega\ ) \\ \vdots \\ \vdots \\ \Phi_{\epsilon_n\epsilon_1}(\ \omega\ ) \dots \dots \Phi_{\epsilon_n\epsilon_n}(\ \omega\ ) \end{bmatrix} + \begin{bmatrix} \Phi_{n_1 n_1}(\ \omega\ ) & & \\ & \ddots & 0 \\ & & \ddots \\ & 0 & & \\ & & & \Phi_{n_1 n_1}(\ \omega\ ) \end{bmatrix} \right) F(\ \Delta, -s\ )^T$$

(37)

Because each elastic waveguide couples the spatially non-colocated strain measurements, there will be off-diagonal elements appearing in the $\Phi_{ww}(\omega)$ matrix. These cross-spectra terms are essential for determining the optimal sensor spacing along a member. If no correlation exists between the spatially non-collocated sensors then relative phase information between each sensor is lost and it is impossible to infer the magnitude and directionality of each wave component.

Example L4 (Longitudinal Waves in a Rod)
The power spectral density matrix for wave propagation along a longitudinal rod is given by

$$\Phi_{ww}(\ \omega\ ) = \begin{bmatrix} F_{11}(\ \Delta, s\ ) & F_{12}(\ \Delta, s\ ) \\ F_{21}(\ \Delta, s\ ) & F_{22}(\ \Delta, s\ ) \end{bmatrix} \Phi_{\epsilon\epsilon}(\ \omega\ ) + \Phi_{nn}(\ \omega\ ) \begin{bmatrix} F_{11}(\ \Delta, -s\ ) & F_{21}(\ \Delta, -s\ ) \\ F_{12}(\ \Delta, -s\ ) & F_{22}(\ \Delta, -s\ ) \end{bmatrix}$$

(38)

where $\Phi_{\epsilon 2\epsilon 1}(\omega) = (\Phi_{\epsilon 1\epsilon 2}(\omega)^*)$-(*-denotes complex conjugate). The estimated rms response of the rightward and leftward wave components are available from the diagonal elements of this matrix.

$$\left(\Phi_{w_r w_r}(\ \omega\ ) \right)_{rms} = \left(\Phi_{w_l w_l}(\ \omega\ ) \right)_{rms}$$

$$= \sqrt{\frac{\Phi_{\epsilon_1\epsilon_1} + \Phi_{\epsilon_2\epsilon_2} - 2\cos(k\Delta)Re(\Phi_{\epsilon_1\epsilon_2}) - 2\sin(k\Delta)Im(\Phi_{\epsilon_1\epsilon_2})}{4 k^2 \sin^2(k\Delta)}}$$

(39)

where Re and Im denote the real and imaginary parts of the of the cross-spectra term $\Phi_{\epsilon 1\epsilon 2}(\omega)$ respectively.

The points where this expression has an extremum can be found by computing its derivative with respect to Δ and equating the result to zero. Hence, the necessary condition for the existence of a maximum is

$$\cos^2(\ k\Delta\ ) - \frac{\Phi_{\epsilon_1\epsilon_1} + \Phi_{\epsilon_2\epsilon_2} + \Phi_{nn}}{Re(\Phi_{\epsilon_1\epsilon_2})}\cos(\ k\Delta\ ) + \frac{Im(\Phi_{\epsilon_1\epsilon_2})}{Re(\Phi_{\epsilon_1\epsilon_2})}\sin(\ k\Delta\ )\cos(\ k\Delta\ ) - 1 = 0$$

(40)

Finding the exact solution of equation (40) is cumbersome since it requires solving a fourth order polynomial. To gain insight into the optimal sensor spacing we can make some limiting approximations

which spectrally factor the solution into its low and high frequency parts. At low frequencies-($k\Delta<<1$) it is reasonable to assume that the $\text{Im}(\Phi_{\epsilon1\epsilon2}(\omega))<<\text{Re}(\Phi_{\epsilon1\epsilon2}(\omega))$. This implies that the non-dimensional optimal spacing can be found from the following expression

$$k\Delta = \cos^{-1}\left\{\left(\frac{\Phi_{\epsilon_1\epsilon_1} + \frac{\Phi_{nn}}{2}}{\text{Re}(\Phi_{\epsilon_1\epsilon_2})}\right) \pm \sqrt{1 + \left(\frac{\Phi_{\epsilon_1\epsilon_1} + \frac{\Phi_{nn}}{2}}{\text{Re}(\Phi_{\epsilon_1\epsilon_2})}\right)^2}\right\}; \quad (Low\ Frequency)$$

(41)

where $\Phi_{\epsilon1\epsilon1}(\omega)=\Phi_{\epsilon2\epsilon2}(\omega)$. The sign of the real part of ($\Phi_{\epsilon1\epsilon2}(\omega)$) determines whether the positive or negative sign of the radical should be used to compute the optimal sensor spacing. When the argument of this expression is equal to +/-1 there is ambiguity in determining the optimal sensor spacing-($\cos(n\pi)=\cos(k\Delta)=+/-1$ for n=0,1,2....). However, this expression is restricted to the low frequency part of the spectrum where spatial aliasing does not occur for $k\Delta<<1$. To first order the linear approximation to equation (40) gives

$$k\Delta = \frac{2\Phi_{\epsilon_1\epsilon_1} + \Phi_{nn}}{\text{Im}(\Phi_{\epsilon_1\epsilon_2})}; \quad \text{Im}(\Phi_{\epsilon_1\epsilon_2}) \neq 0$$

(42)

as a rough estimate for the optimal sensor spacing.

At high frequencies or $k\Delta >>1$ the full non-linear form of equation (40) is required to determine the optimal spacing between point sensors, but the solution is of little practical importance.

3.2.4 Transient Behavior of the Spatially Sequential Approach

The preceding sections of this paper have developed all ideas in the frequency domain. Although general transients are not excluded from this frequency domain discussion, it is often difficult to make the transition to time response. This section presents a particular transient response of a particular wave sensing scheme. The example is motivated by a desire to enhance intuitive understanding of the wave decoupling procedure.

Example 1.5-(Longitudinal Waves in a Rod)

This section calculates the transient response of a first order-(linear in $k\Delta$) wave-mode filter using two strain sensors spaced a distance Δ apart. We excite the sensor with a sinusoidal wave train arriving from the left at t=0. If we assume that the rod is semi-infinite and that only a rightward travelling longitudinal wave is present in the member than we would hope that our approach would indicate the presence of only a rightward going wave. Before we attempt to examine how well the first order approximation achieves decoupling of wave components along a rod, it is convenient to express equation (20) in state-space form:

$$x = Ax + B\epsilon$$

$$w = \begin{bmatrix} C_{11} \\ C_{21} \end{bmatrix} x + \begin{bmatrix} C_{12} \\ C_{22} \end{bmatrix} x + D\epsilon$$

(43)

where the linear time invariant matrices are

$$A = \begin{bmatrix} 0 & 1 \\ 0 & 0 \end{bmatrix}; \quad B = \begin{bmatrix} 0 \\ 1 \end{bmatrix}; \quad C_{11} = \begin{bmatrix} \frac{-c^2}{2\Delta} & \frac{-c}{4} \end{bmatrix}; \quad C_{12} = \begin{bmatrix} \frac{c^2}{2\Delta} & \frac{-c}{4} \end{bmatrix};$$

$$C_{21} = \begin{bmatrix} \frac{-c^2}{2\Delta} & \frac{c}{4} \end{bmatrix}; \quad C_{22} = \begin{bmatrix} \frac{c^2}{2\Delta} & \frac{c}{4} \end{bmatrix}; \quad D = \begin{bmatrix} 0 \end{bmatrix}; \quad c = \sqrt{\frac{EA}{\rho A}}$$

Assuming that we have perfect strain sensors, we can describe the evolution of rightward and leftward components using the following convolution integrals

$$\begin{bmatrix} \hat{w}_r(0,t) \\ \hat{w}_l(0,t) \end{bmatrix} = \begin{bmatrix} C_{11} \\ C_{21} \end{bmatrix}_0^t e^{A(t-\tau)}B\epsilon_1(\tau)d\tau + \begin{bmatrix} C_{12} \\ C_{22} \end{bmatrix}_0^t e^{A(t-\tau)}B\epsilon_2(\tau)d\tau$$

(44)

where ϵ_1 and ϵ_2 are the strain measurements taken at location 1-(x=-Δ/2) and 2-(x=Δ/2). As mentioned earlier suppose a cosine deflection u(x,t)=Mcos(ω_n(t-t$_0$)) wave is incident from the left arriving at sensor 1 at t=0. Then sensors 1 and 2 would measure the following strains

$$\epsilon_1(t) = M\frac{\omega_o}{c}\sin(\omega_o t); \quad t \geq 0$$

$$\epsilon_2(t') = M\frac{\omega_o}{c}\sin(\omega_o(t-t_o)); \quad t \geq t_o = \frac{\Delta}{c}$$

(45)

where M is the strain amplitude and ω_o is the frequency of the travelling wave. Substituting for ϵ_1 and ϵ_2 in

equation (43) we find that

$$
\begin{bmatrix} \hat{w}_r \,(\,0\,,t\,) \\ \hat{w}_l \,(\,0\,,t\,) \end{bmatrix} = \begin{bmatrix} C_{11} \\ C_{21} \end{bmatrix} \int_0^t e^{A(t-\tau)} BM \frac{\omega_o}{c} \sin(\,\omega_o \tau\,)\, d\tau + \begin{bmatrix} C_{12} \\ C_{22} \end{bmatrix} \int_0^t e^{A(t-t_o-\tau)} BM \frac{\omega_o}{c} \sin(\,\omega_o \tau\,)\, d\tau
$$

$$ t \geq 0 \qquad\qquad\qquad t \geq t_o = \frac{\Delta}{c} $$

(46)

Substituting for matrices A and B and integrating equation (45) with all initial conditions set to zero leads to the following temporal evolution of the rightward and leftward travelling components

$$
\begin{bmatrix} \hat{w}_r \,(\,0\,,t\,) \\ \hat{w}_l \,(\,0\,,t\,) \end{bmatrix} = \begin{bmatrix} C_{11} \\ C_{21} \end{bmatrix} \begin{bmatrix} \dfrac{-\sin(\,\omega_o t\,)}{\omega_o^2} + \dfrac{t}{\overline{\omega}_o} \\[4mm] \dfrac{-\cos(\,\omega_o t\,)}{\omega_o^2} + \dfrac{1}{\overline{\omega}_o} \end{bmatrix} M \frac{\omega_o}{c} + \begin{bmatrix} C_{21} \\ C_{22} \end{bmatrix} \begin{bmatrix} \dfrac{-\sin(\,\omega_o(t-t_o)\,)}{\omega_o^2} + \dfrac{t-t_o}{\overline{\omega}_o} \\[4mm] \dfrac{-\cos(\,\omega_o(t-t_o)\,)}{\omega_o^2} + \dfrac{1}{\overline{\omega}_o} \end{bmatrix} M \frac{\omega_o}{c}
$$

$$ (\,t \geq 0\,) \qquad\qquad\qquad (\,t \geq t_o = \frac{\Delta}{c}\,) $$

(47)

Notice in these expressions how the restriction on the initial condition leads to steady state sinusoidal dynamics superposed upon a ramp. Fortunately, for $t > t_o$ the effect of the ramp cancels out and we are only left with the dynamics of a sinusoid. This is apparent when we substitute for the C matrices, i.e.

$$
\hat{w}_r \,(\,0\,,t\,) = \left\{ \frac{c \sin(\,\omega_o t\,)}{2\,\Delta\omega_o} - \frac{ct}{2\,\Delta} + \frac{\cos(\,\omega_o t\,)}{4} - \frac{1}{4} \right\} M + \qquad (\,t \geq 0\,)
$$

$$
\left\{ \frac{c}{2\,\Delta}\left(\frac{-\sin(\,\omega_o(t-t_o)\,)}{\omega_o} \right) + \left(\frac{\cos(\,\omega_o(t-t_o)\,)}{4} \right) - \frac{1}{4} + \frac{c(t-t_o)}{2\,\Delta} \right\} M \quad (\,t \geq t_o = \frac{\Delta}{c}\,)
$$

(48)

and

$$
\hat{w}_l \,(\,0\,,t\,) = \left\{ \frac{c \sin(\,\omega_o t\,)}{2\,\Delta\omega_o} - \frac{ct}{2\,\Delta} - \frac{\cos(\,\omega_o t\,)}{4} + \frac{1}{4} \right\} M + \qquad (\,t \geq 0\,)
$$

$$
\left\{ -\frac{c}{2\,\Delta}\left(\frac{\sin(\,\omega_o(t-t_o)\,)}{\omega_o} \right) - \left(\frac{\cos(\,\omega_o(t-t_o)\,)}{4} \right) + \frac{1}{4} + \frac{c(t-t_o)}{2\,\Delta} \right\} M \quad (\,t \geq t_o = \frac{\Delta}{c}\,)
$$

(49)

For $t < t_o$ no decoupling is achieved and the both wave component estimates undergo a transient phase which leads to a dc offset in the temporal evolution of their approximate decoupled state. This offset can be estimated for every frequency component in the spectrum of the measurement by considering only the temporal history of equations (48) and (49) up until t_o. Thus, the dc offset in the rightward and leftward wave components can be estimated at each frequency ω_o from the following expressions:

$$
\hat{w}_r \,(\,0\,,t_o\,) = \left(\frac{-5\,\omega_o^2\,\Delta^2}{24\,c^2} \right) M
$$

(50)

$$
\hat{w}_l \,(\,0\,,t_o\,) = \left(\frac{\omega_o^2\,\Delta^2}{24\,c^2} \right) M
$$

(51)

For $t > t_o$ decoupling is approximately achieved; the effect of the ramp cancels and we are only left with the steady state dynamics about the dc offset for each wave component.

$$
\hat{w}_r \,(\,0\,,t\,) = M\,(\cos(\,\omega_o(t)\,) - 1\,) - \frac{5\,\omega_o^2\,\Delta^2}{24\,c^2} M \quad (\,t \geq t_o\,)
$$

(52)

$$
\hat{w}_l \,(\,0\,,t\,) = \frac{\omega_o^2\,\Delta^2}{24\,c^2} M \cos(\,\omega_o t\,) + \frac{\omega_o^2\,\Delta^2}{24\,c^2} M \quad (\,t \geq t_o\,)
$$

(53)

The above expressions are good to second order in the argument $\omega_o t_o$. Figure 8 shows the transient and steady state dynamics for a generic wave travelling to the right along a rod.
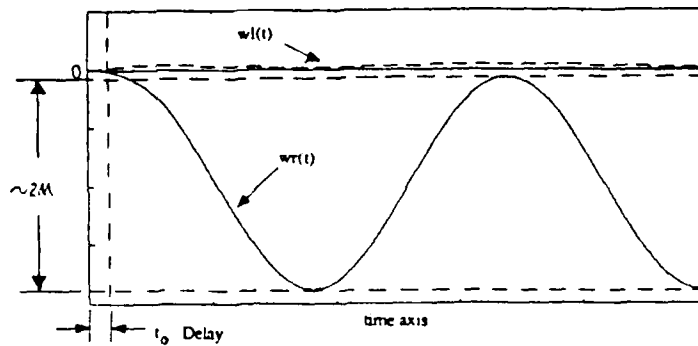
Figure 8 Temporal evolution of rightward and leftward propagating components along a longitudinal rod.
$u(x,t) = M \sin \omega_0(t - x/c)$

3.2.5 The Wave Sensor Transfer Function

Because of the assumed form of the solution which is used to infer wave propagation along 1-dimensional structures, an inherent difficulty associated with the decoupling of rightward and leftward wave components is the realizability of elements of the observation matrix $F(\Delta,\omega)$. Since the elements of this matrix are typically infinite dimensional we must approximate them by low order elements-(e.g. linear in $k\Delta$) which are physically realizable. Unfortunately, this linearization limits our ability to achieve perfect decoupling of rightward and leftward wave components from discrete measurements. However, if the condition $k\Delta \ll 1$ is satisfied we expect that rightward and leftward components will be sufficiently decoupled from one another.

The required transfer function from actual wave-modes present to wave-mode estimates delivered by the sensor is given by

$$\hat{w} = H(\Delta,\omega)w + F(\Delta,\omega)n \tag{54}$$

where $H(\Delta,\omega)$ is the wave sensor transfer function, n is the vector of uncorrelated noises, w is the vector of actual wave-modes and w represents the vector of wave sensor estimates. In all of these approaches the wave-modes which are present in a member are infered from physical variables $y(x,\omega)$ using a frequency dependent transformation of the form:

$$y = \left[F^{-1}(\omega) \right]w \tag{55}$$

Each approach works by attempting to invert $F^{-1}(\omega)$. This is done approximately for a variety of reasons:

1. Not always possible to implement $F(\omega)$ with causal filters.

2. Prefer a first order approximation to $F(\omega)$ rather than an infinite-order solution.
3. The model is not accurate over all frequencies.

Further, the physical measurements $y(x,\omega)$ are corrupted with noise. This leads to two kinds of imperfections in the approaches outlined in this paper; $\hat{F}$ is not F and $\hat{y}$ is not y. The wave sensor output for w is thus $\hat{w}$.

$$\hat{w} = \hat{F}(\Delta,\omega)\,\hat{y}$$

$$= \hat{F}(\Delta,\omega)(y + noise) \tag{56}$$

But $y = F^{-1}(\Delta,\omega)w$. This implies that

$$\hat{w} = \hat{F}(\Delta,\omega)F^{-1}(\Delta,\omega)w + \hat{F}(\Delta,\omega)(noise) \tag{57}$$

Example L6 (Longitudinal Waves in a Rod)

Considering examples L2 and L5 again we know from the exact model given in equations (17) and (18) that

$$\begin{bmatrix} u'(\frac{-\Delta}{2},\omega) \\ u'(\frac{\Delta}{2},\omega) \end{bmatrix} = F^{-1}w = jk \begin{bmatrix} -e^{jk\frac{\Delta}{2}} & e^{-jk\frac{\Delta}{2}} \\ -e^{-jk\frac{\Delta}{2}} & e^{jk\frac{\Delta}{2}} \end{bmatrix} \begin{bmatrix} w_r(0,\omega) \\ w_l(0,\omega) \end{bmatrix} \tag{58}$$

Substituting equations (20) and (58) into equation (57) gives the corresponding wave sensor transfer function to first order for a rod.

$$
\begin{bmatrix} \hat{w}_r \\ \hat{w}_l \end{bmatrix} = \begin{bmatrix} 1 & \dfrac{k^2 \Delta^2}{24} \\ \dfrac{k^2 \Delta^2}{24} & 1 \end{bmatrix} \begin{bmatrix} w_r \\ w_l \end{bmatrix} + \begin{bmatrix} \dfrac{1}{2k^2\Delta} - \dfrac{1}{4jk} & -\dfrac{1}{2k^2\Delta} - \dfrac{1}{4jk} \\ \dfrac{1}{2k^2\Delta} + \dfrac{1}{4jk} & -\dfrac{1}{2k^2\Delta} + \dfrac{1}{4jk} \end{bmatrix} \begin{bmatrix} n_1 \\ n_2 \end{bmatrix}
$$

(59)

The first order approximation to F(Δ,ω) leads to off-diagonal terms of second order which couple actual rightward and leftward wave components to their estimates. However, for low frequencies-(kΔ<<1) these off-diagonal contributions can be considered to be negligible. The estimated wave components are thus decoupled except for the presence of measurement noise in the sensors.

4.0 IMPLEMENTATION ISSUES

The previous sections have outlined two similar approaches for observing wave components from spatially discrete local measurements along a compression rod and a Bernoulli-Euler beam. For the rod analog circuitry will suffice to implement the elements of the observation matrix F(Δ,ω). In the case of the beam, altough methods have been developed which can simulate terms with $(i\omega)^{(1/2)}$ dependencies[16], all the schemes developed in this paper required further acausal filtering. We have not yet discovered a causal scheme, applicable to the B-E beam over an arbitrarily broad frequency range. However, the observation methods discussed in this paper are only valid in the frequency range where the mathematical models provide an accurate description of the system dynamics. Thus, the bandwidth of accuracy will not only be limited by the model accuracy but also by spatial aliasing, instrumentation and the level of the signal to noise ratio.

In addition to giving rise to the phenomenon of spatial aliasing, discretization also affects the resolution of a measured distubance. Since a single sensor spacing stencil will only provide optimal resolution in a narrowband about $\Delta_{opt}(\omega_b)$-(b denotes bandwidth of signal), broadband signals may suffer some loss in resolution for frequencies $\omega<<\omega_b$. To improve the resolution for these frequency components, it may be advantageous to construct an additional wave-mode observer which has higher sensitivity in a lower frequency range(See Figure 9). This will require that a second sensor stencil be estabilished to resolve the lower frequency components. The two observers can be combined by passing the higher frequency components through the first stencil and lower frequency components through the second and then summing the resulting signals. This approach leads to higher resolution of a broadband measurement.
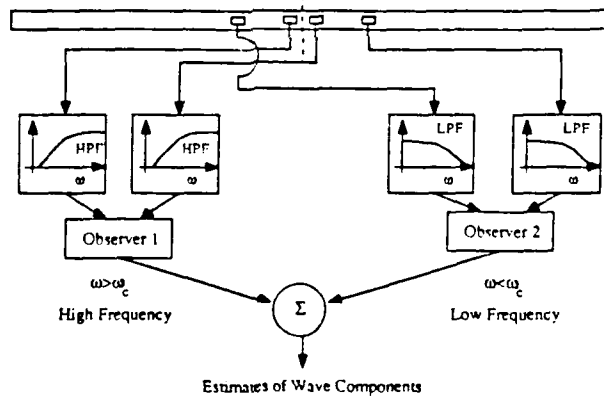

Figure 9 Possible scheme for resolving broadband signals. Two sensor stencils are employed to resolve the high and low frequency ends of the spectrum.

5.0 SUMMARY

In this paper theoretical procedures have been developed for estimating wave components which propagate along one-dimensional members from spatially colocated and non colocated measurements. In each procedure we have derived temporal filters which decouple wave-mode states from local physical measurements in a member. The problem with these filters, however, is that for dispersive mediums they are not guaranteed to be causal. This acausal behavior makes it difficult to observe all wave components which may propagate along a dispersive member. For certain physical geometries, however, where the response of the member is dominated by evanescent or propagating dynamics, approximations can be made to render a subset of the full wave-mode vector observable by exploiting only the causal entries of the observation matrix, or by limiting interest to a relatively narrow frequency range.

Besides being limited by the dispersive nature of the medium, the non-colocated approach is also complicated by the phenomenon of spatial aliasing. This arises from the fact that this approach uses point sensors which are postitioned symmetrically about the location where waves are to be inferred. For wavelengths which are small compared to sensor spacing there will be ambiguity in determing the true wavelength being resolved by this observation scheme. This restricts the non-colocated scheme to those wavelengths which are large compared to sensor spacing. Thus, a first-order approximation to the entries of the observation matrix is sufficient for practical implementation.

Sensor noise further restricts the bandwidth of the non-colocated observation scheme to those signals which are large compared to the noise level. Optimal resolution is achieved when the sensor spacing is chosen to maximize the signal-to-noise ratio of each wave component at each frequency. Of couse for broadband signals multiple sensor stencils may be required to adequately resolve all frequencies which may be present in the dynamics.

The next logical step in this work is to experimentally verify the procedures outlined in this paper and to subsequently combine them with previously developed active wave control methods.

6.0 REFERENCES

[1]   M.J. Balas, "Direct Velocity Feedback Control of Large Space Structures," *Journal of Guidance, Control, and Dynamics*, Vol. 2, No. 3, May-June 1979.

[2]   J-N. Auburn, J.A. Breakwell, N.K. Gupta, M.G. Lyons, and G. Marguiles, "ACOSS FIVE(Active Control of Space Structures) PHASE 1A, "*Lockheed Missiles and Space Co.*, Inc. Report AD-A116655, Mar. 1980-sept. 1981.

[3]   M.J. Balas, "Trends in Large Space Structure Control Theory: Fondest Hopes, Wildest Dreams, "*IEEE Transactions on Automatic Control*, Vol. AC-27, No. 3, June 1982, pp. 522-535.

[4]   A.H. von Flotow, "The Acoustic Limit of Structural Dynamics," *Large Space Structures; Dynamics and Control*, chapter edited by S. Atluri and T. Amos, Springer Verlag, 1987.

[5]   D.J. Pines and A.H. von Flotow, "Active Control of Bending Waves at Acoustic Frequencies," *1989 Automatic Control Corference*, Pittsburg, Pa.

[6]   C.H. Hansen, S.D. Snyder and C.R. Fuller, "Active Control of Structurally-Radiated Noise using Piezoceramic Actuators," *in print for Internoise-89*, Newport Beach, CA.

[7]   D.W. Miller, "Modelling and Active Modification of Wave Scattering in Structural Networks," *1988 PhD Dissertation, Department of Aeronautics and Astronautics*, Massachusetts Institute of Technology, Cambridge, Mass.

[8]   A.H. von Flotow, "Disturbance Propagation in Stuctural Networks," *Journal of Sound and Vibration*, 106(3), pp 433-450, 1986.

[9]   A.H. von Flotow and B. Schaefer, "Wave-Absorbing Controllers for a Flexible Beam", *Journal of Guidance, Control and Dynamics*, Vol. 9 No. 6, pp 673-680, Nov-Dec 1986.

[10]   Mace, B.R., "Active Control of Flexural Vibrations," *Journal of Sound and Vibration*, 114(2), pp. 253-270, 1987.

[11]   R.J. Mckinnell, "Active Vibration Isolation by Cancelling Bending Waves," *Proceedings of the Royal Society of London*, A 421, pp 357-393, 1989.

[12]   G. Pavic, "Measurement of Structure Borne Wave Intensity Part I: Formulation of the methods," *Journal of Sound and Vibration*, 49(2), pp 221-230, 1976.

[13]   G. Pavic, Measurement of Vibrations By Strain Gauges, Part I: Theoretical Basis," *Journal of Sound and Vibration*, 102(2), pp 153-163, 1985.

[14]   G. Pavic, Measurement of Vibrations By Strain Gauges, Part II: Selection of Measurement Parameters," *Journal of Sound and Vibration*, 102(2), pp 163-188, 1985.

[15]   L. Cremer, M. Heckl and E.E. Ungar, "Structure-Borne Sound," *Springer Verlag*, Berlin, 1973.

[16]   C.A. Halijak, G.E. Carlson, "Approximation of Fractional Operators $(1/s)^{1/n}$ by a Regular Newton Process," *IEEE Transactions on Circuit Theory*, June 1964, pp 210-213.